

Some pages of this thesis may have been removed for copyright restrictions.

If you have discovered material in Aston Research Explorer which is unlawful e.g. breaches copyright, (either yours or that of a third party) or any other law, including but not limited to those relating to patent, trademark, confidentiality, data protection, obscenity, defamation, libel, then please read our [Takedown policy](#) and contact the service immediately (openaccess@aston.ac.uk)

**SYNTHESIS AND CHARACTERISATION OF
INTERFACIAL LAYERS IN ORGANIC SOLAR CELLS**

by

Anna Isakova

Doctor of Philosophy

Aston University

Chemical Engineering and Applied Chemistry

September 2015

©Anna Isakova, 2015

Anna Isakova asserts her moral right to be identified as the author of this thesis.

This copy of the thesis has been supplied on condition that anyone who consults it is understood to recognise that its copyright rests with its author and that no quotation from the thesis and no information derived from it may be published without appropriate permission or acknowledgement.

Preamble

This thesis is a result of collaborative work, carried out as a part of the European Project ESTABLIS (FP7/ 2011 under grant agreement 290022). This project is dedicated to research into organic photovoltaics, aiming at extending their lifetime to 10-15 years in order to make this technology widely available and marketable. The collaborative effort of Establis includes synthesis of new materials, device fabrication and studies of their stability under operational conditions, spectroscopic, electric, physical and mechanical measurements, all resulting in unravelling the mechanisms of device degradation and, as a result, development of new, more stable organic solar cells.

The work described in this thesis is a result of a cotutelle agreement between Aston University (Birmingham, UK) under supervision of Dr Paul Topham and Autonomous University of Madrid (Madrid, Spain), carried out at IMDEA Nanociencia (Madrid, Spain) under supervision of Dr Larry Lüer.

Aston University

Synthesis and characterisation of interfacial layers in organic solar cells

Anna Isakova

Doctor of Philosophy

2015

Thesis summary

The quest for renewable energy sources has led to growing attention in the research of organic photovoltaics (OPVs), as a promising alternative to fossil fuels, since these devices have low manufacturing costs and attractive end-user qualities, such as ease of installation and maintenance. Wide application of OPVs is majorly limited by the devices lifetime. With the development of new encapsulation materials, some degradation factors, such as water and oxygen ingress, can almost be excluded, whereas the thermal degradation of the devices remains a major issue. Two aspects have to be addressed to solve the problem of thermal instability: bulk effects in the photoactive layer and interfacial effects at the photoactive layer/charge-transporting layers.

In this work, the interface between photoactive layer and electron-transporting zinc oxide (ZnO) in devices with inverted architecture was engineered by introducing polymeric interlayers, based on zinc-binding ligands, such as 3,4-dihydroxybenzene and 8-hydroxyquinoline. Also, a cross-linkable layer of poly(3,4-dimethoxystyrene) and its fullerene derivative were studied. At first, controlled reversible addition-fragmentation chain transfer (RAFT) polymerisation was employed to achieve well-defined polymers in a range of molar masses, all bearing a chain-end functionality for further modifications. Resulting polymers have been fully characterised, including their thermal and optical properties, and introduced as interlayers to study their effect on the initial device performance and thermal stability.

Poly(3,4-dihydroxystyrene) and its fullerene derivative were found unsuitable for application in devices as they increased the work function of ZnO and created a barrier for electron extraction. On the other hand, their parental polymer, poly(3,4-dimethoxystyrene), and its fullerene derivative, upon cross-linking, resulted in enhanced efficiency and stability of devices, if compared to control. Polymers based on 8-hydroxyquinoline ligand had a negative effect on the initial stability of the devices, but increased the lifetime of the cells under accelerated thermal stress. Comprehensive studies of the key mechanisms, determining efficiency, such as charge generation and extraction, were performed by using time-resolved electrical and spectroscopic techniques, in order to understand in detail the effect of the interlayers on the device performance. Obtained results allow deeper insight into mechanisms of degradation that limit the lifetime of devices and prompt the design of better materials for the interface stabilisation.

Keywords: organic photovoltaics; thermal stability; polymeric interlayers; RAFT; transient absorption spectroscopy.

List of publications

- A. Isakova, S. Dowland, S. Karuthedath, A. Distler, H.-J. Egelhaaf, P. D. Topham, and L. L  er, "Decoupling Blend Morphology Segregation from Other Degradation Effects in Organic Photovoltaics Using Time-Resolved Techniques," *submitted*, 2015.
- A. Isakova, P. D. Topham, and A. J. Sutherland, "Controlled RAFT Polymerization and Zinc Binding Performance of Catechol-Inspired Homopolymers," *Macromolecules*, vol. 47, no. 8, pp. 2561–2568, Apr. 2014.

Acknowledgments

There are no words enough to express my gratitude and admiration to Dr Paul Topham: without him this thesis would never be possible. It's his support and advice that kept me going through these three years of hard work and lots of fun.

My biggest "thank you" goes to Dr Larry L  er for all his patience and for showing me what great fun physics can be. Work with him was a life-changing experience.

A special "thank you" is addressed to Dr Melanie Pedeutour and Dr Roger Hiorns, who made Establis possible and running for almost four years. It was never easy but it was worth it. It has been a genuine pleasure to be a part of the Establis community. Those meetings and conferences we attended together will always be remembered with a good laugh. Especially, I would like to thank those people whose input into this work led to great results: Aurelien Tournebize, Dr Hugo Santos Silva, Dr Graham Morse, Dr Johannes Gierschner and Dr Juan Cabanillas-Gonzalez. Especially, Dr Simon Dowland has forever earned my gratitude for enduring me during my stay at Belectric OPV and his studies will all my endless materials.

Of all these people, Shafkath Karuthedath is acknowledged the most for being an amazing labmate and friend, his expertise in anything time-dependent, our endless discussions and all the good times we shared together.

I'd love to pass my gratitude to my colleagues at IMDEA Nanociencia Institute, especially my office fellows Water Liu and Benny, for their friendship and support during such short but amazing visit to Madrid.

I also would like to give thanks to Dr Dan Toolan (Sheffield University) for his help with AFM and all our collaborative work.

From the bottom of my heart, I want to thank all CEAC members, past and present, and especially current residents of MB111, namely Jefferies, Robsy, Christian, Georgie, Sim-Sim, Selma and Taylor. Our fun, our parties and our tea breaks were the fuel that pushed me forward at all times. I can hardly express my devotion to you for being my friends throughout all of these years.

My special thanks also go to Dr Olga Efremova (University of Hull) for becoming my true friend and for sharing the lab life with me in such a delightful manner of hers.

A big "spasibo" (thank you) is addressed to my best friends and family Christina, Hulia and Zoya for their endless support and inspiration. They prove that for real friendship there is no time and distance.

The last and undoubtedly the most important words of gratitude go to my Mum. I want to believe that her impregnable faith in me, her consolation in times of despair, her smile and tears have never been in vain. Her presence in my life is the greatest gift I have received.

Abbreviations

AFM	atomic force microscopy
AIBN	α,α' -azoisobutyronitrile
BHJ	bulk heterojunction
CDCl_3	chloroform
CTA	chain transfer agent
\bar{D}	molar mass dispersity
DDMAT	S-1-dodecyl-S'-(α,α' -dimethyl- α'' -acetic acid)trithiocarbonates
DFT	density functional theory
DMS	3,4-dimethoxystyrene
D_p	degree of polymerisation
DSC	differential scanning calorimetry
EADS	evolution-associated differential spectrum
EQE	external quantum efficiency
ETL	electron-transporting layer
FF	fill factor
FUL	fullerene C60
FTIR	Fourier-transform infrared
GPC	gel permeation chromatography
HOMO	highest occupied molecular orbital
HTL	hole-transporting layer
ITO	indium tin oxide
J_{sc}	short circuit current density
$J-V$	current-voltage
LUMO	lowest unoccupied molecular orbital
M_n	number-average molecular weight
M_w	weight-average molecular weight
NMR	nuclear magnetic resonance
NP	nanoparticles
OPV	organic photovoltaic
P3HT	poly(3-hexylthiophene)
P_a	localised polaron
PAL	photoactive layer
PCBM	[6,6]-phenyl-C60-butyric acid methyl ester
PCE	power conversion efficiency
PDHS	Poly(3,4-dihydroxystyrene)

PDMS	poly(3,4-dimethoxystyrene)
PEDOT:PSS	poly(3,4-ethylenedioxythiophene) polystyrene sulfonate
P _o	delocalised polaron
PP	polaron pair
pm	parts per million
PQuiBoc	poly(<i>tert</i> -butyl-{5-[2-(4-vinylbenzyl)-2 <i>H</i> -1,2,3-triazol-4-yl]quinolin-8-yl}) carbonate)
PQuiOH	poly(5-[2-(4-vinylbenzyl)-2 <i>H</i> -1,2,3-triazol-4-yl]quinolin-8-ol)
QuiBoc	<i>tert</i> -butyl-{5-[2-(4-vinylbenzyl)-2 <i>H</i> -1,2,3-triazol-4-yl]quinolin-8-yl}) carbonate
RAFT	reversible addition-fragmentation chain transfer
RT	room temperature
S _a	localised singlet exciton
SADS	species-associated differential spectrum
SAM	self-assembling monolayer
SEM/EDXA	scanning electron microscopy/ energy dispersive X-ray spectroscopy
S _o	delocalised singlet exciton
TA	transient absorption
TAS	transient absorption spectroscopy
T _g	glass transition temperature
TPC	transient photocurrent
TPV	transient photovoltage
UV-Vis	ultraviolet-visible
V _{oc}	open circuit voltage
XL	cross-linking
ZnO	zinc oxide

List of contents

Preamble	2
Thesis summary	3
List of publications	4
Acknowledgments	5
Abbreviations	6
List of contents	8
List of tables	12
List of figures	14
List of schemes	21
List of equations	22
CHAPTER 1 INTRODUCTION	23
1.1 World energy problem	24
1.2 Silicon to plastic (various photovoltaic technologies)	26
1.3 Device architecture and key layers	28
1.4 Device physics	32
1.4.1 Light absorption and exciton formation	32
1.4.2 Exciton diffusion and dissociation	33
1.4.3 Charge transport	34
1.4.4 Charge extraction	35
1.5 Current-voltage curves and performance parameters	36
1.6 Measurement techniques to address the device physics	38
1.7 Degradation of OPVs	44
1.7.1 Chemical degradation	44
1.7.2 Intrinsic stability of the solar cell	48
1.7.3 Interface degradation and stabilisation	53
1.8 Polymerisation techniques	54
1.9 Aims	57
1.10 References	58
CHAPTER 2 MATERIALS AND EXPERIMENTAL METHODS	71
2.1 Methodology of computational modelling	72
2.2 Materials	73
2.3 Synthetic methods	75
2.3.1 Synthesis of poly(3,4-dimethoxystyrene), PDMS, via RAFT polymerisation	75
2.3.2 Synthesis of poly(3,4-dihydroxystyrene), PDHS	76
2.3.3 Synthesis of 1,2-(4'-hydroxycyclohexano)buckminsterfullerene (FUL-OH)	76
2.3.4 Synthesis of fullerene-linked poly(3,4-dimethoxystyrene) (PDMS-FUL)	77

2.3.5	Synthesis of 5-bromo-8- <i>tert</i> -butoxycarbonyloxyquinoline	78
2.3.6	Synthesis of 5-chloro-8- <i>tert</i> -butoxycarbonyloxyquinoline	78
2.3.7	Synthesis of 8- <i>tert</i> -butoxycarbonyloxy-5-ethynylquinoline	79
2.3.8	Synthesis of 4-vinylbenzyl azide	81
2.3.9	Synthesis of <i>tert</i> -butyl-{5-[2-(4-vinylbenzyl)-2 <i>H</i> -1,2,3-triazol-4-yl]quinolin-8-yl} carbonate, QuiBoc monomer	81
2.3.10	Synthesis of PQuiBoc by RAFT polymerisation of the quinoline monomer	82
2.3.11	Synthesis of PQuiOH by basic deprotection of PQuiBoc.	83
2.4	Thin-film deposition by spin-coating	84
2.4.1	Zinc oxide nanofilm deposition	84
2.4.2	Spin-coating of other films	84
2.5	Solution and bulk solid characterisation methods	84
2.5.1	Nuclear Magnetic Resonance Spectroscopy (NMR)	84
2.5.2	Fourier transform infrared (FTIR) spectroscopy	84
2.5.3	Gel permeation chromatography (GPC)	85
2.5.4	Ultraviolet and visible light spectroscopy (UV-Vis)	85
2.5.5	Photoluminescence (PL) spectroscopy	85
2.5.6	Differential scanning calorimetry (DSC)	85
2.6	Microscopy techniques	85
2.6.1	Scanning electron microscopy (SEM)	85
2.6.2	Atomic force microscopy (AFM)	86
2.7	Thin-film spectroscopy techniques	86
2.7.1	Ultraviolet and visible light spectroscopy (UV-Vis)	86
2.7.2	X-ray and ultraviolet photoelectron spectroscopy (XPS and UPS)	86
2.8	Contact angle measurements	86
2.9	Cyclic voltammetry (CV)	87
2.10	Device fabrication	87
2.11	Time-resolved measurements	87
2.11.1	Transient absorption spectroscopy (TAS)	88
2.11.2	Transient photovoltage (TPV) and photocurrent (TPC) measurements	90
2.12	References	91
CHAPTER 3 SYNTHESIS AND APPLICATION OF POLYMERIC SELF-ASSEMBLING MONOLAYER		92
3.1	Interface stabilisation	93
3.2	Choice of ligands	93
3.3	Synthesis of PDMS/PDHS	97
3.3.1	General approach	97
3.3.2	RAFT Polymerisation of PDMS	98
3.3.3	Demethylation of PDMS	104

3.3.4	Synthesis of PDMS/PDHS-FUL	105
3.4	Thermal studies	111
3.5	Material properties and thin film characterisation	115
3.5.1	Zinc binding experiment	115
3.5.2	XPS measurements	117
3.6	Device studies on PDHS and PDHS-FUL	119
3.7	Time-resolved studies of devices with PDHS and PDHS-FUL interlayers	122
3.7.1	Exciton generation, dissociation and separation	123
3.7.2	TPC and TPV	125
3.8	Conclusions and future work for PDHS and PDHS-FUL materials	127
3.9	References	128
CHAPTER 4 CROSS-LINKED LAYERS		131
4.1	Introduction	132
4.2	Contact angles	133
4.3	Absorbance measurements	135
4.4	Cross-linked PDMS layer	137
4.5	Cross-linked PDMS-FUL layer	141
4.6	Transient absorption spectroscopy	144
4.6.1	Control sample	144
4.6.2	PDMS-FUL 1 mg/ml	146
4.6.3	PDMS-FUL 10 mg/ml	147
4.7	Conclusions and suggestions for future work	151
4.8	References	153
CHAPTER 5 8-HYDROXYQUINOLINE LIGAND		155
5.1	Introduction	156
5.2.	Insight into 8-hydroxyquinoline binding	156
5.3.	Synthesis and characterisation	157
5.3.1	Monomer synthesis	157
5.3.2.	Polymerisation and deprotection	160
5.4	Optical and electronic properties	165
5.5.	Thin-film studies	170
5.5.1	SEM EDXA	170
5.5.2	Atomic Force Microscopy (AFM)	171
5.6.	Quinoline polymer for electron transport	174
5.6.1	Device studies	174
5.6.2.	Transient absorption spectroscopy	177
5.6.3	Electron transport in PQuiBoc polymer	179
5.7.	Quinoline polymer as interfacial layer	180

5.7.1	Device studies	180
5.7.2	Transient absorption spectroscopy	184
5.7.3	Interface stabilisation by a PQuiBoc layer	187
5.8	Conclusions and suggestions for future work	187
5.9	References	190
CHAPTER 6 GENERAL CONCLUSIONS		192

List of tables

Table 1.1.	Spectral contributions from excited states, corresponding photobleach and their respective energy values.	41
Table 2.1.	List of reagents adopted in the synthesis of poly(3,4-dimethoxystyrene), poly(3,4-dihydroxystyrene), poly(3,4-dimethoxystyrene)-fullerene and poly(3,4-dihydroxystyrene)-fullerene, featured in chapters 3 and 4 .	73
Table 2.2.	List of reagents adopted in the synthesis of quinoline polymer.	74
Table 2.3.	List of materials used in thin film deposition and device fabrication.	74
Table 3.1.	Simulated interaction energies of different complexes and conformers of ligands and zinc oxide inorganic clusters (in kcal/mol).	97
Table 3.2.	Molar mass data and monomer conversions of the polymerisation of 3,4-dimethoxystyrene in THF at 60 °C and 1:1 monomer to solvent ratio for the target $D_p = 150$ and $D_p = 30$ (experiment 4A).	99
Table 3.3.	Summary of monomer conversion and molar mass data for the homopolymerisation of DMS using AIBN and DDMAT in THF at 60 °C.	103
Table 4.1.	Data about the PDMS-FUL film thickness remaining on ZnO after cross-linking and washing (average for 3 films), based on the absorbance intensity.	136
Table 4.2.	Initial photovoltaic values obtained for solar cells incorporating cross-linked PDMS layers, deposited from solutions of different concentrations, as interfacial layers between ZnO and PAL (average for 12-16 devices).	138
Table 4.3.	Initial photovoltaic values obtained for devices incorporating cross-linked PDMS-FUL layers, deposited from solutions of different concentrations, as interfacial layers between ZnO and PAL (average for 12-16 devices).	141
Table 4.4.	Total charge yield and current density in pristine samples and losses of ultrafast charge yield and corresponding current density losses for the devices with cross-linked PDMS-FUL layers.	150
Table 5.1.	Summary of monomer conversion and molar mass data for the homopolymerisation of QuiBoc using AIBN and DDMAT in THF at 60 °C.	161
Table 5.2.	Theoretical energies (E) of the electronic transition to the first excited singlet state (S_1) for the QuiBoc monomer and	167

PQuiBoc, with oscillator strength (f) and configuration interaction (CI) description, as obtained from TD DFT modelling.

Table 5.3.	HOMO and LUMO levels of QuiBoc and PQuiBoc as estimated from cyclic voltammetry and UV-Vis absorption spectroscopy.	168
Table 5.4.	Initial average photovoltaic values obtained for solar cells incorporating PQuiBoc annealed at different temperatures, as an interfacial layer between ZnO and the PAL.	181

List of figures

Figure 1.1.	Energy consumption data from the International Energy Agency, USA.	24
Figure 1.2.	Estimated levelised cost of new generation resources in 2020 (2013 USD/MWh).	25
Figure 1.3.	Potential fields of OPV application.	28
Figure 1.4.	Schematic representation of a bilayer (a) and BHJ (b) solar cells.	29
Figure 1.5.	Chemical structures of the materials typically used in PALs.	29
Figure 1.6.	Schematic representation of conventional (a) and inverted architectures (b) and their corresponding energetic levels diagrams (c and d, respectively).	31
Figure 1.7.	Simplified schematic representation of the basic processes happening in an organic solar cell; (i) photo absorption and singlet exciton generation; (ii) exciton diffusion to the donor/acceptor interface; (iii) exciton dissociation; (iv) separation of coulombically bound exciton into charge carriers; (v) charge percolation to the corresponding electrodes by hopping between localised states and (vi) extraction.	32
Figure 1.8.	(a) J - V curves of an inverted device under first illumination (black line, S-shaped) and after treatment with forward bias of 1.3 V for 10 min (red line). (b) Proposed mechanism of doping ZnO with oxygen and de-doping by UV irradiation and electrochemical treatment.	35
Figure 1.9.	Current-voltage (J - V) curve of a solar cell with a fill factor of 56%.	37
Figure 1.10.	Schematic representation of the solar cell with shunt and series resistance.	37
Figure 1.11.	Scheme of a pump–probe experiment.	39
Figure 1.12.	(a) Experimental TA spectrum of pristine P3HT:PCBM blend; (b) continuous representation of three EADS calculated for this experimental TA spectrum.	40
Figure 1.13.	EADS0 of pristine P3HT:PCBM film with a lifetime of 1.5 ps, as obtained from a global analysis of experimental TA spectra using a 3 sequential steps model (thin solid curve), spectral fits to the EADS (thick solid curve) and contributions to fits from polaron pair, localised and delocalised singlet exciton and polaron states with their respective bleach contributions (negative differential absorption).	41

Figure 1.14.	Charge transients in P3HT:PCBM films at different light intensities, upon termination of excitation, where (a) is pristine P3HT:PCBM film and (b) degraded P3HT:PCBM to 2% loss of optical density.	43
Figure 1.15.	TA traces of (a) pristine and (b) photodegraded P3HT:PCBM solar cells under open circuit (OC) and short circuit (SC) conditions.	43
Figure 1.16.	Chain oxidation processes in polymers.	45
Figure 1.17.	Black and white schematic morphologies of annealed P3HT:PCBM films cast from chloroform, toluene, chlorobenzene, and xylene solutions, as reconstructed from the results of various measurements.	49
Figure 1.18.	Model for transport in low molar mass (a) and high molar mass (b) P3HT films.	50
Figure 1.19.	Optical microscopy images of the P3HT/PCBM films containing 0 or 15% P3HT-azide copolymer after annealing at 150 °C for 24 h.	52
Figure 1.20.	Mechanism of RAFT according to Vana.	56
Figure 2.1.	(ZnO) ₁₂ cluster simulated using DFT calculations, where grey atoms are Zn and red atoms are oxygen.	72
Figure 2.2.	Simplified schematic for transient absorption spectroscopy (TAS).	89
Figure 2.3.	Simplified schematic for transient photovoltage (TPV) measurements.	90
Figure 2.4.	Schematic interpretation of the effect of the excitation pulse length on the shape of transient photocurrent signal.	90
Figure 3.1.	Structures of the ligands proposed for modelling: 1 –tetrazole, 2 –imidazole, 3 –pyridine, 4 –8-hydroxyquinoline, 5 –(dimethylamino)methyl benzene, 6 –benzoic acid, 7 –dihydroxybenzene.	93
Figure 3.2.	Simulated inorganic cluster (ZnO) ₁₂ where red atoms represent oxygen and grey – carbon.	94
Figure 3.3.	Simulated complex of ligand 4 and (ZnO) ₁₂ cluster: conformer 1 (a) and conformer 2 (b).	95
Figure 3.4.	Simulated complex of ligand 5 and (ZnO) ₁₂ cluster	95
Figure 3.5.	Simulated complex of ligand 6 and (ZnO) ₁₂ cluster: conformer 1 (a) and conformer 2 (b).	96
Figure 3.6.	Simulated complex of ligand 7 and (ZnO) ₁₂ cluster: conformer 1 (a) and conformer 2 (b).	96

Figure 3.7.	Plot of molar mass against conversion in RAFT polymerisation in (a) 1:1 DMS:THF ratio; (b) 1:2 DMS:THF ratio and (c) 1:3 PDMS:THF ratio at 60 °C and $[AIBN]_0/[DDMAT]_0 = 1.0$ with D_p target = 30.	100
Figure 3.8.	(a) Plot of molar mass, M_n , and dispersity (M_w/M_n , \bar{D}) against RAFT polymerisation time; (b) plot of M_n versus monomer conversion; (c) semi-logarithmic plot and (d) GPC traces for the RAFT polymerisation of PDMS with a target degree of polymerisation equal to 30. Conditions were as follows: $[AIBN]_0/[DDMAT]_0 = 1.0$ at 1:2 DMS:THF at 60 °C.	101
Figure 3.9.	(a) Semi-logarithmic plot and (b) GPC traces for the RAFT polymerisation of PDMS with a target degree of polymerisation equal to 150 ($k_{app}=0.039 \text{ h}^{-1}$); (c) semi-logarithmic plot and (d) GPC traces for the RAFT polymerisation of PDMS with a target degree of polymerisation equal to 300 ($k_{app}=0.039 \text{ h}^{-1}$). Conditions were as follows: $[AIBN]_0/[DDMAT]_0 = 1.0$ at 1:2 DMS:THF at 60 °C.	102
Figure 3.10.	MALDI-ToF-MS spectrum of PDMS ₂₇ .	103
Figure 3.11.	¹ H NMR spectra of (a) PDMS ₂₇ in CDCl ₃ and (b) PDHS ₂₇ in MeOD.	104
Figure 3.12.	UV-Vis absorption (a) and FTIR (b) spectra of PDMS ₂₇ and PDHS ₂₇ .	105
Figure 3.13.	¹ H NMR spectra of (a) starting polymer PDMS (in CDCl ₃), (b) fullerenol precursor FUL-OH (acetone-d ₆ :CDCl ₃) and resulting (c) PDMS-FUL (in CDCl ₃) and (d) PDHS-FUL (in MeOD).	108
Figure 3.14.	¹³ C NMR spectra of (a) PDMS (in CDCl ₃); (b) FUL-OH (in acetone-d ₆ :CDCl ₃) and (c) PDMS-FUL (in CDCl ₃).	109
Figure 3.15.	FTIR spectra of PDMS (blue), FUL-OH (red), PDMS-FUL (black) and PDHS-FUL (green).	110
Figure 3.16.	GPC traces of PDMS (5,000 g/mol) and PDMS-FUL.	111
Figure 3.17.	Thermograms of PDMS (black) and PDMS-FUL (red) over 2 heating runs. Inset shows the T_g of the cross-linked PDMS at the second heating run.	112
Figure 3.18.	Photograph of the UV-induced emission of pristine PDMS polymer (right) and PDMS after cross-linking and resuspension in THF (left).	113
Figure 3.19.	FTIR spectra of PDMS before (black) and after the 1 st heating run (red).	113
Figure 3.20.	Thermogram of PDHS over 2 heating runs. Inset shows the T_g region of the polymer.	114

Figure 3.21.	Thermograms of PDHS-FUL over two heating runs. Inset shows the T_g region of the polymer at the first heating run.	114
Figure 3.22.	Surface zinc coverage for PDMS, PDHS (both at three different molar masses) and PS.	116
Figure 3.23.	SEM images before (left) and after (right) zinc acetate coverage treatment for PDHS ₂₇ (a and b), PDMS ₂₇ (c and d) and PS ₂₄₀ (e and f).	116
Figure 3.24.	XPS survey spectrum of the bare ZnO surface, where all peaks are assigned according to the energy levels of electrons extracted from corresponding electronic levels.	117
Figure 3.25.	XPS survey spectra of the bare ZnO surface (black line), with PDMS (red line) and PDMS-FUL (blue) after washing.	118
Figure 3.26.	XPS survey spectra of PDHS (a) and PDHS-FUL (b) on ZnO after washing with acetone.	118
Figure 3.27.	Visible and NIR spectra of PDHS (a) and PDHS-FUL (b) deposited onto ZnO and annealed at 100 °C before washing and after washing with acetone.	119
Figure 3.28.	Representative J - V curves of the devices ITO/ZnO/IL/P3HT:PCBM/ PEDOT:PSS/Ag, where IL represents the interlayer of PDHS or PDHS-FUL.	120
Figure 3.29.	Statistical lay-out of the key photovoltaic parameters of devices, incorporating PDHS and PDHS-FUL as interfacial layers, alongside a control without interlayer.	120
Figure 3.30.	Electronic levels of the corresponding layers in the studied devices. Left: control device. Right: device with PDHS-FUL interfacial layer, represented as purple insert.	122
Figure 3.31.	EADS of (a) PDHS-FUL device and (b) control device, as obtained from a global analysis of experimental TA spectra using a 3 sequential steps model.	124
Figure 3.32.	Evolution of excited states concentration according to their respective EADS in PDHS-FUL cells (a) and control cells (b).	125
Figure 3.33.	Transient photocurrent (a) and photovoltage (b) traces for control (black) and PDHS-FUL (red) cells.	126
Figure 4.1.	Contact angles of PDMS-FUL layer deposited on glass before heating, after heating and after washing with toluene.	133
Figure 4.2.	Contact angles of PDMS and PDMS-FUL layer deposited on ZnO before heating, after heating and after washing with toluene and bare ZnO before and after washing.	134
Figure 4.3.	Simulations of logP of PDMS dimer and PDMS dimer where one methoxy group was involved in formation of a new ether	134

	bond with a benzene ring of the neighbouring monomer.	
Figure 4.4.	UV-Vis absorbance spectra of PDMS and PDMS-FUL layers, deposited onto ZnO, from acetone solutions of different concentrations. ZnO spectrum is shown as thin red line.	135
Figure 4.5.	Schematic representation of resulting film thicknesses upon cross-linking (XL) and washing in PDMS layers deposited from solutions of different concentrations.	137
Figure 4.6.	Schematic representation of the inverted architecture stack used for the study of effect of cross-linked PDMS or PDMS-FUL polymer as an interfacial layer on the thermal stability of the cells.	137
Figure 4.7.	Normalised average photovoltaic parameters as a function of annealing time for devices incorporating cross-linked penetrating PDMS interfacial layers deposited from solutions of different concentrations.	139
Figure 4.8.	Normalised average photovoltaic parameters as a function of annealing time for devices incorporating cross-linked PDMS-FUL interfacial layers deposited from solutions of different concentrations.	143
Figure 4.9.	EADS of the control stack ITO/ZnO/PAL, pristine (a) and degraded at 150 °C for 3 h (b), as obtained from the global analysis of experimental TA spectra using a three sequential steps model.	144
Figure 4.10.	Evolution of excited state concentrations according to their respective EADS in the control film stack ITO/ZnO/PAL before (a) and after degradation (b) at 150 °C for 3 h.	145
Figure 4.11.	EADS of ITO/ZnO/PDMS (1 mg/ml)/PAL stack, pristine (a) and degraded at 150 °C for 3 h (b), as obtained from the global analysis of experimental TA spectra using a three sequential steps model	146
Figure 4.12.	Evolution of excited states concentration according to their respective EADS in ITO/ZnO/XL PDMS 1 mg/ml/PAL film stack before (a) and after degradation (b) at 150 °C for 3 h.	146
Figure 4.13.	EADS of ITO/ZnO/XL PDMS 10 mg/ml/PAL stack, pristine (a) and degraded at 150 °C for 3 h (b), as obtained from the global analysis of experimental TA spectra using a 3 sequential steps model.	148
Figure 4.14.	Evolution of excited states concentration according to their respective EADS in ITO/ZnO/PDMS 110 mg/ml/PAL film stack before (a) and after degradation (b).	148
Figure 5.1	Generic structure of a Znq_2 complex.	156

Figure 5.2.	^1H NMR spectra of precursor 3 (a) and QuiBoc monomer 5 (b).	159
Figure 5.3.	FTIR spectra of the monomer precursor 3 (top red) and monomer QuiBoc 5 (bottom black).	160
Figure 5.4.	GPC traces of PQuiBoc ₁₄ and PQuiBoc ₂₈ produced by RAFT under following conditions: $[\text{AIBN}]_0/[\text{DDMAT}]_0 = 1.0$, QuiBoc:THF = 1:10 at 60 °C.	162
Figure 5.5.	^1H NMR spectra of PQuiBoc (a) and the corresponding deprotected PQuiOH (b).	163
Figure 5.6.	DSC thermograms of PQuiBoc ₂₈ polymer.	164
Figure 5.7.	FTIR spectra of PQuiBoc ₂₈ (black) and resulting PQuiOH ₂₈ (red).	164
Figure 5.8.	UV-Vis absorbance spectra of QuiBoc monomer in solution (dotted line), PQuiBoc polymer in solution (dashed line) and thin film (solid line).	165
Figure 5.9.	Normalised photoluminescence spectra of QuiBoc monomer in solution (dotted line) and PQuiBoc polymer in solution (dashed line) and in a thin film (solid line).	166
Figure 5.10.	DFT calculated geometry of the QuiBoc monomer.	166
Figure 5.11.	Frontier MOs of the monomer and polymer, calculated by TD DFT modelling.	167
Figure 5.12.	UV-Vis absorbance spectra of PQuiBoc polymer deposited onto glass (dashed lines) and ZnO surface (solid lines) and annealed at different temperatures.	169
Figure 5.13.	(a) Photoluminescence spectra of PQuiBoc film on ZnO before (blue line) and after deprotection (green) and (b) corresponding photographs of the films illuminated with a UV lamp at 330 nm.	170
Figure 5.14.	SEM images of the polymeric films with ZnO nanoparticles on the surface: (a) polystyrene, PS ₂₄₀ ; (b) PQuiBoc annealed at 140 °C and (c) PQuiBoc annealed at deprotection temperature 160 °C.	171
Figure 5.15	AFM topography images and corresponding 3D representations of PQuiBoc deposited on glass (a, e), deposited on ZnO (b, f) and annealed at 140 °C (c, g) or 160 °C (d, h).	172
Figure 5.16.	AFM topography images and corresponding 3D representations of P3HT:PCBM blend deposited by spin-coating from 27 mg/ml xylene solution at 4,000 rpm onto PQuiBoc non-annealed (a, e), annealed at 140 °C (b, f) and annealed at 160 °C (c, g) and also blend deposited directly onto ZnO (d, h). Schematic representation of each image shows blue pillars of PQuiBoc on ZnO and PAL (purple)	173

deposited on the PQuiBoc surface.

Figure 5.17.	Schematic representation of the inverted architecture device stack with PQuiBoc as an electron-transporting layer.	175
Figure 5.18.	Distribution of key photovoltaic parameters of the cells incorporating ZnO and PQuiBoc as electron-transporting layers and bare ITO cells – before and after 5 min annealing at 140 °C (denoted as ‘an’), where QX indicates PQuiBoc layer deposited from X mg/ml acetone solution by doctor blading.	176
Figure 5.19.	EADS of ITO/PQuiBoc (140 °C)/PAL stack before (a) and after 5 min annealing at 140 °C (b), as obtained from a global analysis of experimental TA spectra using a 3 sequential steps model.	177
Figure 5.20.	Evolution of excited state concentration according to their respective EADS for ITO/PQuiBoc (140 °C)/PAL stack before (a) and after annealing (b) for 5 min at 140 °C.	178
Figure 5.21.	Simplified schematic representation of the nanomorphology organisation in P3HT:PCBM blend between two pillars of PQuiBoc (a) before and (b) after annealing at 140 °C for 5 min.	179
Figure 5.22.	Schematic representation of the inverted architecture stack used to study the effect of PQuiBoc polymer as an interfacial layer on the stability of the cells.	181
Figure 5.23.	Representative <i>J-V</i> curves of the devices incorporating a PQuiBoc layer annealed at different temperatures prior to deposition of the PAL.	182
Figure 5.24.	Normalised average photovoltaic parameters as a function of degradation time for devices incorporating PQuiBoc interfacial layer annealed at different temperatures post-deposition.	183
Figure 5.25.	EADS of ITO/ZnO/PQuiOH (160)/PAL stack, pristine (a) and degraded at 140 °C for 5 h (b), as obtained from a global analysis of experimental TA spectra using a 3 sequential steps model.	185
Figure 5.26.	Evolution of excited states concentration according to their respective EADS in ITO/ZnO/PQuiOH (160)/PAL film stack before and after degradation (a and b, respectively) and ITO/ZnO/PAL stack (c and d, respectively).	185

List of schemes

Scheme 2.1.	Synthesis of PDMS by RAFT polymerisation.	75
Scheme 2.2.	Synthesis PDHS by demethylation of PDMS.	76
Scheme 2.3.	Synthesis of fullerene precursor FUL-OH from fullerene C60.	76
Scheme 2.4.	Synthesis of PDMS-FUL by coupling PDMS and fullerene precursor FUL-OH.	77
Scheme 2.5.	Synthesis of 5-bromo-8- <i>tert</i> -butoxycarbonyloxyquinoline.	78
Scheme 2.6.	Synthesis of 5-chloro-8- <i>tert</i> -butoxycarbonyloxyquinoline.	78
Scheme 2.7.	Synthesis of 8- <i>tert</i> -butoxycarbonyloxy-5-ethynylquinoline from 5-bromo-8- <i>tert</i> -butoxycarbonyloxyquinoline by ligand-free Sonogashira coupling.	79
Scheme 2. 8.	Synthesis of 8- <i>tert</i> -butoxycarbonyloxy-5-ethynylquinoline from 5-chloro-8- <i>tert</i> -butoxycarbonyloxyquinoline by ligand-supported Sonogashira coupling.	80
Scheme 2.9.	Synthesis of 4-vinylbenzyl azide.	81
Scheme 2.10.	Synthesis of <i>tert</i> -butyl-{5-[2-(4-vinylbenzyl)-2 <i>H</i> -1,2,3-triazol-4-yl]quinolin-8-yl}) carbonate, QuiBoc monomer, by 'click' coupling.	81
Scheme 2.11.	Synthesis of PQuiBoc polymer via RAFT polymerisation of the QuiBoc monomer.	82
Scheme 2.12.	Synthesis of PQuiOH by basic deprotection of PQuiBoc.	83
Scheme 3.1.	Synthetic route for the preparation of poly(3,4-dihydroxystyrene), PDHS.	98
Scheme 3.2.	Synthetic route towards PDHS-FUL: (i) RAFT polymerisation of DMS; (ii) synthesis of the fullerenol precursor FUL-OH; (iii) Coupling of PDMS and FUL-OH towards fullerene-functionalised PDMS-FUL; (iv) demethylation of PDMS-FUL to obtain PDHS-FUL.	106
Scheme 5.1.	Synthetic route toward the QuiBoc monomer.	157
Scheme 5.2.	Sonogashira coupling of the protected aryl chloride, using Buchwald ligand Xphos in acetonitrile (ACN).	158
Scheme 5.3.	RAFT polymerisation of QuiBoc monomer 5 .	161
Scheme 5.4.	Basic deprotection of PQuiBoc polymer with piperidine in solution.	162

List of equations

Equation 1.1	Power conversion efficiency	36
Equation 1.2	Open circuit voltage	36
Equation 1.3	Kinetic model for charge carrier concentration	37
Equation 1.4	Current density	38
Equation 1.5	External quantum efficiency	38
Equation 1.6	Time-dependent charge yield	42
Equation 2.1	LUMO energy	87
Equation 3.1	Degree of polymerisation	102
Equation 3.2	Molar mass (M_n)	103
Equation 4.1	Percentage of the film remaining after cross-linking and washing.	136
Equation 5.1	HOMO level energy	168
Equation 5.2	PAL thickness	174

CHAPTER 1 INTRODUCTION

1.1 World energy problem

The world energy problem has become one of the major concerns in the last few decades, when various scientific and political groups around the globe started to raise awareness about the economic and environmental costs of conventional energy sources. Nowadays, along with the major quest for renewable energy sources, which would substitute fossil fuels (natural gas, petroleum, coal, etc.) that are widely believed to run out if consumed at the same levels, the focus is made on the actual costs of the produced energy, its availability and ethical distribution and CO₂ emissions. For example, it is known that there is not only a significant imbalance in energy consumptions between the developed countries (more than 400 British thermal units, Btu) and developing countries (less than 5 Btu, Figure 1.1), but a big difference in environmental costs of different energy resources used.¹ For example, the growing Chinese economy consumes larger amounts of energy every year, using conventional sources with higher CO₂ emission coefficients compared to those used in Germany or France (8547.7 million metric tons for China in 2012 against 788.3 for Germany and 364 for France).²



Figure 1.1. Energy consumption data from the International Energy Agency, USA.¹ The map includes electricity, as well as fossil and gathered fuels. Based on the numbers from 2010.

In those regions where the economic growth is mostly stimulated by the growth in price of fossil fuel energy, the effect of fuel extraction is usually more devastating for the environment because quite often the legal aspects of the extraction are not properly addressed. The impact of uncontrolled fuel extraction on the environment is much bigger than one would expect. For example, it often includes the destruction of the natural habitat of animals, disappearance of forests and agricultural territories alongside the sites of extraction.

The solution to all of these problems originating from fossil fuel consumption lies in two main directions. First is the implementation of worldwide policies designed to comprehensively control the extraction, distribution, pricing and consumption of the fossil fuels. The second direction entails research into possible renewable and more environmentally friendly energy sources. These are usually identified as the sources that cannot be depleted by regular consumption and include: sunlight, wind, tidal, waves and geothermal heat. These sources are also designed to decrease the influence of energy sources on the global market in the long term and solve the problem of unethical energy distribution by providing electricity to the rural areas of developing countries off the grid.

US Energy Information Administration (EIA) estimates that approximately 21% of world electricity generation was from renewable energy in 2011, with a projection for nearly 25% in 2040.² In 2011, the leading renewable source of energy – hydroelectric – accounted for almost 80% of all renewables, whereas solar, tidal and wave sources together accounted for just 1.3%. The big gap between renewable and conventional energy sources is majorly associated with several problems: unavailability of the resources for renewable energy production in different regions (like tidal and wave), insufficient development of the technologies (like for solar power) and the high costs of mass-scale production for the grid.

Indeed, if the estimated prices for energy from different sources are compared, one can observe that the costs for solar energy are much higher than those from conventional non-renewable sources (Figure 1.2).³ The established technologies that are used in wind, tidal and hydro power sources have made it possible to decrease the costs, whereas the developments in solar technology are not yet advanced enough to make a significant reduction in costs.

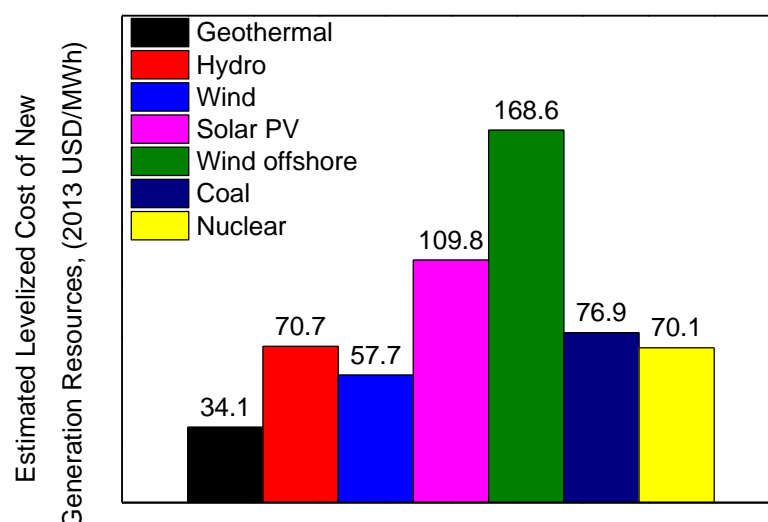


Figure 1.2. Estimated levelised cost of new generation resources in 2020 (2013 USD/MWh).³

On the other hand, solar power provides numerous advantages over other energy sources:

- Sunlight is one the most powerful energy sources with more than 86 000 TW per hour after reflection and atmospheric absorption,⁴ whereas the average annual consumption of the world population does not exceed 150 TW;²
- Solar energy will not deplete in the foreseeable future;
- The CO₂ emissions from solar energy usage are much less than those of conventional fossil fuels;
- The impact on the environment is less negative;
- The worldwide available solar energy is more favourable for the stability of the global market and political situation.

1.2 Silicon to plastic (various photovoltaic technologies)

The issues of clean and worldwide available energy were first addressed by inorganic solar cells, which initially had a power conversion efficiency (PCE) of 8%.⁵ These devices are made from crystalline silicon and nowadays are dominating the market of photovoltaic technologies.⁶

With the development of thin film deposition technologies, the next generation of inorganic solar cells was introduced; made of amorphous silicon,⁷ cadmium telluride,⁸ or copper indium gallium selenide (CIGS).⁹ The deposition techniques¹⁰ that made thin film photovoltaics viable included high temperature and, in some cases, low temperature plasma¹¹ and chemical vapour deposition.¹² In comparison to the heavy and bulky crystalline silicon cells, second generation solar cells are made of thin films and can be deposited on flexible substrates,¹³ although the use of high-temperature deposition to obtain devices with higher efficiency limits the substrates to stainless steel^{14,15} or glass.¹⁶

Although developments in inorganic solar cells have allowed the PCE to increase and have improved consumer-focused properties of the solar cell modules (including the weight), the cost of these devices remains high, mainly due to the costs (economic and environmental) of material purification and deposition.^{17,18}

The costs of thin film inorganic cells have turned the attention of researchers to more sustainable and inexpensive alternatives: organic and inorganic-organic hybrid materials that have several advantages. In general, they can be easily deposited from solution; they can be synthesised and modified on various scales (from laboratory scale to factory production); and they are easier to recycle. Nowadays, three types of solution processed solar cells exist:

- polymer solar cells (also known as 'organic solar cells', OSC, or 'organic photovoltaics', OPVs);
- dye-sensitised solar cells (DSSC);
- perovskites.

Indeed, DSSCs do not need any special deposition techniques for fabrication of the cells and they exploit organic molecules as photoactive material which can be easily deposited from solution onto a flexible substrate.¹⁹ Their PCE of 11.9% is still lower than that of the CIGS cells (20.5%).²⁰ The main disadvantage of DSSCs is that their construction requires an electrolyte which has poor stability at both high and low temperatures and compromises the encapsulation of the cell, the major factor of protection against oxygen and UV light degradation.^{21,22} Current research focuses on substitution of conventional electrolytes for more stable, solid-state or liquid crystal materials, but the efficiency of the resulting devices is generally lower.²¹

Recent newcomers to the field (2009), perovskite-based solar cells, enjoy the advantages of DSSCs, yet have already reached a higher efficiency of 20.1%.²³ They can be fabricated by low-temperature solution deposition onto various substrates, including flexible materials.²⁴ Perovskite solar cells stand between the inorganic and organic types of cells as they incorporate a perovskite absorber, usually lead or tin halide-based organic-inorganic materials which are believed to be environmentally hazardous.^{25,26} The total cost of the perovskite module, although benefited from the advantages of processing, would still be comparatively high because of the cost of encapsulation.^{27,28} The need for extra protective barrier layers (such as glass, etc.) is explained by the extreme sensitivity of perovskite compounds to moisture and sunlight.^{28,29} Despite all of the developments in the efficiency of these cells, the stability of the devices has not been thoroughly studied and the commercial application remains arguable.²⁵

Polymer based solar cells (OPVs or OSCs) currently have the lowest efficiency of the described cells. In 2015 the highest reported efficiency for a single junction cell reached 11.1% and 9.5% for a minimodule.²³ Nevertheless, the system cost calculations have demonstrated that for a module to be able to compete with existing commercial inorganic modules, the efficiency of a 10 m² cell should not be less than 10%.³⁰ Scharber *et al.* have concluded that with a typical performance loss of 40% for the module efficiency in comparison to that of a single cell, the expected efficiency of the module would only reach ca. 6%, which is not enough to make solar cells commercially attractive.³⁰ On the other hand, OPV modules have several advantages for the ultimate customer:

- the modules are thin and lightweight (as thin as 2 microns)³¹ and the weight of the cells depends on the substrate and encapsulation;

- variability of the substrates, including plastics and paper;³²
- flexibility and stretchability;³³
- colour-tunability;³⁴
- semitransparency or transparency;³⁵
- low production and installation costs in a constant, high throughput process;^{30,36}
- designer integration of the OPV elements into functional elements (such as parasols, sheds, windows, etc).

There are fields where these properties are crucial for utility. For example, lightweight modules are important for aerospace installations (to reduce the transport costs) as well as in consumer electronics (Figure 1.3).

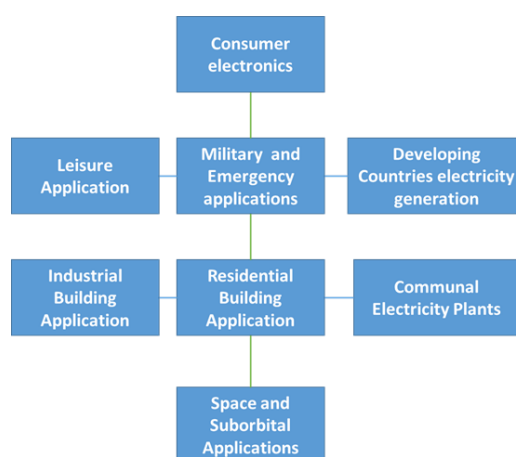


Figure 2.3. Potential fields of OPV application.

All of these advantages allow OPVs to take on their own market niche if the requirements of costs, efficiency and stability can be fulfilled. However, it is unlikely that OPV will completely replace inorganic cells.³⁷ The estimations given in 2013 predict that by 2023 the market for OPVs will rise up to \$87 million.³⁸

1.3 Device architecture and key layers

A simplified organic solar cell typically consists of a photoactive layer (PAL) sandwiched between two electrodes. The PAL is usually made of polymers or small molecules whereas the electrodes are metallic, although current research is going on to replace them by metal-free materials. Initially, the photovoltaic effect was observed in an active layer consisting of only one material,³⁹ but in 1992 the first charge transfer from the conducting polymer layer to a buckminsterfullerene layer was observed⁴⁰ with a PCE of 0.04% under monochromatic light (Figure 1.4a).

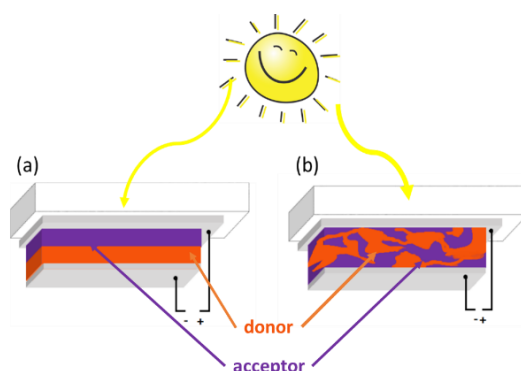


Figure 1.4. Schematic representation of a bilayer (a) and BHJ (b) solar cells.

The blending of two materials with different affinities to positive and negative charges, which resulted in the formation of a bulk heterojunction (BHJ) PAL layer, allowed the PCE to reach 2.5% (Figure 1.4b).⁴¹

The materials used in a typical PAL blend are presented in Figure 1.5 and include poly(alkylthiophenes), polybenzodithiazoles and polyphenylenevinylenes as donor polymers and various fullerene derivatives as acceptor materials.

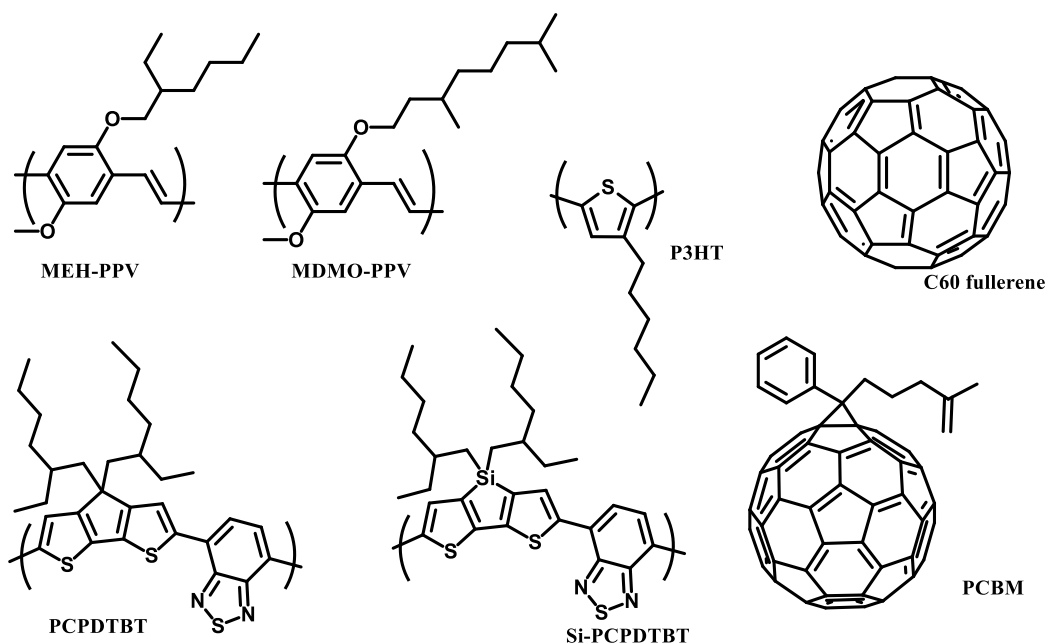


Figure 1.5. Chemical structures of the materials typically used in PALs: poly[2-methoxy-5-(2-ethylhexyloxy)-1,4-phenylenevinylene] (MEH-PPV), poly[2-methoxy-5-(3',7'-dimethyloctyloxy)-1,4-phenylenevinylene] (MDMO-PPV), poly(3-hexylthiophene-2,5-diyl) (P3HT), buckminsterfullerene C60, poly[2,6-(4,4-bis(2-ethylhexyl)-4H-cyclopenta[2,1-b;3,4-b']dithiophene)-alt-4,7(2,1,3-benzothiadiazole)] (PCPDTBT), poly[2,6-(4,4-bis(2-ethylhexyl)dithieno[3,2-b:2,3-d]silole)-alt-4,7-(2,1,3-benzothiadiazole)] (Si-PCPDTBT) and [6,6]-phenyl-C60-butyric acid methyl ester (PCBM).

While discussing the PAL components, it is necessary to note that for P3HT, typically used donor polymer in blend with PCBM, two variations of regioregularity exist. In regiorandom P3HT (RRa), the monomers are aligned so that the hexyl tail is positioned randomly in the chain, whereas in regioregular (RR) P3HT the monomers are aligned head-to-tail along the whole polymer chain.⁴² Thus, RR-P3HT has higher crystallinity and is capable of forming well-ordered lamellar domains. Although RR-P3HT was shown to have numerous advantages for device performance, RRa P3HT is widely used in studies. It helps to provide deeper insight into the physics of the device since it has much higher disorder which processes occurring in amorphous phases to be more pronounced.^{43,44}

To enable the best possible performance, devices consist of stacked layers and usually include interlayers, such as a hole-transporting layer (HTL) and an electron-transporting layer (ETL), that enable best electronic coherence and more efficient charge transfer to the electrodes.⁴⁵

HTLs are introduced into the devices between the PAL and the anode. For the HTL, dispersions of poly(3,4-ethylenedioxythiophene):poly(4-styrenesulfonate) (PEDOT:PSS) are typically used because they produce transparent and highly conductive films. PEDOT:PSS is a mixture of two polymers which form a salt, where PSS is the anion and PEDOT the cation. Current research is focused on producing new PEDOT:PSS dispersions with novel surfactants that enhance the efficiency and stability of the cells.⁴⁶ Other HTL materials that have been used are transition metal oxides, V_2O_5 and MoO_3 .^{47,48}

ETLs, sometimes also called 'hole-blocking', 'electron extraction' or 'electron transport' layers, are introduced between the PAL and the cathode. ETLs usually consist of lithium or caesium fluoride,⁴⁹ titanium oxide,⁵⁰ zinc oxide,⁵¹ graphene and graphene oxide,^{52–57} or chromium oxide.⁵⁸ Zinc and titanium oxides are both good semiconductors with a wide band gap (3.37 eV for zinc oxide and 3.06-3.23 eV for titanium oxide).^{59,60} Compared to TiO_x , ZnO has a higher electron mobility.⁶¹ The conduction band edge of zinc oxide is lower in energy than that of the LUMO of PCBM (4.3 eV), which facilitates electron transfer on the surface contact and extraction from the PAL.⁶²

ZnO and TiO_x also serve as oxygen diffusion barriers to reduce oxidation damage of the PAL.^{63,64} Various methods of deposition, like spray pyrolysis,⁶⁵ sol-gel process,⁶⁶ and solvent casting of prepared nanoparticles,⁶⁷ allow inexpensive and easy processing of these layers under ambient conditions, and in the case of nanoparticles, allows subsequent modification of the layers.⁶⁸

Both intermediate layers result in enhanced contact between the PAL and the electrodes. The agreeing band gaps between the buffering layers and the electrodes guarantee more efficient charge extraction than without the buffer layers.⁶⁹

Conventional devices initially were illuminated from the bottom and contained indium-tin oxide (ITO) as a transparent anode (Figure 1.6). The overall configuration requires the use of a low work function calcium/aluminium electrode (ca. 1.4-1.5 eV), which is extremely susceptible to the environmental conditions such as water and oxygen.⁷⁰⁻⁷³ The second major problem associated with conventional architectures is the instability of the ITO/PEDOT:PSS interface.^{74,75}

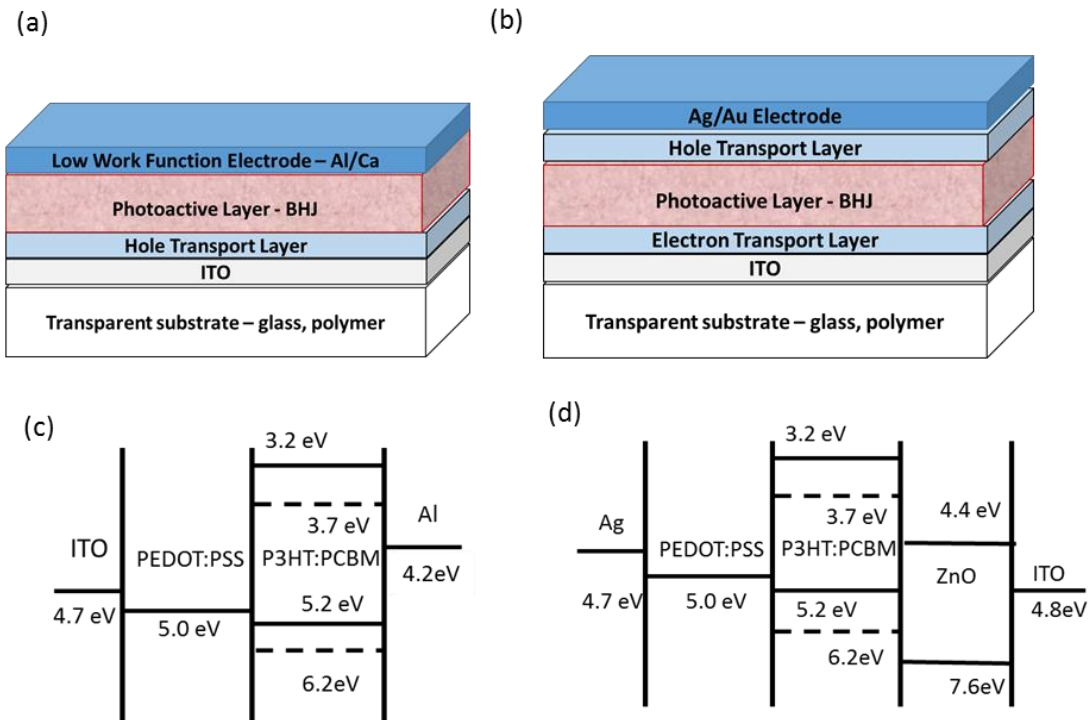


Figure 1.6. Schematic representation of conventional (a) and inverted architectures (b) and their corresponding energetic levels diagrams (c and d, respectively). Modified from Zhang *et al.*⁷⁶

Both of these problems can be overcome by using an inverted device architecture, where electron extraction takes place through the ITO electrode (Figure 1.6b). This allows the use of a high work function (4.7-4.8 eV) silver electrode for hole extraction, which is more intrinsically stable to oxidation than conventional low work function metals.⁷³ The ITO/PEDOT:PSS interface is also avoided since in inverted devices titanium or zinc oxide is used to facilitate electron collection on ITO. One drawback, however, is that the use of these oxides results in inverted devices having generally lower power conversion efficiencies due to defects present in the zinc or titanium oxide surfaces.⁷⁷

1.4 Device physics

The photovoltaic effect in polymer solar cells is based on a number of key processes taking place upon absorption of the photon (Figure 1.7). The efficiency of these and competing processes determines the final efficiency of the solar cells:

1. light absorption and exciton formation;
2. exciton diffusion;
3. exciton dissociation;
4. charge separation;
4. charge transport and
5. charge collection on the electrodes.



Figure 1.7. Simplified schematic representation of the basic processes happening in an organic solar cell; (i) photo absorption and singlet exciton generation; (ii) exciton diffusion to the donor/acceptor interface; (iii) exciton dissociation; (iv) separation of coulombically bound exciton into charge carriers; (v) charge percolation to the corresponding electrodes by hopping between localised states and (vi) extraction.⁷⁸

1.4.1 Light absorption and exciton formation

The external quantum efficiency (EQE) of the cells is based on the ability of one material (normally the donor) to absorb a photon of light, resulting in excitation of an electron from the ground state (GS), or highest occupied molecular orbital (HOMO), to the lowest unoccupied molecular orbital (LUMO).

The energy required to excite an electron from HOMO to LUMO, known as the electrical band gap, should be as low as possible. Thus, the lower the band gap, the more efficient

should be the material, but this statement has its own limitations. It has been demonstrated that the sunlight has higher irradiance in the longer wavelengths, especially in the IR region of the spectrum. The Shockley-Queisser equation shows that the maximum possible efficiency of a single solar cell is limited in a specific interval of the band gap between 1 and 2 eV.⁷⁹ Everything higher than 2 eV will not absorb the daylight photons (solar spectrum in UV-Vis region); everything too low will mean that most photons will be wasted because they have much higher energy than required to excite the electron.⁸⁰

For example, the widely used donor polymer, P3HT, has a band gap of 650 nm (1.9 eV) and only can collect up to 23% of available photons. If the band gap is extended by 100 nm (to 1.64 eV), this would allow harvesting 55% of the photon flux, increasing the potential current density to 20.8 mA/cm².⁸⁰

The electron and resulting hole are held together by Coulombic interactions and together form an exciton. There are various possible types of excitons, but for organic solar cells only one type is characteristic: the Frenkel exciton with a small binding radius of 10 Å.⁷⁸ Depending on their spin state, excitons can be singlet (spin state zero) and triplet (spin state 1).⁷⁸ Excitons bear no charge and do not represent any charge transfer as they travel through the PAL as quasiparticles.⁸¹

1.4.2 Exciton diffusion and dissociation

An exciton is mobile and diffuses through the donor material until it finds the donor-acceptor interface or recombines. Exciton binding (or dissociation) energy is 0.5-1 eV,^{82,83} which is very high. Thus, the thermal energy at room temperature is not sufficient to break it. In inorganic solar cells, on the other hand, the dissociation energy of the exciton is lower than thermal energy at room temperature, therefore free charges are formed spontaneously.⁸¹

Formed singlet excitons have a lifetime of a nanosecond, whereas triplet excitons are longer-lived and last for milliseconds. Subsequently, both types of excitons decay radiatively. The triplet exciton energy is much higher than that of the singlet, thus triplets decay by phosphorescence, whereas singlets decay by photoluminescence.⁸⁴ There is a possibility of the intersystem crossing, so that the singlets transit into triplets.⁷⁸ In general, the triplet states, with higher energy and longer lifetime, have little utility for the charge generation processes in the solar cells and thus represent a loss mechanism.

Since the thermal energy of the donor semiconductor at room temperature is not enough for exciton dissociation, the presence of the acceptor is needed to provide an energy offset for dissociation. The best acceptors to date, buckminsterfullerenes and their chemical

derivatives, benefit both from their high electronegativity and spherical shape.⁸⁵ An electron is transferred to the acceptor owing to the LUMO having lower energy than that of the donor; the hole remains in the donor. Thus, the difference between LUMO energies of the donor and acceptor is the driving force of electron dissociation and can be tuned by choosing a different donor/acceptor combination.⁸⁶

Before the exciton actually dissociates, it must diffuse to the donor-acceptor interface from the point of its generation. It has been demonstrated that in neat films of P3HT the exciton diffusion length is 2-4 nm.^{87,88} In a P3HT:PCBM blend this length increases up to 8-10 nm due to the delocalisation of excitation.^{43,89} Thus, BHJ structure of the PAL, where the donor and acceptor materials are blended together to increase the interfacial surface area, has proven to be extremely efficient in exciton dissociation due to the optimal distribution of interfaces.⁷⁸

Both exciton diffusion and energy transfer upon exciton dissociation are extremely fast processes (tens of femtoseconds)^{40,90} and prevail over the slower processes. The polaron pair generated from the dissociated exciton is still coulombically bound and the energetic disorder of the materials is essential for the charges to be separated and diffuse to the respective electrodes.⁷⁸ On the other hand, the polaron pair can recombine to the ground state. This loss mechanism is called geminate recombination: a process when the polaron pairs recombine non-radiatively when they encounter an interfacial trap (such as an impurity in the donor material).^{91,92} Another loss mechanism is the formation of triplet states when the electron of the polaron pair is transferred back to the exciton to form a triplet exciton in the donor.⁷⁸

1.4.3 Charge transport

The key feature of charge transport in OPVs, in contrast to inorganic crystalline cells, is that due to the high level of system disorder, the charges cannot diffuse by band transport, therefore they hop from one localised state to the next. This hopping transport has a complex nature and can be described by various models.⁹³ Majorly, this type of charge transfer is ensured by consistent charge percolation paths which are extremely efficient in the bilayer OPVs but compromised in the BHJ. For example, hole transport through the polymer phase is interrupted by the acceptor molecules or crystals dissolved in the polymer matrix.⁹⁴ During the transport of charge carriers to their respective electrodes, recombination takes place in such disordered systems, like semi-crystalline polymers, decreasing the number of charge carriers available for extraction.⁹⁵

Morphology of the bulk heterojunction results in a number of trapped charge carriers that will meet their counterparts and recombine, whereas in a bilayer architecture the chance of so-called non-geminate recombination is extremely low.⁹⁶ This type of recombination is treated as a bimolecular process if the density of the trapped charge carriers is lower or equal to that of the mobile carriers. In this case both would be depleted while recombining. In a degraded solar cell the trapped carriers significantly exceed the number of mobile carriers and thus this reaction is of *pseudo* first order.⁹⁷ The bimolecular type of recombination, Langevin recombination, depends on two factors; (i) the mobility of the charge carriers and (ii) the possibility of encountering the recombination partner. The mobility in organic solar cells is lower than in more ordered inorganic semiconductors. Therefore, mostly the possibility of recombination through traps, defects and immobile carriers is higher in organic systems and determines the recombination rate.⁹⁸

1.4.4 Charge extraction

Charge extraction depends on a number of key factors; (i) the field or voltage throughout the device; (ii) recombination on the surface of the electrodes; (iii) differences in charge transfer rates at the interfaces and (iv) background carriers.⁹⁷

Indeed, it has been widely demonstrated that hindered charge transport at the interfaces between electrodes and the PAL leads to the accumulation of trapped charges at the interface (Figure 1.8) and therefore gives rise to the appearance of so-called S-shapes on the *J-V* curves.^{77,99}

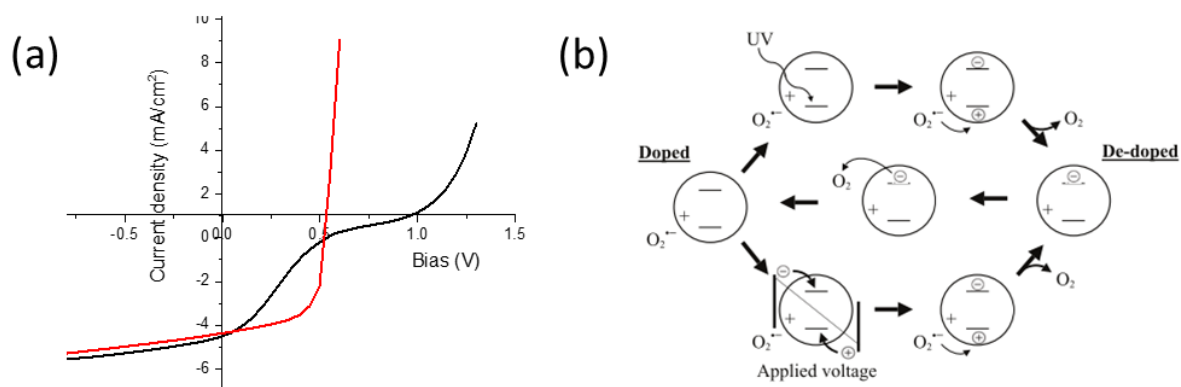


Figure 1.8. (a) *J-V* curves of an inverted device under first illumination (black line, S-shaped) and after treatment with forward bias of 1.3 V for 10 min (red line). (b) Proposed mechanism of doping ZnO with oxygen and de-doping by UV irradiation and electrochemical treatment.¹⁰²

In inverted cell structures, the appearance of S-shaped J - V curves is generally attributed to intrinsic defects in the ETL, resulting in increased series resistance and charge recombination on the surface of the electrode.¹⁰⁰ The appearance of S-shapes is often a problem in ZnO, due to its variable conductance and the natural presence of the bound oxygen radicals that act as electron traps.¹⁰¹ The chemical mechanism for doping of ZnO with oxygen has been proposed by Krebs *et al.* (Figure 1.8b).¹⁰² These electron traps can be removed by UV-irradiation or electrochemically, by creating persistent charge flow (20 V for 10 s).¹⁰³ The background charge carrier density (trapped immobile carriers) also has impact on the extraction by shielding the built-in field, leading to enhanced recombination and loss of the extracted current.⁹⁷

1.5 Current-voltage curves and performance parameters

Conclusively, the final PCE of a solar cell can be described as a ratio of the output power divided by the power of the incident light. The output power is defined by several factors, as shown by Equation 1.1.

$$\text{Power conversion efficiency, } PCE\% = \frac{FF \times J_{SC} \times V_{OC}}{P_L} \quad (\text{Equation 1.1})$$

where FF is the fill factor; J_{SC} – current density (in A/cm²); V_{OC} – open circuit voltage (V), P_L – power of incident light (W).⁷⁸

Open circuit voltage is the difference in potential between the electrodes when the current between them is absent. In various models, it is usually determined as difference between the HOMO of the donor and the LUMO of the acceptor.¹⁰⁴ Thus, for a common acceptor, such as PCBM, there is an acceptable range of energies for the HOMO of the donor that would result in an optimal V_{OC} . Low band gap polymers that fit in this range are likely to allow an efficient charge transfer.⁸⁰ Maurano *et al.* have also demonstrated that V_{OC} not only depends on the electronic levels of the materials but also on the charge carrier lifetime and recombination rates and can serve as an indirect way to observe the morphology of the blend.¹⁰⁵ This can be represented by Equation 1.2, which also reflects the dependence of the open-circuit voltage on the operating temperature.

$$\text{Open circuit voltage, } V_{OC} = \frac{E_{gap}}{q} - \frac{kT}{q} \left(\frac{(1-P)\gamma N_c^2}{PG} \right) \quad (\text{Equation 1. 2})$$

where E_{gap} is the electronic band gap between HOMO and LUMO, P – probability of the excitons to dissociate into polarons, G – exciton generation rate, γ - Langevin recombination strength, N_c – donor and acceptor density of states, kT/q – thermal voltage.⁷⁸

Fill factor (FF) is defined as a ratio of maximum power of the cell to the product of J_{SC} and V_{OC} . It can be experimentally determined from the J - V curve as a ratio of square A to square B in Figure 1.9.

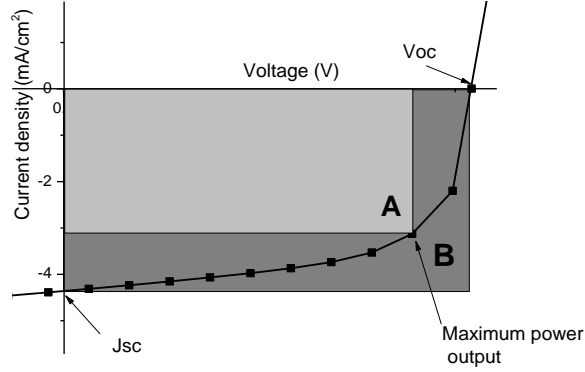


Figure 1.9. Current-voltage (J - V) curve of a solar cell with a fill factor of 56%.

Fill factor provides information about charge extraction and, in an ideal device, would be 1.0, corresponding to 100% of the generated charge carriers being extracted. As other competing processes occur in parallel with extraction, the fill factor will decrease.¹⁰⁶ The fill factor is affected by the intrinsic shunt resistance (R_{sh}), which reflects the leakage of the current through the manufacturing defects, and by the series resistance (R_s), which represents the resistivity between different contacts.¹⁰⁷ A low shunt resistance is evidence of major defects, whereas the series resistance of an ideal cell would be equal to zero.

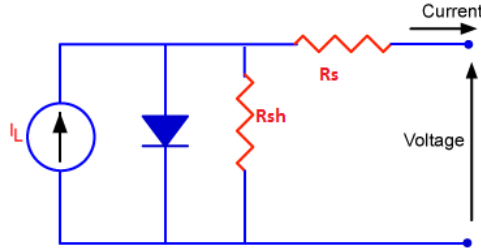


Figure 1.10. Schematic representation of the solar cell with shunt (R_{sh}) and series resistance (R_s).

Short circuit current density (J_{SC}), as discussed in Section 1.4, is a product of various competing processes. If all of these processes are brought to the resulting charge carrier concentration, one can describe them with the kinetic model shown in Equation 1.3,⁹⁷ for n charge density in a device with d thickness of the PAL:

Kinetic model for charge carrier concentration,

$$\frac{dn}{dt} = G - k_L \cdot n \cdot n - \mu \cdot n \cdot \frac{E_{bi}}{d} \quad (\text{Equation 1.3})$$

where G is the photoinduced generation of extractable charge carriers, μ the effective mobility, E_{bi} a constant built-in field and k_L the Langevin recombination coefficient. At steady state ($dn/dt=0$) the current density would be defined by Equation 1.4.⁹⁷

Current density, $J_{SC} = \mu \cdot n_{ss} \cdot E_{bi}/d$ (Equation 1.4)

Thus, the current density is determined by the mobility (μ), charge carrier density (n_{ss}) and the charge percolation efficiency defined by the strength of the built-in field (E_{bi}) distributed over the layer thickness (d).

1.6 Measurement techniques to address the device physics

To address the efficiency of the cells, it is necessary to introduce a cross-correlation term that would encompass all parameters. One of the indicators of solar cell efficiency is external quantum efficiency (EQE). EQE is the ratio of charge carriers collected by the electrode to the number of photons that were shone onto the cell at a given wavelength, in contrast to internal quantum efficiency (IQE) that takes into consideration only the photons that are absorbed by the cell.⁹⁷ Thus, EQE can be represented by Equation 1.5:

External quantum efficiency,

$$EQE = \varphi_{abs} \cdot \varphi_{diss} \cdot \varphi_{sep} \cdot \varphi_{extr} \quad (\text{Equation 1.5}),$$

where φ represents the yields of all key processes: absorption, exciton dissociation, charge separation and charge extraction.

If all processes had a 100% efficiency at all wavelengths of the solar spectrum, the EQE within the whole spectrum would be 100% or even more than 100%, in the case of multiple exciton generation from one photon. As discussed previously, absorption is dictated by the band gap of the donor material and would not be the same at all wavelengths. Evidently from the Equation 1.5, exciton dissociation and charge extraction are also main factors in determining the EQE.

Absorption of a material can be determined at the ground steady state by conventional spectroscopy techniques in the ultraviolet-visible range of the solar spectrum. All other processes are time-dependent, since all excited states (singlet excitons, charges and triplet states) are 'live' features and have life-times, diffusion lengths, decay profiles, etc. Thus, exciton dissociation, charge separation and charge extraction have to be monitored on a certain timescale to determine the order of the corresponding reaction. Here, the transient spectroscopic and electrical measurements are introduced. The timescale of these

measurements depends on the rate of the processes that are monitored. Exciton dissociation and charge separation occur on femto- and picosecond timescale, thus femtosecond transient absorption spectroscopy (TAS) is employed to study these two processes. Charge transport, extraction and recombination take up to milliseconds (depending on the material and degradation level of the device) and would be observed by microsecond TAS or by transient electrical measurements, transient photocurrent and photovoltage (TPC and TPV, correspondingly). TPC and TPV are typically used to observe the extraction and recombination, respectively, since TPC is measured under short circuit conditions and TPV under open circuit.¹⁰⁸ Microsecond TAS can also be measured in both open and short circuit conditions, providing information about the fate of generated charges. The difference between TAS and TPC/TPV is that in TAS the charges are detected by spectroscopy, whereas in TPC/TPV the electrical signal is observed.

All transient techniques are based on one principle: a short pulse from the light source (LED or laser) is used for excitation, and the signal is observed upon switching off the illumination. The difference between electrical and spectroscopic methods is that in TPC/TPV the signal is recorded by an oscilloscope, and in TAS the excited states are detected by use of a light source, called a probe. Passing through the excited sample, the probe light, according to the Lambert-Beer law, is absorbed by the excited states, resulting in a differential absorption spectrum (Figure 1.11). Thus, the overlap of the probe with the pump is the crucial parameter in a TAS experiment.¹⁰⁹ Between pump and probe pulses there is a time delay (τ) that determines at what time after excitation the TAS signal is recorded. The set-up, typically used for femtosecond TAS and employed in this work for studies of P3HT:PCBM blends, is described in detail in Section 2.10.

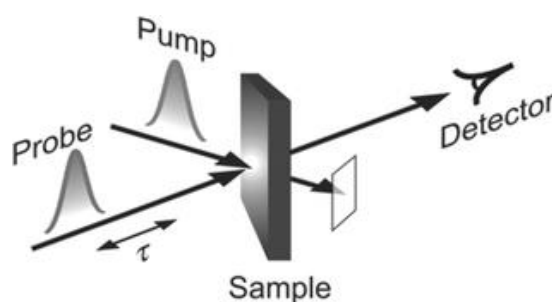


Figure 1.11. Scheme of a pump–probe experiment.¹¹⁰

An experimental femtosecond TA spectrum is illustrated in Figure 1.12a. It consists of multiple differential absorption spectra in the visible and NIR range of 450–1350 nm at every time-delay step of the probe (200 fs instrumental resolution). As can be seen from the TA spectrum, data analysis is complicated by high level of noise. For ease of calculation, an experimental TA spectrum is reproduced by superposition of three *so-called* evolution-associated differential spectra (EADS 0, 1 and 2, respectively), each with an associated

lifetime, following a first order sequential reaction of type $0 \rightarrow A \rightarrow B \rightarrow C \rightarrow 0$. This representation is purely mathematical since the spectra of A, B and C bear no physical meaning and do not correspond to real excited states (singlet excitons or charge carriers) but to superpositions of such. Thus, transformation of experimental TA spectrum into three EADS follows a number of exponential decay functions with calculated constants (or rates) which afterwards are transformed into EADS lifetimes.

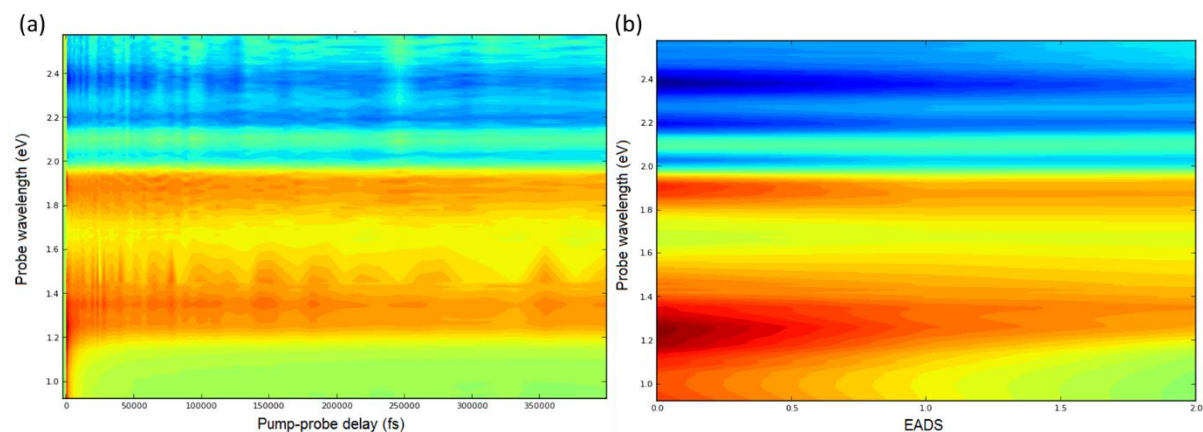


Figure 1.12. (a) Experimental TA spectrum of pristine P3HT:PCBM blend; (b) continuous representation of three EADS calculated for this experimental TA spectrum.

The contributions of singlets and charged states to each EADS can be obtained by spectral fitting, described in details by Stokkum *et al.*¹¹¹ At this point, photophysical knowledge is applied to resolve the spectra, essentially by accepting that different states have different photoabsorption (PA) bands and that both excitons and charged states share the same transient photobleach (PB). This method has been previously demonstrated for a silicon-based low band gap polymer by Karuthedath *et al.*⁹⁷ However, spectral modelling for P3HT is complicated by the presence of two types of excited states, localised (in the amorphous phase) and delocalised (in the ordered phase), which have different PA bands.^{43,97} To assign different bands to their respective excited states, it is useful to study their decay kinetics and correlate this to the fluorescence.¹¹² Thus, comprehensive studies by various researchers, summarised by Ohkita,¹¹² concluded that the TA spectrum of a P3HT:PCBM blend consists of several contributions (Table 1.1). Korovyanko *et al.* have shown that, in contrast to regiorandom P3HT, regioregular P3HT does not have the band attributed to stimulated emission, a process of self-relaxation of excited states accompanied by the emission of light.⁴³ It is necessary to note that for ease of measurement and data analysis, the blends are excited at 387 nm, where the absorption of PCBM is negligible compared to that of P3HT, so that the TA spectra do not have any contributions from excited states of PCBM.

Table 1.1. Spectral contributions from excited states, corresponding photobleach and their respective energy values.^{43,90,112–115}

Spectral contribution	Annotation	Probe energy (eV)
Photobleach of the ordered phase of P3HT	PB _o	1.95-2.6
Photobleach of the amorphous phase of P3HT	PB _a	2.25-2.6
Localised singlet in the amorphous phase of P3HT	S _a	0.88-1.05
Delocalised singlet in the ordered phase of P3HT	S _o	1.12-1.18
Localised polaron	P _a	1.25-1.35
Delocalised polaron	P _o	1.85-1.96
Polaron pair (bound electron and hole)	PP	1.96-2.05

Generally, global analysis comprises deconvolution of each EADS into corresponding spectral contributions of each excited state, species-associated differential spectra (SADS). SADS typically consists of the photoabsorption and photobleach part, and the relative concentration of each excited state is obtained from the intensity of differential absorption in both parts, and not from the photoabsorption intensity exclusively. This approach allows calculation of relative concentrations without information about absolute cross-sections of each excited state. The shape of the photobleach is determined by vibronic transitions of ground-state P3HT in amorphous and ordered phases, whereas the photoabsorption bands typically have a Gaussian shape, although some bands can be bimodal or asymmetric (Figure 1.13).

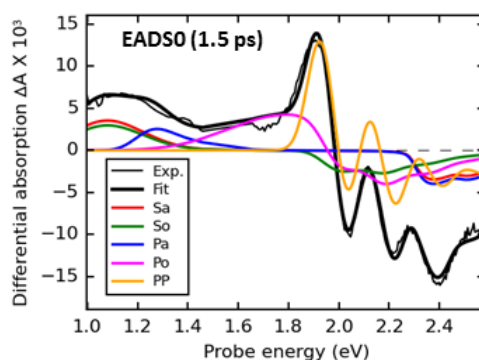


Figure 1.13. EADS0 of pristine P3HT:PCBM film with a lifetime of 1.5 ps, as obtained from a global analysis of experimental TA spectra using a 3 sequential steps model (thin solid curve), spectral fits to the EADS (thick solid curve) and contributions to fits from polaron pair, localised and delocalised singlet exciton and polaron states with their respective bleach contributions (negative differential absorption).

The total sum of excited states immediately after excitation (EADS0) is proportional to the number of absorbed photons, therefore time-dependent yields of the excited states can be calculated according to Equation 1.6:

$$\text{Time-dependent charge yield, } \varphi_i^{t=x} = \frac{c_i^{t=x}}{\sum (c_i^{t=0})} \quad (\text{Equation 1.6})$$

where $\varphi_i^{t=x}$ is the yield of the excited state at a given time (or in a given EADS), and C_i is the concentration of the excited state as calculated from absorption band integration. From Equation 1.6, ultrafast charge yield can be calculated as the sum of polaron concentrations in EADS0 divided by the sum of excited states at EADS0, whereas the total charge yield is calculated as the sum of polaron concentrations in EADS2 divided by the sum of excited states in EADS0.

As demonstrated by Guo *et al.*,¹¹³ the ultrafast charge yield is exclusively determined by the dissociation of excitons that are generated not further than 4 nm from the donor/acceptor interface. These excitons do not require extra time for diffusion, thus they are dissociated immediately. All excitons further than that will have to diffuse to the interface to be dissociated, thus contributing to the total charge dissociation. Polaron pair (or bound charges) is not normally considered in calculations since bound charges do not contribute to the final current, but recombine geminately within several nanoseconds and, thus, represent a loss pathway.^{78,90} Typical total charge yields of 60-75% have been observed for pristine P3HT:PCBM cells.^{90,115} Generally, ultrafast and total charge yields give an understanding of the exciton dissociation efficiency in films, indicative of the morphology of the bulk. Thus, information about morphological factors can be obtained from femtosecond TAS, such as approximate domain size, density of donor/acceptor interfaces, ratio of crystalline to amorphous phases in P3HT, single molecules of PCBM dissolved in polymer matrix, etc.

TPC, TPV and microsecond TAS address processes, such as charge extraction and recombination. According to Equation 1.3, in the absence of the excitation $G = 0$, and under the open circuit conditions there is no extraction, thus recombination of the generated charges can be observed by TAS.

According to Shuttle *et al.*, decay of the polarons in microsecond TAS follows a second order bimolecular recombination reaction, since the decay kinetics depend strongly on the excitation intensity and, therefore, on the density of the generated charges, n .¹¹⁶ Under these conditions, equal concentrations of positive and negative polarons are observed, as it is expected when only photoinduced polarons are present. In degraded cells, the amount of background carriers (trapped carriers, triplet states, oxygen-induced states) increases and the reaction does not follow second order anymore, because in degraded cells recombination

involves not only electrons and holes, recombining with the same constant, but the background carriers, that participate in recombination with different rate constants.⁷⁸ Thus, Karuthedath *et al.* have shown that in pristine P3HT:PCBM films the background carrier concentration was negligible and upon degradation in oxygen, the background carriers evolved (Figure 1.14), whereas Si-PCPDTBT polymer showed a notable concentration of background carriers even in its pristine form.⁹⁷

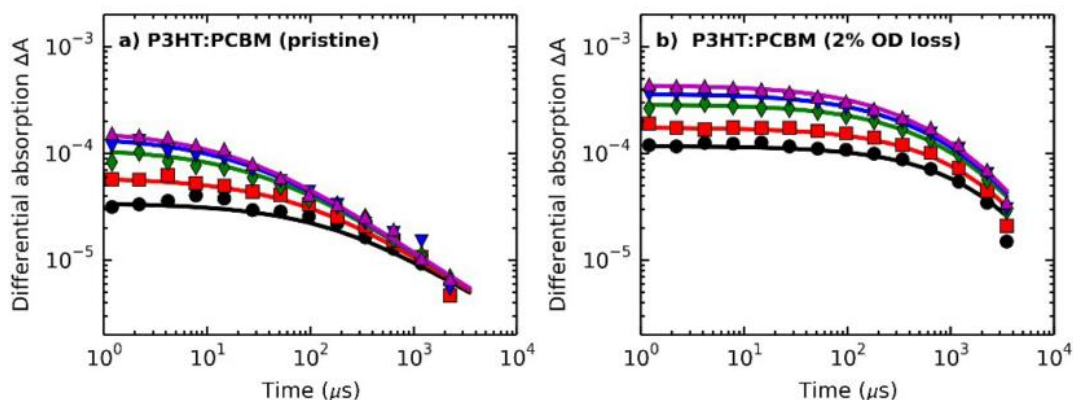


Figure 1.14. Charge transients in P3HT:PCBM films at different light intensities, upon termination of excitation, where (a) is pristine P3HT:PCBM film and (b) degraded P3HT:PCBM to 2% loss of optical density.⁹⁷

If microsecond TAS is performed under short circuit conditions, the extraction of generated charges can be observed as the polaron signal is significantly reduced in contrast to open circuit conditions. Only when the extraction is compromised, the decay traces in open circuit and short circuit are essentially similar (Figure 1.15).

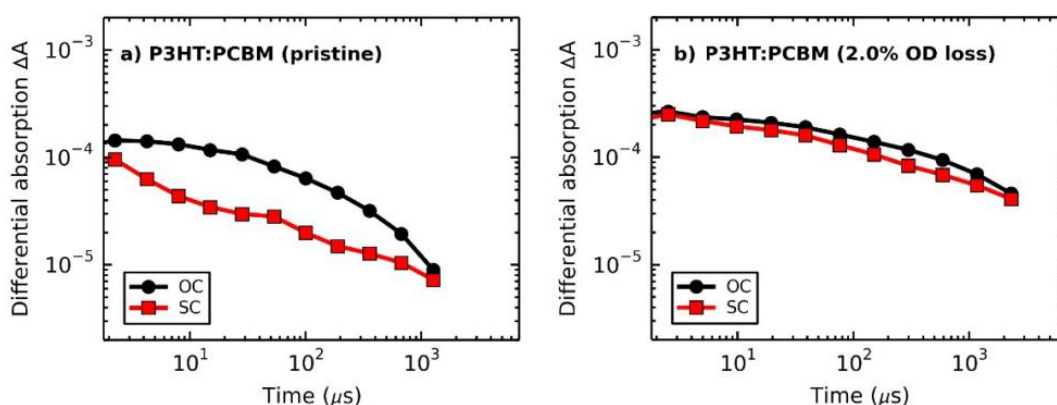


Figure 1.15. TA traces of (a) pristine and (b) photodegraded P3HT:PCBM solar cells under open circuit (OC) and short circuit (SC) conditions.⁹⁷

TPV and TPC traces are also capable of showing the charge decay under short circuit and open circuit conditions. Electrical techniques can give information about charge carrier

density that can be related to the current density, carrier lifetimes and bimolecular recombination constant, k_{rec} , if used in combination.¹¹⁷ Moreover, Huemüller *et al.* have demonstrated the use of TPV measurements to study open circuit voltage loss in photodegraded blends of various crystallinity and correspond it to the disorder-induced change of density of states (DOS).¹¹⁸

1.7 Degradation of OPVs

When speaking of the instability of organic solar cells, it is important to distinguish three types of degradation that occur in the cells and are triggered by different factors: chemical, physical and mechanical degradation. While physical degradation is mostly caused by intrinsic factors arising from operational conditions, such as temperature and light, chemical degradation is normally caused by external factors, namely oxygen and water, the presence of which can be excluded by effective encapsulation of the device.

1.7.1 Chemical degradation

As aforementioned, oxygen and water are the major reasons for the chemical degradation occurring in organic solar cells. Due to the complex nature of the processes that account for the final PCE of the device, the degradation mechanisms caused by oxygen and water are also wide ranging.

First of all, it has been demonstrated that diffusion of oxygen and water into the device occurs mainly through the counter electrode to ITO via microscopic pinholes and metal grains.¹¹⁹ Irradiation of the devices proved to accelerate oxygen diffusion and oxidation of the sub-electrode layers so that the oxygen diffused throughout all layers in the devices to reach the ITO.¹²⁰

Diffused oxygen can undergo transformations and promote further radical reactions in the polymer systems, producing more reactive species *via* cascade reactions or cause direct oxidation of organic compounds (Figure 1.16). Moreover, titanium oxide or zinc oxide nanoparticles that are typically employed in inverted cells are known for their photocatalytic activity and would form electron-hole pair upon UV illumination. The formed electron would attack molecular oxygen and form a highly reactive superoxide radical anion that readily oxidises organic material.¹²¹ This effect, however, has lately been shown to be advantageous for the stability; as TiO_x sol-gel derived films scavenged oxygen in a photocatalytic reaction with organic molecules bound to the titania.¹²²

The loss of efficiency upon photooxidation is mainly associated with the photobleaching of the polymer and, as a result, interruption of π -conjugation, and loss of optical density (OD) which affects photon absorption.¹²³

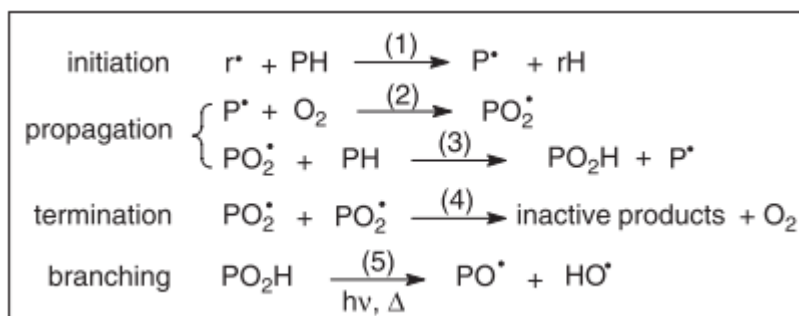


Figure 1.16. Chain oxidation processes in polymers.¹²³

1.7.1.1 Photooxidation of the photoactive layer

The oxidation of various polymers in the PAL has been demonstrated, with examples including polyphenylenevinylenes,^{124–126} poly(alkylthiophenes),¹²⁷ PCDTBT,¹²⁸ and Si-PCPDTBT.¹²⁹ In P3HT, oxygen doping has been shown to enhance charge carrier density,^{130,131} although it has been further demonstrated that oxygen creates deeper traps and decreases the mobility of charges in P3HT:PCBM.¹³¹ The singlet oxygen species (1O_2), initially suspected for the oxidative reaction, has been proven inactive towards polymer films.^{127,132} Thus, a radical mechanism for oxidation has been proposed, based on the thorough investigations of oxidation kinetics and resulting products by Manceau *et al.*¹²⁷

It should be noted that the degradation pathways in the donor-acceptor blend are more complex than those in a single polymer film. For example, in a blend of P3HT:PCBM, the latter can act as a radical scavenger and a UV-filter as it strongly absorbs in the UV region. PCBM is also susceptible to oxidation, although at a lower rate.¹³³ The same behaviour is observed in MDMO-PPV:PCBM blends where PCBM retards photooxidation of the polymer by a factor of ten.¹³⁴

Degradation studies of new low band gap polymers also reveal multiple oxidation pathways that lead to chain scissions, side chain and main chain oxidation (with the formation of volatile products) and extensive cross-linking. For example, in PCDTBT, these processes have a big impact on the morphology of the polymer films and their nanomechanical properties.¹³⁵ The volatile by-products induce an increase in roughness of the films and even the formation of holes and bubbles, whereas cross-linking of the chains leads to an initial (albeit small) increase in nanohardness in the first hours of photoirradiation. However, subsequently the nanohardness decreases due to the polymer chain scissions.

Various groups have shown that the conjugate polymer side-chains are the most susceptible to photooxidation,¹³⁶ although the side-chains are known to be crucial for polymer solubility and processing. One approach to address this issue uses thermally cleavable side-chains to facilitate the polymer processing and after deposition the side-chains are cleaved, providing better photostability.¹³⁷

There are various reports on the oxidation of polymers without irradiation, in the dark, although light is known to promote it.¹²³ On the other hand, photoreactions are also possible in an inert atmosphere, especially those induced by the UV part of the spectrum, for example in MDMO-PPV.¹³⁸

1.7.1.2 Oxidation of electrodes and PEDOT:PSS

The second chemical degradation mechanism that utilises oxygen is electrochemical transformation on the electrodes and their oxidation. In conventional architecture solar cells, aluminium or calcium electrodes are employed due to their low work function. These electrodes are extremely susceptible to oxidation (Ca more than Al). Water and oxygen diffuse through small pinholes and defects on the surface into the bulk of the electrode where they cause expansion of the inner voids, deformation of the electrodes and finally creating insulating spots where charge transfer between PAL and the electrode is significantly reduced.¹³⁹ This process is reflected in the observed increased series resistance and decreased fill factor. In worst cases, under mechanical or thermal stress the degraded electrode may completely delaminate from the PAL.

Low work function metals, on the other hand, have high reductive power, which results in reduction of the polymers via reductive electron-transfer and formation of Al-C bonds.¹⁴⁰ Formed organo-aluminium compounds are highly reactive and would react with underlying PAL or PEDOT:PSS. The direct reaction between C60 and aluminium (from the electrode) observed by Nishinaga *et al.*¹⁴¹ has been concluded to be the main reason for the disrupted charge transport.¹⁴²

Furthermore, the oxidation of an electrode might affect its charge extracting properties due to the mismatch in energy levels. In a conventional structure, an oxidative increase in the work function of the silver electrode leads to decreased ability to extract electrons sufficiently.¹³⁹ In an inverted cell structure, evolution of the Ag electrode work function has been found beneficial for hole collection.

As a counter electrode to the metal, transparent indium tin oxide (ITO) is used. In conventional solar cells, PEDOT:PSS is employed as an electron transporting layer due to various advantages: higher work function, enhanced wettability of the PAL on electrode,

decreased roughness of the ITO/PEDOT:PSS interface and thus high shunt resistance. Due to the high hygroscopic nature of PEDOT:PSS, the residual and diffused water molecules catalyse reactions between acidic PSS groups and ITO, releasing indium ions into the PAL that diffuse through all of the layers to the counter electrode.^{74,75} The absence of the ITO/PEDOT:PSS interface in inverted solar cells is another reason towards their enhanced stability as compared to conventional cells.

On its own, PEDOT:PSS has been demonstrated to be unstable to oxidation due to the excess of easily oxidised PSS in the formulations. The mechanism reported by Norrman *et al.*¹²⁰ demonstrated that the oxido-substitution reaction in PSS leads to cross reactions in the polymer blends resulting in particle formation, although it hasn't been yet clarified how these particles affect the overall device performance.¹³⁶ To stabilise the electrodes metal oxides are used as mentioned previously in this chapter (Section 1.3).

1.7.1.3 Encapsulation

Numerous stability studies of devices in inert atmosphere suggest that, if the devices are thoroughly encapsulated, detrimental effects of oxygen and water can be significantly reduced. The most efficient known way to encapsulate the devices with almost zero transmission rate for oxygen and water is using glass as both substrate and cover with glue to seal them together.¹¹⁹ This type of encapsulation would, however, render the flexibility and lightweight nature of the cells completely impossible. Thus, the search for new barrier materials is focused on several properties: efficiency, lightweight, flexibility, and finally, costs. It is believed that the cost of the encapsulation materials would determine the cost-efficiency of the polymer solar cells, when the compromise between the application and efficiency is found.¹⁴³

Often the barrier layers for OPVs are based on the experience of their use in organic light emitting diodes (OLEDs), but some believe that the requirements for gas and water permeability in OPV barrier layers should be less strict.¹⁴⁴ For material to be employed in OPVs, the acceptable level of permeation is $10^{-3} \text{ cm}^3\text{m}^{-2} \text{ day}^{-1}$ for oxygen and $10^{-3} \text{ cm}^3\text{m}^{-2} \text{ day}^{-1}$ for water vapour transmission¹⁴⁴ and has to be chosen based on the intrinsic stability of the solar cells to be encapsulated. This is much less demanding than for OLED encapsulation. Gevorgyan *et al.* have demonstrated that barrier films typically used for OLED encapsulation allowed extended stability of OPVs over 1,000 h of illumination and elevated temperature (45 °C).¹⁴⁵

Initial encapsulation tests were done with simple barrier foils, such as poly(ethylene terephthalate) (PET) which were not sufficient for encapsulation. Combinations of polymeric

films, such as poly(ethylene/ethyl vinyl alcohol) copolymer/poly(ethylene terephthalate) (PE/EVOH/PET) or polypropylene/poly(vinyl alcohol)/inorganic layer/polyethylene (PP/PVA/In/PE), have been shown more suitable for preventing water uptake.¹⁴⁴ The approach to combine organic and inorganic materials in a stack of alternating films for encapsulation was used by Gaume *et al.*,^{146–148} which subsequently led to research in polymer nanoclay composites as cheap and efficient barrier materials. For example, PVA/smectite nanocomposites are very flexible, transparent, easily processable, photostable, inexpensive and have excellent oxygen barrier properties.¹⁴⁹ The main disadvantage of these nanocomposites is the increased rate of PVA degradation upon irradiation, resulting in degradation products eroding the surface and destroying the barrier layer.¹²³ Furthermore, mechanical properties of nanocomposites compromise their stability; processing defects and mechanical stress can lead to decreased cohesion and adhesion, which results in cracks or even delamination.¹⁵⁰ Thus, further developments in the nanocomposite materials are needed to achieve inexpensive and efficient barrier foils.

1.7.2 Intrinsic stability of the solar cell

Upon effective encapsulation, atmospheric factors (water and oxygen) can be excluded and the harmful UV component of the solar spectrum can be filtered. In this case, the intrinsic stability of the cells is determined by susceptibility of the donor/acceptor blend to thermal treatment since elevated temperature is a non-avoidable operational factor. To understand the importance of thermal stability for overall stability of the solar cells, it is necessary to consider how the optimum morphology of the blend is established and how it is affected by temperature.

1.7.2.1 Optimal nanomorphology of the blend

As aforementioned (Section 1.4), morphology of the PAL has a major influence on the exciton dissociation and charge transport. Exciton dissociation is enhanced in a highly disordered bulk heterojunction morphology which allows almost all excitons to dissociate at the interface, whereas the charge transport is more efficient in consistent bilayer devices, where a charge carrier can diffuse without being trapped or finding a partner to recombine.

The deposition parameters constitute a key factor in establishing the optimum nanomorphology of the blend. Optimal deposition parameters, such as solvent, deposition method, rate, annealing time and temperature, additives, etc., can be determined during device optimisation studies. For example, the solvent used for casting the mixture of MDMO-PPV:PCBM has a direct effect on the morphology of the films.¹⁵¹ Films cast from toluene had

a specific nanostructure with a domain size of 0.5 microns, whereas films cast from chlorobenzene had domains of 0.1 μm . As a result, the current density in the devices cast from chlorobenzene was two-fold higher than in toluene-cast films.¹⁵¹ Later, it was demonstrated that the faster evaporation rate of the solvent serves the formation of larger domains of PCBM.¹⁵²

The same observation is valid for P3HT:PCBM blends. Ruderer *et al.* studied the vertical and lateral distribution of both phases depending on the solvent (chloroform, toluene, chlorobenzene and xylene) (Figure 1.17).¹⁵³ The blends deposited from chloroform demonstrated no lateral ordering, almost a bilayer structure, due to very poor solubility of PCBM in chloroform, whereas chlorobenzene and xylene showed the best domain distribution over the bulk, owing to similar solubility of both components in these solvents.



Figure 1.17. Black and white schematic morphologies of annealed P3HT:PCBM films cast from chloroform, toluene, chlorobenzene, and xylene solutions, as reconstructed from the results of various measurements.¹⁵³ Black areas correspond to pure PCBM phases and white to pure P3HT phases. Characteristic lengths are indicated.

Varying the solvent evaporation rate, Li *et al.* demonstrated that the EQE of the slow grown blend is much higher than that for a fast grown blend.¹⁵⁴ In concert with increased mobility, charge carrier transport and decreased series resistance, slow evaporation resulted in improved efficiencies. Also, spin-coating conditions as a function of time of spinning and time of solvent drying have a major impact on the nanomorphology of the blend of regioregular P3HT:PCBM.¹⁵⁵ Shorter spin-coating time and longer solvent drying time allow the optimum nanomorphology to evolve as a result of better P3HT ordering.

Furthermore, thermal treatment of the BHJ after deposition has a positive effect on the efficiency of the cells.¹⁵⁶ Post-deposition annealing induces the mobility of polymer chains and the diffusion of PCBM into the polymer matrix.¹⁵⁷ Polymer chains self-organise into fibrillar-based crystals that upon annealing extend into big P3HT domains.¹⁵⁸ The study of different molar masses of P3HT reveals that, with low molar masses the decrease in charge carrier mobility can be attributed to super-organisation of P3HT into big fibrillar clusters (Figure 1.18).

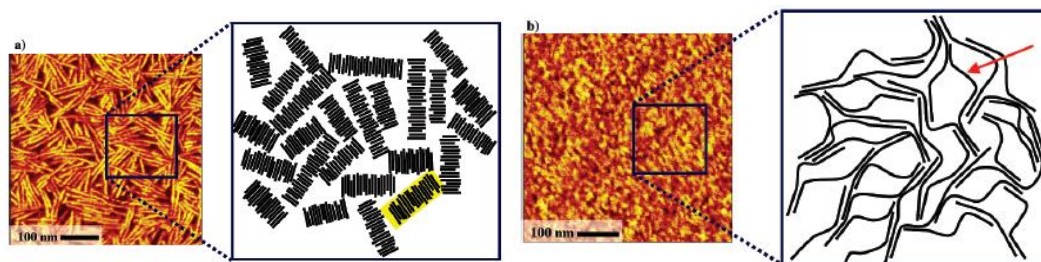


Figure 1.18. Model for transport in low molar mass (a) and high molar mass (b) P3HT films. Charge carriers are trapped within the nanorods (highlighted in yellow) in the low molar mass case. Long fibrils in high molar mass P3HT films bridge the ordered regions and soften the boundaries (marked with an arrow).⁴⁴

However, if low molar mass P3HT chains are processed from a slower evaporating solvent they can obtain nanorod morphology, favourable for mobility.⁴⁴ Thus, thermal annealing is one of the most effective techniques to obtain optimal nanomorphology in the polymer blends with high degree of crystallinity (P3HT, for example).

Optimal nanomorphology in P3HT:PCBM films presents more advantages than just maximised exciton dissociation and charge carrier percolation pathway due to evolution of interconnected donor-rich and acceptor-rich domains. Modelling has shown that the ordered regions in the polymer matrix have a higher HOMO level than the polymer in disordered regions. This HOMO level serves as a driving force for hole transfer and polaron pair dissociation, decreasing the geminate recombination.¹⁵⁹

After optimum annealing treatment, the polymer chains and PCBM exist in a non-equilibrium state of continuously intermixed heterojunctions. Thermodynamically, optimal device morphology is not favoured, so any external thermodynamic factors, such as elevated temperatures or long annealing time, will lead to degradation of the optimal morphology. High temperatures will bring in the energy sufficient to initiate phase separation and, as a result, complete demixing of the blend into two separate layers in the worst case or formation of aggregates and clusters with a significantly reduced exciton dissociation.¹⁶⁰

1.7.2.2. Thermally-induced evolution of morphology

Although donor polymer and typical acceptor PCBM obtain an optimal morphology upon annealing, operational temperatures induce thermodynamically favoured phase segregation of the blend, resulting in two major processes: (i) diffusion of PCBM molecules out of the polymer matrix and aggregation (crystallisation) into micro-sized clusters and (ii) donor polymer crystallisation.¹⁶¹ Both processes have a detrimental effect on the performance of

the devices, mostly affecting current density due to disrupted exciton dissociation and charge percolation, and fill factors due to enhanced recombination and trapped charges.^{90,162}

PCBM diffusion and cluster formation can be controlled by various techniques. To inhibit the growth of nucleated PCBM clusters, C60 molecules can be added. They reduce the nucleation time and, as a result, the size of the crystallites,¹⁶³ however, the stability of the cells only marginally improved and as a compromise with efficiency. Another way to inhibit the crystallisation is to control it through photoinduced PCBM oligomerisation.¹⁶⁴ Chen Wong *et al.* have demonstrated almost complete inhibition of the nucleation in both UV and fluorescent light treated samples of various polymer:PCBM blends, but not growth of any formed crystals.¹⁶⁴ Correspondingly, the stability of the cells was improved significantly after suppression of PCBM crystallisation.

For PCBM crystallisation to occur, the polymer matrix, where PCBM is homogeneously distributed upon deposition, should become labile enough to allow diffusion of PCBM molecules out of the matrix. The chain mobility at certain temperature is determined by the glass transition temperature (T_g) of the materials.^{162,165} Low T_g materials have greater mobility and readily release the dissolved PCBM molecules at elevated temperatures. In higher T_g polymer blends, migration of the polymer chains is less pronounced and, thus, the blend is more stable at elevated temperatures. Zhao *et al.* have tested different materials in a blend with PCBM to correlate the T_g to the phase separation of the blends.¹⁶⁵ In contrast to RR-P3HT, copolymers of MDMO-PPV and MDE-PPV demonstrated liquid-liquid separation of the blend in the molten state, which explains lower morphological stability of the blends. On the other hand, Kesters and Bertho have shown that the blends based on functionalised polythiophenes have improved thermal stability as compared to standard P3HT, although the T_g values of all copolymers are similar to that of P3HT.¹⁶⁶ There is no clear explanation for that but the functionalised side-chain organisation in the bulk might play a role in preventing PCBM from diffusion and crystallisation.^{166,167} The main challenge associated with the use of materials with higher T_g is their solubility. Normally, long side chain substituents are introduced for improvement of the polymer solubility and processing properties, but they decrease the T_g .¹³⁶

One of the main approaches to stabilise the blend is to cross-link donor and acceptor materials once the optimal nanomorphology is established. Cross-linking of the network allows several advantages:

1. rigidity of the final matrix with PCBM molecules entrapped in it;
2. reduced mobility of the polymer chains and low PCBM diffusion rates;
3. possibility of the same solvent deposition onto the cross-linked layer;

4. reduced intermixing of the layers upon long-term thermal treatment.¹⁶⁸

Cross-linking is usually carried out by employing block or random copolymers in the BHJ and include approaches such as using photocurable bromo-derivatives of the donor polymers,^{169–172} epoxy-derivatives,^{173,174} thermally curable azides,^{175,176} and vinyl derivatives.^{177,178} There are examples of PCBM derivatised with epoxy groups,^{174,179} and thermally polymerisable styryl groups.^{180,181} The best advantages arise from those approaches that do not require incorporation of photoinitiators as they tend to compromise the efficiency of the cells.¹⁷⁴ Another type of cross-linker is a small-molecule azide derivative tested by Derue *et al.* that reacts with both P3HT and PCBM.¹⁸² Kim *et al.* have shown an example of a solvent-resistant film based on azide cross-linker group (Figure 1.19), which allowed the fabrication of stable solar cells with preserved PCE of 3.3% after 40 h of annealing at 140 °C.¹⁷⁵

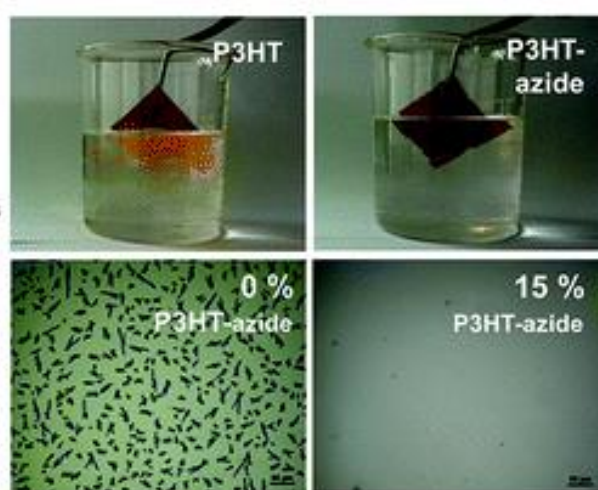


Figure 1.19. Optical microscopy images of the P3HT/PCBM films containing 0 or 15% P3HT-azide copolymer after annealing at 150 °C for 24 h. Scale bar = 100 μm .¹⁷⁵

Another effective approach employed stabilising block copolymers with a compatibilising effect that improved the miscibility of donor and acceptor components by reducing interfacial tension, thus reducing the blend segregation and elevated temperatures.^{183–188}

There are two approaches to prepare compatibilising block copolymers: (i) to graft the functional moieties onto the synthesised polymer or (ii) to make a polymer where one block is similar to that of P3HT and the second is a compatibilising block. The former approach is typically used to graft the fullerene functionalities onto the polymer.^{186,187,189–191} Sivula *et al.* proved that block copolymers incorporating both fullerene moieties and blocks of P3HT can stabilise the morphology without any detrimental effect on the PCE.^{186,187} The second approach employs various other groups, including, for example, copolymers of vinyl pyridine¹⁹² or ethylene oxide.^{183,193,194} Various other applications of block copolymers for stabilisation of solar cells have been extensively reviewed by Topham *et al.*¹⁹⁵

1.7.3 Interface degradation and stabilisation

As previously discussed in Section 1.3, inverted devices employ electron-selective layers deposited on the cathode, such as zinc oxide (ZnO), which also serve as oxygen diffusion barriers to reduce oxidative damage of the PAL.^{63,64} One drawback, however, is that the use of ZnO results in inverted devices having generally lower efficiency and, in certain aspects, lower stability due to defects present in the zinc oxide surface. Such defects create traps for the photogenerated electrons, resulting in increased series resistance and charge recombination.¹⁰⁰

Upon degradation of the device, these defects at the interface between the PAL and the ETL become one of the key factors in the loss of efficiency with decreased electrical coherence.^{61,196} This interface is extremely sensitive to pre- and post-deposition modification to improve stability and charge transport. One strategy that looks promising for enhancing device stability involves the use of polymeric stabilisers to improve inter-particle contact within the ZnO nanoparticles (NPs). For example, incorporation of poly(ethylene oxide) (PEO) into the layer has been demonstrated to improve the series resistance and facilitate electron transport due to nearly Ohmic contact between ZnO NPs and the PAL.¹⁹⁷ Indeed, Hu *et al.*¹⁹⁸ have shown that the introduction of PEO allows the formation of larger conductive clusters with decreased series resistance and improved electronic structure at the ZnO surface. Similarly, Shao *et al.*^{100,199} showed that the incorporation of PEO resulted in a significant increase in current density and fill factor due to the improved electronic coupling at the ZnO/PAL interface.

Another approach exploited the ability of polyelectrolyte layers, when deposited onto ZnO, to decrease the energy barrier for electron transfer from the PAL.^{200,201} The polyelectrolyte structure, based on thiophene units, resulted in the formation of uniform dipoles at the interface between PAL and ZnO, thus increasing the efficiency of the device.

The problem of interfacial stability is commonly addressed by the deposition of self-assembling monolayers (SAM) or by chemically binding the PAL to conductive zinc oxide nanoparticles through cross-linked layers.⁶⁸ The latter example uses a fullerene derivative functionalised with a trichlorosilyl moiety that tends to self-assemble on the surface of the titanium oxide nanoparticles and cross-link with the polymers in the PAL without any photoirradiation or thermal treatment. The silyl groups readily bind to residual hydroxyl groups on the outer shell of the titanium oxide (TiO_x) NPs, decreasing their contribution to PAL erosion.⁶⁸ It should be noted that the cross-linked layers allow same-solvent casting of the subsequent layers and a tighter interface between the electron extracting and active materials.

Introduction of SAMs has been successfully demonstrated with a variety of different organic and inorganic molecules. For example, the inorganic salt, caesium stearate, has been shown to passivate surface traps and decrease the possibility of the trap-induced recombination of charge carriers, leading to improvements in device efficiency.²⁰² Alternatively, tetrafluoroterephthalic acid (TFTPA) was anchored to zinc oxide surface through its carboxylic acid groups so that the aromatic rings of the tetrafluoroterephthalate moiety formed positively charged centres that attracted fullerene species in the PAL by Coulombic interactions.²⁰³

In other work, a SAM based on the Prato fullerene derivative functionalised with a carboxylic acid was deposited onto ZnO, annealed and washed.^{67,204,205} Washing the surface after annealing ensured that only strongly bound molecules remained in the device. Furthermore, this also allowed subsequent casting of the PAL from the same solvent without destruction of the SAM. Devices fabricated with this SAM, both under inert and atmospheric conditions, demonstrated an enhanced efficiency as a consequence of improved photocurrent and fill factor. This enhancement was attributed to a reduction in charge recombination losses at the interface between zinc oxide and the PAL.²⁰⁶ Moreover, this SAM helped to maintain the performance of the solar cells (within 80 % of their original performance) over 40 days under ambient conditions. Later, Hau *et al.* have shown that catechol and phosphonic acid derivatives of the fullerene also enhanced the performance of inverted cells by creating dipoles at the interface.²⁰⁵

1.8 Polymerisation techniques

The possibility of improving the solar cell efficiency and stability through interfacial modification has been widely demonstrated and therefore adopted in this work for polymeric materials. Speaking about block copolymers and interfacial materials, it is necessary to mention the most used routes to fabricate them. In block copolymers it is the ratio between the blocks that matters and their affinity for each other.¹⁹⁵ The key to fine tuning of the block-to-block ratio is using the controlled methods of polymerisation where applicable. Controlled polymerisation has several advantages:

- it yields well-defined polymers with low molar mass dispersities;
- resulting polymers have targeted or predictable molar masses;
- polymers have chain-end functionality;
- good conversion of the monomer (up to 99%) can be observed;
- allows a variety of polymerisation techniques, such as solution, emulsion, bulk, precipitation or suspension polymerisation;

- allows post-polymerisation modification of the polymers or *in-situ* copolymerisation;
- can produce different architectures, such as block copolymers, star-shaped or brush polymers.

Controlled, or living polymerisation, is a type of a chain-growth polymerisation, where monomers add onto the active site of the polymer one at a time, recreating the active site every time, but termination is restricted or completely absent.²⁰⁷ There are various living polymerisation techniques, including anionic, cationic, ring-opening metathesis (ROMP) and controlled radical polymerisation. They are employed depending on the nature of the monomer and its desirable properties, *i.e.* molar mass or chain-end functionality.

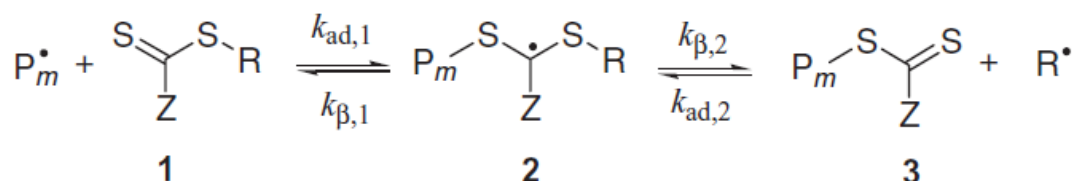
Controlled radical polymerisation (CRP) is of particular interest for this work. In all types of CRP an equilibrium between propagating chains and dormant chains is the key to suppression of termination.²⁰⁸ To establish this equilibrium, mediating agents are required. There are two ways of restricting the termination processes regarding this equilibrium: radicals are cycling between activated/deactivated states, as in atom transfer radical polymerisation (ATRP), or they are involved in a 'reversible transfer' degenerative exchange process as in reversible addition-fragmentation chain transfer polymerisation (RAFT). Also, fast instantaneous initiation enables the simultaneous growth of all chains.

In ATRP, growing chains are constantly deactivated by a stable intermittent species. The dormant species are activated spontaneously whether by light (if the light energy is sufficient for the breakage of the bond) or by a catalyst.²⁰⁹ The advantage of the intermittent species is its stability and inability to self-terminate: it only can react with the radical chain. In this mechanism, the deactivation of the chain radical reduces the concentration of propagating chain ends and therefore, minimises termination. For activation, ATRP uses a transition metal complex with ligands. There is also a counter-ion, usually a halogen, that forms a covalent or ionic bond with the metal centre. The transition metal homolytically cleaves an alkyl halogen bond in the propagating chain, thus working as an activator of the dormant chains. Thus, one of the benefits of ATRP is that it provides a chain-end functionality, although limited upon the polymerisation to the halide-groups, that can subsequently be converted into a suitable group, often an azide, thus allowing post-polymerisation connection of two blocks to each other (through an azide-alkyne click reaction).^{210,211}

RAFT polymerisation employs a chain transfer agent (CTA) to establish an equilibrium between growing and dormant species through constant radical exchange. The transfer of the CTA between growing radical chains, present at a very low concentration, and dormant polymeric chains, present at a higher concentration, regulates the growth of the polymer chains and limits the termination reactions.

Initial monomer radicals are formed like in a conventional radical polymerisation from decomposition of the initiator (thermal or light-induced). Consequently, the growing radical chain adds to the C=S bond in the CTA (which is very reactive) and forms an intermediate **2** (Figure 1.20). This intermediate fragments in two ways: either releasing the initial growing chain **3** or the R leaving group. Residual R group can reinitiate the polymerisation and start a new growing polymer chain.

Pre-equilibrium:



Main equilibrium:

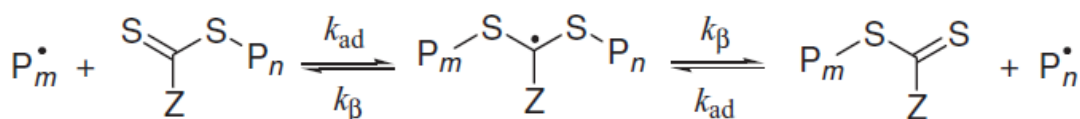


Figure 1.20. Mechanism of RAFT according to Vana.²¹²

When the initial CTA is fully consumed, the equilibrium is established. In the state of this equilibrium, all chains have an equal chance of propagation as the exchange between dormant (on the CTA) and growing polymer chains is very fast. This ensures that all polymer chains have very low polydispersity indices. Propagation continues to the point when conversion reaches 80-95% and the probability of termination increases considerably.

The choice of CTA (*i.e.* S and Z groups) depends on the nature of the monomer. Monomers are divided into two groups: less-activated monomers (LAMs) and more-activated monomers (MAMs). LAMs, such as vinyl esters or N-vinylcarbazole, are characterised by electron-rich double bonds and a lack of radical-stabilising substituent.²¹³ MAMs, such as styrene, methyl methacrylate or acrylonitrile, carry a radical-stabilising substituent, and, if polymerised together with LAMs, will be preferentially incorporated into the polymer. Thus, MAMs are typically polymerised with trithiocarbonates, whereas LAMs can be polymerised with xanthates.^{214–216}

The useful property of the CTAs is that most of them can be obtained in a well-established one-pot synthesis process.^{217–219} Or, if the one-pot synthesis of the CTA isn't available, upon polymerisation, the resulting macro CTA can be subsequently derivatised, depending on which chain-end functionality is required for the next synthetic steps.

The resulting polymer still bearing all features of the CTA can also be referred to as a macro-CTA, and when purified from the residual monomer, it can be used for further polymerisation of a different monomer to form a block copolymer. This only occurs if the CTA is equally good for both monomers, though the conditions (i.e. solvent, temperature) can vary.²¹⁷

In RAFT polymerisation, the control over the molar mass is primarily mediated by the CTA, not the initiator, and the degree of polymerisation (*i.e.* the number of monomers in a polymer chain) depends on the ratio of CTA to monomer, if the concentration of the initiator is much smaller than that of the CTA. Furthermore, to achieve targeted molar masses, high conversion and low polydispersities, appropriate polymerisation conditions, such as solvent, temperature, ratio of solvent to monomer, initiator, CTA and the ratio of initiator to CTA, have to be experimentally established.

1.9 Aims

Organic solar cells demonstrate suitability for various applications, including consumer electronics and building integration for autonomous energy production. Belectric OPV GmbH (Germany) have successfully integrated semi-transparent organic photovoltaics into the architecture of the German Pavilion at the 2015 world exhibition in Milan, demonstrating that this technology has a huge market potential even at current developments in power conversion efficiencies. However, the lifetime of the OPVs are still not sufficient to be speaking about mass-production of the modules. A lot of effort is concentrated on studies of stability and prediction of real lifetime of the big modules and research into the main factors that cause loss of performance at operational, storage and transportation conditions.

European project, Establis, is a consortium dedicated to unravelling the mechanisms of the degradation on a laboratory scale and includes physical, mechanical, rheological, spectroscopic and other types of investigations and measurements. At the same time, Establis researchers are focusing on the development of new materials for stabilisation of OPVs. The work herein, as a part of the collaborative effort of Establis, has been dedicated to fabrication of new materials for stabilisation of the ETL/PAL interface and comprehensive studies of their effect on the key processes in the device.

Thus, the first major aim of this work was to produce new materials in a controlled way and characterise them in full. This part of work was done at Aston University (Birmingham, UK). The second major aim was to study the effect of fabricated materials on the performance and stability of the devices, based on conventional P3HT:PCBM blends (at Belectric OPV, Nuremberg, Germany). The third aim was to contribute to general understanding of device

degradation through time-resolved measurements and modelling of corresponding physical processes, and to explore the effect of interfacial layers on the device performance in greater detail. This part of work was carried out at IMDEA Nanociencia (Madrid, Spain).

1.10 References

- (1) MAP: How much energy is the world using? <http://burnanenergyjournal.com/how-much-energy-are-we-using/> (accessed Jul 6, 2015).
- (2) Administration, U.S.E.I. International Energy Statistics <http://www.eia.gov/cfapps/ipdbproject/IEDIndex3.cfm?tid=90&pid=44&aid=8> (accessed Jul 6, 2015).
- (3) Administration, U. S. E. I. *Levelized Cost of New Generation Resources in the Annual Energy Outlook 2015*; 2015.
- (4) Project, S. U. G. C. and E. Global Exergy Resource Chart <http://gcep.stanford.edu/research/exergy/resourcechart.html> (accessed Jul 6, 2015).
- (5) Chapin, D. M.; Fuller, C. S.; Pearson, G. L. *J. Appl. Phys.* **1954**, 25 (5), 676–677.
- (6) Goetzberger, A.; Hebling, C.; Schock, H. W. *Mater. Sci. Eng. R-Reports* **2003**, 40 (1), 1–46.
- (7) Carlson, D. E. *Sol. Energy Mater.* **1980**, 3 (4), 503–518.
- (8) Romeo, A.; Terheggen, M.; Abou-Ras, D.; Bätzner, D. L.; Haug, F.-J.; Kälin, M.; Rudmann, D.; Tiwari, A. N. *Prog. Photovoltaics Res. Appl.* **2004**, 12 (23), 93–111.
- (9) Delahoy, A. E.; Chen, L.; Akhtar, M.; Sang, B.; Guo, S. *Sol. Energy* **2004**, 77 (6), 785–793.
- (10) Terakawa, A. *Sol. Energy Mater. Sol. Cells* **2013**, 119, 204–208.
- (11) Xiao, S. Q.; Xu, S.; Ostrikov, K. *Mater. Sci. Eng. R-Reports* **2014**, 78, 1–29.
- (12) Filtvedt, W. O.; Holt, A.; Ramachandran, P. A.; Melaaen, M. C. *Sol. Energy Mater. Sol. Cells* **2012**, 107, 188–200.
- (13) Mathew, X.; Enriquez, J. P.; Romeo, A.; Tiwari, A. N. *Sol. Energy* **2004**, 77 (6), 831–838.
- (14) Theiss, S. D.; Wagner, S. *IEEE Electron Device Lett.* **1996**, 17 (12), 578–580.
- (15) Wuerz, R.; Eicke, A.; Frankenfeld, M.; Kessler, F.; Powalla, M.; Rogin, P.; Yazdani-Assl, O. *Thin Solid Films* **2009**, 517 (7), 2415–2418.

- (16) Shah, A.; Meier, J.; Buechel, A.; Kroll, U.; Steinhauser, J.; Meillaud, F.; Schade, H.; Dominé, D. *Thin Solid Films* **2006**, 502 (1-2), 292–299.
- (17) Fthenakis, V. *Renew. Sustain. Energy Rev.* **2009**, 13 (9), 2746–2750.
- (18) Kaelin, M.; Rudmann, D.; Tiwari, A. N. *Sol. Energy* **2004**, 77 (6), 749–756.
- (19) Weerasinghe, H. C.; Huang, F.; Cheng, Y.-B. *Nano Energy* **2013**, 2 (2), 174–189.
- (20) Green, M. A.; Emery, K.; Hishikawa, Y.; Warta, W.; Dunlop, E. D. *Prog. Photovoltaics* **2014**, 22 (7), 701–710.
- (21) Wang, J.; Xie, Y.; Zhang, Z.; Li, J.; Chen, X.; Zhang, L.; Xu, R.; Zhang, X. *Sol. Energy Mater. Sol. Cells* **2009**, 93 (3), 355–361.
- (22) Wu, J.; Hao, S.; Lan, Z.; Lin, J.; Huang, M.; Huang, Y.; Fang, L.; Yin, S.; Sato, T. *Adv. Funct. Mater.* **2007**, 17 (15), 2645–2652.
- (23) Green, M. A.; Emery, K.; Hishikawa, Y.; Warta, W.; Dunlop, E. D. *Prog. Photovoltaics Res. Appl.* **2015**, 23 (1), 1–9.
- (24) Jung, J. W.; Williams, S. T.; Jen, A. K.-Y. *RSC Adv.* No. 108, 62971–62977.
- (25) Green, M. a.; Ho-Baillie, A.; Snaith, H. J. *Nat. Photonics* **2014**, 8 (7), 506–514.
- (26) Graetzel, M. *Nat. Mater.* **2014**, 13 (9), 838–842.
- (27) Burschka, J.; Pellet, N.; Moon, S.-J.; Humphry-Baker, R.; Gao, P.; Nazeeruddin, M. K.; Graetzel, M. *Nature* **2013**, 499 (7458), 316–319.
- (28) Niu, G.; Li, W.; Meng, F.; Wang, L.; Dong, H.; Qiu, Y. *J. Mater. Chem. a* **2014**, 2 (3), 705–710.
- (29) Leijtens, T.; Eperon, G. E.; Pathak, S.; Abate, A.; Lee, M. M.; Snaith, H. J. *Nat. Commun.* **2013**, 4, 2885.
- (30) Scharber, M. C.; Sariciftci, N. S. *Prog. Polym. Sci.* **2013**, 38 (12), 1929–1940.
- (31) Kaltenbrunner, M.; White, M. S.; Glowacki, E. D.; Sekitani, T.; Someya, T.; Sariciftci, N. S.; Bauer, S. *Nat. Commun.* **2012**, 3, 1–7.
- (32) Leonat, L.; White, M. S.; Glowacki, E. D.; Scharber, M. C.; Zillger, T.; Rühling, J.; Hübler, A.; Sariciftci, N. S. *J. Phys. Chem. C* **2014**, 118 (30), 16813–16817.
- (33) Lipomi, D. J.; Tee, B. C.-K.; Vosgueritchian, M.; Bao, Z. *Adv. Mater.* **2011**, 23 (15), 1771–1775.
- (34) Subbiah, J.; Choudhury, K. R.; Ellinger, S.; Reynolds, J. R. *IEEE J. Sel. Top. Quantum Electron.* **2010**, 16 (6), 1792–1800.

- (35) Chen, C.-C.; Dou, L.; Zhu, R.; Chung, C.-H.; Song, T.-B.; Zheng, Y. B.; Hawks, S.; Li, G.; Weiss, P. S.; Yang, Y. *ACS Nano* **2012**, 6 (8), 7185–7190.
- (36) Kalowekamo, J.; Baker, E. *Sol. Energy* **2009**, 83 (8), 1224–1231.
- (37) Chandross, E. A. *Science*. **2011**, 333 (6038), 35–36.
- (38) Zervos, H.; Das, R.; Ghaffarzadekh, K. *Organic Photovoltaics (OPV): Technologies, Markets & Players 2013-2023*; 2013.
- (39) Obrzut, J.; Obrzut, M. J.; Karasz, F. E. *Synth. Met.* **1989**, 29 (1), 103–108.
- (40) Sariciftci, N. S.; Smilowitz, L.; Heeger, A. J.; Wudl, F. *Science* **1992**, 258 (5087), 1474–1476.
- (41) Yu, G.; Pakbaz, K.; Heeger, A. J. *Appl. Phys. Lett.* **1994**, 64 (25), 3422–3424.
- (42) McCullough, R. D.; Lowe, R. D.; Jayaraman, M.; Anderson, D. L. *J. Org. Chem.* **1993**, 58 (4), 904–912.
- (43) Korovyanko, O.; Österbacka, R.; Jiang, X.; Vardeny, Z.; Janssen, R. *Phys. Rev. B* **2001**, 64 (23), 235122.
- (44) Kline, R. J.; McGehee, M. D.; Kadnikova, E. N.; Liu, J.; Fre, J. M. J.; Toney, M. F. *Macromolecules* **2005**, 38 (8), 3312–3319.
- (45) Lattante, S. *Electronics* **2014**, 3 (1), 132–164.
- (46) Groenendaal, L.; Jonas, F.; Freitag, D.; Pielartzik, H.; R, R. J. *Adv Mater* **2000**, 12, 481–494.
- (47) Shrotriya, V.; Li, G.; Yao, Y.; Chu, C.-W.; Yang, Y. *Appl. Phys. Lett.* **2006**, 88 (7), 073508.
- (48) Tao, C.; Ruan, S.; Zhang, X.; Xie, G.; Shen, L.; Kong, X.; Dong, W.; Liu, C.; Chen, W. *Appl. Phys. Lett.* **2008**, 93 (19), 193307.
- (49) Yang, L.; Xu, H.; Tian, H.; Yin, S.; Zhang, F. *Sol. Energy Mater. Sol. Cells* **2010**, 94 (10), 1831–1834.
- (50) Sun, L.; Shen, W.; Chen, W.; Bao, X.; Wang, N.; Dou, X.; Han, L.; Wen, S. *Thin Solid Films* **2014**, 573, 134–139.
- (51) Boix, P. P.; Ajuria, J.; Etxebarria, I.; Pacios, R.; Garcia-Belmonte, G.; Bisquert, J. *J. Phys. Chem. Lett.* **2011**, 2 (5), 407–411.
- (52) Hung, L. S.; Tang, C. W.; Mason, M. G. *Appl. Phys. Lett.* **1997**, 70 (2), 152–154.
- (53) Eda, G.; Fanchini, G.; Chhowalla, M. *Nat. Nanotechnol.* **2008**, 3 (5), 270–274.

- (54) Eda, G.; Lin, Y.-Y.; Miller, S.; Chen, C.-W.; Su, W.-F.; Chhowalla, M. *Appl. Phys. Lett.* **2008**, 92 (23), 233305.
- (55) Devan, R. S.; Patil, R. A.; Lin, J.-H.; Ma, Y.-R. *Adv. Funct. Mater.* **2012**, 22 (16), 3326–3370.
- (56) Liu, J.; Xue, Y.; Gao, Y.; Yu, D.; Durstock, M.; Dai, L. *Adv. Mater.* **2012**, 24 (17), 2228–2233.
- (57) Wu, C.-H.; Chin, C.-Y.; Chen, T.-Y.; Hsieh, S.-N.; Lee, C.-H.; Guo, T.-F.; Jen, A. K.-Y.; Wen, T.-C. *J. Mater. Chem. a* **2013**, 1 (7), 2582–2587.
- (58) Wang, M.; Tang, Q.; An, J.; Xie, F.; Chen, J.; Zheng, S.; Wong, K. Y.; Miao, Q.; Xu, J. *ACS Appl. Mater. Interfaces* **2010**, 2 (10), 2699–2702.
- (59) Valencia, S.; Marin, J. M.; Restrepo, G. *Open Mater. Sci. J.* **2010**, 4, 9–14.
- (60) *Wide bandgap semiconductors: fundamental properties and modern photonic and electronic devices*; Takahashi, K., Yoshikawa, A., Sandhu, A., Eds.; Springer: New York, 2007.
- (61) White, M. S.; Olson, D. C.; Shaheen, S. E.; Kopidakis, N.; Ginley, D. S. *Appl. Phys. Lett.* **2006**, 89 (14), 143517.
- (62) Hau, S. K.; Yip, H.-L.; Ma, H.; Jen, A. K.-Y. *Appl. Phys. Lett.* **2008**, 93 (23), 233304.
- (63) Hayakawa, A.; Yoshikawa, O.; Fujieda, T.; Uehara, K.; Yoshikawa, S. *Appl. Phys. Lett.* **2007**, 90 (16), 163517.
- (64) Lee, K.; Kim, J. Y.; Park, S. H.; Kim, S. H.; Cho, S.; Heeger, A. J. *Adv. Mater.* **2007**, 19 (18), 2445–2449.
- (65) Aranovich, J.; Ortiz, A.; Bube, R. H. *J. Vac. Sci. Technol.* **1979**, 16 (4), 994–1003.
- (66) Sekine, N.; Chou, C.-H.; Kwan, W. L.; Yang, Y. *Org. Electron.* **2009**, 10 (8), 1473–1477.
- (67) Hau, S. K.; Yip, H.-L.; Acton, O.; Baek, N. S.; Ma, H.; Jen, A. K.-Y. *J. Mater. Chem.* **2008**, 18 (42), 5113.
- (68) Liang, W.; Chang, C.; Lai, Y.; Cheng, S.; Chang, H.; Lai, Y.; Cheng, Y.; Wang, C.; Hsu, C. *Macromolecules* **2013**.
- (69) Jørgensen, M.; Norrman, K.; Gevorgyan, S. a; Tromholt, T.; Andreasen, B.; Krebs, F. C. *Adv. Mater.* **2012**, 24 (5), 580–612.
- (70) Aziz, H.; Xu, G. *Synth. Met.* **1996**, 80 (1), 7–10.

- (71) Aziz, H.; Popovic, Z. D.; Hu, N. X.; Hor, A. M.; Xu, G. *Science* **1999**, 283 (5409), 1900–1902.
- (72) Aziz, H.; Popovic, Z. D. *Chem. Mater.* **2004**, 16 (23), 4522–4532.
- (73) Lloyd, M. T.; Olson, D. C.; Lu, P.; Fang, E.; Moore, D. L.; White, M. S.; Reese, M. O.; Ginley, D. S.; Hsu, J. W. P. *J. Mater. Chem.* **2009**, 19 (41), 7638.
- (74) De Jong, M. P.; van IJzendoorn, L. J.; de Voigt, M. J. A. *Appl. Phys. Lett.* **2000**, 77 (14), 2255–2257.
- (75) De Jong, M. P.; Simons, D. P. L.; Reijme, M. A.; van IJzendoorn, L. J.; van der Gon, A. W. D.; de Voigt, M. J. A.; Brongersma, H. H.; Gymer, R. W. *Synth. Met.* **2000**, 110 (1), 1–6.
- (76) Zhang, Q.; Yodyingyong, S.; Xi, J.; Myers, D.; Cao, G. *Nanoscale* **2012**, 4 (5), 1436–1445.
- (77) Wagenpfahl, A.; Rauh, D.; Binder, M.; Deibel, C.; Dyakonov, V. *Phys. Rev. B* **2010**, 82 (11), 115306.
- (78) Deibel, C.; Dyakonov, V. *Reports Prog. Phys.* **2010**, 73 (9), 96401.
- (79) Shockley, W.; Queisser, H. J. *J. Appl. Phys.* **1961**, 32 (3), 510.
- (80) Bundgaard, E.; Krebs, F. C. *Sol. Energy Mater. Sol. Cells* **2007**, 91 (11), 954–985.
- (81) Liang, W. Y. *Phys. Educ.* **1970**, 5, 226.
- (82) Campbell, I.; Hagler, T.; Smith, D.; Ferraris, J. *Phys.Rev.Lett.* **1996**, 76 (11), 1900–1903.
- (83) Alvarado, S.; Seidler, P.; Lidzey, D.; Bradley, D. *Phys.Rev.Lett.* **1998**, 81 (5), 1082–1085.
- (84) Hwang, I.; Moses, D.; Heeger, A. J. *J. Phys. Chem. C* **2008**, 112 (11), 4350–4354.
- (85) Verlaak, S.; Beljonne, D.; Cheyns, D.; Rolin, C.; Linares, M.; Castet, F.; Cornil, J.; Heremans, P. *Adv. Funct. Mater.* **2009**, 19 (23), 3809–3814.
- (86) Gadisa, A.; Svensson, M.; Andersson, M. R.; Inganäs, O. *Appl. Phys. Lett.* **2004**, 84 (9), 1609.
- (87) Pirijs, J.; Dykstra, T. E.; Bakulin, A. a.; Loosdrecht, P. H. M. Van; Knulst, W.; Trinh, M. T.; Schins, J. M.; Siebbeles, L. D. a. *J. Phys. Chem. C* **2009**, 113 (32), 14500–14506.
- (88) Lüer, L.; Cerullo, G.; Zavelani-Rossi, M.; Lanzani, G. *Chem. Phys. Lett.* **2003**, 381 (5-6), 751–758.

- (89) Vacar, D.; Maniloff, E.; McBranch, D.; Heeger, A. *Phys.Rev.B* **1997**, *56* (8), 4573–4577.
- (90) Howard, I.; Mauer, R.; Meister, M.; Laquai, F. *J. Am. Chem. Soc.* **2010**, *132* (42), 14866–14876.
- (91) Cowan, S.; Roy, A.; Heeger, A. *Phys.Rev.B* **2010**, *82* (24), 245207.
- (92) Groves, C.; Blakesley, J. C.; Greenham, N. C. *Nano Lett.* **2010**, *10* (3), 1063–1069.
- (93) Sirringhaus, H.; Brown, P. J.; Friend, R. H.; Nielsen, M. M.; Bechgaard, K.; Langeveld-Voss, B. M. W.; Spiering, A. J. H.; Janssen, R. A. J.; Meijer, E. W.; Herwig, P.; de Leeuw, D. M. *Nature* **1999**, *401* (6754), 685–688.
- (94) Kniepert, J.; Lange, I.; van der Kaap, N. J.; Koster, L. J. A.; Neher, D. *Adv. Energy Mater.* **2014**, *4* (7).
- (95) Das, S.; Khlyabich, P. P.; Burkhart, B.; Roberts, S. T.; Couderc, E.; Thompson, B. C.; Bradforth, S. E. *J. Phys. Chem. C* **2014**, *118* (13), 6650–6660.
- (96) Walzer, K.; Maennig, B.; Pfeiffer, M.; Leo, K. *Chem. Rev.* **2007**, *107* (4), 1233–1271.
- (97) Karuthedath, S.; Sauermann, T.; Egelhaaf, H.-J.; Wannemacher, R.; Brabec, C. J.; L  r, L. *J. Mater. Chem. A* **2014**, *3*, 3399–3408.
- (98) Pope, M.; Swenberg, C. E. *Electronic Processes in Organic Crystals and Polymers*; Oxford University Press, 1999.
- (99) Kumar, A.; Sista, S.; Yang, Y. *J. Appl. Phys.* **2009**, *105* (9), 094512.
- (100) Shao, S.; Zheng, K.; Pullerits, T.; Zhang, F. *ACS Appl. Mater. Interfaces* **2013**, *5* (2), 380–385.
- (101) Saive, R.; Mueller, C.; Schinke, J.; Lovrincic, R.; Kowalsky, W. *Appl. Phys. Lett.* **2013**, *103* (24), 243303.
- (102) Krebs, F. C.; Tromholt, T.; J  rgensen, M. *Nanoscale* **2010**, *2* (6), 873–886.
- (103) Manor, A.; Katz, E. a.; Tromholt, T.; Krebs, F. C. *Sol. Energy Mater. Sol. Cells* **2012**, *98*, 491–493.
- (104) Scharber, M. C.; Wuhlbacher, D.; Koppe, M.; Denk, P.; Waldauf, C.; Heeger, A. J.; Brabec, C. L. *Adv. Mater.* **2006**, *18* (6), 789–794.
- (105) Maurano, A.; Hamilton, R.; Shuttle, C. G.; Ballantyne, A. M.; Nelson, J.; O'Regan, B.; Zhang, W.; McCulloch, I.; Azimi, H.; Morana, M.; Brabec, C. J.; Durrant, J. R. *Adv. Mater.* **2010**, *22* (44), 4987–4992.
- (106) Green, M. A. *Solid. State. Electron.* **1981**, *24*, 788–789.

- (107) Grossiord, N.; Kroon, J.; Andriessen, R.; Blom, P. *Org. Electron.* **2012**, *13* (3), 432–456.
- (108) Guo, X.; Zhou, N.; Lou, S. J.; Smith, J.; Tice, D. B.; Hennek, J. W.; Ortiz, R. P.; Navarrete, J. T. L.; Li, S.; Strzalka, J.; Chen, L. X.; Chang, R. P. H.; Facchetti, A.; Marks, T. J. *Nat. Photonics* **2013**, *7* (10), 825–833.
- (109) Cabanillas-Gonzalez, J.; Grancini, G.; Lanzani, G. *Adv. Mater.* **2011**, *23* (46), 5468–5485.
- (110) Cerullo, G.; Manzoni, C.; Lüer, L.; Polli, D. *Photochem. Photobiol. Sci.* **2007**, *6* (2), 135–144.
- (111) Van Stokkum, I. H. M.; Larsen, D. S.; van Grondelle, R. *Biochim. Biophys. Acta* **2004**, *1657* (2-3), 82–104.
- (112) Ohkita, H.; Ito, S. *Polymer (Guildf)*. **2011**, *52* (20), 4397–4417.
- (113) Guo, J.; Ohkita, H.; Bente, H.; Ito, S. *J. Am. Chem. Soc.* **2009**, *131* (46), 16869–16880.
- (114) Guo, J.; Ohkita, H.; Bente, H.; Ito, S. *J. Am. Chem. Soc.* **2010**, No. 6, 6154–6164.
- (115) Deschler, F.; De Sio, A.; von Hauff, E.; Kutka, P.; Sauermann, T.; Egelhaaf, H.-J.; Hauch, J.; Da Como, E. *Adv. Funct. Mater.* **2012**, *22* (7), 1461–1469.
- (116) Shuttle, C.; O'Regan, B.; Ballantyne, a.; Nelson, J.; Bradley, D.; Durrant, J. *Phys. Rev. B* **2008**, *78* (11), 113201.
- (117) Guo, X.; Zhou, N.; Lou, S. J.; Smith, J.; Tice, D. B.; Hennek, J. W.; Ortiz, R. P.; Navarrete, J. T. L.; Li, S.; Strzalka, J.; Chen, L. X.; Chang, R. P. H.; Facchetti, A.; Marks, T. J. *Nat. Photonics* **2013**, *7* (10), 825–833.
- (118) Heumueller, T.; Burke, T. M.; Mateker, W. R.; Sachs-Quintana, I. T.; Vandewal, K.; Brabec, C. J.; McGehee, M. D. *Adv. Energy Mater.* **2015**.
- (119) Norrman, K.; Madsen, M. V.; Gevorgyan, S. A.; Krebs, F. C. *J. Am. Chem. Soc.* **2010**, *132* (47), 16883–16892.
- (120) Norrman, K.; Alstrup, J.; Jørgensen, M.; Lira-Cantu, M.; Larsen, N. B.; Krebs, F. C. In *SPIE Optics + Photonics*; Kafafi, Z. H., Lane, P. A., Eds.; International Society for Optics and Photonics, 2006; p 63340O.
- (121) Jorgensen, M.; Norrman, K.; Krebs, F. C. *Sol. Energy Mater. Sol. Cells* **2008**, *92* (7), 686–714.
- (122) Li, J.; Kim, S.; Edington, S.; Nedy, J.; Cho, S.; Lee, K.; Heeger, A. J.; Gupta, M. C.; Yates Jr, J. T. *Sol. Energy Mater. Sol. Cells* **2011**, *95* (4), 1123–1130.

- (123) Rivaton, A.; Tournebize, A.; Gaume, J.; Bussière, P.-O.; Gardette, J.-L.; Therias, S. *Polym. Int.* **2014**, 63 (8), 1335–1345.
- (124) Dam, N.; Scurlock, R. D.; Wang, B.; Ma, L.; Sundahl, M.; Ogilby, P. R. *Chem. Mater.* **1999**, 11 (5), 1302–1305.
- (125) Cumpston, B. H.; Jensen, K. F. *J. Appl. Polym. Sci.* **1998**, 69 (12), 2451–2458.
- (126) Gu, S.; Neugebauer, H.; Sariciftci, N. S. *Chem. Rev.* **2007**, 107 (4), 1324–1338.
- (127) Manceau, M.; Rivaton, A.; Gardette, J.-L.; Guillerez, S.; Lemaître, N. *Polym. Degrad. Stab.* **2009**, 94 (6), 898–907.
- (128) Tournebize, A.; Bussiere, P.-O.; Wong-Wah-Chung, P.; Therias, S.; Rivaton, A.; Gardette, J.-L.; Beaupre, S.; Leclerc, M. *Adv. Energy Mater.* **2013**, 3 (4), 478–487.
- (129) Fraga Domínguez, I.; Topham, P. D.; Bussière, P.-O.; Bégué, D.; Rivaton, A. *J. Phys. Chem. C* **2015**, 119 (4), 2166–2176.
- (130) Abdou, M. S. A.; Orfino, F. P.; Son, Y.; Holdcroft, S. *J. Am. Chem. Soc.* **1997**, 119 (19), 4518–4524.
- (131) Schafferhans, J.; Baumann, A.; Wagenpfahl, A.; Deibel, C.; Dyakonov, V. *Org. Electron.* **2010**, 11 (10), 1693–1700.
- (132) Chambon, S.; Rivaton, A.; Gardette, J.-L.; Firon, M. *J. Polym. Sci. Part A Polym. Chem.* **2009**, 47 (22), 6044–6052.
- (133) Tournebize, A.; Bussiere, P.-O.; Rivaton, A.; Gardette, J.-L.; Medlej, H.; Hiorns, R. C.; Dagron-Lartigau, C.; Krebs, F. C.; Norrman, K. *Chem. Mater.* **2013**, 25 (22), 4522–4528.
- (134) Chambon, S.; Rivaton, A.; Gardette, J.-L.; Firon, M. *Sol. Energy Mater. Sol. Cells* **2007**, 91 (5), 394–398.
- (135) Tournebize, A.; Rivaton, A.; Gardette, J.-L.; Lombard, C.; Pépin-Donat, B.; Beaupré, S.; Leclerc, M. *Adv. Energy Mater.* **2014**, 4 (10), 1301530.
- (136) Jorgensen, M.; Norrman, K.; Gevorgyan, S. A.; Tromholt, T.; Andreasen, B.; Krebs, F. C. *Adv. Mater.* **2012**, 24 (5), 580–612.
- (137) Manceau, M.; Helgesen, M.; Krebs, F. C. *Polym. Degrad. Stab.* **2010**, 95 (12), 2666–2669.
- (138) Chambon, S.; Rivaton, A.; Gardette, J.-L.; Firon, M. *Polym. Degrad. Stab.* **2011**, 96 (6), 1149–1158.
- (139) Lloyd, M. T.; Olson, D. C.; Lu, P.; Fang, E.; Moore, D. L.; White, M. S.; Reese, M. O.; Ginley, D. S.; Hsu, J. W. P. *J. Mater. Chem.* **2009**, 19 (41), 7638–7642.

- (140) Lögdlund, M.; Brédas, J. L. *J. Chem. Phys.* **1994**, *101* (5), 4357.
- (141) Nishinaga, J.; Aihara, T.; Yamagata, H.; Horikoshi, Y. *J. Cryst. Growth* **2005**, *278* (1-4), 633–637.
- (142) Vogel, M.; Doka, S.; Breyer, C.; Lux-Steiner, M. C.; Fostiropoulos, K. *Appl. Phys. Lett.* **2006**, *89* (16), 163501.
- (143) Scharber, M. C.; Sariciftci, N. S. *Prog. Polym. Sci.* **2013**, *38* (12), 1929–1940.
- (144) Cros, S.; de Bettignies, R.; Berson, S.; Bailly, S.; Maisse, P.; Lemaitre, N.; Guillerez, S. *Sol. Energy Mater. Sol. Cells* **2011**, *95*, S65–S69.
- (145) Gevorgyan, S. A.; Madsen, M. V.; Dam, H. F.; Jorgensen, M.; Fell, C. J.; Anderson, K. E.; Duck, B. C.; Mescheloff, A.; Katz, E. A.; Elschner, A.; Roesch, R.; Hoppe, H.; Hermenau, M.; Riede, M.; Krebs, F. C. *Sol. Energy Mater. Sol. Cells* **2013**, *116*, 187–196.
- (146) Gaume, J.; Wong-Wah-Chung, P.; Rivaton, A.; Thérias, S.; Gardette, J.-L. *RSC Adv.* **2011**, *1* (8), 1471.
- (147) Gaume, J.; Taviot-Gueho, C.; Cros, S.; Rivaton, A.; Thérias, S.; Gardette, J.-L. *Sol. Energy Mater. Sol. Cells* **2012**, *99*, 240–249.
- (148) Gaume, J.; Rivaton, A.; Thérias, S.; Gardette, J.-L. *Polym. Degrad. Stab.* **2012**, *97* (4), 488–495.
- (149) Djouani, F.; Israël, Y.; Frezet, L.; Rivaton, A.; Lessard, R. A.; Bolte, M. *J. Polym. Sci. Part A Polym. Chem.* **2006**, *44* (3), 1317–1325.
- (150) Mechanical integrity of multi-layered structures for flexible displays <http://www.tue.nl/en/publication/ep/p/d/ep-uid/210946/> (accessed Dec 17, 2014).
- (151) Shaheen, S. E.; Brabec, C. J.; Sariciftci, N. S.; Padinger, F.; Fromherz, T.; Hummelen, J. C. *Appl. Phys. Lett.* **2001**, *78* (6), 841–843.
- (152) Martens, T.; D’Haen, J.; Munters, T.; Goris, L.; Beelen, Z.; Manca, J.; D’Olieslaeger, M.; Vanderzande, D.; Schepper, L. De; Andriessen, R. *Org. Polym. Mater. Devices-Optical, Electr. Optoelectron. Prop.* **2002**, *725*, 169–175.
- (153) Ruderer, M. a.; Guo, S.; Meier, R.; Chiang, H.-Y.; Körstgens, V.; Wiedersich, J.; Perlich, J.; Roth, S. V.; Müller-Buschbaum, P. *Adv. Funct. Mater.* **2011**, *21* (17), 3382–3391.
- (154) Li, G.; Yao, Y.; Yang, H.; Shrotriya, V.; Yang, G.; Yang, Y. *Adv. Funct. Mater.* **2007**, *17* (10), 1636–1644.
- (155) Li, G.; Shrotriya, V.; Huang, J.; Yao, Y.; Moriarty, T.; Emery, K.; Yang, Y. *Nat. Mater.* **2005**, *4* (11), 864–868.

- (156) Kim, H.; So, W.; Moon, S. *J. Korean Phys. Soc.* **2006**, *48* (3), 441–445.
- (157) Nguyen, L. H.; Hoppe, H.; Erb, T.; Günes, S.; Gobsch, G.; Sariciftci, N. S. *Adv. Funct. Mater.* **2007**, *17* (7), 1071–1078.
- (158) Yang, X.; Loos, J.; Veenstra, S. C.; Verhees, W. J. H.; Wienk, M. M.; Kroon, J. M.; Michels, M. A. J.; Janssen, R. A. J. *Nano Lett.* **2005**, *5* (4), 579–583.
- (159) Ohkita, H.; Cook, S.; Astuti, Y.; Duffy, W.; Tierney, S.; Zhang, W.; Heeney, M.; McCulloch, I.; Nelson, J.; Bradley, D. D. C.; Durrant, J. R. *J. Am. Chem. Soc.* **2008**, *130* (10), 3030–3042.
- (160) Huang, J.-H.; Yang, C.-Y.; Ho, Z.-Y.; Kekuda, D.; Wu, M.-C.; Chien, F.-C.; Chen, P.; Chu, C.-W.; Ho, K.-C. *Org. Electron.* **2009**, *10* (1), 27–33.
- (161) Campoy-Quiles, M.; Ferenczi, T.; Agostinelli, T.; Etchegoin, P. G.; Kim, Y.; Anthopoulos, T. D.; Stavrinou, P. N.; Bradley, D. D. C.; Nelson, J. *Nat. Mater.* **2008**, *7* (2), 158–164.
- (162) Bertho, S.; Janssen, G.; Cleij, T. J.; Conings, B.; Moons, W.; Gadisa, A.; D'Haen, J.; Goovaerts, E.; Lutsen, L.; Manca, J.; Vanderzande, D. *Sol. Energy Mater. Sol. Cells* **2008**, *92* (7), 753–760.
- (163) Richards, J. J.; Rice, A. H.; Nelson, R. D.; Kim, F. S.; Jenekhe, S. A.; Luscombe, C. K.; Pozzo, D. C. *Adv. Funct. Mater.* **2013**, *23* (4), 514–522.
- (164) Wong, H. C.; Li, Z.; Tan, C. H.; Zhong, H.; Huang, Z.; Bronstein, H.; McCulloch, I.; Cabral, J. T.; Durrant, J. R. *ACS Nano* **2014**, *8* (2), 1297–1308.
- (165) Zhao, J.; Bertho, S.; Vandenberg, J.; Van Assche, G.; Manca, J.; Vanderzande, D.; Yin, X.; Shi, J.; Cleij, T.; Lutsen, L.; Van Mele, B. *Phys. Chem. Chem. Phys.* **2011**, *13* (26), 12285–12292.
- (166) Kesters, J.; Kudret, S.; Bertho, S.; Van den Brande, N.; Defour, M.; Van Mele, B.; Penxten, H.; Lutsen, L.; Manca, J.; Vanderzande, D.; Maes, W. *Org. Electron.* **2014**, *15* (2), 549–562.
- (167) Bertho, S.; Campo, B.; Piersimoni, F.; Spoltore, D.; D'Haen, J.; Lutsen, L.; Maes, W.; Vanderzande, D.; Manca, J. *Sol. Energy Mater. Sol. Cells* **2013**, *110*, 69–76.
- (168) Wantz, G.; Derue, L.; Dautel, O.; Rivaton, A.; Hudhomme, P.; Dagron-Lartigau, C. *Polym. Int.* **2014**, *63* (8), 1346–1361.
- (169) Kim, B. J.; Miyamoto, Y.; Ma, B.; Fréchet, J. M. J. *Adv. Funct. Mater.* **2009**, *19* (14), 2273–2281.
- (170) Griffini, G.; Douglas, J. D.; Piliago, C.; Holcombe, T. W.; Turri, S.; Fréchet, J. M. J.; Mynar, J. L. *Adv. Mater.* **2011**, *23* (14), 1660–1664.

- (171) Xu, Q.; Wang, F.; Qian, D.; Tan, Z.; Li, L.; Li, S.; Tu, X.; Sun, G.; Hou, X.; Hou, J.; Li, Y. *ACS Appl. Mater. Interfaces* **2013**, 5 (14), 6591–6597.
- (172) Qian, D.; Xu, Q.; Hou, X.; Wang, F.; Hou, J.; Tan, Z. *J. Polym. Sci. Part A Polym. Chem.* **2013**, 51 (15), 3123–3131.
- (173) Farinhas, J.; Ferreira, Q.; Di Paolo, R. E.; Alcácer, L.; Morgado, J.; Charas, A. *J. Mater. Chem.* **2011**, 21 (33), 12511.
- (174) Zhu, Z.; Hadjikyriacou, S.; Waller, D.; Gaudiana, R. *J. Macromol. Sci. Part A* **2004**, 41 (12), 1467–1487.
- (175) Kim, H. J.; Han, A.-R.; Cho, C.-H.; Kang, H.; Cho, H.-H.; Lee, M. Y.; Fréchet, J. M. J.; Oh, J. H.; Kim, B. J. *Chem. Mater.* **2012**, 24 (1), 215–221.
- (176) Nam, C.-Y.; Qin, Y.; Park, Y. S.; Hlaing, H.; Lu, X.; Ocko, B. M.; Black, C. T.; Grubbs, R. B. *Macromolecules* **2012**, 45 (5), 2338–2347.
- (177) Chen, L.; Li, X.; Chen, Y. *Polym. Chem.* **2013**, 4 (23), 5637.
- (178) Ouhib, F.; Tomassetti, M.; Manca, J.; Piersimoni, F.; Spoltore, D.; Bertho, S.; Moons, H.; Lazzaroni, R.; Desbief, S.; Jerome, C.; Detrembleur, C. *Macromolecules* **2013**, 46 (3), 785–795.
- (179) Drees, M.; Hoppe, H.; Winder, C.; Neugebauer, H.; Sariciftci, N. S.; Schwinger, W.; Schäffler, F.; Topf, C.; Scharber, M. C.; Zhu, Z.; Gaudiana, R. *J. Mater. Chem.* **2005**, 15 (48), 5158.
- (180) Cheng, Y.-J.; Hsieh, C.-H.; Li, P.-J.; Hsu, C.-S. *Adv. Funct. Mater.* **2011**, 21 (9), 1723–1732.
- (181) Hsieh, C.-H.; Cheng, Y.-J.; Li, P.-J.; Chen, C.-H.; Dubosc, M.; Liang, R.-M.; Hsu, C.-S. *J. Am. Chem. Soc.* **2010**, 132 (13), 4887–4893.
- (182) Derue, L.; Dautel, O.; Tournebize, A.; Drees, M.; Pan, H.; Berthumeyrie, S.; Pavageau, B.; Cloutet, E.; Chambon, S.; Hirsch, L.; Rivaton, A.; Hudhomme, P.; Facchetti, A.; Wantz, G. *Adv. Mater.* **2014**, 26 (33), 5831–5838.
- (183) Deribew, D.; Pavlopoulou, E.; Fleury, G.; Nicolet, C.; Renaud, C.; Mougner, S.-J.; Vignau, L.; Cloutet, E.; Brochon, C.; Cousin, F.; Portale, G.; Geoghegan, M.; Hadziioannou, G. *Macromolecules* **2013**, 46 (8), 3015–3024.
- (184) Chen, J.; Yu, X.; Hong, K.; Messman, J. M.; Pickel, D. L.; Xiao, K.; Dadmun, M. D.; Mays, J. W.; Rondinone, A. J.; Sumpter, B. G.; Kilbey II, S. M. *J. Mater. Chem.* **2012**, 22 (26), 13013.
- (185) Liao, H.-C.; Chen, P.-H.; Chang, R.; Su, W.-F. *Polymers (Basel)*. **2014**, 6 (11), 2784–2802.

- (186) Sivula, K.; Ball, Z. T.; Watanabe, N.; Fréchet, J. M. J. *Adv. Mater.* **2006**, *18* (2), 206–210.
- (187) Ball, Z. T.; Sivula, K.; Fréchet, J. M. J. *Macromolecules* **2006**, *39* (1), 70–72.
- (188) Gernigon, V.; Leveque, P.; Brochon, C.; Audinot, J.-N.; Leclerc, N.; Bechara, R.; Richard, F.; Heiser, T.; Hadziioannou, G. *Eur. Phys. Journal-Applied Phys.* **2011**, *56* (3), 34107.
- (189) Heuken, M.; Komber, H.; Erdmann, T.; Senkoyskyy, V.; Kiriya, A.; Voit, B. *Macromolecules* **2012**, *45* (10), 4101–4114.
- (190) Gholamkhash, B.; Peckham, T. J.; Holdcroft, S. *Polym. Chem.* **2010**, *1* (5), 708.
- (191) Palermo, E. F.; Darling, S. B.; McNeil, A. J. *J. Mater. Chem. C* **2014**, *2* (17), 3401.
- (192) Sary, N.; Richard, F.; Brochon, C.; Leclerc, N.; Lévêque, P.; Audinot, J.-N.; Berson, S.; Heiser, T.; Hadziioannou, G.; Mezzenga, R. *Adv. Mater.* **2010**, *22* (6), 763–768.
- (193) Erothu, H.; Sohdi, A. a.; Kumar, A. C.; Sutherland, A. J.; Dagron-Lartigau, C.; Allal, A.; Hiorns, R. C.; Topham, P. D. *Polym. Chem.* **2013**, *4* (13), 3652.
- (194) Chen, J.; Yu, X.; Hong, K.; Messman, J. M.; Pickel, D. L.; Xiao, K.; Dadmun, M. D.; Mays, J. W.; Rondinone, A. J.; Sumpter, B. G.; Kilbey II, S. M. *J. Mater. Chem.* **2012**, *22* (26), 13013.
- (195) Topham, P. D.; Parnell, A. J.; Hiorns, R. C. *J. Polym. Sci. Part B-Polymer Phys.* **2011**, *49* (16), 1131–1156.
- (196) Waldauf, C.; Morana, M.; Denk, P.; Schilinsky, P.; Coakley, K.; Choulis, S. A.; Brabec, C. J. *Appl. Phys. Lett.* **2006**, *89* (23), 233517.
- (197) Jo, S. B.; Lee, J. H.; Sim, M.; Kim, M.; Park, J. H.; Choi, Y. S.; Kim, Y.; Ihn, S.-G.; Cho, K. *Adv. Energy Mater.* **2011**, *1* (4), 690–698.
- (198) Hu, T.; Li, F.; Yuan, K.; Chen, Y. *ACS Appl. Mater. Interfaces* **2013**, *5* (12), 5763–5770.
- (199) Shao, S.; Zheng, K.; Zidek, K.; Chabera, P.; Pullerits, T.; Zhang, F. *Sol. Energy Mater. Sol. Cells* **2013**, *118* (118), 43–47.
- (200) Xie, C.; Chen, L.; Chen, Y. *J. Phys. Chem. C* **2013**, *117* (47), 24804–24814.
- (201) Chang, Y.-M.; Leu, C.-Y. *J. Mater. Chem. A* **2013**, *1* (21), 6446–6451.
- (202) Wang, G.; Jiu, T.; Tang, G.; Li, J.; Li, P.; Song, X.; Lu, F.; Fang, J. *Acs Sustain. Chem. Eng.* **2014**, *2* (5), 1331–1337.

- (203) Cheng, Y.-S.; Liao, S.-H.; Li, Y.-L.; Chen, S.-A. *ACS Appl. Mater. Interfaces* **2013**, *5* (14), 6665–6671.
- (204) Hau, S. K.; Yip, H.-L.; Ma, H.; Jen, A. K.-Y. *Appl. Phys. Lett.* **2008**, *93* (23), 233304.
- (205) Hau, S. K.; Cheng, Y.-J.; Yip, H.-L.; Zhang, Y.; Ma, H.; Jen, A. K.-Y. *ACS Appl. Mater. Interfaces* **2010**, *2* (7), 1892–1902.
- (206) Hau, S. K.; Yip, H.-L.; Acton, O.; Baek, N. S.; Ma, H.; Jen, A. K.-Y. *J. Mater. Chem.* **2008**, *18* (42), 5113–5119.
- (207) Moad, G.; Solomon, D. H. *The Chemistry of Radical Polymerization*; Elsevier, 2006.
- (208) Braunecker, W. A.; Matyjaszewski, K. *Prog. Polym. Sci.* **2007**, *32* (1), 93–146.
- (209) Matyjaszewski, K.; Xia, J. H. *Chem. Rev.* **2001**, *101* (9), 2921–2990.
- (210) Dong, X.-H.; Zhang, W.-B.; Li, Y.; Huang, M.; Zhang, S.; Quirk, R. P.; Cheng, S. Z. D. *Polym. Chem.* **2012**, *3* (1), 124.
- (211) Opsteen, J. A.; van Hest, J. C. M. *Chem. Commun.* **2005**, No. 1, 57–59.
- (212) Vana, P. *Macromol. Symp.* **2007**, *248* (1), 71–81.
- (213) Harrisson, S.; Liu, X.; Ollagnier, J.-N.; Coutelier, O.; Marty, J.-D.; Destarac, M. *Polymers (Basel)*. **2014**, *6* (5), 1437–1488.
- (214) Moad, G.; Rizzardo, E.; Thang, S. H. *Aust. J. Chem.* **2005**, *58* (6), 379–410.
- (215) Moad, G.; Rizzardo, E.; Thang, S. H. *Polymer (Guildf)*. **2008**, *49* (5), 1079–1131.
- (216) Yan, Y.; Zhang, W.; Qiu, Y.; Zhang, Z.; Zhu, J.; Cheng, Z.; Zhang, W.; Zhu, X. *J. Polym. Sci. Part A Polym. Chem.* **2010**, *48* (22), 5206–5214.
- (217) Lai, J. T.; Filla, D.; Shea, R. *Macromolecules* **2002**, *35* (18), 6754–6756.
- (218) Gondi, S. R.; Vogt, A. P.; Sumerlin, B. S. *Macromolecules* **2007**, *40* (3), 474–481.
- (219) Postma, A.; Davis, T. P.; Evans, R. A.; Li, G.; Moad, G.; O'Shea, M. S. *Macromolecules* **2006**, *39* (16), 5293–5306.

CHAPTER 2 MATERIALS AND EXPERIMENTAL METHODS

2.1 Methodology of computational modelling

Computational modelling was performed by project collaborator Hugo Santos Silva at the Université de Pau et des Pays de l'Adour, France, under supervision of Dr Didier Bégué and Dr Roger Hiorns. Molecular geometries of the ligands were fully optimised within the density functional theory (DFT) methodology, using the B3LYP exchange-correlation functional and an Ahlrichs-type *triple- ζ* polarised basis set (TZVP).¹ Energies and geometries were corrected throughout this work for long-range dispersion interactions, delimited by a van der Waals-like potential and semi-empirically parameterised by Stefan Grimme up to the 6th order (vdW06).² All calculations were done using Orca 2.9 software. In the case of hydrogen migration, the energy of the ligand alone was corrected by optimisation of only hydrogen atoms.

Calculated ground-state configuration of $(\text{ZnO})_{12}$ is predicted to be a cage-like structure, consisting of six $(\text{ZnO})_2$ and eight $(\text{ZnO})_3$ rings forming a truncated octahedron in which all Zn and O vertices remain equivalent (Figure 2.1). These results are consistent with other reports throughout literature as well as the structural parameters of such cluster.^{3,4}

For each chosen ligand, all of the possible conformers that could interact with the $(\text{ZnO})_{12}$ cluster were calculated. Only the conformers with the lowest values of interaction energy were reported, representing the best ligand to cluster binding.



Figure 2.1. $(\text{ZnO})_{12}$ cluster simulated using DFT calculations, where grey atoms are Zn and red atoms are oxygen.

For all other calculations, including the electronic levels and absorbance spectra, time-dependent density functional theory, (TD)DFT, measurements were used, employing the B3LYP basis set and the 6-311G* basis set as defined in the Gaussian09 program package. These were performed by Dr Johannes Gierschner at IMDEA Nanociencia (Madrid, Spain).

LogP measurements were performed using ChemBioUltra3D 14.0 package. The energy was minimized with a MMFF94 force field set. Calculations of the log P were made by in-built ChemPropPro tool with pre-set parameters.

2.2 Materials

For readability purposes, materials and synthetic methods used for synthesis of different ligand materials have been divided into corresponding tables. A separate table contains details of materials used for thin film deposition and devices preparation.

Table 2.1. List of reagents adopted in the synthesis of poly(3,4-dimethoxystyrene), poly(3,4-dihydroxystyrene), poly(3,4-dimethoxystyrene)-fullerene and poly(3,4-dihydroxystyrene)-fullerene, featured in chapters 3 and 4 .

Name	Denotation	Supplier	Grade
2,2'-azobis(isobutyronitrile)	AIBN	Fisher	
boron tribromide	BBr ₃	Alfa Aesar	≥99.99 %
carbon disulfide	CS ₂	Alfa Aesar	99.90%
dichloromethane	DCM	Fisher	laboratory grade
anhydrous dichloromethane	dry DCM	Sigma-Aldrich	≥99.8%, contains 50-150 ppm amylene as stabiliser
<i>N,N'</i> -dicyclohexylcarbodiimide	DCC	Alfa Aesar	99%
diisobutylaluminum hydride	DIBAL-H	Alfa Aesar	1M solution in hexane
3,4-dimethoxystyrene	DMS	Sigma-Aldrich	technical grade, 99 %
4-(dimethylamino)pyridine	DMAP	Alfa Aesar	99%
dithranol		Sigma-Aldrich	≥98.0 %
2-(dodecylthiocarbonothioylthio)-2-methylpropionic acid	DDMAT	synthesised	
fullerene	C60	Solenne BV	>99.5%
hexane		Fisher	laboratory grade
magnesium sulfate	MgSO ₄	Alfa Aesar	≥99.5%
methanol		Fisher	laboratory grade
sodium hydroxide	NaOH	Alfa Aesar	98%, extra pure
styrene	S	Sigma-Aldrich	ReagentPlus®, ≥ 99 %
anhydrous tetrahydrofuran	THF	Sigma-Aldrich	≥99.9 %, inhibitor free
anhydrous toluene	dry toluene	Sigma-Aldrich	99.80%
triethylamine	TEA	Sigma-Aldrich	≥99 %
2-[(trimethylsilyl)oxy]-1,3-butadiene		TCI Europe	≥95%
zinc acetate	ZnAc	Sigma-Aldrich	99.99 % trace metal basis

Table 2.2. List of reagents adopted in the synthesis of quinoline polymer.

Name	Denotation	Supplier	Grade
acetonitrile	ACN	Sigma-Aldrich	anhydrous, 99.8%
bis(acetonitrile)dichloro palladium(II)	$\text{Pd}(\text{acn})_2\text{Cl}_2$	Alfa Aesar	Pd 40.5%
5-bromo-8-hydroxyquinoline		TCI Europe	>96.0%
5-chloro-8-hydroxyquinoline		Alfa Aesar	95%
copper iodide	CuI	Sigma-Aldrich	99.999% trace metals basis
2-dicyclohexylphosphino-2',4',6'-triisopropylbiphenyl	XPhos	Alfa Aesar	>98%
diethyl ether	ether	Fisher	laboratory grade
4-(dimethylamino)pyridine	DMAP	Sigma-Aldrich	ReagentPlus®, ≥ 99%
di- <i>tert</i> -butyl dicarbonate	$(\text{Boc})_2\text{O}$	Sigma-Aldrich	ReagentPlus®, ≥ 99%,
<i>N</i> -ethyl-diisopropylamine	DIPEA	Sigma-Aldrich	99%
ethynyltrimethylsilane	TMS-acetylene	Alfa Aesar	98%
hexane		Fisher	laboratory grade
magnesium sulfate	MgSO_4	Alfa Aesar	≥99.5%
potassium fluoride	KF	Sigma-Aldrich	anhydrous, powder, ≥99.99% trace metals basis
sodium azide	NaN_3	Sigma-Aldrich	ReagentPlus®, ≥99.5%
tetrakis(triphenylphosphine) palladium(0)	$\text{Pd}(\text{PPh}_3)_4$	Alfa Aesar	99.8% metals basis, Pd 9% min
4-vinylbenzyl chloride	VBC	Sigma-Aldrich	90%
dimethylformamide	DMF	Fisher	laboratory grade

Table 2.3. List of materials used in thin film deposition and device fabrication.

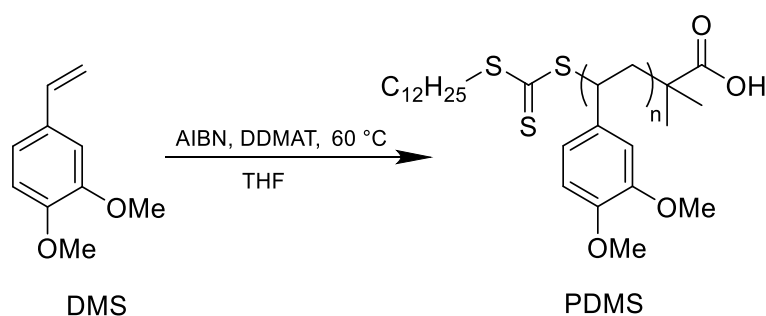
Name	Denotation	Supplier	Grade
acetone		Fisher	laboratory grade
ethanolamine		Alfa Aesar	≥98%

continued on the next page

2-methoxyethanol		Alfa Aesar	99%
1-methylnaphthalene		Sigma-Aldrich	purum, ≥97.0% (GC)
poly(3,4-ethylenedioxythiophene): polystyrene sulfonate	PEDOT:PSS	Heraeus	Clevios™ HTL Solar
poly(3-hexylthiophene)	P3HT	Merck	
[6,6]-phenyl-C61-butyric acid methyl ester	PCBM	Solenne BV	>99%
o-xylene		Alfa Aesar	99%
ZnO nanoparticles	ZnO NPs	Belectric OPV	

2.3 Synthetic methods

2.3.1 Synthesis of poly(3,4-dimethoxystyrene), PDMS, via RAFT polymerisation

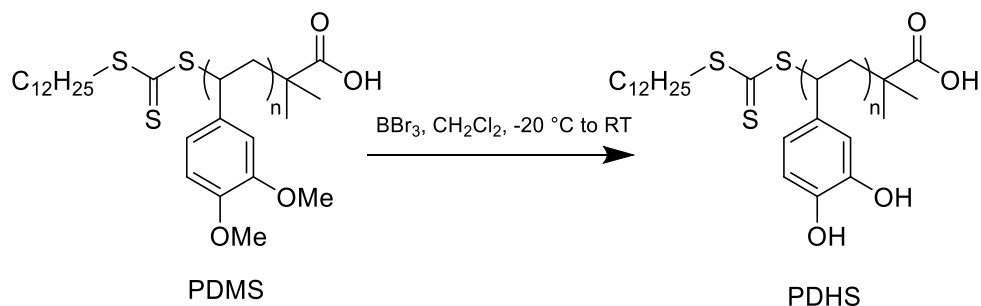


Scheme 2.1. Synthesis of PDMS by RAFT polymerisation.

The following example describes the polymerisation of DMS in THF at 60 °C with $[\text{AIBN}]_0/[\text{DDMAT}]_0/[\text{DMS}]_0 = 1/1/30$ (*i.e.* a target degree of polymerisation, D_p , of 30); this is representative of all DMS polymerisations undertaken in this work (Scheme 2.1). A 25 ml polymerisation tube equipped with a magnetic follower was charged with a mixture of DMS (3 g, 18.27 mmol), AIBN (101 mg, 0.61 mmol), DDMAT (222 mg, 0.61 mmol) and THF (6 ml). The flask was sealed with a rubber septum and the solution was stirred and purged with nitrogen for 15 minutes. Following which, the flask was placed in an oil bath at 60 °C. Aliquots were taken periodically and the polymerisation was monitored to high conversion. Upon completion, the polymerisation was cooled rapidly to 0 °C to allow immediate termination. 10 ml THF was added and the resulting solution was precipitated in 250 ml of hexane. The precipitate was collected by filtration, washed with hexane several times and dried *in vacuo* to obtain a pale yellow powder. For the fullerene coupling described in Section 2.3.4 PDMS was synthesised according to the procedure outlined above except at the ratio of $[\text{AIBN}]_0/[\text{DDMAT}]_0/[\text{DMS}]_0 = 0.1/1/30$. Details of the full spectroscopic characterisation of

PDMS are provided in Section 3.3.2. For the comparative studies, polystyrene was also synthesised via RAFT polymerisation using the procedure outlined above except at the ratio of $[AIBN]_0/[DDMAT]_0/[S]_0 = 0.1/1/250$.

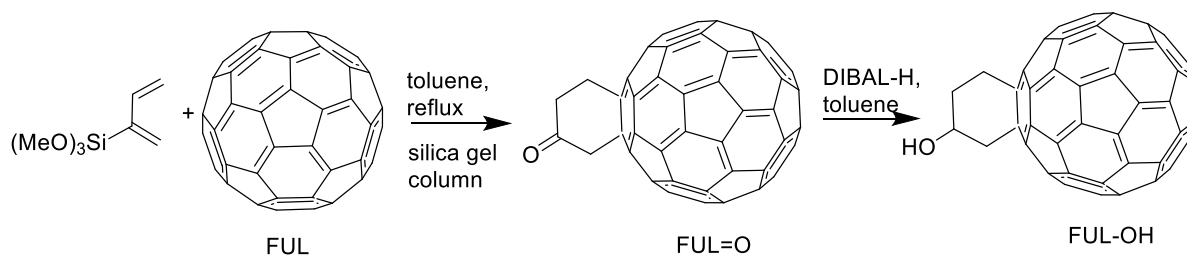
2.3.2 Synthesis of poly(3,4-dihydroxystyrene), PDHS



Scheme 2.2. Synthesis PDHS by demethylation of PDMS.

PDMS (3 mmol) was dissolved in 30 ml DCM in a 100 ml round-bottomed flask equipped with a magnetic follower. The flask was sealed with a rubber septum and the solution was stirred and purged with nitrogen for 15 minutes. After purging, the solution was cooled to $-20\text{ }^\circ\text{C}$, stirred for 10 minutes and then boron tribromide (2.26 g, 870 μl , 9 mmol) was added slowly via the rubber septum. After 30 minutes, the mixture was allowed to warm to room temperature and then stirred for a further 18 hours. The dark purple solution was subsequently cooled to $-0\text{ }^\circ\text{C}$ and 30 ml of deionised water were added. Following evolution of fumes, the mixture was slowly warmed to room temperature. It should be noted that PDHS is insoluble in both DCM and water, and thus precipitates from the reaction mixture, facilitating its purification. The precipitate was collected by filtration and sequentially washed with water and DCM, before the resultant purple powder was dried *in vacuo*. Details of the full spectroscopic characterisation of PDHS are provided in Section 3.3.3.

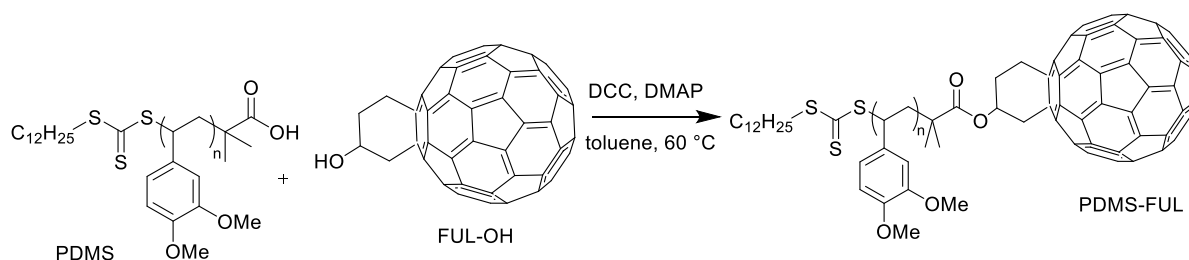
2.3.3 Synthesis of 1,2-(4'-hydroxycyclohexano) buckminsterfullerene (FUL-OH) (adapted from An et al⁶)



Scheme 2.3. Synthesis of fullerene precursor FUL-OH from fullerene C₆₀.

1.5 ml of 2-[(trimethylsilyl)oxy]-1,3-butadiene was slowly added via a syringe pump to a refluxing solution of 1.00 g (1.39 mmol) of fullerene C₆₀ in 400 ml of dry toluene under inert atmosphere. After addition, reflux was continued for 24 h and the reaction mixture was cooled to room temperature. The solvent was evaporated and the solids were redissolved in the minimum amount of CS₂ and charged into the silica gel column overnight. After the silica gel hydrolysis, unreacted fullerene and product were separated by flash chromatography with hexane/CS₂ 1:1, then with toluene. Obtained brown powder was dried *in vacuo* to yield 430 mg of FUL=O (39% yield). ¹H NMR (CDCl₃, δ ppm): 4.66 (s, *unresolved*, 1H), 4.43 (s, *unresolved*, 1H), 3.91 (s, *unresolved*, 1H), 3.62 (t, *J* = 16 Hz, 4 Hz, 1H), 3.48 (t, *J* = 14 Hz, 4 Hz, 1H), 3.29 (t, *J* = 16 Hz, 3.9 Hz, 1H). 200 mg (0.253 mmol) of FUL=O was dissolved in 20 ml of dry toluene. 0.8 ml (0.8 mmol) of a 1.0 M solution of diisobutylaluminum hydride (DIBAL-H) in hexane was added dropwise. Reaction mixture was stirred for 3 h at room temperature and then stirred with 40 ml of saturated ammonium chloride for 3 h. Subsequently, organic layer was separated and the aqueous layer was twice extracted with 50 ml of toluene. Combined organic phases were dried and the solvent evaporated. Dry residue was purified by flash chromatography to yield 170 mg (85%) of the black solid. ¹H and ¹³C NMR data are provided in Section 3.3.4. Details of the full spectroscopic characterisation of FUL-OH can be found elsewhere.⁵

2.3.4 Synthesis of fullerene-linked poly(3,4-dimethoxystyrene) (PDMS-FUL)

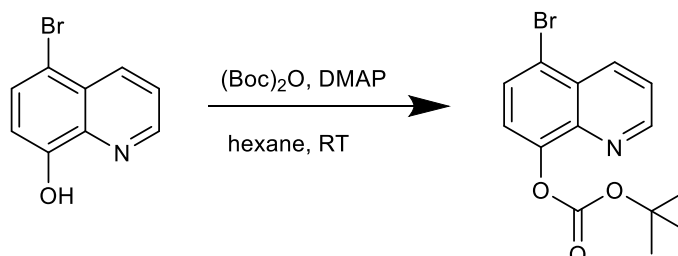


Scheme 2.4. Synthesis of PDMS-FUL by coupling PDMS and fullerene precursor FUL-OH.

A 50 ml round-bottom flask, equipped with a stir bar, was charged with 500 mg of PDMS ($M_n \sim 4$ kg/mol, ~ 0.125 mmol) and 110 mg of fullerenol precursor (0.140 mmol). Contents of the flask was dissolved in dry toluene and dichloromethane (4:1) upon sonication. DCC (29 mg, 0.140 mmol) and DMAP (17 mg, 0.140 mmol) were added to the solution. The flask was sealed, purged with nitrogen through a needle and then its contents stirred for 38 hours at 60 °C. Afterwards, mixture was cooled to room temperature, filtered through a silica pad and the solvent evaporated. Solids were redissolved in cold THF (5 ml) and filtered. Filtrates were washed with cold THF and concentrated. The resulting fullerene copolymer was

precipitated into 200 ml of cold hexane, and the precipitate was collected by filtration, washed with hexane several times and dried *in vacuo* to obtain a brown powder (577 mg, 96%).

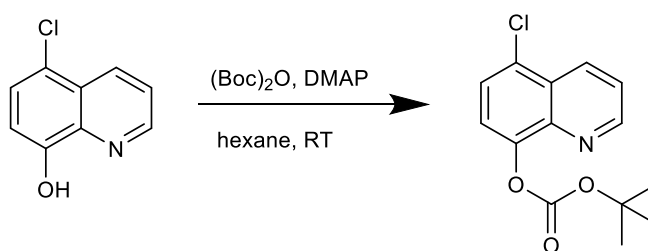
2.3.5 Synthesis of 5-bromo-8-*tert*-butoxycarbonyloxyquinoline



Scheme 2.5. Synthesis of 5-bromo-8-*tert*-butoxycarbonyloxyquinoline.

5.0 g (22.3 mmol) of 5-bromo-8-hydroxyquinoline was stirred with 5.9 g (27 mmol) of di-*tert*-butyl dicarbonate and 136 mg (1.12 mmol) of DMAP in 300 ml of hexane at room temperature until all solids are completely dissolved (30 min). The solvent was then removed by evaporation. Resulting white powder was recrystallised from hexane to obtain 6.2 g of white crystals of 5-bromo-8-*tert*-butoxycarbonyloxyquinoline precursor (yield 85.8%). ^1H NMR (CDCl_3 , δ ppm): 8.96 (dd, $J = 1.6\text{ Hz}$, 4 Hz, 1H), 8.53 (dd, $J = 1.6\text{ Hz}$, 8.3 Hz, 1H), 7.82 (dd, $J = 8.2\text{ Hz}$, 1H), 7.53 (dd, $J = 4\text{ Hz}$, 8.3 Hz, 1H), 7.42 (d, $J = 8.2\text{ Hz}$, 1H), 1.61 (s, 9H). Other spectroscopical data can be found elsewhere.⁶

2.3.6 Synthesis of 5-chloro-8-*tert*-butoxycarbonyloxyquinoline



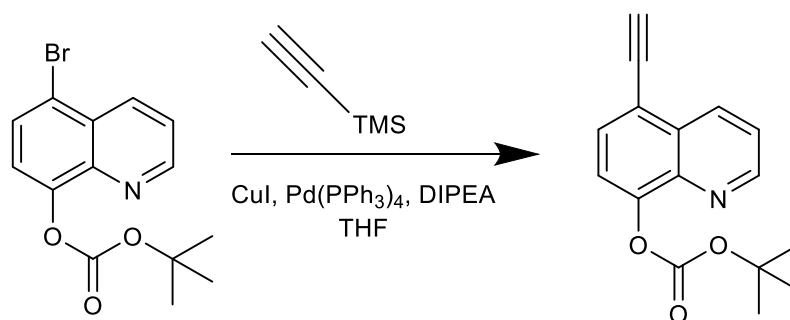
Scheme 2.6. Synthesis of 5-chloro-8-*tert*-butoxycarbonyloxyquinoline.

To synthesise 5-chloro-8-*tert*-butoxycarbonyloxyquinoline the same procedure was employed as described in Section 2.3.5. Final product was recrystallised from hexane to obtain 4.5 g of white crystals of 5-chloro-8-*tert*-butoxycarbonyloxyquinoline precursor (yield 73%). ^1H NMR

(CDCl₃, δ ppm): 8.91 (dd, J = 1.1 Hz, 3.9 Hz, 1H), 8.49 (dd, J = 1.2 Hz, 8.6 Hz, 1H), 7.54 (dd, J = 8.5 Hz, 1H), 7.43 (dd, J = 4.2 Hz, 8.6 Hz, 1H), 7.38 (d, J = 8.5 Hz, 1H), 1.56 (s, 9H).

2.3.7 Synthesis of 8-*tert*-butoxycarbonyloxy-5-ethynylquinoline

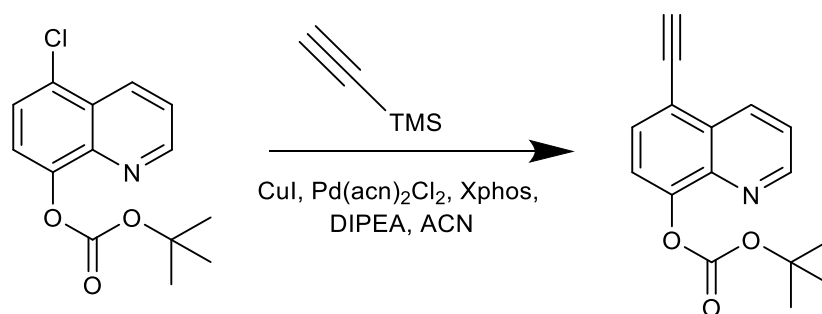
2.3.7.1 Method 1: from 5-bromo-8-*tert*-butoxycarbonyloxyquinoline



Scheme 2.7. Synthesis of 8-*tert*-butoxycarbonyloxy-5-ethynylquinoline from 5-bromo-8-*tert*-butoxycarbonyloxyquinoline by ligand-free Sonogashira coupling.

A 500 ml oven-dried round-bottom flask was backfilled twice with nitrogen and charged with 3.0 g (9.25 mmol) of 5-bromo-8-*tert*-butoxycarbonyloxyquinoline, 500 mg of Pd(PPh₃)₄ and 88 mg (0.46 mmol) of CuI and 350 ml of dry THF. Solution was purged with nitrogen for 15 min. Flask was equipped with a magnetic follower and sealed with a rubber septum. DIPEA (30 ml) and trimethylsilylacetylene (6.54 ml, 46.27 mmol) were added via the rubber septum and the reaction mixture was stirred at 60 °C for 24 h. Afterwards, the crude product was filtered through celite to remove the copper salts, using diethyl ether as eluent. Filtrate was concentrated, and the residue redissolved in methanol and stirred with 800 mg of potassium fluoride at room temperature for 5 h. To the mixture filtered through a filter paper, 40 ml of water were added and methanol was evaporated at room temperature. The residue was extracted twice with 300 ml of DCM. Organic layer was separated, dried over MgSO₄ and concentrated under vacuum. Product was purified by column chromatography (15% ethyl acetate in hexane) to yield 2.26 g of yellowish powder (yield 91%).

2.3.7.2 Method 2: from 5-chloro-8-*tert*-butoxycarbonyloxyquinoline.

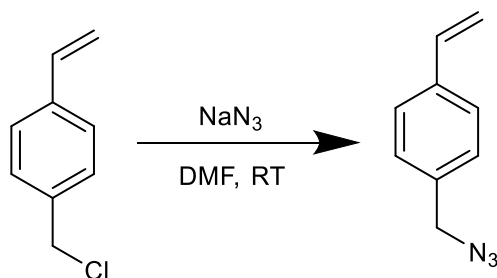


Scheme 2. 8. Synthesis of 8-*tert*-butoxycarbonyloxy-5-ethynylquinoline from 5-chloro-8-*tert*-butoxycarbonyloxyquinoline by ligand-supported Sonogashira coupling.

A 500 ml oven-dried round-bottom flask was backfilled twice with nitrogen and charged with 5.0 g (17.88 mmol) of 5-chloro-8-*tert*-butoxycarbonyloxyquinoline, 50 mg of Pd(acn)₂Cl₂ and 255 mg of XPhos ligand. The flask was equipped with a magnetic follower and sealed with a rubber septum. Contents of the flask were evacuated and backfilled with nitrogen three times. 35 ml of anhydrous acetonitrile and 12 ml of DIPEA (69 mmol) were added via the rubber septum and the yellow suspension was stirred for 10 min. Trimethylsilylacetylene (3.8 ml, 26.82 mmol) was added to the suspension and the reaction mixture was stirred at 80 °C for 24 hrs. Afterwards, reaction mixture was concentrated *in vacuo*, and the residue was dissolved in methanol and stirred with 1.350 g of KF for 5 h. The reaction mixture is filtered through a filter paper, 40 ml of water were added and methanol was evaporated at room temperature. The residue was extracted twice with 300 ml of DCM. Organic layer was separated, dried over MgSO₄ and concentrated under vacuum. The product was purified by column chromatography (15% ethyl acetate in hexane) to yield 3.46 g of yellowish powder (yield 72%).

¹H NMR (CDCl₃, δ ppm): 8.96 ppm (dd, J=1.7, 4.2 Hz, 1H), 8.63 (dd, J=1.7, 8.5 Hz, 1H), 7.76 (d, J=7.9 Hz, 1H), 7.52 (dd, J=4.2, 8.5 Hz, 1H), 7.48 (d, J=7.9 Hz, 1H), 1.59 (s, 9 H), 3.47 (s, 1H). Other spectroscopic data can be found elsewhere.⁶

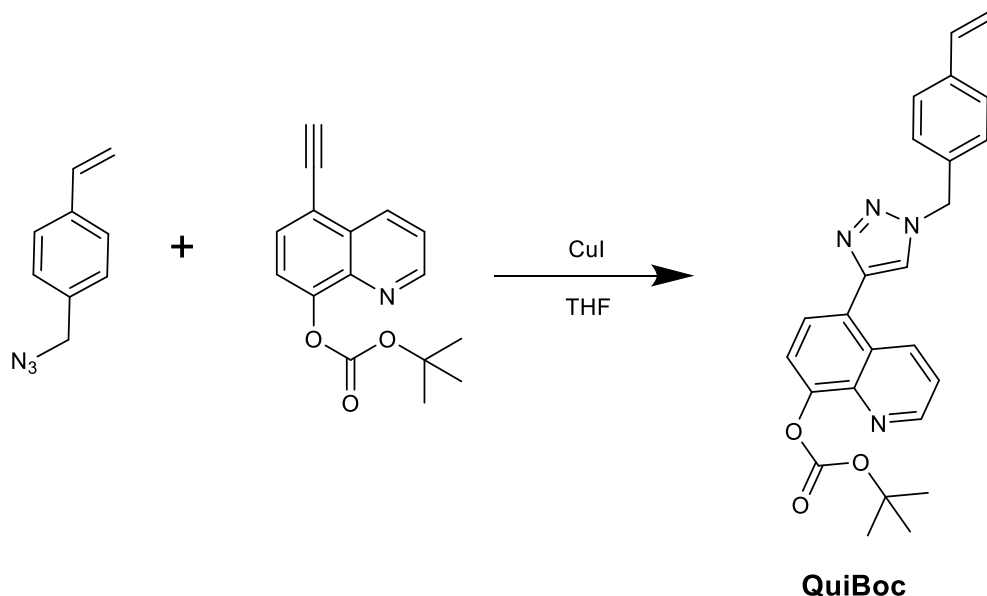
2.3.8 Synthesis of 4-vinylbenzyl azide



Scheme 2.9. Synthesis of 4-vinylbenzyl azide.

To 5 g of 4-vinylbenzyl chloride (32.7 mmol) dissolved in 40 ml of DMF, 2.4 g of sodium azide (0.037 mmol) were added and the resulting mixture was stirred overnight at room temperature. After reaction completion, the mixture was poured onto water and extracted with 2 x 100 ml of ether. Organic fractions were washed with multiple portions of saline and then the solvent was carefully evaporated. Drying the resulting dense liquid resulted in final product as pale yellow liquid (3.7 g, 71.4%). ^1H NMR (CDCl_3 , δ ppm): 7.46 (d, $J = 8.1$ Hz, 2H), 7.31 (d, $J = 8.1$ Hz, 2H), 6.72 (dd, $J = 11$ Hz, 18 Hz, 1H), 5.79 (d, 18 Hz, 2H), 5.31 (d, 10 Hz, 1H), 4.35 (s, 2H). Other spectroscopic data can be found elsewhere.⁷

2.3.9 Synthesis of *tert*-butyl-{5-[2-(4-vinylbenzyl)-2*H*-1,2,3-triazol-4-yl]quinolin-8-yl} carbonate, QuiBoc monomer

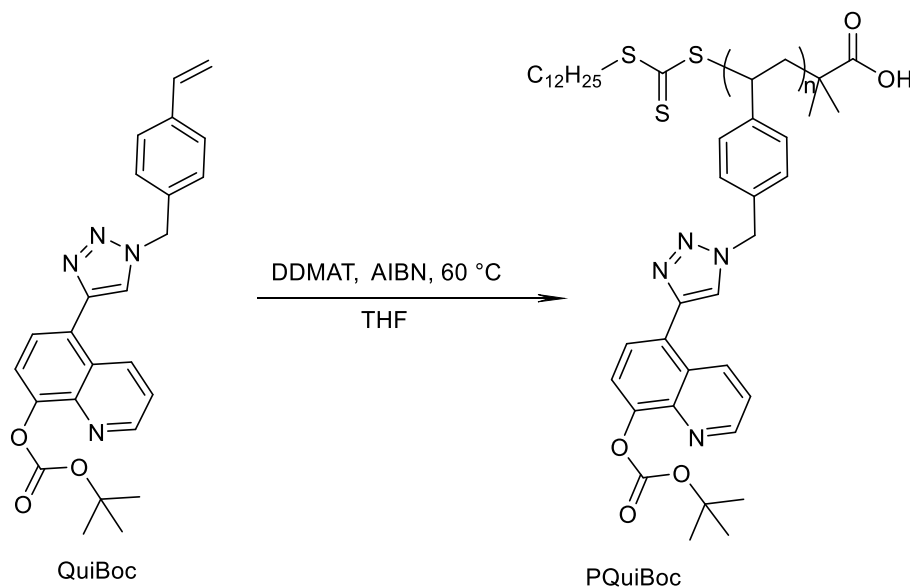


Scheme 2.10. Synthesis of *tert*-butyl-{5-[2-(4-vinylbenzyl)-2*H*-1,2,3-triazol-4-yl]quinolin-8-yl} carbonate, QuiBoc monomer, by 'click' coupling.

A solution of 8-*tert*-butoxycarbonyloxy-5-ethynylquinoline (1.2 g, 4.45 mmol), 4-vinylbenzyl azide (0.71 g, 4.46 mmol) and 5 mg CuI in dry THF (50 ml) were charged to a 100 ml round-bottom flask and purged with nitrogen with stirring for 15 minutes. After purging, the solution was heated to 40 °C and left stirring overnight. Solvent was evaporated and the solid was redissolved in DCM and washed with water to remove the copper catalyst. The organic phase was subsequently dried over MgSO₄. DCM was evaporated under vacuum and the residue purified using column chromatography on silica gel (ethyl acetate:hexane, 1:1) to provide the product (1.83 g, yield 96%) as a white powder. M.p. 136-138°C.

¹H NMR (CDCl₃, δ ppm): 1.62 (s, 9H), 5.31 (d, *J* = 10.9 Hz, 1H), 5.67 (s, 2H), 5.75 (d, *J* = 17.5Hz, 1H), 6.69 (dd, *J* = 17.5, 10.9 Hz, 1H), 7.34 (d, *J* = 8.2 Hz, 2H), 7.46-7.49 (d, *J* = 8.2 Hz, 2H), 7.45-7.51 (q, *J* = 8.2, 4.4 Hz, 1H), 7.53 (d, *J* = 7.85 Hz, 1H), 7.65 (d, *J* = 7.85 Hz, 1H), 7.72 (s, 1H), 8.93 (dd, *J* = 5.7, 1.6, 1H), 8.98 (s, 1H). ¹³C PENDANT NMR (CDCl₃): 25.75 (CH₃), 54.33 (CH₂), 83.90 (C*), 115.28 (CH₂), 122.18 (C*), 122.3 (CH), 127.02 (CH), 127.47 (CH), 133.61 (C*), 134.77 (CH), 138.40 (C*), 150.62 (C=O). ESI-MS [*M*⁺]: found 429.1909, calculated: 429.1927. Elemental analysis calcd. (%) for C₂₅H₂₄N₄O₃: C 70.08%, H 5.65%, N 13.07%, O 11.20%; found C 70.02%; H 5.63%, N 13.22%, O 11.13%.

2.3.10 Synthesis of PQuiBoc by RAFT polymerisation of the quinoline monomer

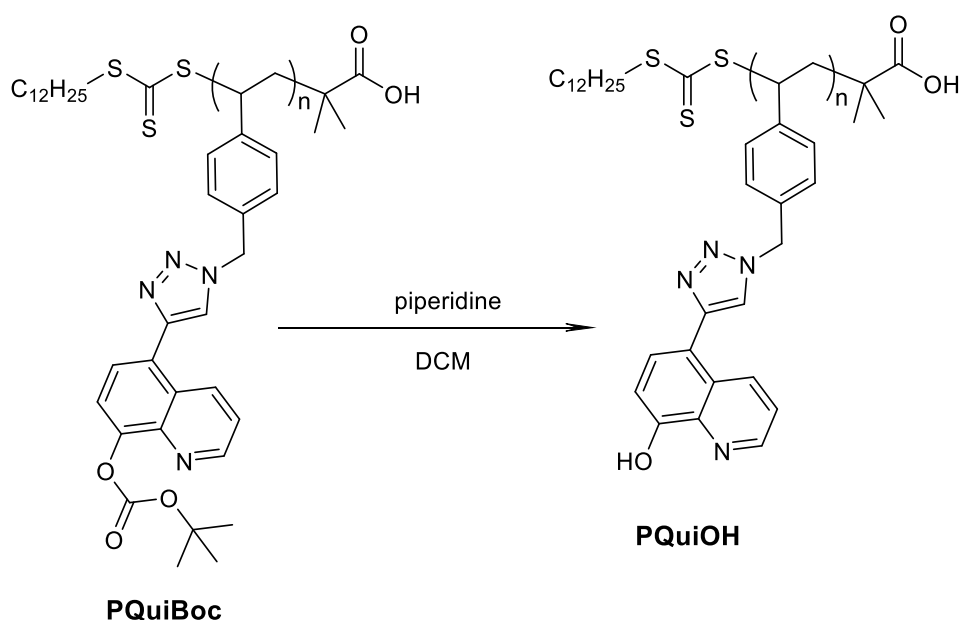


Scheme 2.11. Synthesis of PQuiBoc polymer via RAFT polymerisation of the QuiBoc monomer.

The following example describes the polymerisation of QuiBoc in THF at 60 °C with [AIBN]₀/[DDMAT]₀/[QuiBoc]₀ = 0.1/1/20 (i.e. a target degree of polymerisation, *D_p*, of 20); this is representative of all QuiBoc polymerisations undertaken in this work (Scheme 2.11). A 25

ml polymerisation tube equipped with a magnetic follower was charged with a mixture of monomer (0.4 g, 0.93 mmol), AIBN (7.7 mg, 0.047 mmol), DDMAT (17 mg, 0.047 mmol) and THF (4 ml). The flask was sealed with a rubber septum and the solution was stirred and purged with nitrogen for 15 minutes. Following which, the flask was placed in an oil bath at 60 °C. After 36 h polymerisation was cooled rapidly to 0 °C to allow immediate termination. 10 ml THF was added and the resulting solution was precipitated in 100 ml of cold diethyl ether. The precipitate was collected by filtration, washed with cold diethyl ether several times and dried *in vacuo*. Details of the full spectroscopic characterisation of PQuiBoc are provided in Section 4.1.2.

2.3.11 Synthesis of PQuiOH by basic deprotection of PQuiBoc.



Scheme 2.12. Synthesis of PQuiOH by basic deprotection of PQuiBoc.

20 mg of PQuiBoc polymer were dissolved in DCM before 2 drops of piperidine were added to the solution while stirring. After 5 min the polymer solution turned yellow and later precipitated in yellow flakes. The flakes were separated by filtration to give 17 mg of the resulting product (yield 98%). Details of the full spectroscopic characterisation of PQuiOH are provided in Section 4.1.2.

2.4 Thin-film deposition by spin-coating

2.4.1 Zinc oxide nanofilm deposition

A precursor solution of 0.75M zinc acetate dihydrate (164 mg/ml) in 2-methoxyethanol was mixed with precursor solution of 0.75M ethanolamine (46 mg/ml) in 2-methoxyethanol in a 1:1 ratio and stirred until clear and homogenous. Approximately 250 μ l of the resulting solution was spin-coated onto a suitable substrate at 2,000 rpm for 30 s. The films were subsequently annealed at 150 °C for 15 min.

2.4.2 Spin-coating of other films

“Interfacial polymers” were deposited by spin-coating onto a suitable substrate from *o*-xylene, acetone, methanol, or THF at appropriate concentrations (depending on the suitability of the solvent for a particular material) at 2,000 rpm for 20 s.

Photoactive layer (PAL) films were deposited from *o*-xylene solution, using 12 mg of PCBM and 15 mg of P3HT per ml of solvent. The P3HT:PCBM solution was stirred at 80 °C prior to deposition to ensure homogenous dissolution of all components. This solution was spin-coated at 4,000 rpm for 30 s and subsequently dried at room temperature.

2.5 Solution and bulk solid characterisation methods

2.5.1 Nuclear Magnetic Resonance Spectroscopy (NMR)

^1H and ^{13}C NMR spectra were recorded using a Bruker NMR spectrometer (300 MHz) at 300 MHz and 75 MHz for ^1H and ^{13}C analyses, respectively. Appropriate deuterated solvents or solvent systems were used to dissolve the analytes. Where possible, water peaks were suppressed using Watergate sequence, incorporated in TopSpin Bruker software. All chemical shifts are reported in ppm (δ) and referenced to the chemical shifts of the residual solvent resonances. For ^{13}C , PENDANT spectra were collected. ^1H NMR was used also for monitoring monomer conversion during polymerisation, which is discussed in Sections 3.3.2 and 5.2.2.

2.5.2 Fourier transform infrared (FTIR) spectroscopy

FTIR spectra were recorded using a Thermo Scientific Nicolet 380 instrument. Solid samples were placed directly onto a diamond plate, and the analysis was carried out by collecting 32 scans of attenuated total reflectance (ATR). The background transmittance was measured through the analysis of a blank sample at resolution of 4 cm^{-1} over the range 525 – 4000 cm^{-1} . In separate cases, FTIR spectra were obtained from KBr discs on a Perkin Elmer

Spectrum One spectrometer over the range 4000–500 cm^{-1} for 16 scans with a resolution of 4 cm^{-1} .

2.5.3 Gel permeation chromatography (GPC)

Number-average molar mass (M_n) and dispersity (M_w/M_n , D) were measured using gel permeation chromatography (GPC) (flow rate 1 ml/min) through three PL gel 5 mm 300 × 7.5 mm mixed-C columns using a degassed THF eluent system containing 2 % (v/v) trimethylamine (TEA), calibrated with narrow polystyrene standards (M_p range = 162 to 6 035 000 g/mol). The system was set to perform at 40 °C and a pressure of 6-8 kPa. Laboratory grade toluene was used as a flow rate marker to compensate fluctuations of the system pressure during analysis. Samples with a concentration of approximately 4 mg/ml were formulated using eluent THF as a solvent. All data were analysed using PL Cirrus software (version 2.0) supplied by Agilent Technologies (previously Polymer Laboratories).

2.5.4 Ultraviolet and visible light spectroscopy (UV-Vis)

Ultraviolet and visible (UV-vis) absorbance spectra were obtained using a Perkin Elmer Lambda 35 system in the wavelength range 300 - 800 nm, using THF or chloroform as solvent at appropriate concentrations.

2.5.5 Photoluminescence (PL) spectroscopy

Photoluminescence spectra of analysed materials in THF (0.01 mg/ml) were obtained on a Hitachi FL-2500 spectrophotometer with 5 mm slit width and excitation wavelength at the maximum absorbance. Emission spectra were scanned in the range 350-700 nm.

2.5.6 Differential scanning calorimetry (DSC)

Thermal behaviour of the materials (including melting points, T_m , glass transition temperatures, T_g and deprotection temperatures, where applicable) was studied using differential scanning calorimetry (DSC, DSC 1 STARe, Mettler Toledo) at a heating rate of 10 °C/min under nitrogen atmosphere with flow rate of 60 ml/min. Typically, one analysis included a heating step from 0 to 200 °C, a cooling step to 0 °C, and the second heating run from 0 to 200 (or 300) °C. This approach allowed identification of one-time thermal events, such as cross-linking or decomposition.

2.6 Microscopy techniques

2.6.1 Scanning electron microscopy (SEM)

Surface morphology and zinc binding performance were studied using scanning electron microscopy with energy dispersive X-ray analysis (SEM/EDXA) on a Link system AN10000

and Cambridge Scanning Electron Microscope Stereoscan S90, 22X resolution surface in bulk and an acceleration voltage of 25 kV. The polymer was deposited (via spin-coating) directly onto the aluminium SEM holders before a saturated aqueous solution of zinc acetate was spin-coated on top and the sample annealed at the appropriate temperature. After annealing, the films were thoroughly washed with water and sonicated in water for 10 minutes. Finally, the films were annealed again at the appropriate temperature for 10 min and dried *in vacuo* for 10 min to remove all residual water. Each polymer was prepared in this way in triplicate prior to assessment.

2.6.2 Atomic force microscopy (AFM)

Topography and phase images of the films were obtained using Digital Instruments Dimension 3100 equipment. Silicon tips (Bruker OLTESPA-R3, resonant frequency 70 kHz) were used for measurements in tapping mode. Nanoscope software was used for image acquisition. WsxM Shell Access software was used for image analysis.

2.7 Thin-film spectroscopy techniques

2.7.1 Ultraviolet and visible light spectroscopy (UV-Vis)

Ultraviolet and visible (UV-vis) absorbance spectra and emission spectra were obtained using a Varian UV-Vis-NIR Cary 5000 spectrophotometer system in the wavelength range 300 - 800 nm with a resolution of 1 nm. Spectra were acquired and processed by WinUV Scan software. The films were deposited onto quartz glass with a spectral cut-off point at 220 nm.

2.7.2 X-ray and ultraviolet photoelectron spectroscopy (XPS and UPS)

XPS and UPS measurements were performed by the project partner Aurelien Tournbize at the Eberhard Karls University, Tübingen, Germany. Measurements were carried out using a multi-chamber UHV system (base pressure 2×10^{-10} mbar), equipped with a SPECS Phoibos 150 cylindrical hemispherical analyzer, a monochromatic Al K_{α} source (Focus 500 monochromator, XR50m X-ray source, Al K_{α} 1486.74 eV) and a UVS 300 He discharge lamp (21.22 eV excitation energy). The energy scale for XPS was calibrated to the binding energy (BE) of Ag 3d_{5/2}.

2.8 Contact angle measurements

Contact angle measurements of the thin-films were carried out using Digidrop goniometer (GBX). Distilled water with an average drop size of 2 μ l was used as reference liquid at a

rate of drop formation of 2.7-3.3 $\mu\text{l/s}$. Contact angles were measured 8 ms after deposition and processed by GBX software.

2.9 Cyclic voltammetry (CV)

Cyclic voltammetry measurements were done by Dr Graham Morse at Merck (Southampton), using a Princeton Applied Research VersaSTAT 4 potentiostat. Films of the polymers were cast from a concentrated chloroform solution onto a platinum wire working electrode. These solid films were measured in an anhydrous acetonitrile solution containing 0.1 M tetrabutyl ammonium tetrafluoroborate electrolyte with a platinum wire counter electrode and 0.1 M Ag/AgNO₃ in acetonitrile reference electrode. Solutions were purged with nitrogen gas prior to use. The samples were referenced to an external ferrocene solution which was also used to calculate the LUMO position according to Equation 2.1:

$$\text{LUMO energy, } E_{\text{LUMO}} = -(E_{\text{red}}^{\text{onset}} + 5.1) \text{ eV} \quad (\text{Equation 2.1})$$

See chapter 5 for further details and application of Equation 2.1.

2.10 Device fabrication

To fabricate solar cells, flexible PET substrates pre-coated with ITO were used. ITO substrates were wiped with a soft propan-2-ol (IPA) soaked tissue before being sonicated in IPA for 15 min. A thin layer of ZnO nanoparticles was deposited by doctor blading from an ethanol solution onto the ITO-substrate and annealed at 140 °C for 10 min. The interfacial layers were deposited and processed as described in corresponding sections. Afterwards, a solution of P3HT and PCBM 15:12 mg/ml in 95% xylene and 5% 1-methylnaphthalene, was doctor bladed to give a thickness of ~250 nm. Subsequently, a PEDOT: PSS solution (final thickness ~100 nm) was directly doctor bladed onto the photoactive layer and annealed for 5 min at 140 °C under N₂. A 90 nm thick silver electrode was vacuum deposited on top to complete the device. The control samples were fabricated in the same way without the intermediate layer. Device performance was characterised by *J-V* parameters using a Keithley source meter and Xenon lamp.

2.11 Time-resolved measurements

All time-resolved measurements and corresponding fitting and modelling experiments were performed at IMDEA Nanoscience Institute (Madrid, Spain) under supervision of Dr Larry Lüer.

2.11.1 Transient absorption spectroscopy (TAS)

Femto-picosecond transient absorption (TA) spectra have been obtained with a regeneratively amplified system at 500 Hz repetition rate 50 (Clark-MXR CPA2101). The 775 nm pulses were split into two parts: one part was frequency doubled using an LBO crystal (pump pulses), the other part was focused onto a 2 mm thick sapphire plate, producing a femtosecond white light super continuum from 420 – 1600 nm (probe pulses). Probe pulses were focused onto the sample (approximately 150 μm diameter) and overlapped with the pump pulse (approximately 300 μm diameter). Intensity of the pump beam was set to 200 nJ. After transmission through the sample the probe pulses were sent to a prism spectrometer (Entwicklungsbüro Stresing GmbH) with a CCD array (256 pixels, VIS-enhanced InGaAs, Hamamatsu Photonics Inc.). The measurements were performed within two regions of white light, separated from each other by corresponding lenses. First, the visible part of the spectrum, from 450 to 650 nm, was scanned. Subsequently, the near-infrared part of the spectrum was scanned in the range from 900 to 1400 nm. Data acquisition and modelling was undertaken by home-built Python software, developed by Dr Larry Lürer.

Devices for TAS studies were deposited into the Oxford Cryostat where they were connected to external power supply (Keithley). The measurements were done under vacuum in transmission mode on the area not covered by the electrode.

A simplified set-up scheme is presented in Figure 2.2. The 775 nm pulses generated by the Clark laser source (red arrows) were split into two separate pulses. One pulse was passed through the second harmonic generation crystal (SHG), where the frequency was doubled, resulting in a pulse with a wavelength of 382 nm (blue arrows in Figure 2.2). This pulse was chopped at 500 Hz and used for the sample excitation (pump pulse). Delay of the excitation pulse was controlled by a mechanical translation stage and a corner cube. The second pulse was sent to the sapphire crystal where it produced a white light supercontinuum (yellow arrows in Figure 2.2). After passing through a set of lenses and attenuators, the white light pulse was split again. One pulse (probe) was set to overlap the pump pulse on the sample, whereas the second white light pulse (reference) was sent directly onto the detector (2 channel CCD camera). This arrangement of the pulse paths allowed reduction of the noise and laser fluctuations, since the signal from the reference pulse was subtracted from the probe signal.

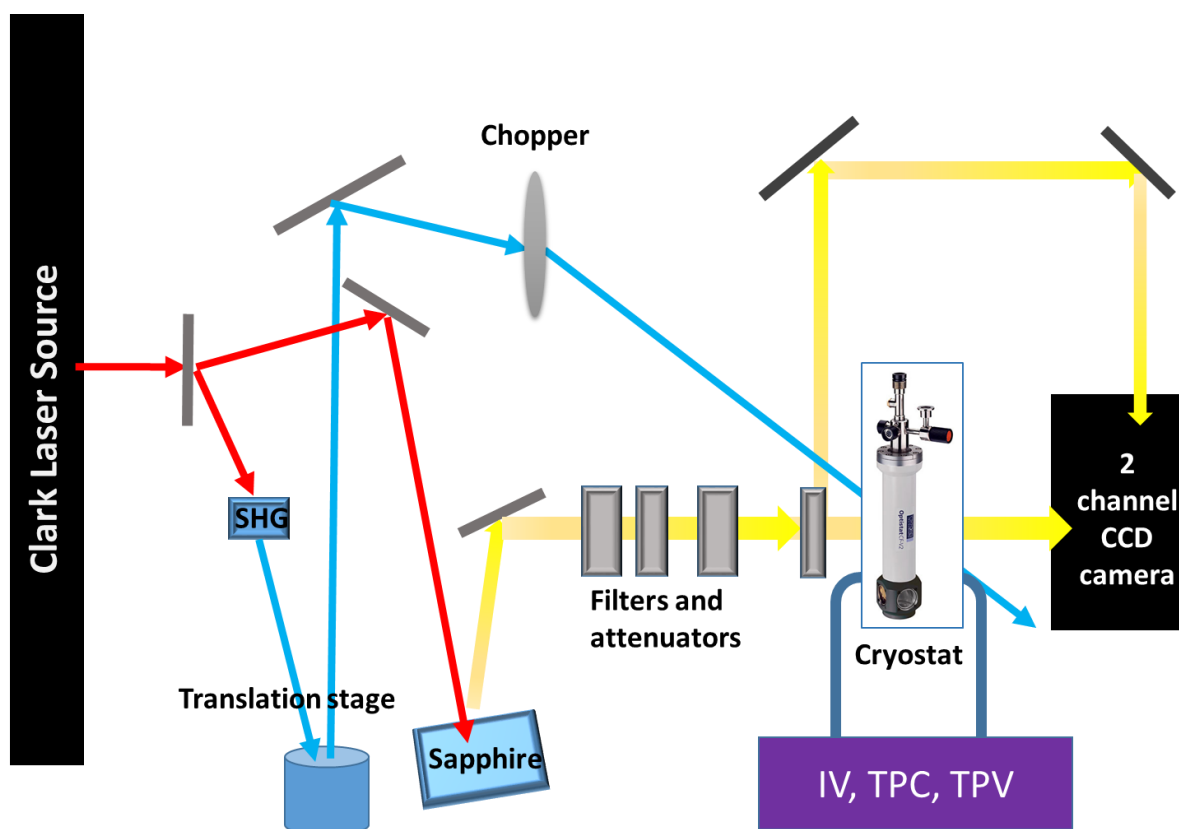


Figure 2.2. Simplified schematic for transient absorption spectroscopy (TAS).

The procedure employed herein was initially described by Stokkum *et al.* as target analysis.⁸ Target analysis is a matrix-based method to extract the concentration-time dependence of various photoexcited species from time-resolved TA spectra in which their respective optical probes are strongly superposed. In a first step, the complete TA matrix (time versus probe energy) is reproduced by a global fit using a three-state purely sequential model. The result of a global fit is a set of characteristic spectra with associated exponential lifetimes. If the real photophysics of the sample is actually purely sequential, then these characteristic spectra represent directly the species-associated differential spectra (SADS) for each of the excited states. If the true photophysics is more complex (including backward processes, parallel processes, impulsive generation of more than one state), then the characteristic spectra are called evolution-associated differential spectra (EADS), and therefore are weighted superpositions of the SADS. In this case, a second step is necessary.

In the second step, the spectral weight of each SADS in each EADS is found by spectral modelling involving additional photophysical knowledge. Together with the EADS lifetimes obtained in step 1, one can now calculate the concentration-time dependence of each state by a simple recursion formula. Application of the procedure was in details reported by Karuthedath *et al.*⁹

2.11.2 Transient photovoltage (TPV) and photocurrent (TPC) measurements

Solar cell devices were connected with an external 50 Ω (for photocurrent measurements) resistor or without any resistor (for photovoltage measurements) to the input terminal of the oscilloscope (Picoscope 6424) and the voltage upon excitation was sampled by an oscilloscope connected to a PC using custom built Python software. All devices were excited with 387 nm 150 fs probe laser pulses of 200 nJ intensity, as described in Section 2.10.1. The signal from the chopper at 500 Hz was connected to the oscilloscope to work as a trigger for sampling as the time-dependant voltage traces were recorded in the 'light-off' configuration. Figure 2.3 depicts a simplified set-up for transient photovoltage measurements.

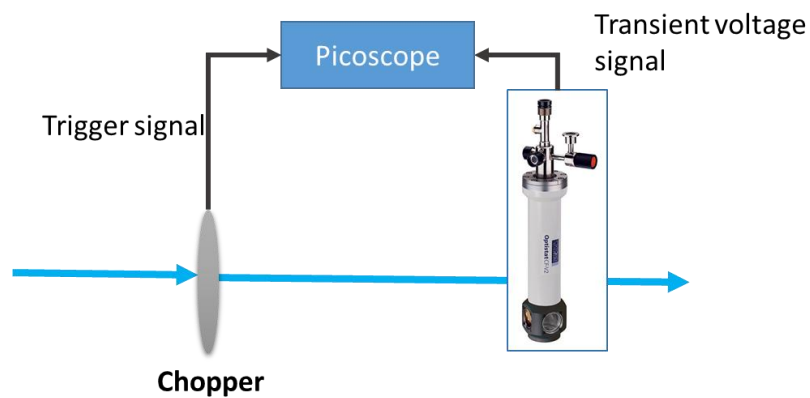


Figure 2.3. Simplified schematic for transient photovoltage (TPV) measurements. The blue arrows represent the pump pulses used for sample excitation, and the picoscope collects the trigger signal from the function generator system of the chopper and the electrical signal from the sample.

It should be noted that the excitation pulse duration has an effect on the transient electrical measurements. In femtosecond length pulsed samples, the effect of the parallel continuous charge carrier build up and decay processes can be completely eliminated, thus, only the dynamics of the once generated charges would be traced (Figure 2.4).

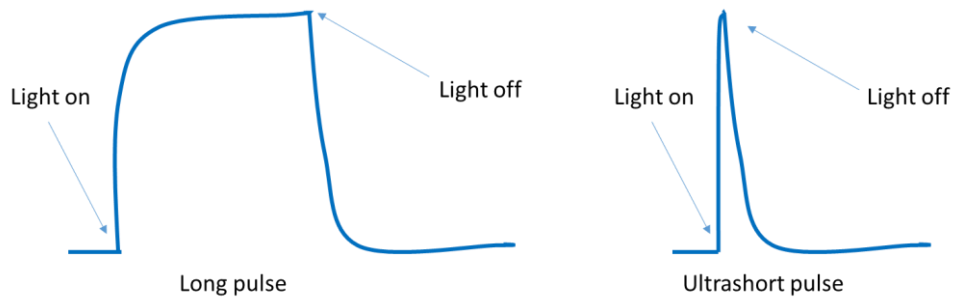


Figure 2.4. Schematic interpretation of the effect of the excitation pulse length on the shape of transient photocurrent signal.

2.12 References

- (1) Schafer, A.; Horn, H.; Ahlrichs, R. *J. Chem. Phys.* **1992**, 97 (4), 2571–2577.
- (2) Grimme, S. *J. Comput. Chem.* **2006**, 27 (15), 1787–1799.
- (3) Wang, B.; Nagase, S.; Zhao, J.; Wang, G. *J. Phys. Chem. C* **2007**, 111 (13), 4956–4963.
- (4) Cheng, X.; Li, F.; Zhao, Y. *J. Mol. Struct.* **2009**, 894 (1-3), 121–127.
- (5) An, Y.-Z.; Chen, C.-H. B.; Anderson, J. L.; Sigman, D. S.; Foote, C. S.; Rubin, Y. *Tetrahedron* **1996**, 52 (14), 5179–5189.
- (6) Pohl, R.; Anzenbacher, P. *Org. Lett.* **2003**, 5 (16), 2769–2772.
- (7) Porta, R.; Benaglia, M.; Coccia, F.; Cozzi, F.; Puglisi, A. *Adv. Synth. Catal.* **2015**, 357 (2-3), 377–383.
- (8) Van Stokkum, I. H. M.; Larsen, D. S.; van Grondelle, R. *Biochim. Biophys. Acta* **2004**, 1657 (2-3), 82–104.
- (9) Karuthedath, S.; Sauermann, T.; Egelhaaf, H.-J.; Wannemacher, R.; Brabec, C. J.; Lüer, L. *J. Mater. Chem. A* **2014**.

CHAPTER 3 SYNTHESIS AND APPLICATION OF POLYMERIC SELF-ASSEMBLING MONOLAYER

3.1 Interface stabilisation

As reviewed in Section 1.8, self-assembling monolayers (SAM) have been demonstrated as an efficient and facile approach to stabilisation of electron-transporting layer (ETL)/photoactive layer (PAL) interface, with a positive impact on the electronic coherence, charge extraction and initial performance of the OPV devices. Thus, the concept of SAMs was adopted in this work for polymeric materials. Zinc-binding ligands have been polymerised and functionalised with a fullerene molecule to enhance the electronic coherence of the interfacial layer with the PAL and their chemical compatibility. The effect of these polymers on device performance was studied by means of the steady-state and time-resolved measurements.

3.2 Choice of ligands

There is a number of studies that reports ligands for zinc and zinc oxide binding, based on different types of interaction, including hydrogen bonding, covalent bonding or Van der Waals forces. To identify ligands with the highest binding potential, the computational modelling of the best ligand type was performed at Université de Pau et des Pays de l'Adour, Pau, France by project collaborator Hugo Santos Silva (Figure 3.1).

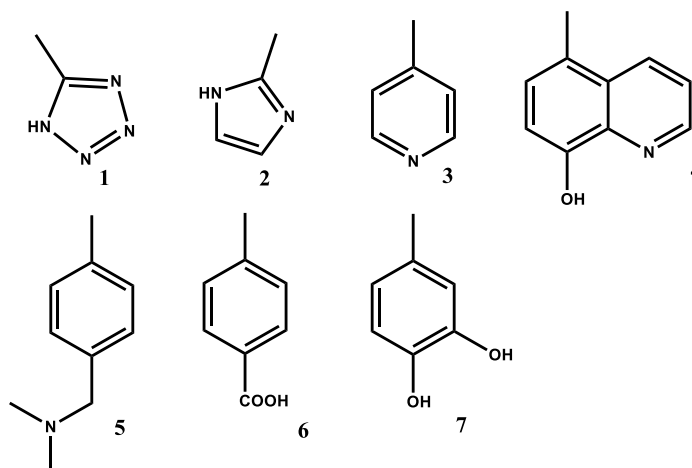


Figure 3.1. Structures of the ligands proposed for modelling: **1** – tetrazole, **2** – imidazole, **3** – pyridine, **4** – 8-hydroxyquinoline, **5** – (dimethylamino)methyl benzene, **6** – benzoic acid, **7** – dihydroxybenzene.

Zinc oxide surface was modelled as a $(\text{ZnO})_{12}$ cluster in order to study the interaction energy between an organic and inorganic layer. This approach allows one to define the character of interaction: whether it is physisorption or chemisorption and, moreover, to estimate the

energetic gain for the system due to the formation of new bonds. Moreover, it also allows simulation of the inorganic surface closer to reality as it is not flat and chemically homogenous, but consists of different atoms with different, non-predictable positions in space. $(\text{ZnO})_{12}$ was chosen as representative of an inorganic ZnO layer since it simulates zinc atoms of equivalent valence and has two distinct faces that can interact with organic molecules (Figure 3.2). The literature confirms that for such cluster size, most of its energetic parameters have already converged, *i.e.* the energetic potential has reached the functional limit and can be represented as corresponding HOMO and LUMO energies.^{1–3}



Figure 3.2. Simulated inorganic cluster $(\text{ZnO})_{12}$ where red atoms represent oxygen and grey – carbon. Potential binding sites are highlighted by black lines, where (a) is $(\text{ZnO})_3$ and (b) is $(\text{ZnO})_2$.

The inorganic cluster has two possible binding sites: the $(\text{ZnO})_2$ or $(\text{ZnO})_3$ “rings” (Figure 3.2). Interactions that they are involved in depend mostly on the size of the attaching group in the ligand molecule, since the energy potentials are distributed homogeneously in the cluster. If this group needs more three-dimensional space to bind, it would preferably bind to a $(\text{ZnO})_3$ ring. These interactions are separated during modelling and are assumed to exist with an equal possibility when the binding energies are equal, and with one prevailing conformer when its binding energy is higher. Moreover, ligand molecules with more than one binding group are considered to be interacting with both rings on the inorganic structure.

Ligands from heterocycles groups (tetrazole, imidazole, pyridine, **1-3**) have such small binding energies that they are considered almost unreactive with the zinc oxide cluster. The main reason is the inflexibility of the heterocycles, thus the shape of the binding site on the ligand is unapproachable for the cluster to bind. However, these have been reported in the literature to form complexes with zinc ions because separate zinc ions can be held by electrostatic forces between two flat heterocycles.⁴

Conformers calculated for ligand **4** (8-hydroxyquinoline, Figure 3.3) are based on two binding sites; the pyridine-type nitrogen in the quinoline ring and the hydroxyl group can both donate lone pairs from the oxygen or form a covalent bond upon migration of the hydrogen. Thus, the first conformer is formed by binding of the nitrogen atom directly to the zinc centre. At the same time, the hydroxyl group forms a donor-acceptor bond with an oxygen on the cluster.

During the binding interaction, the charge on the Zn centre decreases from $0.86e^-$ to $0.82e^-$, meaning the bond is formed mostly due to delocalisation of the lone pair of the nitrogen on this metallic centre. The second conformer is formed by the same type of N-Zn bonding on one zinc atom and through covalent bonding of the hydroxyl group to another zinc centre, resulting in a tightly packed complex. The hydrogen is taken by an oxygen centre on the cluster. Covalent bonding always provides more gain in energy than donor-acceptor bonding, thus, the second conformer has higher binding energy (90 kcal/mol *versus* 47 kcal/mol). The charge on the zinc centre decreases from $0.86e^-$ to $0.80e^-$ after binding, which indicates a delocalisation of the nitrogen lone pair on the metallic centre and the redistribution of the charge over the formed complex.

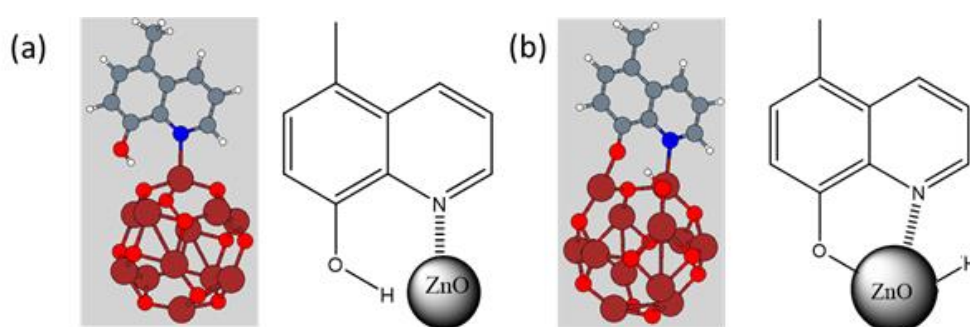


Figure 3.3. Simulated complex of ligand **4** and $(\text{ZnO})_{12}$ cluster: conformer 1 (a) and conformer 2 (b), where large dark red - zinc atoms, small red - oxygen atoms, blue - nitrogen atoms, grey - carbon atoms, white - protons.

Ligand **5** has only one binding position (Figure 3.4). The charge on the zinc centre also decreases from $0.86e^-$ to $0.80e^-$ after the binding, which indicates a charge redistribution in the formed complex. This indicates that ligand **5** can serve as an electron extracting layer through the creation of dipoles on the surface.

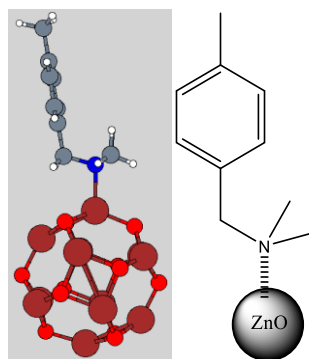


Figure 3.4. Simulated complex of ligand **5** and $(\text{ZnO})_{12}$ cluster, where large dark red - zinc atoms, small red - oxygen atoms, blue - nitrogen atoms, grey - carbon atoms, white - protons.

The structure of the ZnO-ligand **6** complex shows two possible conformers (Figure 3.5). First conformer is formed by the covalent bond between the oxygen on the carboxylic acid group and the zinc atom on the cluster. The energy saving resulting from migration of hydrogen in this interaction is higher than for the second conformer (69 kcal/mol vs. 21 kcal/mol), which is formed by lone pair donation from the carbonyl oxygen.

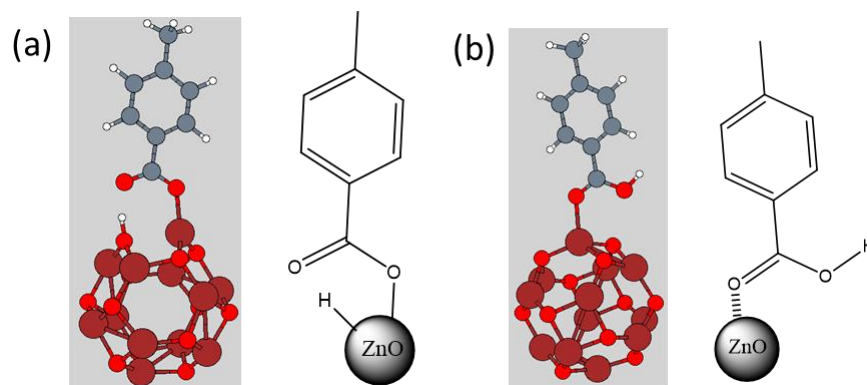


Figure 3.5. Simulated complex of ligand **6** and $(\text{ZnO})_{12}$ cluster: conformer 1 (a) and conformer 2 (b), where large dark red - zinc atoms, small red - oxygen atoms, grey - carbon atoms, white - protons.

Ligand **7** has two equivalent binding sites (Figure 3.6), thus they were expected to form two identical covalent bonds upon migration of hydrogens, but this is not the case. Only one hydroxyl group participates in the formation of a covalent bond, while the other only donates its lone pair. Conformers 1 and 2 differ slightly in energy (78 kcal/mol *versus* 86 kcal/mol) and, unexpectedly, conformer 2, with one covalent bond, provides the more energetically preferable configuration. The strain arising from elongation of the C-O bond could be the reason why the gain in energy from the formation of the donor-acceptor bond is too low compared to the energy loss.

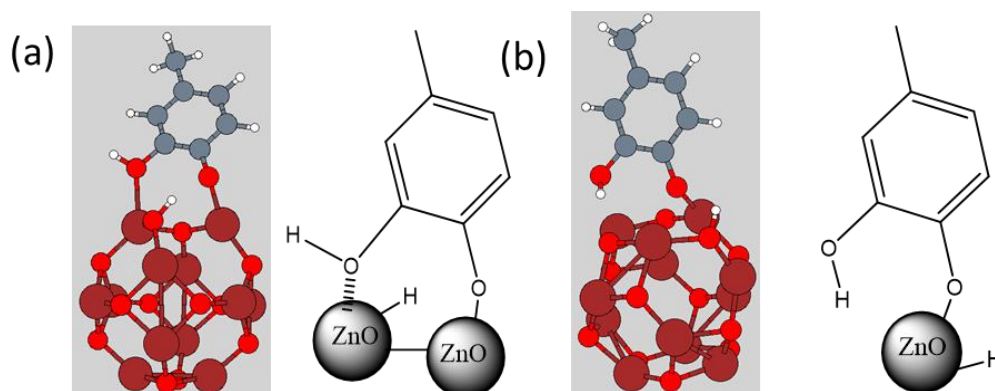
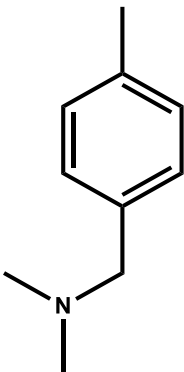
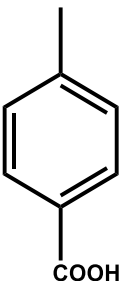
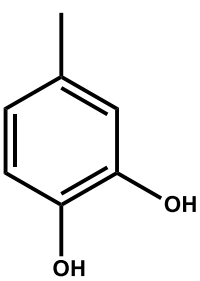
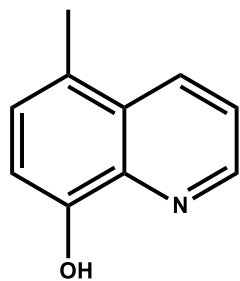


Figure 3.6. Simulated complex of ligand **7** and $(\text{ZnO})_{12}$ cluster: conformer 1 (a) and conformer 2 (b), where large dark red - zinc atoms, small red - oxygen atoms, grey - carbon atoms, white - protons.

Modelling the interactions between various ligands and inorganic zinc oxide cluster has helped to eliminate potentially weak and unsuitable ligands, such as tetrazoles, pyridines and imidazoles. Based on the binding energies of the most promising ligands (Table 3.1), two were selected for future studies: dihydroxybenzene (ligand **7**) and 8-hydroxyquinoline (ligand **4**).

Table 3.1. Simulated interaction energies of different complexes and conformers of ligands and zinc oxide inorganic clusters (in kcal/mol).

	Ligand			
	5	6	7	4
				
Conformer 1	-37.48	-69.16	-78.15	-47.21
Conformer 2	N/A	-21.12	-86.98	-90.81

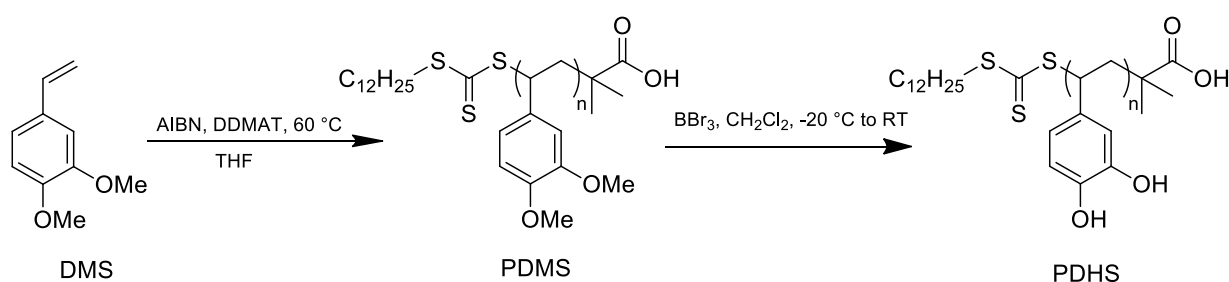
3.3 Synthesis of PDMS/PDHS

3.3.1 General approach

Since the main aim of this research was to synthesise functionalised, well-defined polymers, the focus was made on finding materials and methods, reproducibly yielding similar batches of well-defined materials. Thus, the synthetic strategy employed for the synthesis of poly(3,4-dihydroxystyrene) (PDHS) comprised a straightforward two-step approach, where the first step was to obtain a well-defined parental polymer with pre-determined molar mass. The second step was to transform the parental polymer into PDHS.

To synthesise the parental polymer, 3,4-dimethoxystyrene (DMS) was chosen because of its commercial availability, stability to oxidation during handling and storage and good solubility

in a range of organic solvents. Reversible Addition-Fragmentation chain Transfer (RAFT) polymerisation was employed owing to its good control over polymer chain length and architecture. Moreover, the end-groups of the chain transfer agent (CTA) provide an important opportunity for further material design through block copolymer synthesis (using the polymer as a macroCTA in a “grafting from” approach^{5,6} or as a building block in a “grafting to” approach^{7,8}), derivatisation of the polymer with a wide variety of single molecules⁹ or particles,^{10,11} or anchoring to a solid substrate.¹² The second step of the synthetic route was facile and rapid cleavage of the methoxy groups using a strong Lewis acid, boron tribromide (BBr₃), which resulted in quantitative demethylation of PDMS (Scheme 3.1).



Scheme 3.1. Synthetic route for the preparation of poly(3,4-dihydroxystyrene), PDHS.

3.3.2 RAFT Polymerisation of PDMS

For the RAFT polymerisation, 2-(dodecylthiocarbonothioylthio)-2-methylpropionic acid (DDMAT) was selected as the CTA owing to its ability to successfully control the RAFT polymerisation of other styrenic-based (more-activated) monomers,^{6,13,14} whilst furnishing one end of the polymer chain with a carboxylic acid group, capable of further reaction to produce more complex, hybrid materials.

To identify an appropriate RAFT system to produce well-defined polymers of controllable molar mass, the initiator:CTA ratio was systematically varied ($[AIBN]_0/[DDMAT]_0 = 0.1, 0.5, 0.75, 1.0$ and 2.0). Table 3.2 shows the molar mass, dispersity and monomer conversion data at different initiator to CTA ratios for a fixed targeted degree of polymerisation $D_P = 150$ ($M_n = 25$ kg/mol). Evidently, $[AIBN]_0/[CTA]_0 = 0.1$ yielded the closest to targeted molar mass of 19.2 kg/mol, but the dispersity of this polymer was too high for a controlled polymerisation ($\bar{D} = 1.39$) along with low monomer conversions. For $[AIBN]_0/[CTA]_0 = 0.5$, the monomer conversion was higher, but the obtained polymer had very low molar masses and high dispersity ($\bar{D} = 1.48$). The highest dispersity was demonstrated by the system where $[AIBN]_0/[CTA]_0$ was 2. Thus, it was shown that $[AIBN]_0/[CTA]_0 = 1.0$ was the most effective ratio, as it produced PDMS with low \bar{D} (<1.3) and relatively high monomer conversion ($\geq 80\%$). Interestingly, when $D_P = 30$, even $[AIBN]_0/[CTA]_0 = 0.1$ ratio yielded well-defined

polymers with low dispersity ($\bar{D} = 1.21$) and high monomer conversion of 85 % (Table 3.2, experiment 4A).

Table 3.2. Molar mass data and monomer conversions of the polymerisation of 3,4-dimethoxystyrene in THF at 60 °C and 1:1 monomer to solvent ratio for the target $D_p = 150$ and $D_p = 30$ (experiment 4A).

Experiment	Ratio [AIBN] ₀ /[CTA] ₀	Time (h)	M_n^a (kg/mol)	D_p^a	\bar{D}^a (M_w/M_n)	Monomer conversion ^b (%)
1	0.1	42	19.2	114	1.39	55
2	0.5	33	8.4	49	1.48	72
3	0.75	34	9.5	56	1.34	66
4	1.0	48	14.2	84	1.29	88
4A	1.0	24	4.3	24	1.21	85
5	2.0	42	10.5	61	2.03	87

(a) Calculated by GPC against polystyrene standards in THF at 40 °C.

(b) Calculated using ¹H NMR spectroscopy, comparing the integrals for the methanediyl peak of the CTA fragment to those of the aromatic peaks of the polymer.

Subsequently, the amount of solvent was altered from 1:1 (DMS:THF) to 1:2 to ascertain the effect of monomer concentration in a system with targeted $D_p = 30$. The ratio of DMS:THF of 1:1 produced poorly defined polymers at high monomer conversion (Figure 3.7a). At this ratio, the molar mass increase was not linear, indicating that the polymer chains were not growing simultaneously. This resulted in high dispersity of 1.4. The ratio of DMS:THF of 1:2 produced better defined polymers with low dispersity ($\bar{D} = 1.14$), although at lower rates, in agreement with other reports for both more-activated (e.g. *p*-acetoxystyrene^{14,15}) and less-activated (e.g. vinyl chloride¹⁶) monomers. Concomitantly, this system gave better control over the polymer dispersity at the higher dilution tested (1:2 DMS:THF). On the other hand, even further dilutions (*i.e.*, ratio 1:3 DMS:THF) did not allow the growing chains to reach targeted molar masses (Figure 3.7c), although demonstrated good control over molar mass distributions. For this system, maximum achieved molar mass was 2.7 kg/mol *versus* the targeted 5.4 kg/mol.

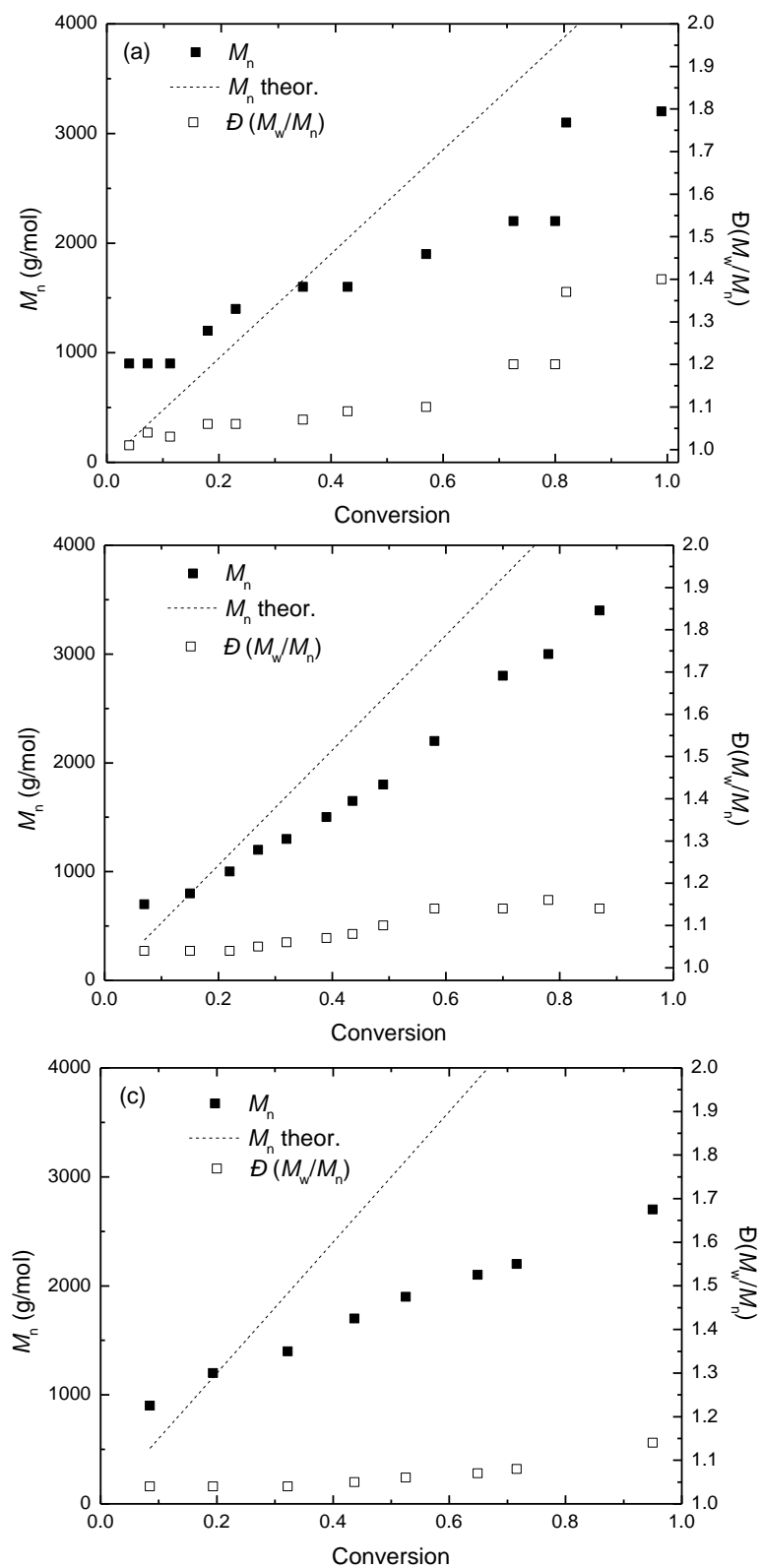


Figure 3.7. Plot of molar mass against conversion in RAFT polymerisation in (a) 1:1 DMS:THF ratio; (b) 1:2 DMS:THF ratio and (c) 1:3 PDMS:THF ratio at 60 °C and $[AIBN]_0/[DDMAT]_0 = 1.0$ with D_P target = 30.

In short, the optimal RAFT system was found to have a 1:1 ratio of initiator to CTA, ($[AIBN]_0/[DDMAT]_0 = 1.0$) at 1:2 DMS:THF. This system afforded good control over the final polymer molar mass and displayed first order kinetics with respect to monomer concentration with an apparent rate constant for polymerisation, k_{app} , of 0.085 h^{-1} (Figure 3.8). This means that under the described conditions, the reaction rate depends on the concentration of one component of the system, monomer, whereas the concentration of radicals remains constant from the start of polymerisation.

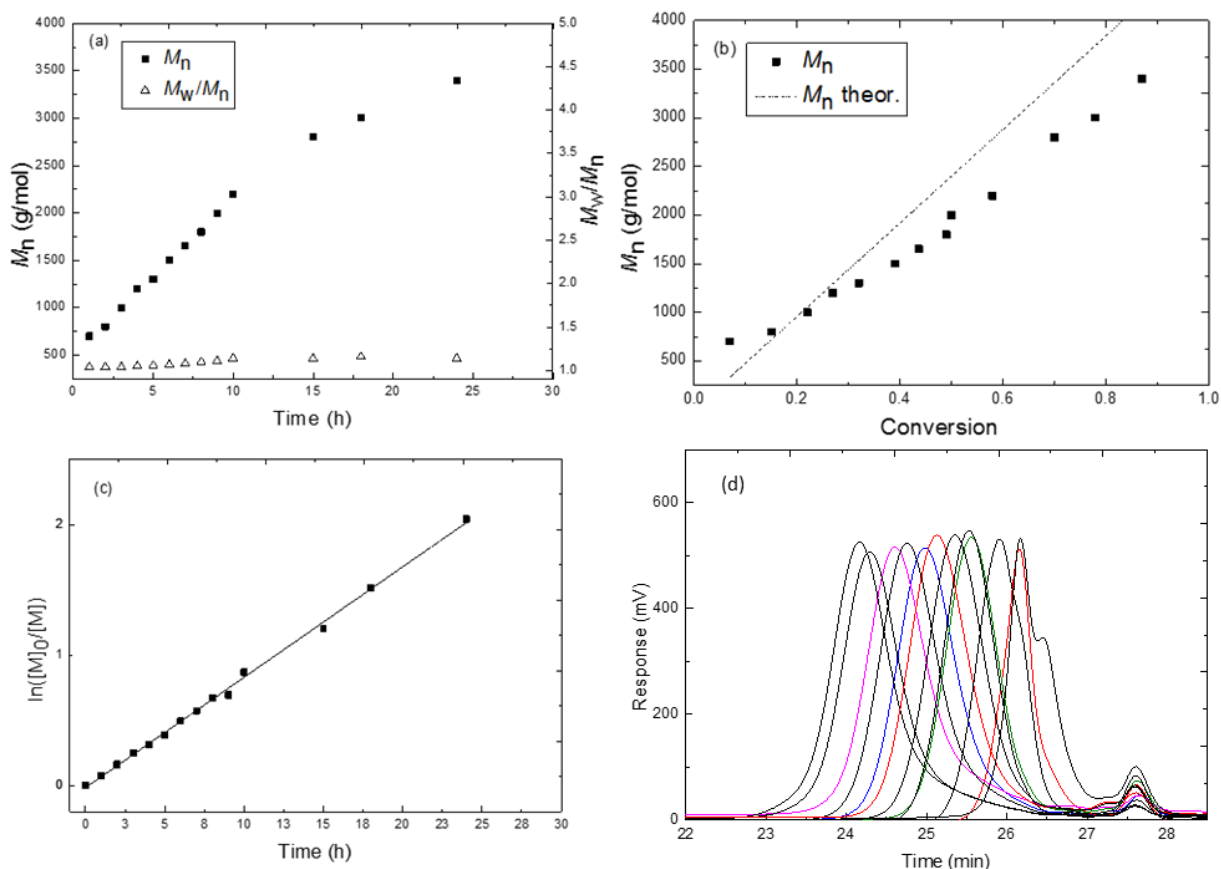


Figure 3.8. (a) Plot of molar mass, M_n , and dispersity (M_w/M_n , \bar{D}) against RAFT polymerisation time; (b) plot of M_n versus monomer conversion; (c) semi-logarithmic plot and (d) GPC traces for the RAFT polymerisation of PDMS with a target degree of polymerisation equal to 30. Conditions were as follows: $[AIBN]_0/[DDMAT]_0 = 1.0$ at 1:2 DMS:THF at 60°C .

Finally, the monomer:CTA ratio was varied to target three different molar masses; 5, 25 and 50 kg/mol (target degree of polymerisation, $D_p = [DMS]/[DDMAT] = 30, 150, 300$, respectively), as shown in Figure 3.9.

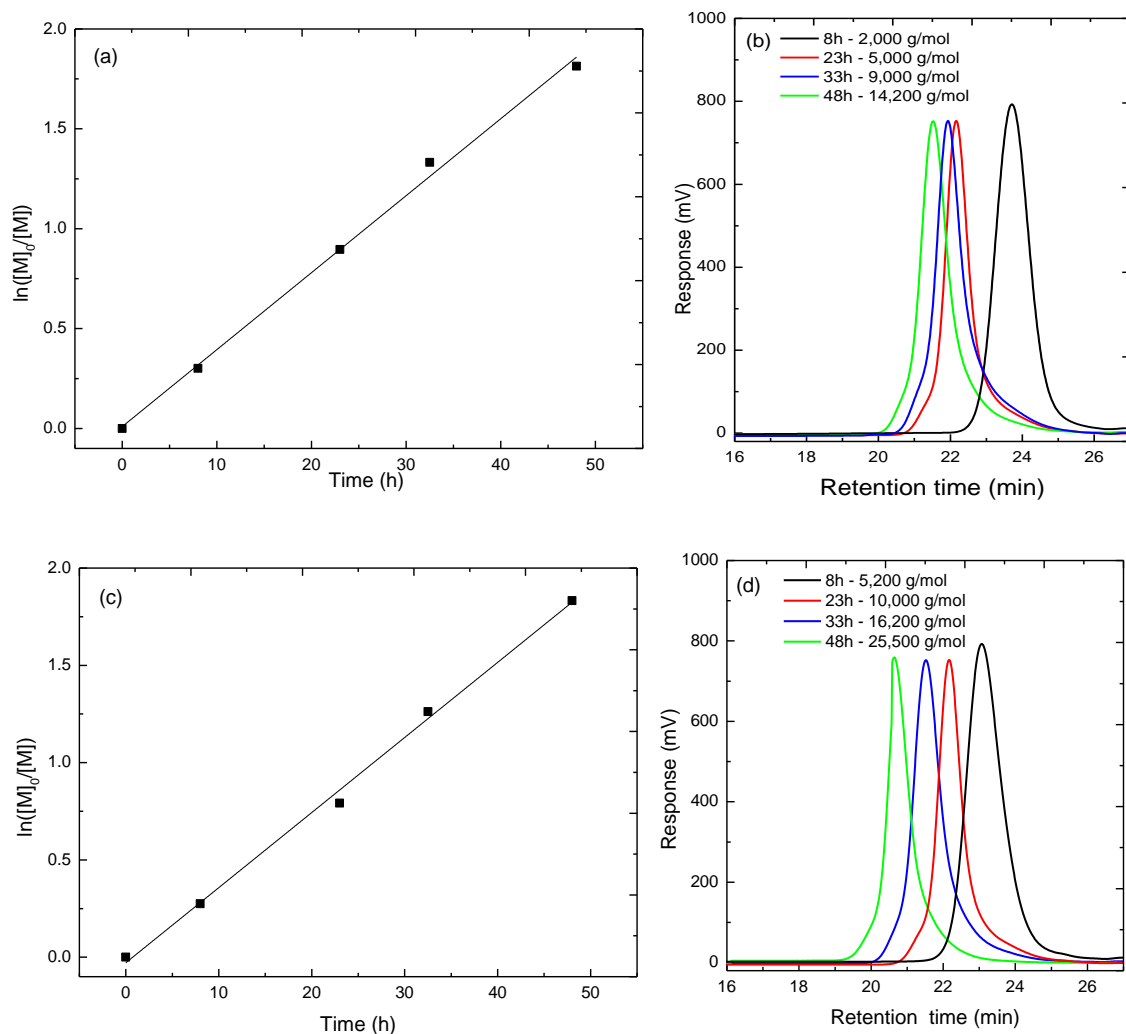


Figure 3.9. (a) Semi-logarithmic plot and (b) GPC traces for the RAFT polymerisation of PDMS with a target degree of polymerisation equal to 150 ($k_{app}=0.039 \text{ h}^{-1}$); (c) semi-logarithmic plot and (d) GPC traces for the RAFT polymerisation of PDMS with a target degree of polymerisation equal to 300 ($k_{app}=0.039 \text{ h}^{-1}$). Conditions were as follows: $[AIBN]_0/[DDMAT]_0 = 1.0$ at 1:2 DMS:THF at 60 °C.

^1H NMR spectroscopy revealed that actual molar masses were close to those targeted for all three PDMS samples; 4.8, 25.7 and 42.7 kg/mol, corresponding to PDMS₂₇, PDMS₁₅₄ and PDMS₂₅₈, respectively. The degree of polymerisation was obtained from the ^1H NMR spectra based on the ratio of the aromatic polymer protons to those of the methanediyl group of the CTA end group according to Equation 3.1:

$$\text{Degree of polymerisation, } D_P = \frac{2[\text{Int}]_{\text{arom.}}}{3[\text{Int}]_{\text{methy.}}} \quad (\text{Equation 3.1})$$

where $[\text{Int}]_{\text{arom}}$ represents the integration of aromatic peaks (from 6.8 to 5.7 ppm) and $[\text{Int}]_{\text{methy}}$ the integration of the methanediyl group (from 3.35 to 3.15 ppm).

Molar mass was calculated according to Equation 3.2.

$$M_n = D_p \times M_r(\text{DMS}) + M_w(\text{CTA}) = D_p \times 164.2 + 364.63 \text{ (g/mol)} \quad (\text{Equation 3.2})$$

It is important to note that the number-average molar mass, M_n , measured by GPC, is much lower than the corresponding M_n value obtained via ^1H NMR spectroscopy (Table 3.2). This is attributed to the use of polystyrene standards in GPC, providing a relative M_n value only. The MALDI spectrum for low molar mass PDMS (4.8 kg/mol) was used to verify the accuracy of the NMR results. As expected, the MALDI data are more consistent with the calculated M_n value obtained by NMR, with the most intense peak at 4377 m/z corresponding to $D_p = 24$ (Figure 3.10).

Table 3.3. Summary of monomer conversion and molar mass data for the homopolymerisation of DMS using AIBN and DDMAT in THF at 60 °C.

Target D_p	M_n^{th} (kg/mol)	Time (h)	Conversion (%)	M_n^{a} (kg/mol)	M_n^{b} (kg/mol)	D_p^{b}	M_w/M_n (\bar{D})
30	5.3	24	87	3.4	4.8	27	1.14
150	25.0	48	84	14.2	25.7	154	1.29
300	49.6	48	84	25.5	42.7	258	1.28

^a Calculated by GPC against polystyrene standards in THF at 40 °C.

^b Calculated using ^1H NMR spectroscopy, comparing the integrals for the methanediyl peak of the CTA fragment to those of the aromatic peaks of the polymer

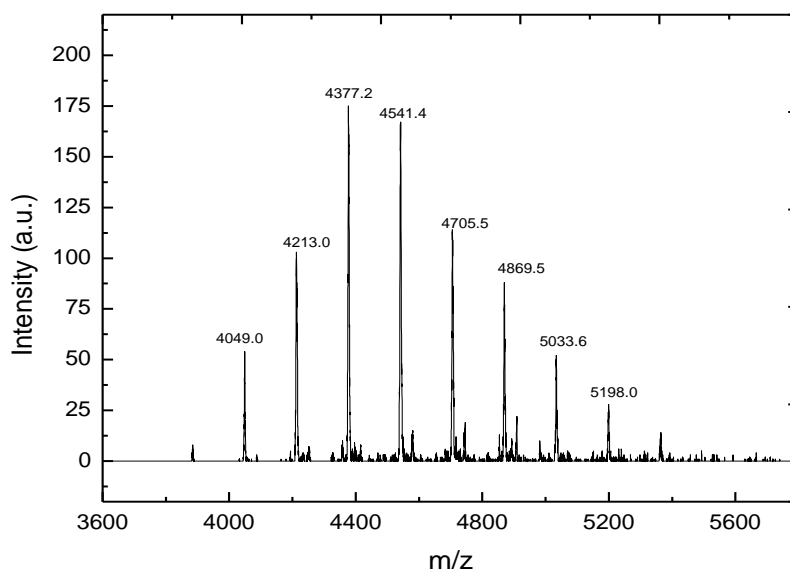


Figure 3.10. MALDI-ToF-MS spectrum of PDMS₂₇.

3.3.3 Demethylation of PDMS

Demethylation of PDMS was carried out in a simple procedure, previously reported by other groups.^{17,18} PDMS was treated with boron tribromide, a very strong Lewis acid, at low temperatures. Previous studies have reported that temperatures as low as -70 °C were employed for quantitative demethylation.¹⁷ Herein, however, a temperature of -20 °C was shown to be sufficient. Success of demethylation has been demonstrated by ¹H NMR, FTIR and UV-Vis spectroscopies.

The ¹H NMR spectrum of PDMS (Figure 3.11a) shows two broad peaks associated with the methoxy groups at 4.0 - 3.5 ppm, which are no longer present in that of PDHS (Figure 3.11b), indicating complete cleavage of the methoxy groups. Concurrently, the characteristic methanediyl peak of the CTA fragment (at approximately 3.25 ppm) is not detectable in this solvent (MeOD) due to the overlapping of peaks. Finally, the peak splitting in the aromatic region (ca. 6 to 7 ppm) changes following demethylation, demonstrating that the substituents on the phenyl ring have been modified, providing further evidence of the success of the reaction.

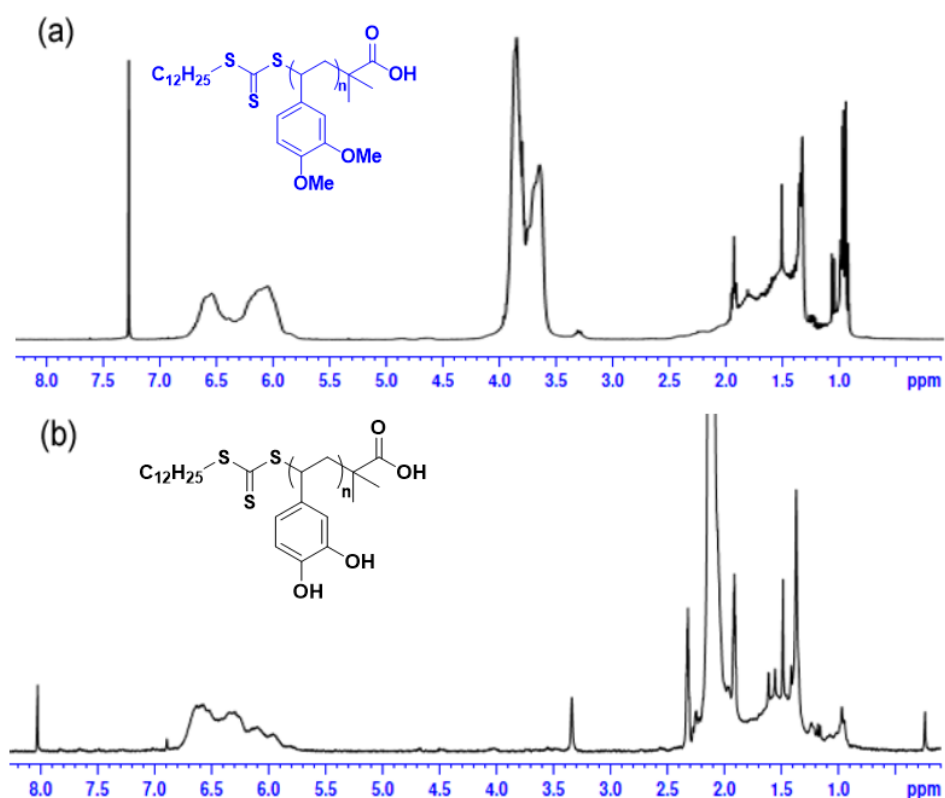


Figure 3.11. ¹H NMR spectra of (a) PDMS₂₇ in CDCl₃ and (b) PDHS₂₇ in MeOD.

UV-Vis spectroscopy (Figure 3.12a) reveals a change in the absorption spectra before and after demethylation, with a new absorption band clearly visible at 480 nm for PDHS. The

FTIR spectra (Figure 3.12b) show complete disappearance of the C-O arylmethoxy stretching bands at 1230 and 1260 cm^{-1} and CH_3 rocking band at 1383 cm^{-1} (characteristic for the methoxy protecting groups on the polymer²¹), going from PDMS to PDHS. As expected, the spectrum of PDHS shows O-H deformation and stretching bands at 1280 and 3400 cm^{-1} , respectively. It is important to note that the RAFT end group functionality did not remain intact following the demethylation step, as demonstrated by the absence of the carboxylic acid carbonyl group from the CTA fragment (IR band at 1735 cm^{-1}). Consequently, should coupling be required to produce more sophisticated materials, such as block copolymers, this should be carried out prior to treatment with boron tribromide.

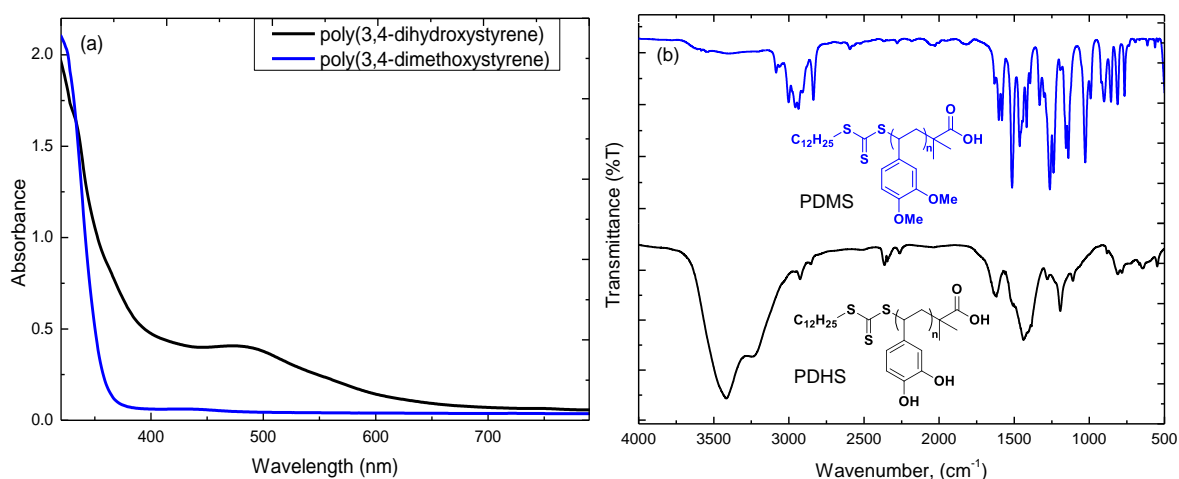
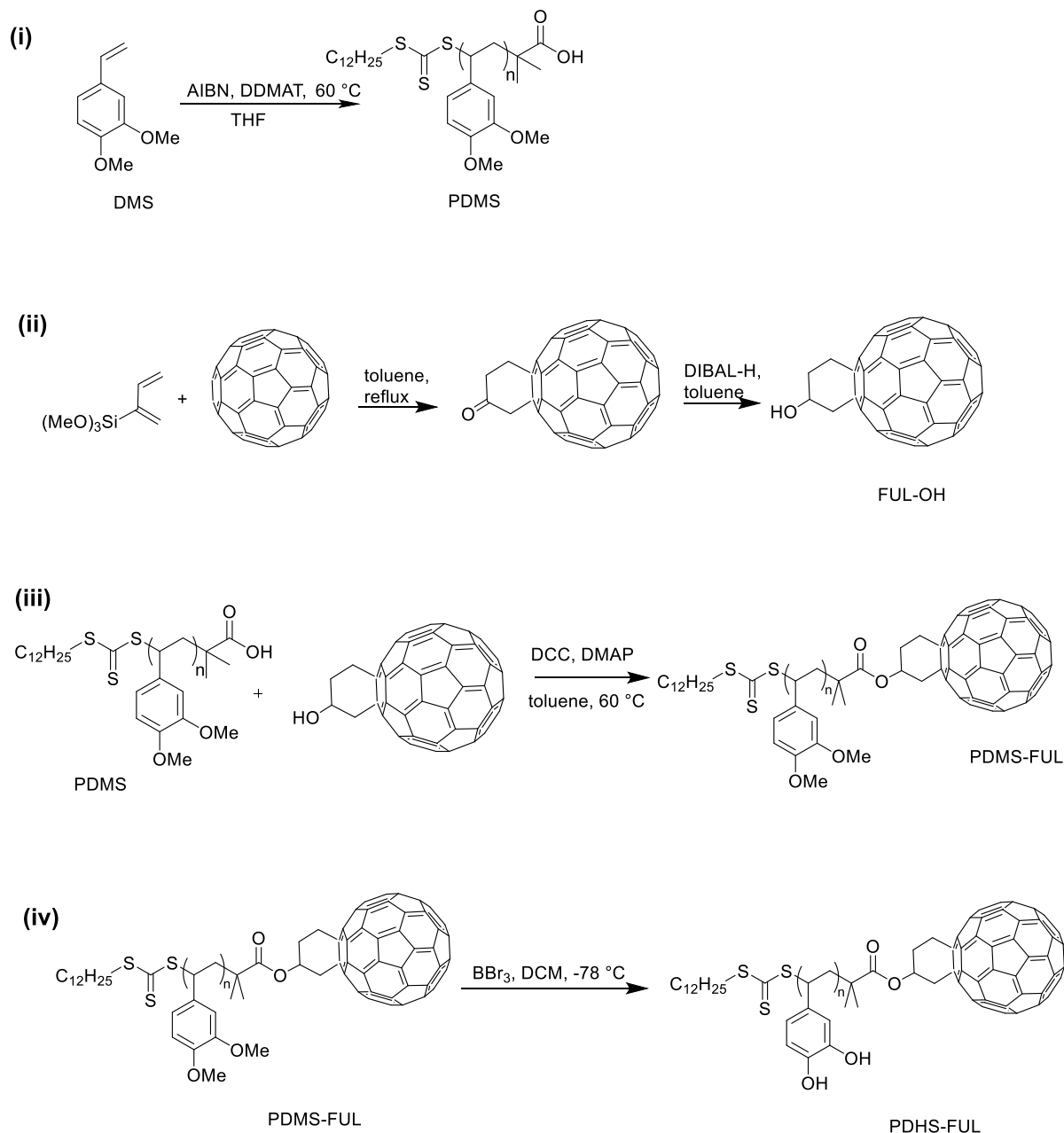


Figure 3.12. UV-Vis absorption (a) and FTIR (b) spectra of PDMS₂₇ and PDHS₂₇. The IR spectra have been translated along the transmittance axis for clarity purposes.

3.3.4 Synthesis of PDMS/PDHS-FUL

Once the best conditions for synthesis of the precursor polymers had been established, the functionalisation of PDMS with a single fullerene-containing molecule was carried out. The main challenge was in identifying a simple process for the derivatisation of the fullerene with high yields. Such reactions are rarely reported for several reasons: (i) fullerenes are poorly soluble in common organic solvents, thus the reaction media typically requires high boiling point chlorinated solvents (such as chlorobenzene or dichlorobenzene) at high temperatures; (ii) fullerene is highly susceptible to oxidation, especially in the presence of UV light, (iii) the fullerene ball experiences multiple attacks and along with monoaddition products, diadducts or triadducts are often found in the reaction mixture; (iv) the multiple addition products are difficult to analyse, distinguish and, furthermore, separate; and (v) due to solubility issues and the nature of fullerene molecule, ^1H and ^{13}C NMR analysis of products is complicated.

The synthetic route towards fullerene-functionalised PDMS and PDHS polymers is presented in Scheme 3.2. To avoid any parallel unwanted reactions, PDMS was first coupled to the fullerene derivative [step (iii)] and only afterwards demethylated to yield PDHS-FUL [step (iv)].



Scheme 3.2. Synthetic route towards PDHS-FUL: (i) RAFT polymerisation of DMS; (ii) synthesis of the fullerene precursor FUL-OH; (iii) Coupling of PDMS and FUL-OH towards fullerene-functionalised PDMS-FUL; (iv) demethylation of PDMS-FUL to obtain PDHS-FUL.

The fullerene derivative was synthesised and purified from 1,2-(4'-oxocyclohexano) buckminsterfullerene [step (ii)] as reported by An *et al.*¹⁹ and coupling was performed in step (iii) using DCC as an acid-activating reagent and DMAP as a base. To achieve addition of

the fullerene moiety to every polymer chain in step (iii), excess fulleranol (FUL-OH) was used. In the case of PDMS-FUL, demethylation was carried out strictly at -78 °C to avoid unwanted cleavage of the ester bond.

Figure 3.13 shows the ^1H NMR spectra of the PDMS (5,000 g/mol) and fulleranol precursor materials [synthesised in steps (i) and (ii), respectively] alongside the PDMS-FUL and PDHS-FUL products. A co-solvent system of deuterated chloroform and acetone (5:1) was required for the fullerene precursor, due to the insufficient solubility of the fullerene precursor in common solvents. Additionally, the poor solubility of the precursor leads to accentuation of peaks associated with soluble hydrogenated fullerene and other impurities in the alkyl region.²⁰

The ^1H NMR spectrum of the conjugated polymer shows two new peaks appearing at 3.5 ppm and 4.0 - 4.1 ppm, which are attributed to methylene protons on the fullerene moiety (Figure 3.13c). These peaks are difficult to assign precisely as the methylene peaks of the fullerene precursor in the region 3.5 – 3.8 ppm are overlapping and cannot be resolved.²¹ Additionally, these peaks cannot be accurately integrated because they overlap with the methoxy protons of the PDMS moiety at 3.5 – 4.0 ppm. Importantly, the presence and shifting of peaks in the FUL-OH cyclohexyl ring provide strong evidence that PDMS and fullerene are covalently bound to one another. The multiplet peak at 5.2 - 5.3 ppm, which overlaps with the residual dichloromethane singlet at 5.22 ppm (Figure 3.13a), is attributed to the proton attached to the tertiary carbon of FUL-OH (H_a), which upon esterification is significantly shifted downfield, where it is obscured by the peaks of the aromatic protons (expected at 6.1 - 6.6 ppm).²² Additionally, the coupled product shows a more defined peak around 3.2 ppm attributed to one of the methylene protons attached to the carbon adjacent to the tertiary carbon (labelled H_b in Figure 3.13c).^{23,24} The remaining peaks arising from the cyclohexyl methylene protons of the fullerene derivative cannot be established as they are completely obscured by the methoxy peaks from PDMS at 3.5 - 4.0 ppm. After demethylation, the spectrum of PDHS-FUL shows complete disappearance of the methoxy peaks and restructuring of the aromatic region. The water peak of the solvent is rather large and couldn't be removed by water peak suppression techniques. It obscures the shifts in 3.3-2.6 ppm range. The peak at 4.1 ppm is attributed to the methylene protons on the cyclohexyl ring, whereas the peak at 3.6 ppm is originating from the CTA methylene protons.

As further evidence, ^{13}C NMR spectroscopy was used to characterise the final product (Figure 3.14), where the spectrum is a close resemblance of a combination of the spectra of the two starting materials, clearly showing contributions from both PDMS and fullerene.

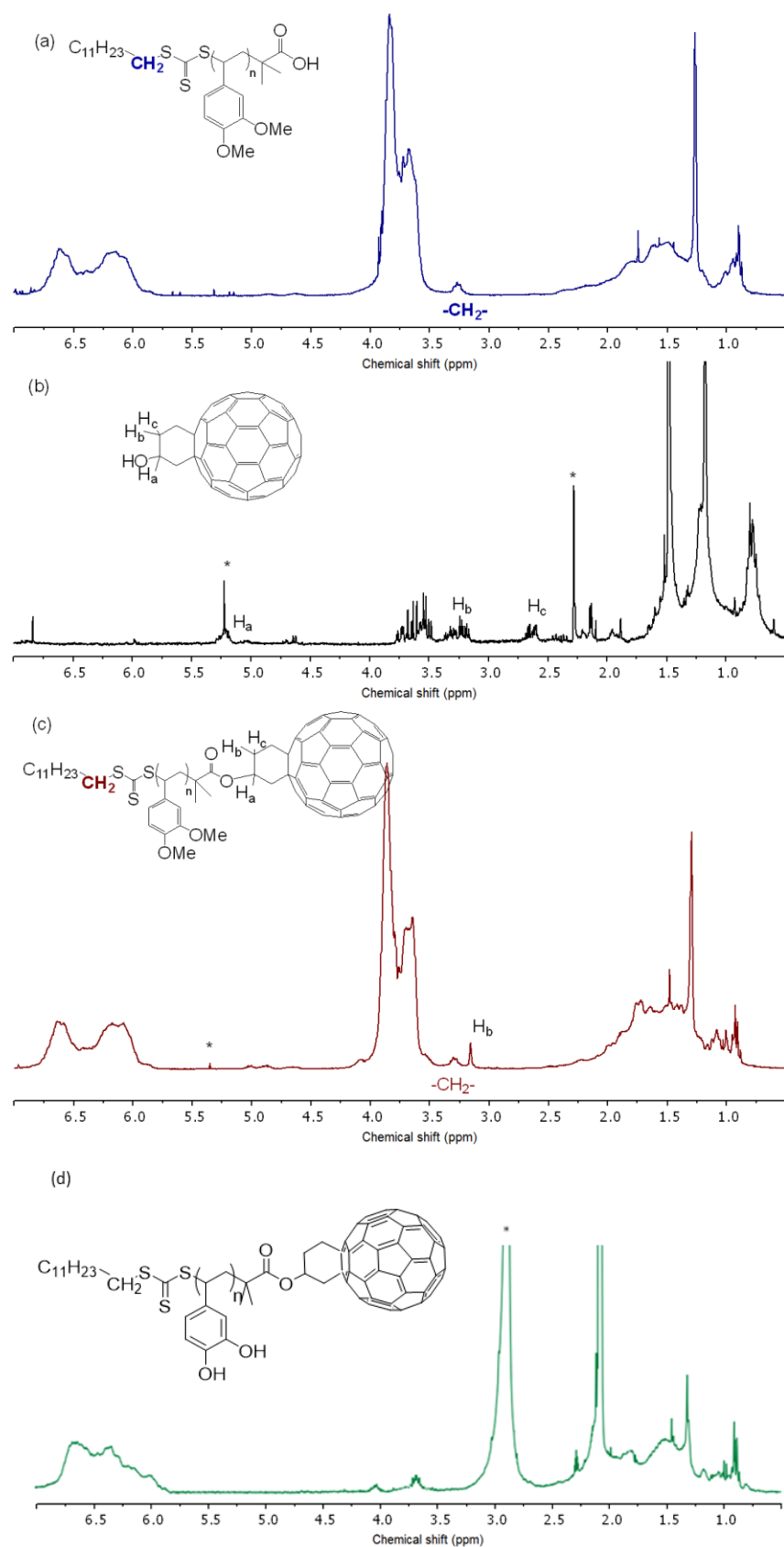


Figure 3.13. ^1H NMR spectra of (a) starting polymer PDMS (in CDCl_3), (b) fulleranol precursor FUL-OH ($\text{acetone-d}_6:\text{CDCl}_3$) and resulting (c) PDMS-FUL (in CDCl_3) and (d) PDHS-FUL (in MeOD). Residual solvent peaks are marked with an asterisk.

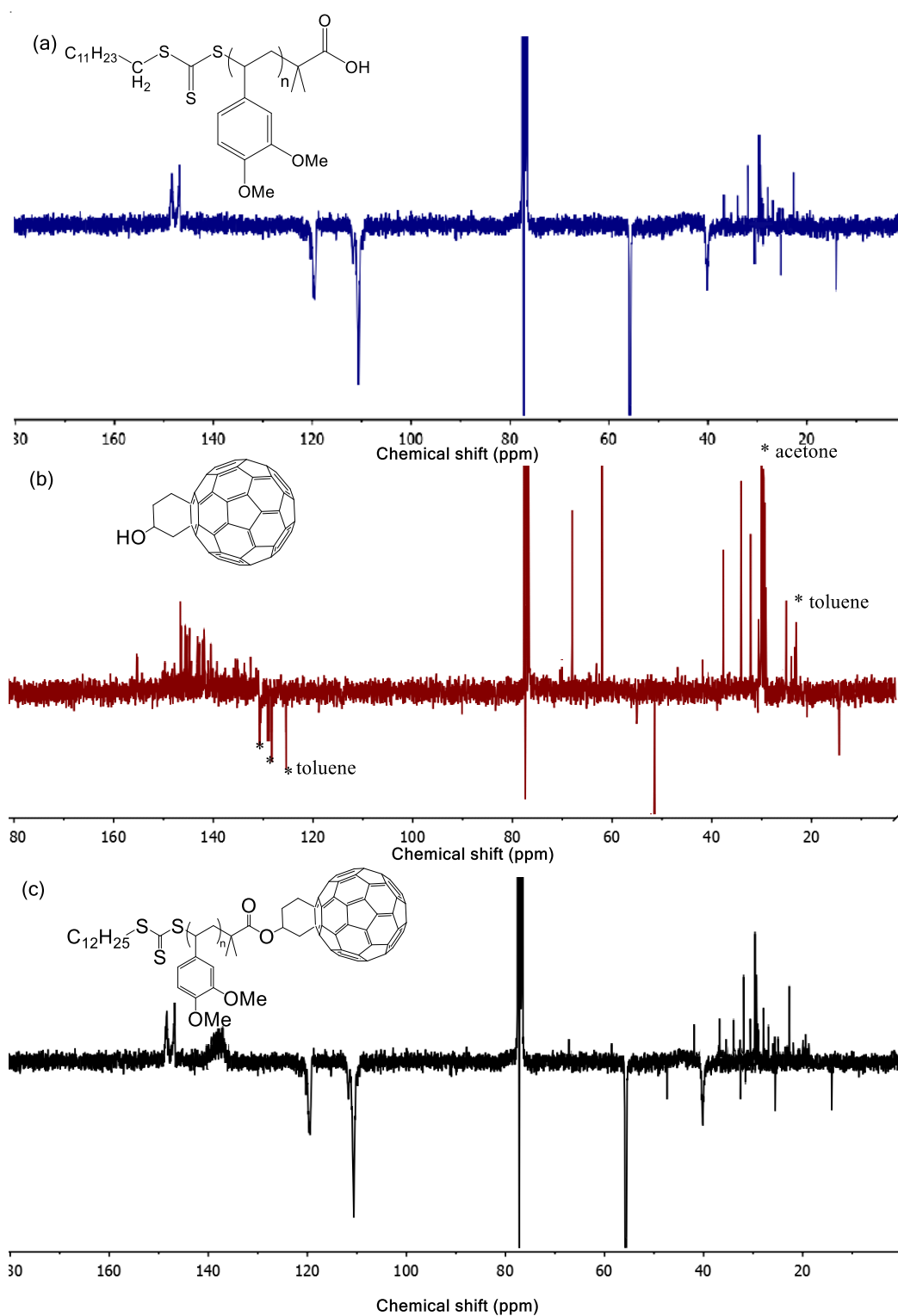


Figure 3.14. ^{13}C NMR spectra of (a) PDMS (in CDCl_3); (b) FUL-OH (in $\text{acetone-d}_6:\text{CDCl}_3$) and (c) PDMS-FUL (in CDCl_3).

The numerous peaks in the alkyl region are attributed to the alkyl tail of DDMAT. The prominent broad peaks at 56 ppm (methoxy carbons), 110 ppm and 120 ppm (tertiary carbons of the benzene ring); and 150 and 148 ppm (quarternary carbons of the benzene ring) belong to the PDMS part of the conjugate material. The quarternary peaks in the region

are typically attributed to the fullerene carbons (135-139 ppm). The observed pattern is more structured than those in various other reports²⁵⁻²⁷ but agrees with a monosubstituted fullerene polymer.^{22,27} Two peaks at 57 and 67 ppm also originate from the quarternary carbon from C-C bond in the fullerene cycloadduct. Unfortunately, the ^{13}C NMR spectra for PDHS-FUL could not be obtained due to limitations of equipment.

Figure 3.15 shows the FTIR spectra of the PDMS and fullerenol starting materials alongside the PDMS-FUL and PDHS-FUL products. The band at 527 cm^{-1} is indicative of the fullerene being present in our macromolecule.²⁸ The characteristic carbonyl band of the carboxylic acid on the chain end of PDMS shifted from 1730 cm^{-1} (typical for a non-hydrogen bonded carboxylic acid group⁷⁴) to 1700 cm^{-1} in agreement with previous reports for fullerene conjugates,²⁹ although lower than expected for a typical carbonyl ester band. Furthermore, the absence of the carboxylic acid carbonyl group in the coupled PDMS-FUL material suggests that there is no detectable unreacted polymer remaining. FTIR spectrum of PDHS-FUL is similar to that of PDHS and shows a broad band for O-H stretching vibrations at 3400 cm^{-1} . Since the features of this spectrum are very broad and merge together, it is difficult to assign any of them unequivocally. A band at 527 cm^{-1} can be observed, corresponding to the fullerene asymmetric vibrations in PDHS-FUL molecule.

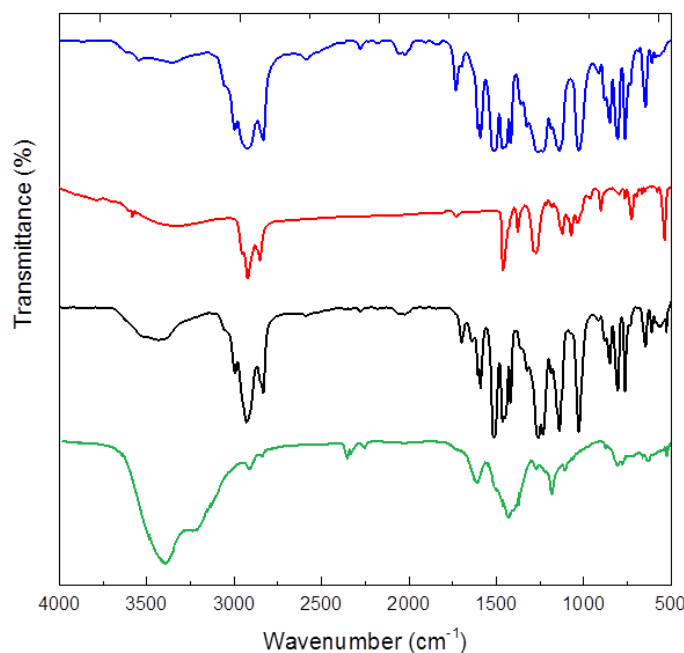


Figure 3.15. FTIR spectra of PDMS (blue), FUL-OH (red), PDMS-FUL (black) and PDHS-FUL (green).

The GPC traces of PDMS and PDMS-FUL in THF are given in Figure 3.16 (FUL-OH and PDHS-FUL could not be analysed due to their insolubility in THF). As expected, a small shift towards higher molar mass is observed for PDMS-FUL, indicating the covalent attachment of

a single fullerene molecule to the end of the PDMS chains. The monotonic shift of the main peak suggests that there is no free PDMS impurity in the final product (in agreement with the FTIR data in Figure 3.15) and the high molar mass shoulder observed is attributed to aggregation of the fullerene moieties in THF, as reported elsewhere for fullerene-containing species.²²

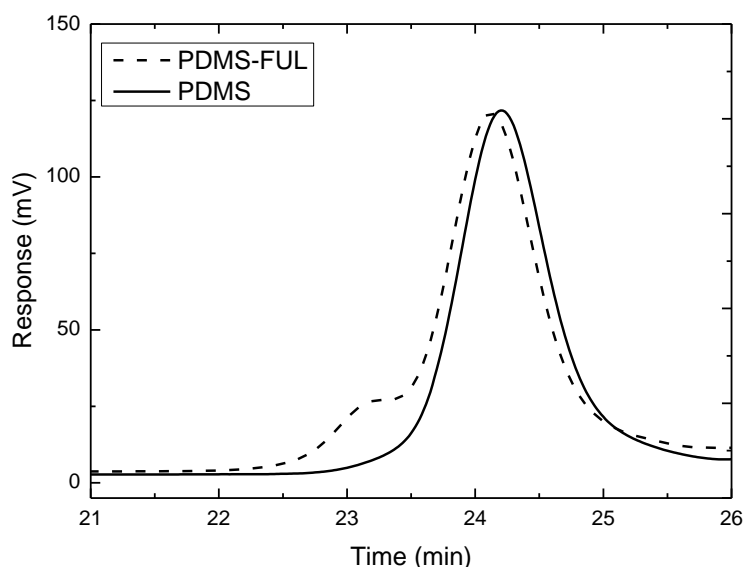


Figure 3.16. GPC traces of PDMS (5,000 g/mol) and PDMS-FUL.

3.4 Thermal studies

To obtain thermal parameters for further processing of the polymers, differential scanning calorimetry (DSC) was used; the thermograms of PDMS and PDMS-FUL polymers are presented in Figure 3.17. The glass transition temperature (T_g) of PDMS can be observed at 60 °C, whereas T_g of PDMS-FUL is observed at slightly higher temperatures (65 °C), demonstrating that the functionalisation of the polymer chain end with a large C60 moiety decreases the flexibility of the polymer chains. It has been demonstrated previously that an end group has an effect on the glass transition temperature of a polymer.³⁰ There is no melting peak observed for both PDMS and PDMS-FUL, indicating amorphous non-crystalline nature of the polymer. On the other hand, in the thermogram of PDMS-FUL, cold crystallisation peak can be observed which could be attributed to the crystallisation of fullerenes on the polymer chain ends.

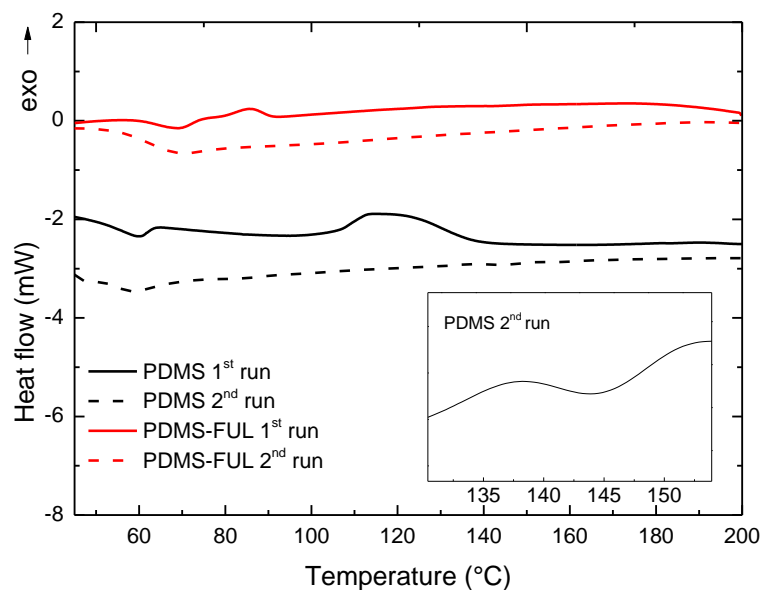


Figure 3.17. Thermograms of PDMS (black) and PDMS-FUL (red) over 2 heating runs. Inset shows the T_g of the cross-linked PDMS at the second heating run.

Interestingly, the thermogram of PDMS shows a broad exothermic peak from 110 to 140 °C. This peak is absent in the 2nd heating run and can be attributed to cross-linking of the polymers. Moreover, in the 2nd heating run of PDMS the second T_g is present at 143 °C (Figure 3.17, inset), indicating that the T_g of the rigid cross-linked polymer has increased. The T_g of the pristine polymer is still observed, indicating that cross-linking was not complete. The thermal cross-linking behaviour hasn't been observed for styrene-based polymers before and in case of PDMS is only possible because of two methoxy groups.

However, cross-linking is not observed in PDMS-FUL polymer. Supposedly, this can be associated with wrapping of PDMS chains around the fullerene molecules which prevents them from accessing the neighbouring chains for reaction. Accordingly, the T_g is preserved in PDMS-FUL over both heating runs.

The cross-linking was further confirmed by the changes in solubility of PDMS after first heating run as it became completely insoluble. Moreover, when suspended in THF, it demonstrated UV-induced yellow-green emission, which was not observed in pristine PDMS, indicating extended conjugation in the cross-linked polymer (Figure 3.18).

The product of crosslinking was studied by FTIR since this technique does not require the analyte to be soluble. FTIR spectra of pristine PDMS and cured PDMS are shown in Figure 3.19. Two strong bands at 1240 cm^{-1} and 1260 cm^{-1} characteristic for a methoxy ether disappear whereas two benzene ether stretching bands at 1140 and 1160 cm^{-1} merge into one band at 1110 cm^{-1} . This shows that methoxy ether groups are responsible for cross-

linking in PDMS polymer and upon heating are involved in formation of new ether bonds. Investigation of the precise cross-linking mechanism is beyond the scope of this study and currently remains unclear.



Figure 3.18. Photograph of the UV-induced emission of pristine PDMS polymer (right) and PDMS after cross-linking and resuspension in THF (left).

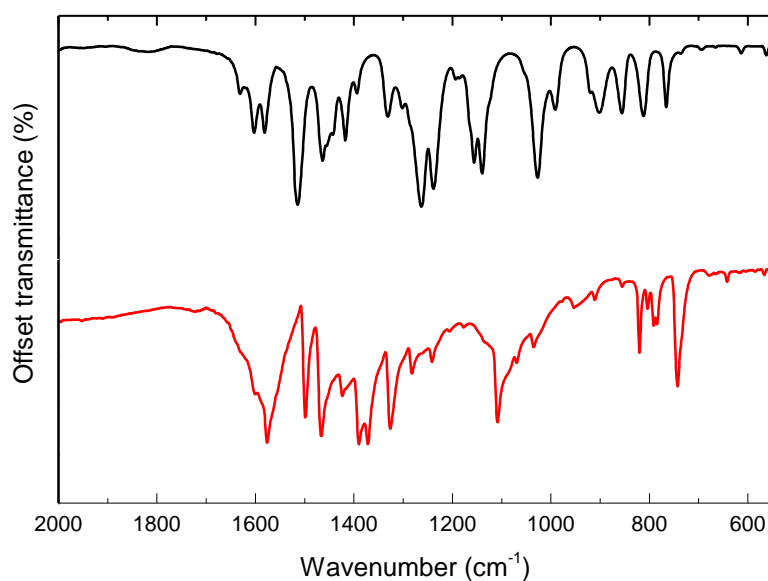


Figure 3.19. FTIR spectra of PDMS before (black) and after the 1st heating run (red).

The DSC thermogram of PDHS (Figure 3.20) shows two merged endothermic peaks. The first peak with a sharp onset at 134 °C is attributed to the melting of highly crystalline PDHS polymer, whereas the second peak is associated with the thermal decomposition of PDHS. Decomposition starts in the molten state and proceeds with increase in temperature. The inset to Figure 3.20 shows the T_g region of the polymer with a midpoint at 103 °C. The second heating run shows no features at all as the polymer has already degraded.

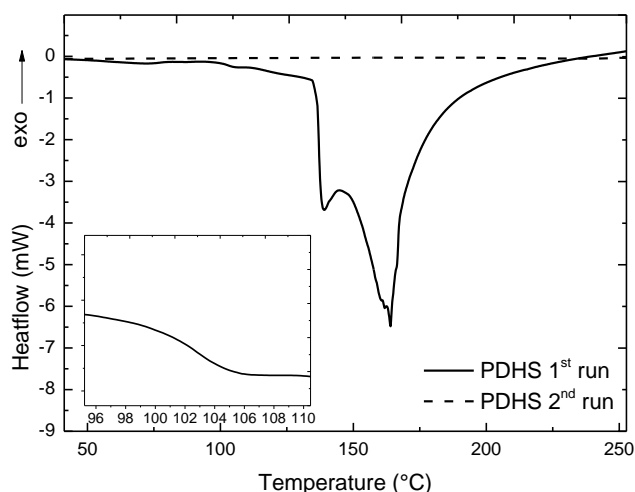


Figure 3.20. Thermogram of PDHS over 2 heating runs. Inset shows the T_g region of the polymer.

The DSC thermogram of PDHS-FUL (Figure 3.21) shows only one endothermic peak with a sharp onset at 140 °C. The peak combines both processes of melting and decomposition as in the 2nd run the thermogram is featureless and corresponds to the complete degradation of the polymer. It should be noted that attachment of the fullerene molecule to the chain-end of the polymer increased the onset temperature of melting and decomposition to 140 °C and decreased the T_g midpoint to 98 °C. The behaviour is different to PDMS-FUL, where attachment of the fullerene increased T_g , due to crystalline nature of PDHS. Attached fullerene molecules disrupt crystallinity in PDHS chains and induce mobility of chains in the amorphous regions, resulting in lower T_g .

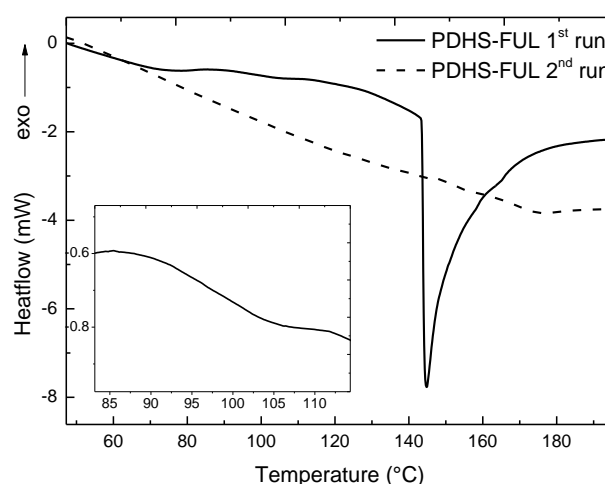


Figure 3.21. Thermograms of PDHS-FUL over two heating runs. Inset shows the T_g region of the polymer at the first heating run.

3.5 Material properties and thin film characterisation

3.5.1 Zinc binding experiment

Zinc binding capacity of PDMS, PDHS and PS (the latter used as a control) was measured indirectly by assessing zinc surface coverage using scanning electron microscopy with energy dispersive X-ray analysis (SEM-EDXA).

SEM/EDXA is a combined technique that allows analysis of the chemical composition of a surface at high magnification. The underlying principle the technique is that the X-ray spectral emission of each element is attributed to its atomic structure and therefore unique for each element. Inner shell electrons are excited with a high-intensity X-ray beam whereas the electrons from the outer shell with a much higher energy take their place. Upon this transfer, excess energy is released radiatively.³¹ Owing to the nature of the technique, it is best applied to heavy atoms, including metals, and normally finds application in the analysis of metallurgical or geological samples. Here, it was used to evaluate the contents of zinc retained by the polymer surface as an indirect measurement for zinc binding capacity of the polymers.

Informed by the data obtained from DSC, the temperature of annealing was set just above the glass transition temperatures of PDMS and PDHS, at 65 °C and 100 °C, respectively. Inorganic zinc acetate was deposited on the polymer films from aqueous solution and after annealing, the films were thoroughly washed to remove all non-bound zinc acetate from the surface. Three different molar mass PDMS and PDHS samples have been studied; 4.8 kg/mol, 25.7 kg/mol and 44.4 kg/mol, alongside PS of 25 kg/mol. The average zinc surface coverage of PDHS was shown to be 85 % (± 1.0 %), whereas that of PDMS was approximately 67 % (± 2.0 %) (Figure 3.22). As expected, the polymer molar mass does not appear to significantly influence zinc binding capability of the films. To eliminate the possibility that the difference in annealing temperature has an effect on zinc binding capacity, PDMS₂₇ (4.8 kg/mol) films were also annealed at 100 °C and the samples scanned in the same manner. The average zinc surface coverage was shown to be approximately the same as the experiment carried out at 65 °C, but with a marginally higher error across the samples (65 ± 2.5 %). Although PDHS has a higher zinc binding affinity, the SEM images (Figure 3.23) clearly show that PDMS produces deposited layers of higher quality, particularly in terms of durability. Moreover, PDMS was shown to be preferable for processing; dissolving in a wide range of common organic solvents (unlike PDHS) and requiring lower annealing temperatures (due to its lower T_g). Finally, Figure 3.22 also shows that polystyrene films only retain a small amount of zinc on the surface, demonstrating that the methoxy and hydroxy groups of PDMS and PDHS, respectively, are responsible for the significantly enhanced zinc binding ability of PDHS polymers.

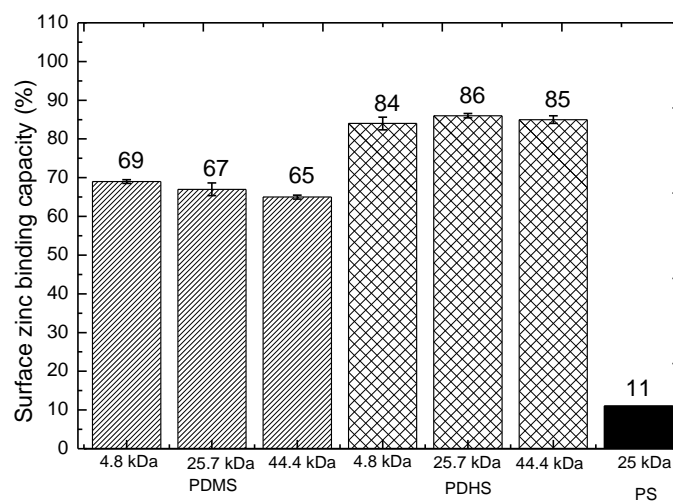


Figure 3.22. Surface zinc coverage for PDMS, PDHS (both at three different molar masses) and PS.

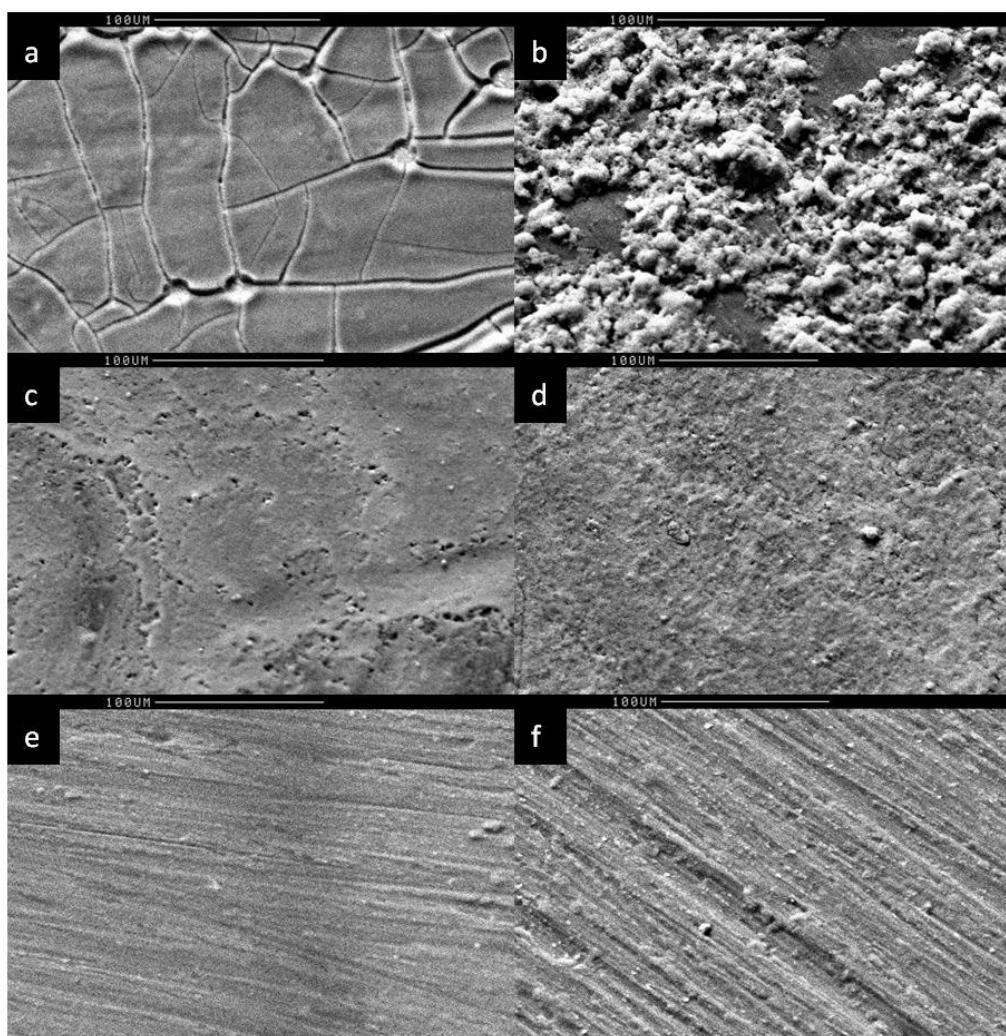


Figure 3.23. SEM images before (left) and after (right) zinc acetate coverage treatment for PDHS₂₇ (a and b), PDMS₂₇ (c and d) and PS₂₄₀ (e and f).

3.5.2 XPS measurements

To obtain explicit understanding of how PDMS and PDHS polymers bind to the ZnO surface, X-ray photoelectron spectroscopy (XPS) studies have been carried out by project partner, Aurelien Tournabize, at the University of Tübingen (Tübingen, Germany).

For this study, the polymers deposited onto ZnO were washed after annealing at temperatures above glass transition and the XPS survey spectra of the resulting layers were taken. Firstly, the composition of the bare surface of ZnO was studied (Figure 3.24). The bare ZnO surface was shown to comprise zinc and oxygen, although small contamination of carbon was also observed at 290 eV.

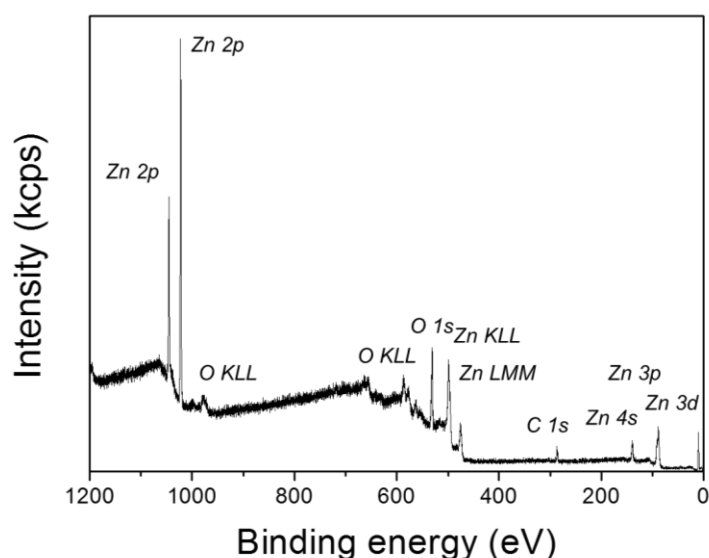


Figure 3.24. XPS survey spectrum of the bare ZnO surface, where all peaks are assigned according to the energy levels of electrons extracted from corresponding electronic levels. KLL peaks represent the energy ejected from the atoms due to filling of the K shell by an electron from the L shell coupled with the ejection of an electron from an L shell.

The spectra of PDMS and PDMS-FUL on the ZnO surface after washing are shown in Figure 3.25. Clearly, there is no detectable difference in the surface composition. It suggests that the interaction of PDMS and PDMS-FUL with zinc oxide is not strong enough to withstand the solvent treatment. Unlike in SEM experiment, here more material can be solvated as most of the polymer is not bound to ZnO, thus the polymer is washed off the surface easier than in case of zinc, being washed off the polymer surface. Moreover, the adhesion of polymer to zinc and zinc oxide might be of a different nature and of different strength.

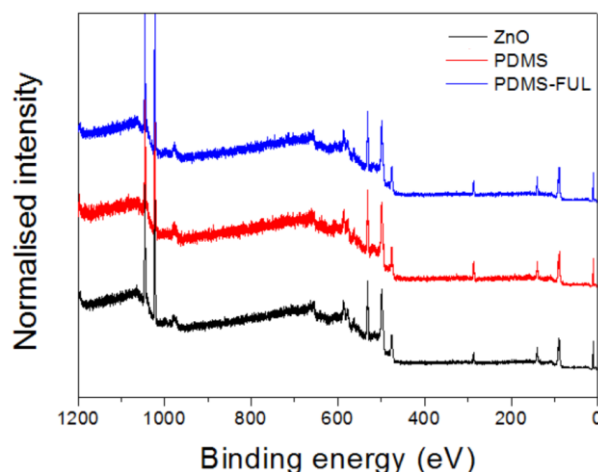


Figure 3.25. XPS survey spectra of the bare ZnO surface (black line), with PDMS (red line) and PDMS-FUL (blue) after washing.

Unfortunately, the adhesion forces could not be measured in this work, because there is no existing reliable procedure to estimate the adhesion forces in a ZnO/polymer system.³² Design of such a procedure was out of scope for this study, thus, only indirect measurements were used to estimate binding of the polymer to the ZnO surface.

Generally, the strategy of forming an adhesive monolayer on ZnO would not work for PDMS and PDMS-FUL layers. Furthermore, if these layers are deposited without washing, subsequent deposition of the PAL from xylene would partially dissolve the underlying PDMS/PDMS-FUL layer and result in redistribution of the polymer molecules within the active layer.

XPS spectra of PDHS and PDHS-FUL on ZnO after washing are shown in Figure 3.26. Two peaks of high intensity are observed for both polymers, carbon C 1s peak and oxygen O 1s peak, which are attributed to the oxygen in hydroxyl binding groups.

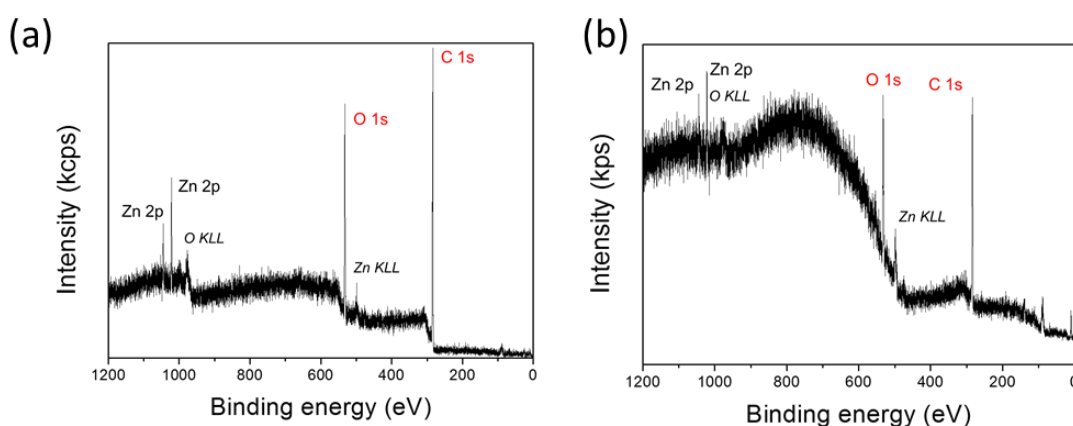


Figure 3.26. XPS survey spectra of PDHS (a) and PDHS-FUL (b) on ZnO after washing with acetone.

Since the core levels of zinc oxide still could be observed at approximately 500 eV (Zn KLL) and 960 eV (O KLL), the thickness of PDHS or PDHS-FUL layers was calculated as approximately 5-6 nm, based on the intensity of the core level peaks, although the measurements do not take the surface inhomogeneity into account.

3.6 Device studies on PDHS and PDHS-FUL

Since only PDHS and PDHS-FUL polymers fulfil the main criterion to form a layer sticking to the surface of ZnO, devices incorporating these polymers only were produced and studied. For PDMS devices, a different strategy is sought in this work, as discussed in Chapter 4.

PDHS/PDHS-FUL polymer was deposited onto the ZnO-coated glass, annealed at 100 °C and subsequently washed with acetone so that only the polymer that adheres to ZnO would remain on the surface. Afterwards, the layer was annealed at 100 °C for 20 min to ensure the optimal morphology of the polymer layer after deposition. As has been observed from XPS studies these monolayers were approximately 5-6 nm thick. Subsequently, the photoactive blend of P3HT:PCBM (1:0.8) was deposited onto the PDHS layer from xylene.

Corresponding absorbance spectra of annealed and washed PDHS and PDHS-FUL on zinc oxide are presented in Figure 3.27. It can be seen from the figure that the PDHS and PDHS-FUL still remained on ZnO surface after washing, although as thinner layers (as observed from the decrease in absorbance), indicating that there was good adhesion of the dihydroxyligands to the surface. Furthermore, in the spectra of PDHS-FUL films, the characteristic fullerene absorbance at near-UV (400-430 nm) visible part of the spectrum can be distinguished.

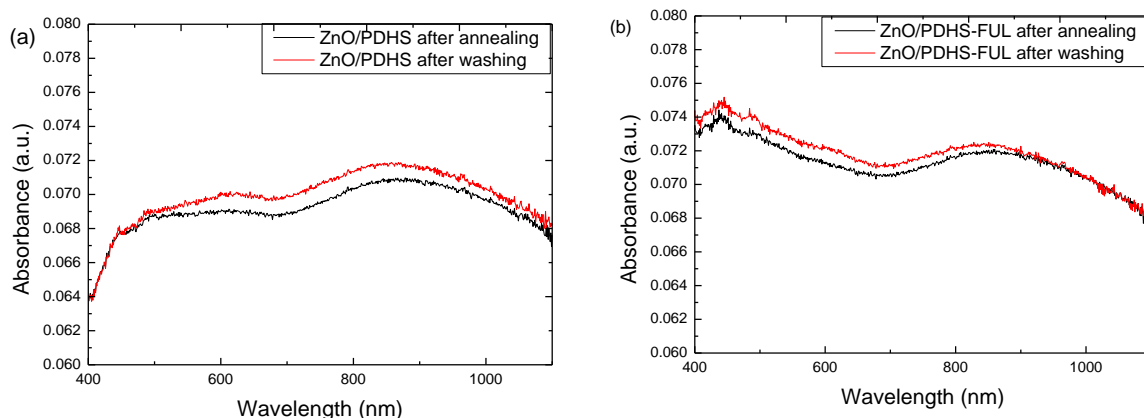


Figure 3.27. Visible and NIR spectra of PDHS (a) and PDHS-FUL (b) deposited onto ZnO and annealed at 100 °C before washing and after washing with acetone.

Typical J - V curves of the devices incorporating PDHS and PDHS-FUL are presented in Figure 3.28 and the key parameters with statistical distribution in Figure 3.29. The control sample demonstrated behaviour very typical for bulk heterojunction cells with P3HT:PCBM as PAL and ZnO and PEDOT:PSS as electron-transporting and hole-transporting layers, respectively, with an open circuit voltage $V_{oc} = 0.54$ V, and average fill factor of 0.55. The average power conversion efficiency (PCE) of the control sample reached 2.3%.

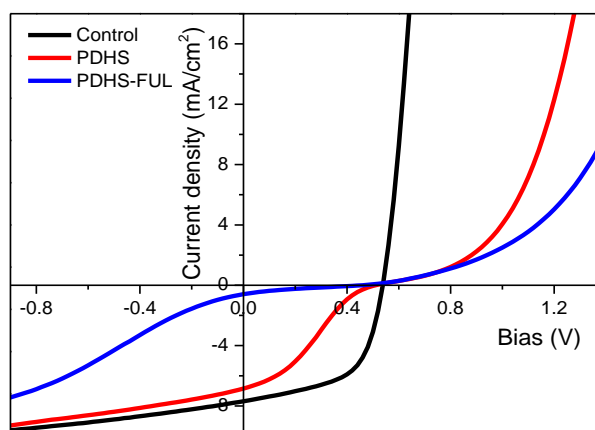


Figure 3.28. Representative J - V curves of the devices ITO/ZnO/IL/P3HT:PCBM/PEDOT:PSS/Ag, where IL represents the interlayer of PDHS or PDHS-FUL.

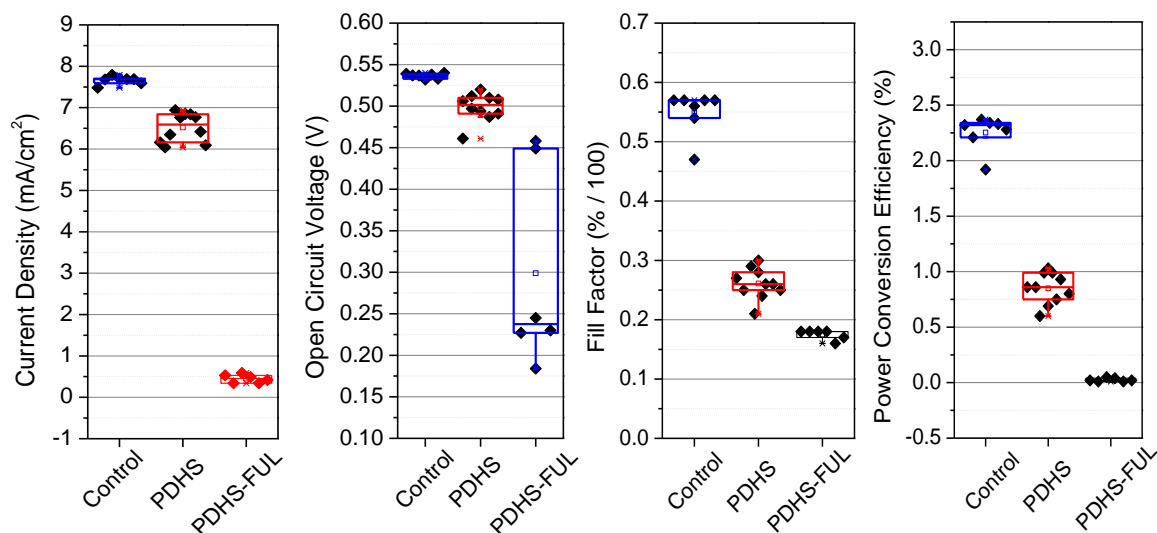


Figure 3.29. Statistical lay-out of the key photovoltaic parameters of devices, incorporating PDHS and PDHS-FUL as interfacial layers, alongside a control without interlayer.

As can be seen from the J - V curves and photovoltaic parameters (Figure 3.28 and 3.29), interfacial layers based on dihydroxybenzylic ligands had a detrimental effect on the performance of the cells. While PDHS-incorporating cells were still capable of demonstrating some photovoltaic performance, PDHS-FUL-incorporating cells behaved like a large double

diode. Primarily, the cells demonstrated *so-called* S-shaped *J-V* curves, which were more pronounced in the PDHS-FUL cells, rendering the PCE values of the cells close to zero. S-shape generation led to a drastic decrease of the fill factor (from 0.56 to 0.26 for PDHS and to 0.11 for PDHS-FUL containing cells). The open circuit voltage (V_{OC}) in PDHS-incorporated cells decreased from 0.54 to 0.5 V, and current density (or short circuit current) J_{SC} decreased from 7.7 to 6.7 mA/cm². In PDHS-FUL cells, the V_{OC} values had a bigger variation, ranging from 0.16 to 0.46 V, which possibly indicates that the coverage of ZnO by PDHS-FUL layer was not homogenous.

As has been demonstrated before by Saive³³ and Kumar,³⁴ S-shaped curves result from hindered charge transport from the acceptor to the cathode and therefore failure of extraction due to the creation of dipoles and local defects at the interface. To specify recombination at the interface, a parameter called 'surface recombination velocity' was introduced. As any interface is a region of very high recombination rates, it gets depleted of charge carriers. According to general diffusion laws, charge carriers flow to the depleted region, or in this particular case, to the interface, and the surface recombination velocity determines the movement of charges. A reduction in surface recombination velocity to *ca.* 10⁻¹¹ m/s would lead to diode characteristics close to those observed for PDHS-FUL cells.

Furthermore, the decrease in V_{OC} in comparison to the control is also indicative of enhanced recombination. Trukhanov *et al.* demonstrated a model where V_{OC} decreased with doping of optimised cells.³⁵ Indeed, if the excess of charge carriers at the interface is higher than the concentration of those charges intrinsically generated in the bulk (and therefore majorly responsible for the built-in field), extensive recombination takes place, resulting in a loss of V_{OC} .

As discussed in Section 1.4.4, an S-shaped *J-V* curve is a typical observation in freshly produced cells incorporating ZnO as an electron-collecting layer, where the oxygen doping produces numerous charge traps, but this effect is reversible by light or thermal treatment. The S-shapes of PDHS-incorporating cells did not show reversible behaviour, thus the hindered charge transport is associated with the introduction of the new layers, not with the intrinsic properties of ZnO. This observation is also supported by the values of electron injection at 1.4 V. Compared to the typical values of electron injection in the control sample (150 mA/cm²), these are very low and equal to 1-4 mA/cm² for PDHS and 0.5-1 mA/cm² for PDHS-FUL cells.

Drastic changes in the electron injection and extraction efficiencies at the interface can be justified by the electronic incoherence between the ETL and the PAL. Indeed, this hypothesis was proven by ultraviolet photoelectron spectroscopy (UPS) measurements. The work function of ZnO with PDHS polymer deposited onto it was 3.7 eV, and that of ZnO with

PDHS-FUL 4.7 eV, whereas the work function of bare zinc oxide was 3.4 eV. The increase in work function created an extraction barrier for electrons (Figure 3.30) that resulted in charge accumulation at the interface and, consequently, S-shape generation.

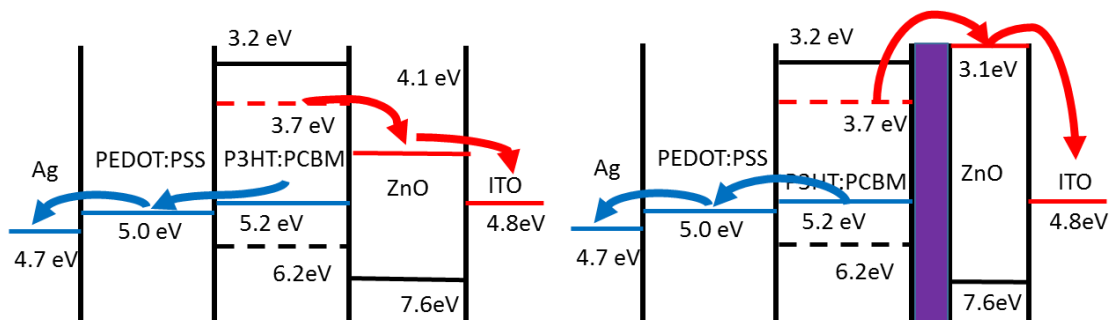


Figure 3.30. Electronic levels of the corresponding layers in the studied devices. Left: control device. Right: device with PDHS-FUL interfacial layer, represented as purple insert.

Evidently, the addition of the fullerene moiety onto the chain end of PDHS has a negative effect on the work function of the electron extracting layer even at a thickness as low as several nm. Indeed, Schulz *et al.* have shown that layer by layer deposition of C60 on zinc oxide increases its work function from 3.7 to 4.4 eV until it reaches the work function of pristine C60.³⁶ In agreement with these findings, linkage of the C60 moiety to the polymer chain also increased the work function, but this increase has a detrimental effect on electron transfer between the PAL and ZnO.

3.7 Time-resolved studies of devices with PDHS and PDHS-FUL interlayers

If the electronic incoherence is the only reason for loss of performance in cells incorporating PDHS and PDHS-FUL layers, only recombination and extraction processes would be affected, in agreement with Equation 1.5 (Section 1.6):

According to Equation 1.5, the external quantum efficiency (EQE) depends on parallel processes, such as photon absorption, exciton dissociation, charge separation and extraction. Since the thickness of the PAL is equivalent in all samples, the effect of absorption can be removed from this equation. Subsequently, exciton dissociation and separation mostly depend of the bulk morphology which can be affected by the substrate layer and thus would depend on incorporation of the PDHS-FUL layer.^{37,38} Furthermore, extraction and recombination, as discussed previously in Section 1.4.4, are directly influenced by electrical incoherence between the layers and, to some extent, by bulk morphology of the PAL.

Thus, looking into these processes separately, it is possible to distinguish if electrical incoherence is the only factor decreasing the device performance. Both exciton dissociation and separation occur in optimised cells on the femto to picosecond timescale and can be detected by transient absorption spectroscopy (TAS), independent of what their fate is: extraction, recombination or decay. Extraction and recombination, on the other hand, are voltage-dependent micro to millisecond processes and can be analysed by time-resolved electrical measurements, where transient photocurrent (TPC) is measured at short circuit and transient photovoltage (TPV) is determined under open circuit.

3.7.1 Exciton generation, dissociation and separation

As discussed in Sections 1.6 and 2.10.1, global fitting of the experimental TA spectrum yields three evolution-associated differential spectra (EADS) with respective fits, consisting of separate species-associated differential spectra (SADS), representing contribution of each excited state. Thus, the experimental spectrum of P3HT:PCBM in this work, typically, was represented by the following functions:

- Photobleach of the ordered phase of P3HT (PB_o);
- Photobleach of the amorphous phase of P3HT (PB_a);
- Localised singlet in the amorphous phase of P3HT (S_a);
- Delocalised singlet in the ordered phase of P3HT (S_o);
- Localised polaron (P_a);
- Delocalised polaron (P_o);
- Polaron pair (PP).

As shown in Figure 3.31, introduction of the PDHS-FUL layer has little effect on the charge generation efficiency. Immediately after excitation, the most intense absorption peak is observed at approximately 1.25 eV. This peak is attributed to the immediate amorphous polaron formation at the donor/acceptor interface, typical for optimised P3HT:PCBM solar cells.^{38–40} Thus, the ultrafast charge yield for PDHS-FUL cells has been calculated as 84.5%, whereas a total final yield of the charges that can be extracted after nanoseconds is 76%. Total charge yield agrees with that in control samples, where P3HT:PCBM layer was deposited directly onto ZnO. Thus, total charge yield was 83%, although it may vary in different spots from 65% to 85%. On the other hand, from Figure 3.31, it is clear that ultrafast charge generation is much more efficient in PDHS-FUL cells when compared to control samples (84.5% and 60.8%, respectively).

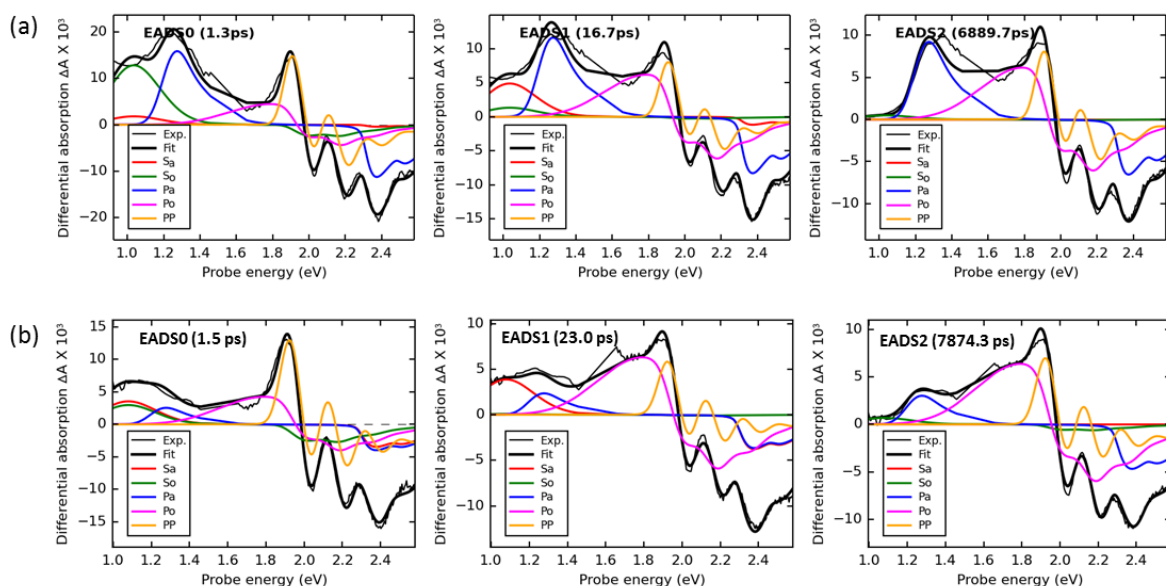


Figure 3.31. EADS of (a) PDHS-FUL device and (b) control device, as obtained from a global analysis of experimental TA spectra using a 3 sequential steps model (thin solid curves, fitted lifetimes are given in the legends), spectral fits to the EADS (thick solid curves) and contributions to fits from polaron pair, localised and delocalised singlet exciton and polaron states with their respective bleach contributions (negative differential absorption).

In a typical P3HT:PCBM cell, the build-up of charged states is normally observed within picoseconds after excitation. In a bulk heterojunction morphology the domain size of P3HT varies, therefore not all charges are generated immediately at the interface, but the excitons formed at a distance of more than 4 nm from the interface have to diffuse to it to dissociate.³⁹

Interestingly, in PDHS-FUL cells this is not the case. A decrease in the total number of polarons mainly occurs due to the loss of localised polarons (P_a) in the amorphous phase. Since ultrafast charge generation is a direct indicator of the PAL morphology, in PDHS-FUL most of the domains appearing to be less than 4 nm size, allowing for efficient exciton dissociation.³⁹ On the other hand, the localised domains of such size would compromise charge hopping, which needs an interconnected network of domains. Thus, the decrease in the total yield of charges available for extraction hundreds of picoseconds after excitation is an indirect observation of enhanced recombination of the free charges with those trapped within localised domains, in agreement with Howard *et al.*³⁸ High yield of ultrafast polarons in such isolated domains does not contribute to the current in photovoltaic devices and thus, is indicative of unfavourable domain distribution in PDHS devices.

Evolution of excited state concentration is illustrated in Figure 3.32, showing that the initial concentrations of delocalised polarons (P_o) and singlets (S_o) in both samples are similar (0.15 for singlet and 0.35 for polarons, respectively).

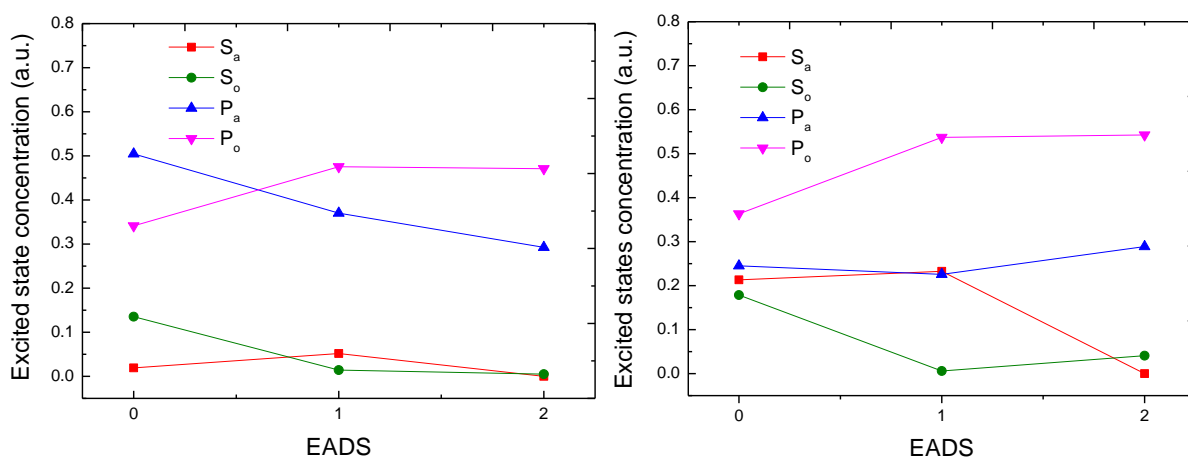


Figure 3.32. Evolution of excited states concentration according to their respective EADS in PDHS-FUL cells (a) and control cells (b): localised singlet excitons (S_a , red) and polarons (P_a , blue), delocalised singlet excitons (S_o , green) and polarons (P_o , magenta).

The main difference between two samples (with and without interlayer) is in the amorphous phase of P3HT. Exciton dissociation efficiency in the amorphous phase of PDHS-FUL cells is enhanced since immediately after excitation all singlets are separated into charges. Further, excess generated charges recombine, thus decreasing the total number of localised polarons (P_a).

Without more in-depth studies, it is difficult to say with absolute certainty why the PDHS-FUL layer has such an effect on the morphology of the layer. The main reason for the optimal morphology in PDHS-FUL cells could be a reduction in surface energy of ZnO from 83 mN/m to 57 mN/m (as seen from contact angle measurements), which is closer to that of the PAL components (24 mN/m for P3HT and 38.2 mN/m for PCBM),⁴¹ thus resulting in enhanced wettability of PDHS-FUL with the PAL and improving film qualities. Furthermore, upon deposition, PCBM would show more affinity to higher surface energy layer and vertically segregate towards the respective electrode.

Surface morphology of the PDHS layer might also play an important role. As seen from SEM images in Figure 3.23a and b, PDHS forms very rough films, therefore the roughness induces domain formation in the active layer.

Thus, TAS measurements have proved that charge generation and exciton dissociation are affected by introduction of the PDHS-FUL layer, however not enough to explain the decrease in current density in the sample with interlayer.

3.7.2 TPC and TPV

Clearly, from Equation 1.5, if absorption, exciton dissociation and polaron pair separation were not affected, the only compromised process was extraction. This is in agreement with

the results of UPS which showed that the work function of ZnO increased too much for efficient electron extraction from PCBM.

It has been shown that the fill factor is a sum of two microsecond scale processes: extraction and recombination.⁴² In a typical pristine P3HT:PCBM solar cell, extraction of 50% of the generated charges occurs as fast as 1-5 μs , whereas recombination can take milliseconds.⁴³ Evidently, if these two processes happen within the same timescale, recombination would prevail over extraction and therefore decrease the fill factor and the current density.

Transient photocurrent (TPC) and photovoltage (TPV) measurements were employed to evaluate the extraction and recombination rates in PDHS-FUL and control cells (Figure 3.33). The TPC measurements show the loss of extracted charges. Compared to $8.6 \times 10^{-9} \text{ q/cm}^3$ charge density in the control sample, PDHS-FUL devices show charge density of only $1.9 \times 10^{-9} \text{ q/cm}^3$. Less charges are extracted faster, therefore 50% of generated charges in PDHS-FUL are extracted in 670 ns, whereas in the control sample extraction of 50% of generated charges takes 1.8 μs .

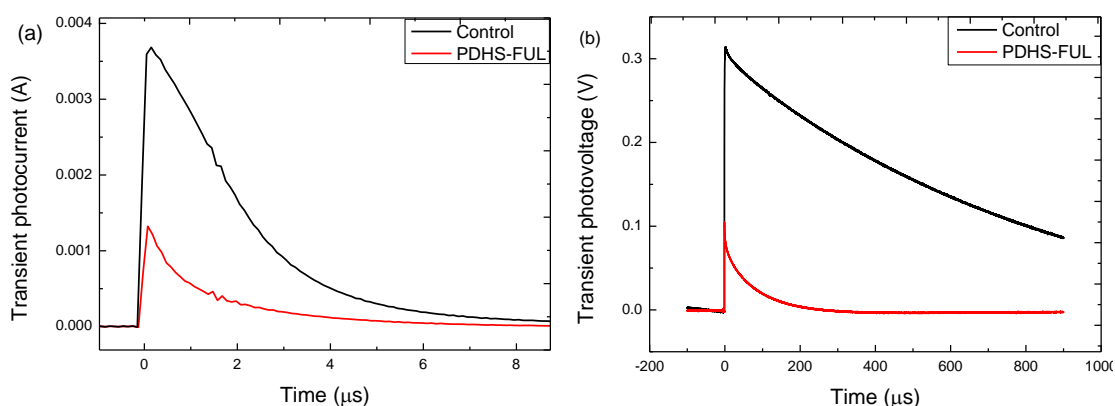


Figure 3.33. Transient photocurrent (a) and photovoltage (b) traces for control (black) and PDHS-FUL (red) cells.

Furthermore, the recombination rate (as obtained from TPV) is much higher in PDHS-FUL devices. 50% of charges recombine within 0.3 μs , whereas in the control sample recombination takes 140 μs . Thus, in PDHS-FUL devices, the recombination rate is higher than the extraction rate, indicating that recombination processes prevail over extraction. Fast recombination could also be observed at much shorter timescales in transient absorption spectroscopy, although to a lesser extent. This is in agreement with the S-shaped J - V curve, where both fill factor and current density reflect the enhanced recombination.

3.8 Conclusions and future work for PDHS and PDHS-FUL materials

Although small molecule self-assembling materials (SAM) based on dihydroxybenzene ligands have been demonstrated to be good interfacial layers and enhance electron collection by ZnO,⁴⁴ in this work it has been shown that polymers based on the dihydroxybenzene ligand are not suitable for application as an interlayer between zinc oxide and the PAL. Incorporated into the cells, both poly(3,4-dihydroxystyrene) and poly(3,4-dihydroxystyrene)-fullerene have a detrimental effect on the initial performance of the photovoltaic devices, creating S-shaped *J-V* curves. Moreover, PDHS-FUL devices gave negligible efficiencies, essentially being a diode, whereas PDHS devices demonstrated some photovoltaic behaviour. As shown by UPS measurements, the major reason for this is the increase in work function of the ZnO electron collecting layer (3.7 eV for PDHS and 4.7 eV for PDHS-FUL). This increase resulted in ZnO being incapable of extracting the majority of electrons, which got trapped at the interface. PDHS-FUL devices have recombination rates of less than a microsecond so that, even in a pristine cell, recombination prevails over extraction. Interestingly, as indirectly observed from transient absorption spectroscopy, PDHS-FUL had a slightly negative effect on the nanomorphology of the photoactive blend. High ultrafast charge yield in PDHS-FUL cells was indicative of increased number of isolated PCBM domains less than 4 nm size and matrix-dissolved PCBM molecules. Such domains and isolated molecules lead to enhanced non-geminate recombination and the charges generated at the interface do not contribute to the current density, but decay or recombine if they encounter their mobile counterparts. Accordingly, total charge yield (76%) is lower than the ultrafast charge yield (84.5%) that confirms the enhanced recombination.

Although PDHS and PDHS-FUL polymers were not suitable for application in organic solar cells, the knowledge obtained during characterisation and study of these materials can be further used in designing new materials. For example, blend nanomorphology and charge generation can be tuned in the PAL deposited onto substrates with different surface energies, thus other interfacial materials can be employed, should they have matching electronic levels and allow good extraction of electrons.

Since the fullerene plays an important role in establishing electronic coherence between the PAL and ZnO, the binding 3,4-dihydroxybenzene ligand can be incorporated as a pendant group into fullerene main chain polymers, such as reported by Hiorns *et al.*⁴⁵

3.9 References

- (1) Cheng, X.; Li, F.; Zhao, Y. *J. Mol. Struct.* **2009**, *894* (1-3), 121–127.
- (2) Wang, B.; Nagase, S.; Zhao, J.; Wang, G. *J. Phys. Chem. C* **2007**, *111* (13), 4956–4963.
- (3) Yong, Y.; Song, B.; He, P. *J. Phys. Chem. C* **2011**, *115* (14), 6455–6461.
- (4) Sun, L.; Li, G.-Z.; Xu, M.-H.; Li, X.-J.; Li, J.-R.; Deng, H. *Zeitschrift Fur Anorg. Und Allg. Chemie* **2012**, *638* (7-8), 1200–1203.
- (5) Gody, G.; Maschmeyer, T.; Zetterlund, P. B.; Perrier, S. *Nat. Commun.* **2013**, *4*, 2505.
- (6) Lai, J. T.; Filla, D.; Shea, R. *Macromolecules* **2002**, *35* (18), 6754–6756.
- (7) Gondi, S. R.; Vogt, A. P.; Sumerlin, B. S. *Macromolecules* **2007**, *40* (3), 474–481.
- (8) Inglis, A. J.; Stenzel, M. H.; Barner-Kowollik, C. *Macromol. Rapid Commun.* **2009**, *30* (21), 1792–1798.
- (9) Kulkarni, S.; Schilli, C.; Grin, B.; Mueller, A. H. E.; Hoffman, A. S.; Stayton, P. S. *Biomacromolecules* **2006**, *7* (10), 2736–2741.
- (10) Lowe, A. B.; Sumerlin, B. S.; Donovan, M. S.; McCormick, C. L. *J. Am. Chem. Soc.* **2002**, *124* (39), 11562–11563.
- (11) Kusolkamabot, K.; Sae-ung, P.; Niamnont, N.; Wongravee, K.; Sukwattanasinitt, M.; Hoven, V. P. *Langmuir* **2013**, *29* (39), 12317–12327.
- (12) Sumerlin, B. S.; Lowe, A. B.; Stroud, P. A.; Zhang, P.; Urban, M. W.; McCormick, C. L. *Langmuir* **2003**, *19* (14), 5559–5562.
- (13) Moad, G.; Chong, Y. K.; Postma, A.; Rizzardo, E.; Thang, S. H. *Polymer (Guildf)*. **2005**, *46* (19), 8458–8468.
- (14) Cauet, S. I.; Wooley, K. L. *J. Polym. Sci. Part A-Polymer Chem.* **2010**, *48* (12), 2517–2524.
- (15) Wood, M. R.; Duncalf, D. J.; Findlay, P.; Rannard, S. P.; Perrier, S. *Aust. J. Chem.* **2007**, *60* (10), 772–778.
- (16) Abreu, C. M. R.; Mendonca, P. V.; Serra, A. C.; Coelho, J. F. J.; Popov, A. V.; Gryn'ova, G.; Coote, M. L.; Guliashvili, T. *Macromolecules* **2012**, *45* (5), 2200–2208.
- (17) Daly, W. H.; Moulay, S. *J. Polym. Sci. Symp.* **1986**, No. 74, 227–242.
- (18) Bernard, J.; Branger, C.; Beurroies, I.; Denoyel, R.; Blanc, S.; Margaillan, A. *Polymer (Guildf)*. **2010**, *51* (12), 2472–2478.
- (19) An, Y.-Z.; Chen, C.-H. B.; Anderson, J. L.; Sigman, D. S.; Foote, C. S.; Rubin, Y. *Tetrahedron* **1996**, *52* (14), 5179–5189.
- (20) Ganapathi, P. S.; Friedman, S. H.; Kenyon, G. L.; Rubin, Y. *J. Org. Chem.* **1995**, *60* (10), 2954–2955.
- (21) Gareis, T.; Köthe, O.; Daub, J. *European J. Org. Chem.* **1998**, 1549–1557.

- (22) Dong, X.-H.; Zhang, W.-B.; Li, Y.; Huang, M.; Zhang, S.; Quirk, R. P.; Cheng, S. Z. D. *Polym. Chem.* **2012**, 3 (1), 124.
- (23) Dong, X.; Zhang, W.; Li, Y.; Huang, M.; Zhang, S.; Quirk, R. P. **2011**, 1–22.
- (24) Zhang, W.-B.; He, J.; Dong, X.; Wang, C.-L.; Li, H.; Teng, F.; Li, X.; Wesdemiotis, C.; Quirk, R. P.; Cheng, S. Z. D. *Polymer (Guildf)*. **2011**, 52 (19), 4221–4226.
- (25) Lawson, G. E.; Liu, B.; Bunker, C. E.; Sun, Y. P. *Preparation and characterization of fullerene-based copolymers and polymer-bound fullerene materials in "Fullerenes, Recent Advances in the Chemistry and Physics of Fullerenes and Related Materials"* ed. K. M. Kadish; Ruoff, R. S. The Electrochemical Society, Pennington, NJ, 1996; Vol. 96.
- (26) Ma, B.; Lawson, G. E.; Bunker, C. E.; Kitaygorodskiy, A.; Sun, Y. P. *Chem. Phys. Lett.* **1995**, 247 (1-2), 51–56.
- (27) Sun, Y. P.; Lawson, G. E.; Bunker, C. E.; Johnson, R. A.; Ma, B.; Farmer, C.; Riggs, J. E.; Kitaygorodskiy, A. *Macromolecules* **1996**, 29 (26), 8441–8448.
- (28) Kuzmany, H.; Winkler, R.; Pichler, T. *J. Physics-Condensed Matter* **1995**, 7 (33), 6601–6624.
- (29) Chamberlain, T. W.; Camenisch, A.; Champness, N. R.; Briggs, G. A. D.; Benjamin, S. C.; Ardavan, A.; Khlobystov, A. N. *J. Am. Chem. Soc.* **2007**, 129 (27), 8609–8614.
- (30) Mathias, L. J.; Lewis, C. M.; Wiegel, K. N. *Macromolecules* **1997**, 30 (19), 5970–5975.
- (31) Goldstein, J. *Scanning Electron Microscopy and X-ray Microanalysis: Third Edition*; Springer US, 2003.
- (32) Gregory, A. unpublished, 2015.
- (33) Saive, R.; Mueller, C.; Schinke, J.; Lovrincic, R.; Kowalsky, W. *Appl. Phys. Lett.* **2013**, 103 (24), 243303.
- (34) Kumar, A.; Sista, S.; Yang, Y. *J. Appl. Phys.* **2009**, 105 (9), 094512.
- (35) Trukhanov, V. A.; Bruevich, V. V.; Paraschuk, D. Y. *Phys. Rev. B* **2011**, 84 (20), 205318.
- (36) Schulz, P.; Kelly, L. L.; Winget, P.; Li, H.; Kim, H.; Ndione, P. F.; Sigdel, A. K.; Berry, J. J.; Graham, S.; Brédas, J.-L.; Kahn, A.; Monti, O. L. A. *Adv. Funct. Mater.* **2014**, 24 (46), 7381–7389.
- (37) Bulliard, X.; Ihn, S.-G.; Yun, S.; Kim, Y.; Choi, D.; Choi, J.-Y.; Kim, M.; Sim, M.; Park, J.-H.; Choi, W.; Cho, K. *Adv. Funct. Mater.* **2010**, 20 (24), 4381–4387.
- (38) Howard, I.; Mauer, R.; Meister, M.; Laquai, F. *J. Am. Chem. Soc.* **2010**, 132 (42), 14866–14876.
- (39) Guo, J.; Ohkita, H.; Bente, H.; Ito, S. *J. Am. Chem. Soc.* **2009**, 131 (46), 16869–16880.
- (40) Lioudakis, E.; Alexandrou, I.; Othonos, A. *Nanoscale Res. Lett.* **2009**, 4 (12), 1475–1480.

- (41) Watts, B.; Belcher, W. J.; Thomsen, L.; Ade, H.; Dastoor, P. C. *Macromolecules* **2009**, *42* (21), 8392–8397.
- (42) Bartesaghi, D.; Pérez, I. D. C.; Kniepert, J.; Roland, S.; Turbiez, M.; Neher, D.; Koster, L. J. A. *Nat. Commun.* **2015**, *6*, 7083.
- (43) Deibel, C.; Dyakonov, V. *Reports Prog. Phys.* **2010**, *73* (9), 96401.
- (44) Hau, S. K.; Cheng, Y.-J.; Yip, H.-L.; Zhang, Y.; Ma, H.; Jen, A. K.-Y. *ACS Appl. Mater. Interfaces* **2010**, *2* (7), 1892–1902.
- (45) Hiorns, R. C.; Cloutet, E.; Ibarboure, E.; Vignau, L.; Lemaitre, N.; Guillerez, S.; Absalon, C.; Cramail, H. *Macromolecules* **2009**, *42* (10), 3549–3558.

CHAPTER 4 CROSS-LINKED LAYERS

4.1 Introduction

XPS measurements showed (Section 3.5.3) that the binding strength of poly(3,4-dimethoxystyrene) (PDMS) and its fullerene derivative, PDMS-FUL, to ZnO was not sufficient to withstand washing and the layer could not be deposited as a monolayer, as initially intended. On the other hand, PDMS demonstrated thermosetting behaviour, with a cross-linking temperature ranging from 120 to 140 °C. Consequently, this property was explored as potentially beneficial for stabilisation of the photoactive layer (PAL)/electron-transporting layer (ETL) interface.

Previous reports have shown various approaches to interface engineering as discussed in Section 3.1. Interestingly, among them there are reports about cross-linked layers used for stabilisation. One of the main advantages of cross-linked interfaces is that they allow same-solvent casting of the subsequent layers and a tighter interface between the ETL and PAL. One example is a fullerene derivative functionalised with a trichlorosilyl moiety that self-assembled on the surface of the TiO_x nanoparticles (NPs) and cross-linked with the materials in the PAL. The silyl groups readily bound to residual hydroxyl groups on the outer shell of the TiO_x, decreasing their contribution to PAL erosion.¹ In organic light-emitting device (OLED) technology, cross-linkable siloxane layers have been widely used for stabilisation of the anode/hole transport layer interface, improving durability and efficiency of these devices.² The main advantage of such layers is that cross-linking occurs spontaneously and does not require any illumination or thermal treatment.

Other example by Cheng *et al.* involves the use of a PCBM-dendron ester functionalised with two styryl groups that thermally cross-link at 160 °C. The cross-linked film had various positive effects on the interface, including enhanced exciton dissociation, passivation of local shunts at the ZnO interface and decreased contact resistance due to better electronic coherence between the PAL and the cross-linked layer. The devices incorporating this cross-linked layer not only had enhanced efficiency, but also improved stability under illumination in the air.^{3,4} The same group reported a similar PCBM-dendron layer, where an oxetane moiety served for cross-linking. Moreover, this moiety was capable of binding to the TiO_x surface, even further stabilising the contact between ETL and PAL.⁵ Unfortunately, resistance of the new layers to thermal stress was not studied.

Thus, cross-linking layers have a great potential for application in stabilisation of the ETL/PAL interface, also improving performance of the devices. To this end, PDMS has several advantages due to its facile polymerisation by RAFT, discussed in Section 3.3.2, and intrinsic cross-linking property at temperatures as low as 110-140 °C (Section 3.4).

4.2 Contact angles

DSC measurements (Section 3.4) demonstrated thermosetting behaviour for PDMS polymers, but not for PDMS-FUL polymers. This was attributed to the wrapping of the PDMS chains around the fullerene molecules, which prevented their cross-linking with the neighbouring chains. However, previously in our group, it has been demonstrated that thermal behaviour of the thin films might be different from that of bulk material.⁶ Contact angle measurements were employed to verify if PDMS-FUL polymers could also be cross-linked. For this, a PDMS-FUL layer was deposited directly onto a glass substrate from toluene solution and, after drying at room temperature, heated for 1 h at 140 °C. Then, the sample was rested overnight and washed with toluene several times. A cross-linked layer should be able to withstand the washing and thus, its contact angle should remain unchanged. Contact angle measurements were carried out before heating, after heating and after washing (Figure 4.1). Contact angle of the glass substrate was 8°.

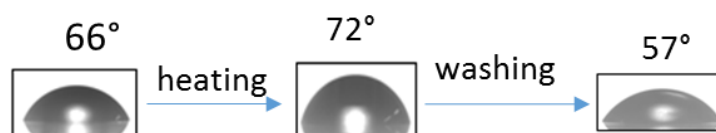


Figure 4.1. Contact angles of PDMS-FUL layer deposited on glass before heating, after heating and after washing with toluene.

Evidently, heating of PDMS-FUL caused rearrangement of the polymer chains so that more hydrophobic moieties were pushed to the surface, leading to an increase in the contact angle. Washing of the layer with toluene resulted in a decrease in the contact angle to 57°, which was lower than the contact angle of the pristine layer. However, this was far from the contact angle of bare glass surface, indicating that the polymer layer (in some form) remained on the substrate, although no confident conclusions could be made about the thickness of the layer. Thus, PDMS-FUL can also be cross-linked in a thin-film.

Further, the contact angles of PDMS and PDMS-FUL deposited onto a ZnO surface were studied (Figure 4.2). SEM measurements (Section 3.5.1) showed that zinc would adhere to PDMS surface, although XPS measurements proved that PDMS adhesion to ZnO was not strong enough to withstand solvent treatment. In any case, there is interaction of the polymer with the substrate, therefore the thermal behaviour might change, depending on the substrate.

As seen from Figure 4.2, heating PDMS induces cross-linking and reorganisation of the molecules so that more hydrophobic moieties are pushed to the surface. This agrees with results, observed previously for PDMS-FUL deposited onto glass. In this case, however,

there was no clear difference between the contact angles of pristine and cross-linked PDMS-FUL. Both PDMS and PDMS-FUL demonstrated similar hydrophobic behaviour with contact angles of 85° and 83°, respectively. Washing of the layers with toluene led to a decrease in contact angles to 70° and 72° for PDMS and PDMS-FUL, respectively.

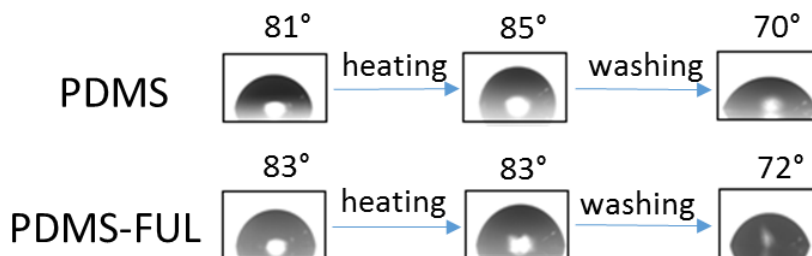


Figure 4.2. Contact angles of PDMS and PDMS-FUL layer deposited on ZnO before heating, after heating and after washing with toluene and bare ZnO before and after washing.

In Section 3.4, a hypothesis about the nature of cross-linking in PDMS polymers was made. Formation of new ether bonds was observed by FTIR (Figure 3.17) in cross-linked samples along with the loss of the methoxy stretching vibration, suggesting that cross-linking occurs by means of methoxy groups reacting with the aromatic rings of the neighbouring chains. During cross-linking the methoxy groups are lost.

Computer simulations (details are given Section 2.1) of a PDMS dimer with two pendant methoxy groups yielded a partition coefficient (logP) of 5.396, whereas PDMS where one methoxy group formed a new ether bond with the benzene ring of the next monomer had a logP of 4.415 (Figure 4.3). More hydrophobic compounds have higher logP values, thus LogP is indicative of the hydrophobicity of the molecule and may serve as an indirect explanation why upon cross-linking and washing the contact angles have decreased.⁷

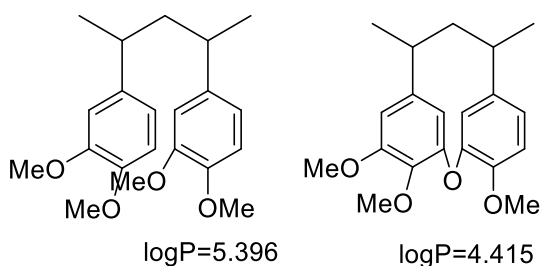


Figure 4.3. Simulations of logP of PDMS dimer and PDMS dimer where one methoxy group was involved in formation of a new ether bond with a benzene ring of the neighbouring monomer.

Generally, both PDMS and PDMS-FUL have proven capable of thermal cross-linking and could withstand washing with toluene. However, the fact that the contact angles did not decrease after heating indicates that cross-linking was not complete within the film and a

layer of PDMS or PDMS-FUL on the surface did not cross-link. Unfortunately, it is difficult to draw any conclusions about how the layer thickness changes with washing, therefore further measurements were performed, such as UV-Vis absorbance, as discussed in the following sections.

4.3 Absorbance measurements

The absorbance measurements were carried out to estimate the amount of non-cross-linked film that was washed away. For this, the PDMS and PDMS-FUL layers were deposited onto ZnO from acetone solutions of different concentrations: 1 mg/ml, 5 mg/ml and 10 mg/ml. The layers were heated at 140 °C for 1 h and subsequently washed with acetone to indirectly estimate the thickness of the remaining films (Figure 4.4).

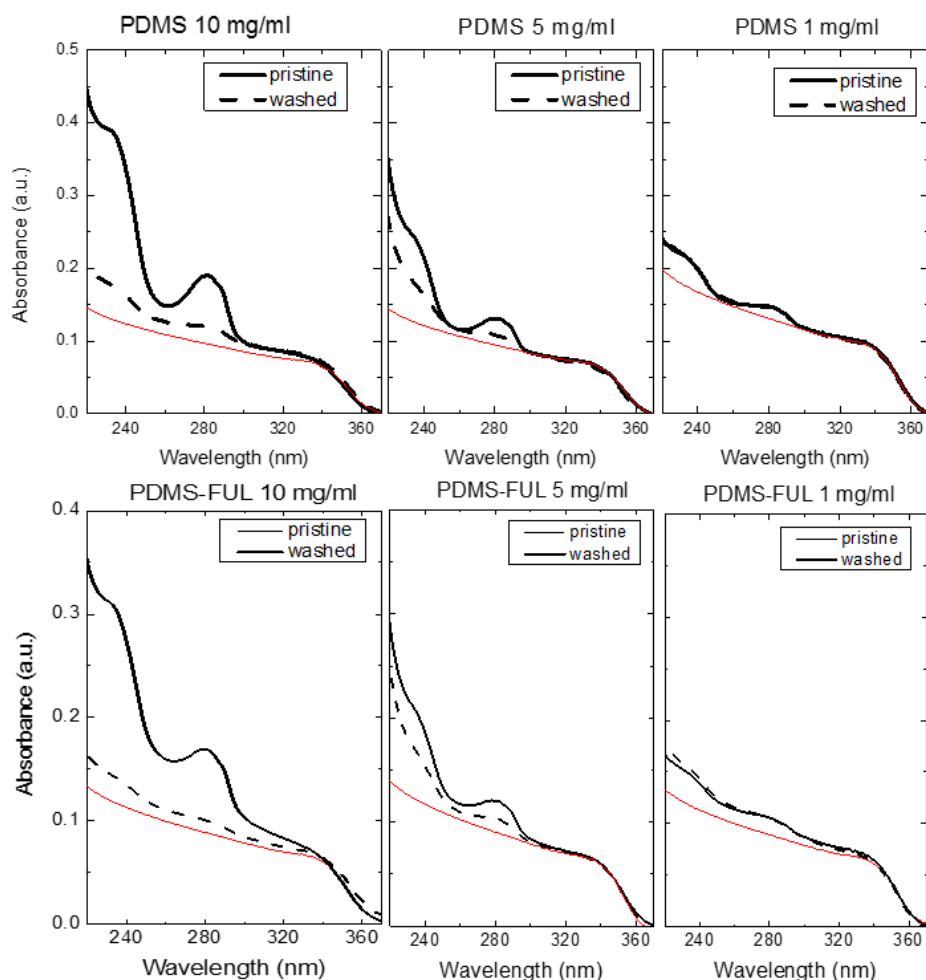


Figure 4.4. UV-Vis absorbance spectra of PDMS and PDMS-FUL layers, deposited onto ZnO, from acetone solutions of different concentrations. ZnO spectrum is shown as thin red line.

As seen from Figure 7, the extent of cross-linking in the films depends on the film thickness, *i.e.* on the solution concentration. Thus, simple measurements according to Equation 4.1 yielded the percentage of the film remaining after cross-linking and washing with acetone (Table 4.1):

Percentage of the film remaining after cross-linking and washing,

$$\% \text{ of remaining film} = [(A_{\text{washed}} - A_{\text{ZnO}}) / (A_{\text{pristine}} - A_{\text{ZnO}})] \times 100\% \quad (\text{Equation 4.1})$$

where A_{washed} stands for absorbance of the washed film after washing, A_{pristine} – absorbance of the pristine film and A_{ZnO} – absorbance of the ZnO substrate, all at 283 nm. Furthermore, corresponding hypothetical solution concentrations are shown in Table 4.1, although these are not real values and serve only for the visualisation purposes.

Table 4.1. Data about the PDMS-FUL film thickness remaining on ZnO after cross-linking and washing (average for 3 films), based on the absorbance intensity.

Solution concentration	% of the remaining film thickness after cross-linking		Absorbance at 283 nm ^b
	Remaining ^a	Washed Away ^a	
PDMS 10 mg/ml	20% (2 mg/ml)	80% (8 mg/ml)	0.108
PDMS 5 mg/ml	46% (2.3 mg/ml)	54% (2.7 mg/ml)	0.111
PDMS 1 mg/ml	100% (1 mg/ml)	0%	0.105
PDMS-FUL 10 mg/ml	23% (2.3 mg/ml)	76% (7.6 mg/ml)	0.105
PDMS-FUL 5 mg/ml	58% (2.9 mg/ml)	42% (2.1 mg/ml)	0.114
PDMS-FUL 1 mg/ml	100% (1 mg/ml)	0%	0.108

(a) Corresponding solution concentration is shown in brackets.

(b) Absorbance at 283 nm is proportional to the layer thickness.

The thickness of remaining film can be represented as a corresponding solution concentration that would result in 100% cross-linked films (Table 4.1). Thus, it can be suggested that the layer deposited from 2-3 mg/ml solution would be completely cross-linked. On the other hand, part of the film that is not cross-linked is washed off by the solvent (Figure 4.5). PDMS and PDMS-FUL are soluble in xylene, the solvent from which the PAL is deposited, therefore if the PAL is deposited onto a cross-linked PDMS or PDMS-FUL layer without prior washing, the molecules of PDMS or PDMS-FUL would intermix with the PAL blend (Figure 4.5). Thus, both cross-linked and intermixed portions of PDMS and PDMS-FUL would be important for understanding how the layers affect device performance and stability.

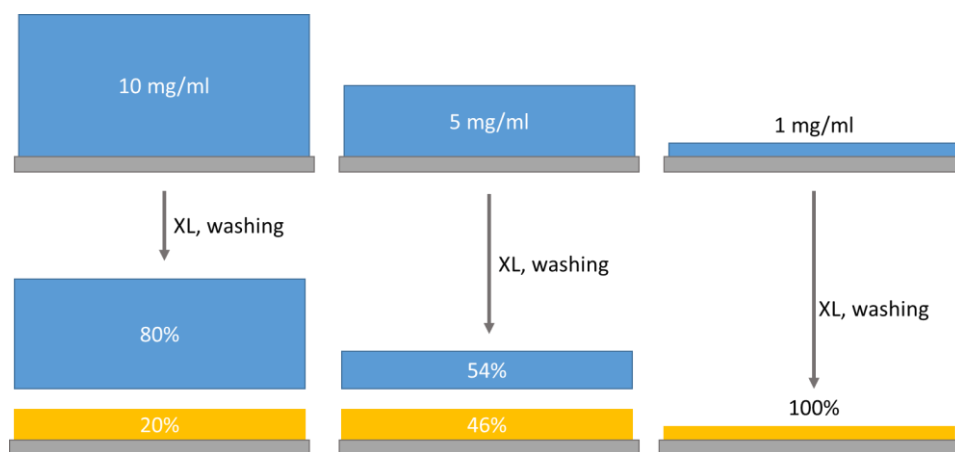


Figure 4.5. Schematic representation of resulting film thicknesses upon cross-linking (XL) and washing in PDMS layers deposited from solutions of different concentrations.

4.4 Cross-linked PDMS layer

To understand what effect PDMS layers have on the initial efficiency and thermal stability of the device in terms of interface stabilisation and bulk effect of the washed molecules, PDMS was incorporated into devices as a penetrating interfacial layer between ZnO and the photoactive layer (Figure 4.6). The layer was treated at 140 °C for 1 h to cross-link and left to rest overnight prior to PAL deposition. Again, the resulting layer thickness was varied by depositing the layers from solutions of different concentrations: 10 mg/ml, 5 mg/ml and 1 mg/ml. Initial photovoltaic parameters for the cells with PDMS layers of different thicknesses are given in the Table 4.2.

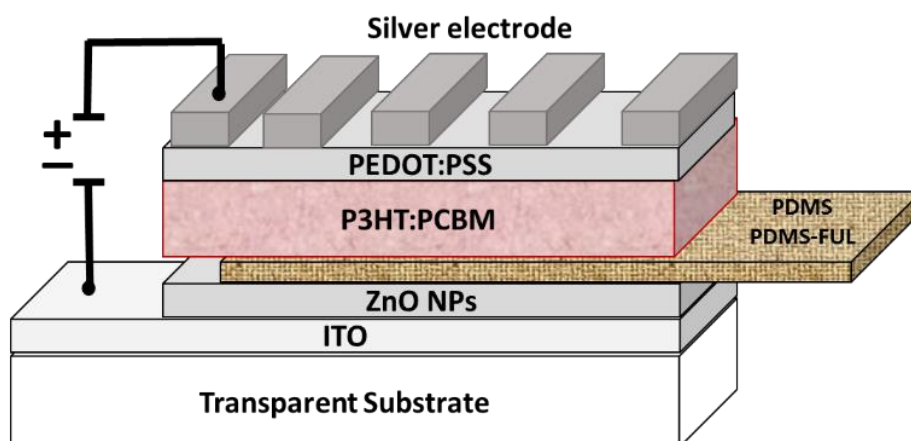


Figure 4.6. Schematic representation of the inverted architecture stack used for the study of effect of cross-linked PDMS or PDMS-FUL polymer as an interfacial layer on the thermal stability of the cells.

Table 4.2. Initial photovoltaic values obtained for solar cells incorporating cross-linked PDMS layers, deposited from solutions of different concentrations, as interfacial layers between ZnO and PAL (average for 12-16 devices).

Sample	Absorbance at $\lambda = 283$ nm ^a , a.u.	Intermixed PDMS molecules ^a	J_{sc} , mA/cm ²	V_{oc} , mV	FF	η , PCE, %
Control (no interlayer)	0.100	-	8.93	556	0.63	3.14
10 mg/ml	0.108	80% (8 mg/ml) ^b	8.97	559	0.64	3.20
5 mg/ml	0.111	54% (2.73 mg/ml) ^b	9.11	559	0.65	3.31
1 mg/ml	0.105	0%	9.12	547	0.63	3.14

(a) Obtained from absorbance studies, as discussed in Section 4.3.

(b) Corresponding solution concentration is shown in brackets.

As seen from Table 4.2, the power conversion efficiency (PCE) of all PDMS-incorporating devices is equal to the control (in PDMS 1 mg/ml) or higher (in PDMS 5 mg/ml and 10 mg/ml). The maximum average PCE value of 3.31% was observed in the PDMS 5 mg/ml device. This increase in PCE is associated with an enhancement of all photovoltaic parameters, where the fill factor (FF) and open circuit voltage (V_{oc}) values correlate with the thickness of the PDMS layer remaining after washing. Thus, the highest FF of 0.65 and V_{oc} of 559 mV is observed in PDMS 5 mg/ml where the absorbance value is the highest (0.111). Accordingly, the lowest FF in PDMS 1 mg/ml devices is equal to that in control samples (0.63) as there is not a sufficient amount of cross-linked interfacial material to make a difference to the electronic properties of the device.

The short circuit current density (J_{sc}) benefits from the introduction of the PDMS layer since the J_{sc} values for all PDMS-incorporating devices are higher than those in the control (8.93 mA/cm²). However, with the increase of PDMS solution concentration from 1 mg/ml to 10 mg/ml, the J_{sc} is decreasing which is associated with the higher content of PDMS molecules intermixed with the photoactive blend. Thus, the lowest J_{sc} of 8.97 mA/cm² is observed for PDMS 10 mg/ml devices, where 80% (8 mg/ml) of the PDMS layer is intermixed with the active blend. Accordingly, the PDMS 1 mg/ml devices with only a thin cross-linked layer and no intermixed PDMS molecules have higher J_{sc} (9.12 mA/cm²) than the control. Since the J_{sc} value mostly reflects the quality of the blend nanomorphology, these data suggest that the intermixed PDMS molecules have a slightly negative effect on the domain distribution in the blend.

Recalling the external quantum efficiency (EQE) equation (Section 1.6), the J_{SC} can be represented as a combined result of several processes, such as photon absorbance, exciton dissociation, charge separation and extraction. Exciton dissociation and charge separation are morphology-dependent processes, and in the absence of tertiary agents in the active blend, they are not majorly affected (in PDMS 1 mg/ml devices). Thus, charge extraction is the important process that benefits from the introduction of a cross-linked PDMS layer. Indeed, this suggestion is supported by enhanced fill factors in devices with cross-linked layers. In PDMS 10 mg/ml and 5 mg/ml, enhanced extraction in the cross-linked PDMS layers competes with the bulk effects of the intermixed PDMS molecules.

Further, the effect of the PDMS layers on the device stability was studied. The devices were degraded for 4 h at 140 °C in the dark in a nitrogen atmosphere to prevent photooxidation. Normalised photovoltaic parameters are plotted against the annealing time in Figure 4.7.

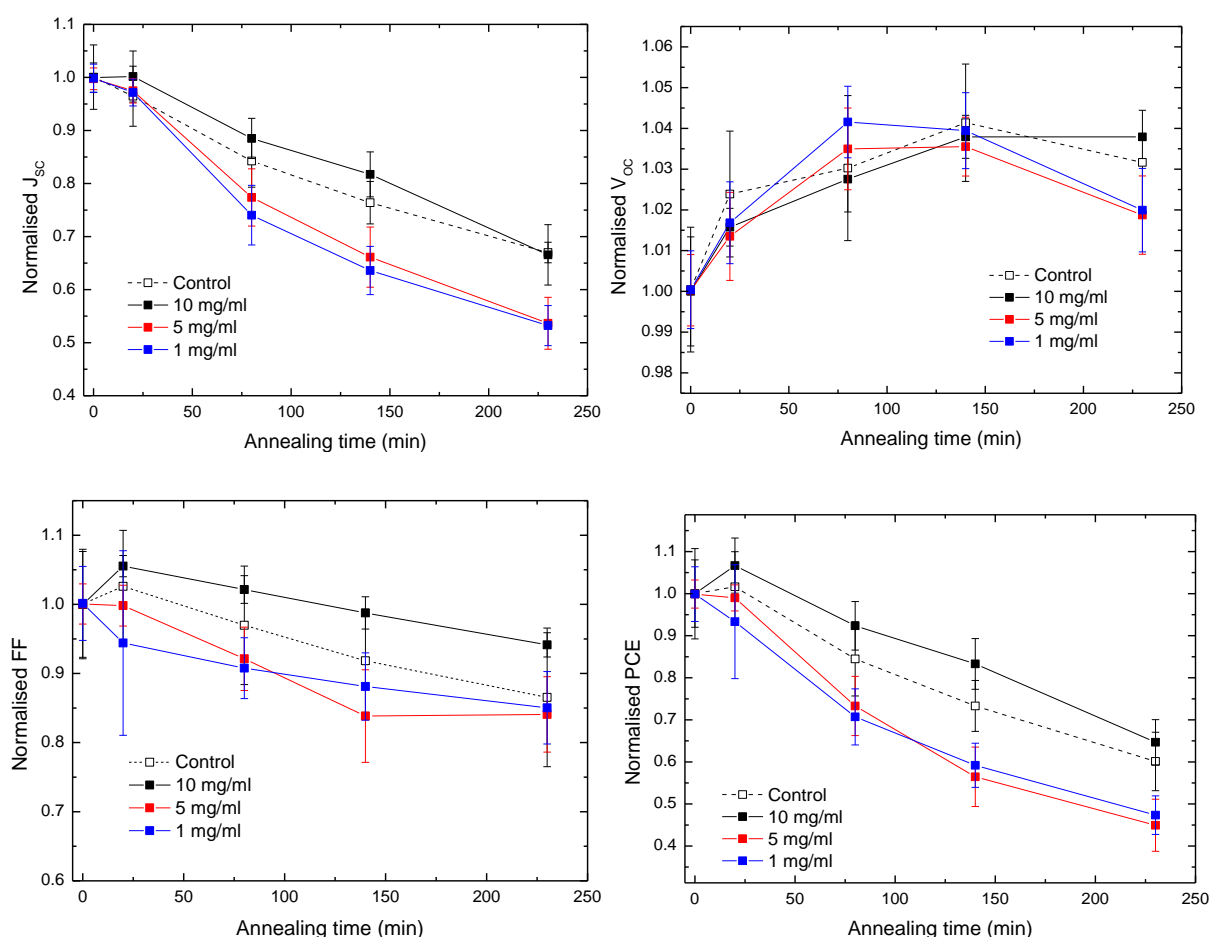


Figure 4.7. Normalised average photovoltaic parameters as a function of annealing time for devices incorporating cross-linked penetrating PDMS interfacial layers deposited from solutions of different concentrations.

Two properties of the new layers were important: (i) the ability to stabilise the interface through cross-linking and (ii) the intermixing of the non-cross-linked molecules with the active

layer and their compatibilising effect. Clearly, PDMS layers have an effect on stability of the devices. As seen in Figure 4.7, the overall thermal stability of the devices is mostly defined by the degradation rates of J_{SC} . Generally, the devices with 1 mg/ml and 5 mg/ml PDMS layer had lower stability than the control sample, owing to a faster J_{SC} decrease. Devices with PDMS 1 mg/ml showed 47% of their initial PCE after 4 h of thermal annealing and the devices with PDMS 5 mg/ml showed 45%. Devices with PDMS 10 mg/ml, however, had improved stability and retained 65% of their initial PCE, compared to 60% retained by the control sample. Although these values are within the experimental error bar, the improved stability of fill factor in PDMS 10 mg/ml speaks for the fact that PDMS 10 mg/ml layers are capable of improving the overall device stability. The fill factor in PDMS 10 mg/ml devices increased after 30 min of annealing and then lost 6%, whereas in the control sample the loss of fill factor was 14% (from its initial values). Moreover, the distribution of FF and V_{OC} values after 4 h of degradation was narrower ($\pm 1.5\%$ for FF and $\pm 4 \times 10^{-4} \%$ for V_{OC}) if compared to the control devices ($\pm 12\%$ and $\pm 1\%$ for FF and V_{OC} , respectively).

This marginal improvement in fill factor stability, cannot be explained by the enhanced contact between ZnO and PAL, because PDMS 5 mg/ml and 1 mg/ml would also be more stable. Potentially, the enhanced fill factor stability can be explained by the compatibilising effect of PDMS molecules which induce favourable vertical distribution of components in the blend towards respective electrodes.

The stabilisation of PCE in PDMS 10 mg/ml devices is attributed to the presence of the intermixed PDMS molecules that have a compatibilising effect on the stability of the blend. Although there are limited reports that fullerene-derivatised polystyrene and polystyrene copolymers can serve for compatibilising the P3HT:PCBM blend and improve the initial device performance,^{45,46} polymers without functionalisation have never been shown to have the same effect. The data herein suggests that PDMS polymers can have a compatibilising effect even without functionalisation, owing to their higher affinity to the blend components due to methoxy groups.

Unlike for initial performance where cross-linked layer was beneficial for electron extraction, the stabilisation in PDMS 10 mg/ml originates from the compatibilising effect of the PDMS molecules in the blend, otherwise PDMS 1 mg/ml and 5 mg/ml would show at least comparable stability. On the contrary, stability study shows that the cross-linked PDMS films are actually detrimental for the device performance, since they affect all photovoltaic parameters in the device, indicating the degradation of the contact between the photoactive layer and ZnO.

Overall, both efficiency and stability devices benefit from incorporation of PDMS 10 mg/ml layer, owing to the combination of cross-linked layer at the ZnO/PAL interface, improving the

extraction, and compatibilising effect of PDMS molecules in the bulk, stabilising the morphology of the blend and inducing favourable vertical distribution of the blend components. Thus, upon degradation, the PCE of PDMS 10 mg/ml decreased from 3.20% to 2.08%, whereas the control lost its PCE from 3.14% to 1.86%, demonstrating that improvements in efficiency and stability can be also observed from incorporating simple polymeric materials.

4.5 Cross-linked PDMS-FUL layer

To study how fullerene-functionalisation of PDMS influence the suitability of PDMS-FUL for improving the device performance and stability, PDMS-FUL was incorporated as a penetrating interfacial layer between ZnO and PAL. The resulting layer thickness was also varied by depositing the layers from solutions of varying concentrations. Initial photovoltaic parameters for the devices with PDMS-FUL layers of different thicknesses are given in Table 4.3.

Table 4.3. Initial photovoltaic values obtained for devices incorporating cross-linked PDMS-FUL layers, deposited from solutions of different concentrations, as interfacial layers between ZnO and PAL (average for 12-16 devices).

Sample	Absorbance at $\lambda = 283$ nm ^a , a.u.	Intermixed PDMS-FUL molecules ^a	J_{SC} , mA/cm ²	V_{OC} , mV	FF	η , PCE, %
Control (no interlayer)	0.100	-	8.93	556	0.63	3.14
PDMS-FUL 10 mg/ml	0.105	76% (7.6 mg/ml) ^b	9.48	550	0.64	3.32
PDMS-FUL 5 mg/ml	0.114	42% (2.1 mg/ml) ^b	8.85	556	0.67	3.23
PDMS-FUL 1 mg/ml	0.108	0%	8.71	557	0.66	3.23

(a) Obtained from absorbance studies, as discussed in Section 4.3.

(b) Corresponding solution concentration is shown in brackets.

As can be seen from Table 4.3, the PCE values of pristine devices with PDMS-FUL layers are higher than those of control devices. The highest efficiency of 3.32% is observed in PDMS-FUL 10 mg/ml devices. Based on the observations made for PDMS layers, for understanding of the complex effects of PDMS-FUL layers on the efficiency of devices, it is necessary to distinguish two aspects: (i) the bulk effect of PDMS-FUL molecules that

penetrate into the active layer and (ii) interfacial effects of cross-linked PDMS-FUL film on ZnO.

Absorbance studies have shown that the amount of PDMS-FUL molecules that intermix with the active blend decreases with the layer thickness, being the highest in PDMS-FUL 10 mg/ml and the lowest in PDMS-FUL 1 mg/ml. Accordingly, the current density (J_{sc}) is improving from 8.71 mA/cm² in the PDMS-FUL 1 mg/ml samples to 9.48 mA/cm² in the PDMS-FUL 10 mg/ml samples. This indicates that, in contrast to PDMS, PDMS-FUL molecules have a compatibilising effect and lead to improvements in the blend morphology. This observation confirms that fullerene moiety is crucial for improving the initial morphology of the blend.

In agreement with observations made for PDMS layers, the FF increases with the PDMS-FUL layer thickness after cross-linking and washing. Thus, maximum FF was observed for PDMS-FUL 5 mg/ml (0.67 for 0.114 a.u. absorbance) and PDMS-FUL 1 mg/ml (0.66 for 0.108 a.u. absorbance intensity). Evidently from the FF, the cross-linked PDMS-FUL layer is beneficial for extraction-recombination equilibrium at the interface, and the fullerene moiety does not seem to play an important role in this improvement, since the fill factors for PDMS and PDMS-FUL are comparable (Section 4.4).

Overall, the incorporation of PDMS-FUL cross-linked layers was beneficial for the device efficiency at all layer thicknesses. Further, the effect of the cross-linked layer on the stability of devices was studied. Normalised averaged photovoltaic parameters are plotted against the annealing time in Figure 4.8.

Clearly, PDMS-FUL layer has an effect on stability of the devices. The PDMS-FUL layers deposited from solutions with concentrations of 1 mg/ml and 5 mg/ml decreased the stability of the devices by mostly affecting the J_{sc} and FF. PDMS-FUL 1 mg/ml showed the worst degradation with a loss of 55% PCE after 4 h heating at 140 °C under inert atmosphere. On the other hand, devices with PDMS-FUL 10 mg/ml layer had improved stability and retained 73% of their initial PCE values, whereas the control retained only 60%. Although, this improvement lies within the experimental error bar, the enhancement of the J_{sc} stability is rather pronounced and speaks towards the ability of PDMS-FUL layer to stabilise the device performance. The improvement in stability of PDMS-FUL 10 mg/ml devices is attributed to the compatibilising effect of PDMS-FUL molecules on the morphology of the blend. Thus, PDMS-FUL 10 mg/ml devices experienced only 21% of current density loss against 33% loss in the control sample.

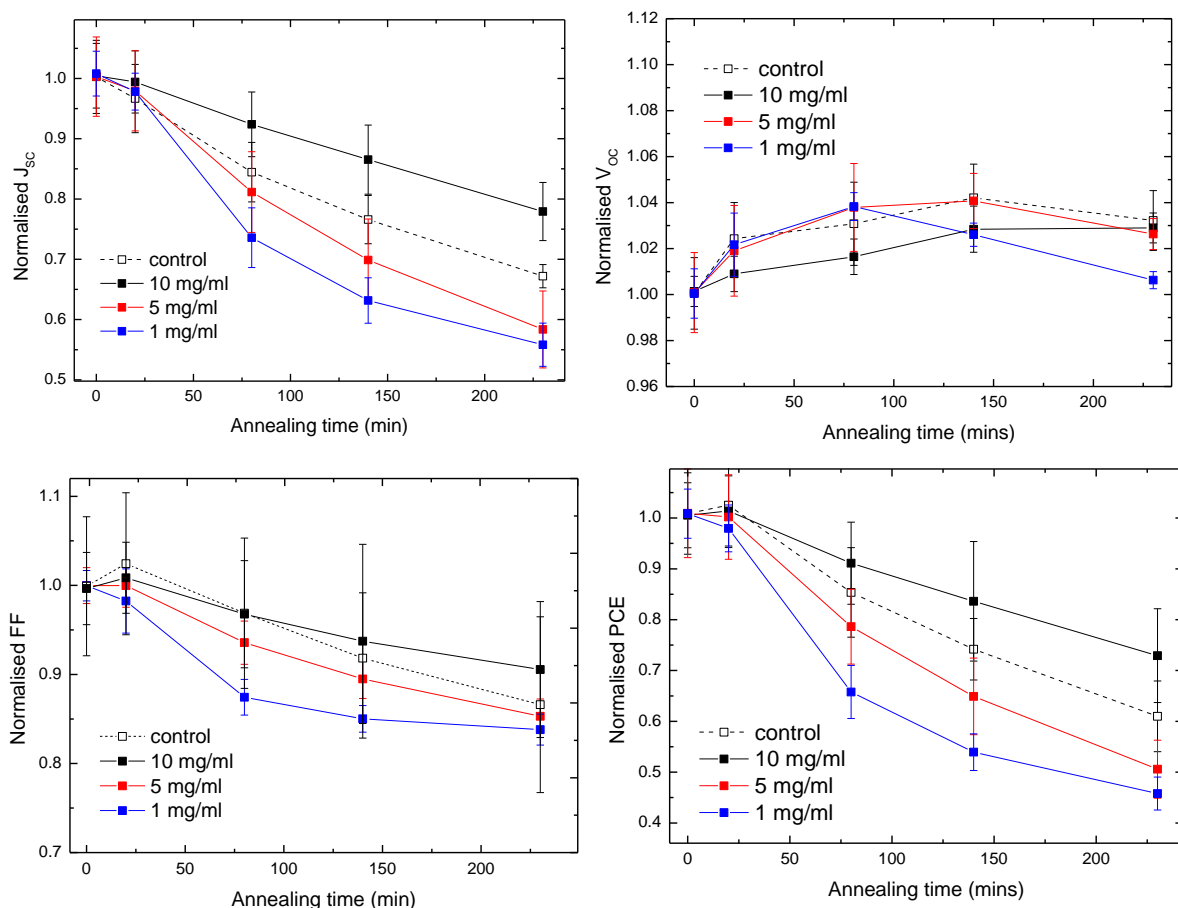


Figure 4.8. Normalised average photovoltaic parameters as a function of annealing time for devices incorporating cross-linked PDMS-FUL interfacial layers deposited from solutions of different concentrations.

Devices with PDMS-FUL 10 mg/ml layer showed enhanced stability of the fill factor, as was also observed in PDMS-incorporating devices. The loss of fill factor in 10 mg/ml devices is only 9%, whereas that in control samples is 14%. As previously, a possible explanation is the vertical distribution of the components in the photoactive blend towards their respective electrodes.

Compared to PDMS 10 mg/ml, devices with PDMS-FUL 10 mg/ml show better stability, retaining 73% of their initial PCE against 65% in PDMS 10 mg/ml samples. The main difference lies in the current density stabilisation. The compatibilising effect of PDMS-FUL molecules is more pronounced due to attachment of fullerene on the end of the PDMS chain. The fullerene-derivatised polymers have been widely reported for blend stabilisation purpose, since the fullerenes can induce controlled crystallisation of PCBM and reduce the size of resulting crystallites.¹⁰

In conclusion, incorporation of PDMS-FUL 10 mg/ml interfacial penetrating layer is beneficial for both efficiency of the pristine devices and their thermal stability, due to combination of interfacial and bulk effects of PDMS-FUL molecules.

4.6 Transient absorption spectroscopy

The effect of the penetrating PDMS-FUL interlayer of different thicknesses on the charge generation was studied by TAS on the film stack ITO/ZnO/PDMS-FUL/PAL in pristine case and after 3 hours heating at 150 °C. PDMS-FUL layer was chosen due to higher efficiency and stability of the devices incorporating this layer compared to those devices with PDMS layer. First, the charge generation was measured for the stacks with PDMS-FUL 1 mg/ml layer with no PDMS-FUL molecules penetrating the blend. Subsequently, the stacks with PDMS-FUL 10 mg/ml were studied, representing the case where 76% of PDMS-FUL molecules were intermixed with the blend. Both cases were compared to the control.

4.6.1 Control sample

As described in Section 1.6, global fitting of the experimental TA spectrum of the control stack (ITO/ZnO/PAL) yielded three evolution-associated differential spectra (EADS) with respective fits, consisting of separate species-associated differential spectra (SADS), representing contribution of each excited state (Figure 4.9). The relative concentrations of excited states were extracted from these SADS and plotted against their respective EADS in Figure 4.10.

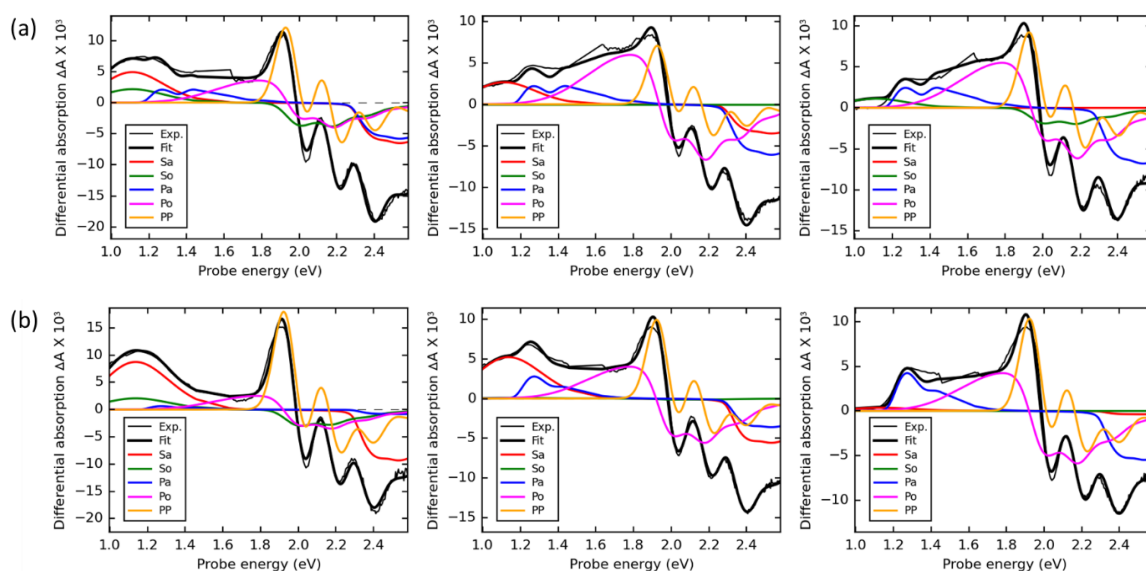


Figure 4.9. EADS of the control stack ITO/ZnO/PAL, pristine (a) and degraded at 150 °C for 3 h (b), as obtained from the global analysis of experimental TA spectra using a three sequential steps model (thin solid curves), spectral fits to the EADS (thick solid curves) and contributions to fits from polaron pair, localised and delocalised singlet exciton and polaron states with their respective bleach contributions (negative differential absorption).

As seen in Figures 4.9a and 4.10a, EADS0 of the pristine blend consists of contributions from all excited states, with domination of singlets (S_a) and polarons (P_a) in the amorphous phase. Thus, ultrafast charge yield in the control sample is 50% and the total charge yield is 67%, owing to the build-up of polarons in the ordered phase of P3HT (P_o) and complete dissociation of localised singlets (S_a).

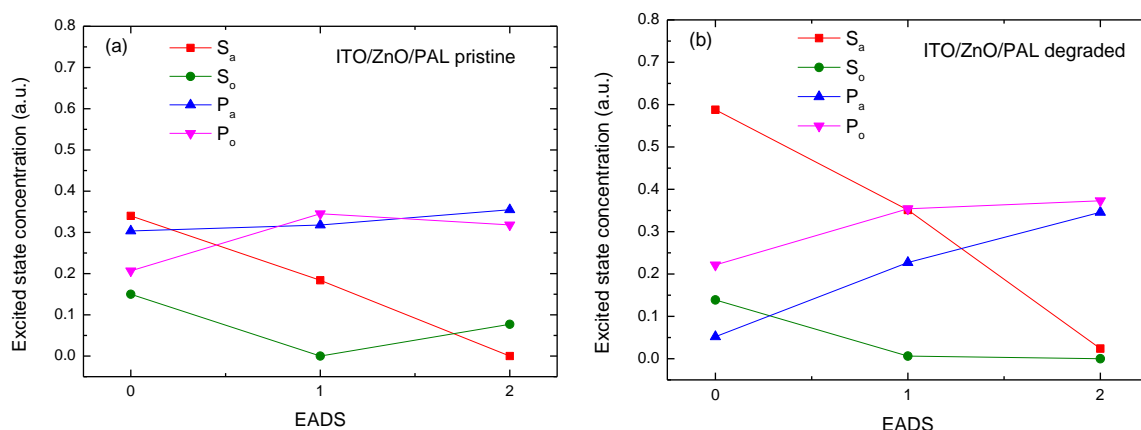


Figure 4.10. Evolution of excited state concentrations according to their respective EADS in the control film stack ITO/ZnO/PAL before (a) and after degradation (b) at 150 °C for 3 h: localised singlet excitons (S_a , red) and polarons (P_a , blue), delocalised singlet excitons (S_o , green) and polarons (P_o , magenta).

Upon degradation (Figures 4.9b and 4.10b), a rise in population of ultrafast localised singlets (S_a) from 0.34 a.u. to 0.59 a.u. is observed in EADS0. On the other hand, concentration of the ultrafast polarons in the amorphous phase (P_a), on the other hand, decreases from 0.30 a.u. to 0.05 a.u. The dynamics of charge generation in the ordered phase of P3HT remains very similar to that in the pristine sample, yielding only 0.22 a.u of delocalised polarons (P_o). Thus ultrafast charge of polarons in degraded blend is only 27%. However, within 400 ps, all singlets dissociate completely, resulting in a build-up of polarons in the amorphous phase (P_a) and a total charge yield of 72% in the control sample upon degradation.

This increase in the total charge yield is an evidence of two processes happening in the blend. First process is the diffusion-depended charge yield, *i.e.* in bigger domains of P3HT resulting from phase segregation of the blend, the exciton requires time to reach the donor/acceptor interface for dissociation. Second process is the exciton dissociation at the interface with the isolated islands of PCBM or even single PCBM molecules, dissolved inhomogeneously in the polymer matrix. A specific property of this process is the fate of the polarons generated at such interfaces: since they cannot escape the isolated domains and be extracted, they can only recombine with their counterparts. Therefore upon degradation, these combined processes result in J_{SC} decrease, even though the total charge yield is higher than that in pristine devices.

4.6.2 PDMS-FUL 1 mg/ml

Three EADS, with respective fits, obtained from TA experimental spectrum, consisting of separate SADS, representing contribution of each excited state, are shown in Figure 4.11. The relative concentrations of excited states were extracted from these SADS and plotted against their respective EADS in Figure 4.12.

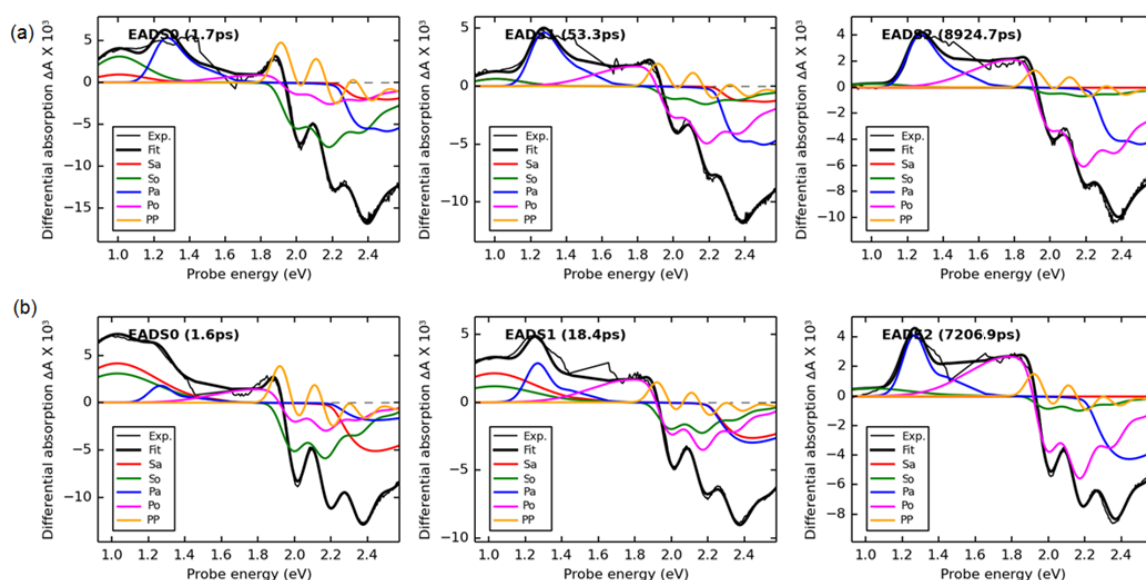


Figure 4.11. EADS of ITO/ZnO/PDMS (1 mg/ml)/PAL stack, pristine (a) and degraded at 150 °C for 3 h (b), as obtained from the global analysis of experimental TA spectra using a three sequential steps model (thin solid curves, fitted lifetimes are given in the legends), spectral fits to the EADS (thick solid curves) and contributions to fits from polaron pair, localised and delocalised singlet exciton and polaron states with their respective bleach contributions (negative differential absorption).

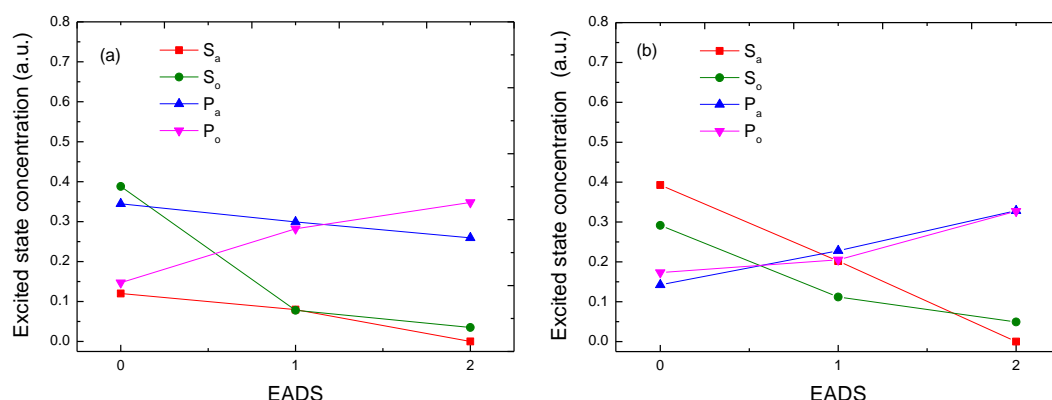


Figure 4.12. Evolution of excited states concentration according to their respective EADS in ITO/ZnO/XL PDMS 1 mg/ml/PAL film stack before (a) and after degradation (b) at 150 °C for 3 h: localised singlet excitons (S_a , red) and polarons (P_a , blue), delocalised singlet excitons (S_o , green) and polarons (P_o , magenta).

As can be observed from Figure 4.11a and 4.12a, EADS0 (immediately after excitation) of pristine stack is dominated by the contributions from delocalised singlets (S_o) and localised polarons (P_a), which have similar concentrations (0.39 a.u. and 0.35 a.u., respectively). The singlet excitons rapidly dissociate in EADS2, whereas the amount of generated delocalised polarons (P_o) increases to 0.38 a.u, indicating that the crystalline regions of P3HT in the blend are exceeding 4 nm optimal size, as shown by Guo,¹¹ and the polaron build-up results from diffusion of excitons to the interface. In pristine PDMS-FUL 1 mg/ml stack, the yield of ultrafast polarons is 49% and after several hundred picoseconds it reaches 61% of polarons available for extraction. These values are lower than those demonstrated in Section 4.6.1 for control samples, but generally agree with typical values for pristine P3HT:PCBM blends.¹² These findings correspond to the data from absorbance measurements which show that in PDMS-FUL 1 mg/ml samples, the extent of cross-linking was 100% and no intermixing of PDMS-FUL molecules with PAL occurred.

After thermal annealing of PDMS-FUL 1 mg/ml stack (Figure 4.11b and 4.12b), a drastic increase in population of localised singlet excitons (S_a) from 0.11 a.u. to 0.41 a.u. is observed in EADS0, indicating the growth of amorphous domains of P3HT in the blend. At the same time, the concentration of singlets in the ordered phase (S_o) decreased from 0.39 a.u. to 0.3 a.u. Consequently, the ultrafast charge yield was reduced from 49% to 32% in degraded films. As seen from Figure 4.12, the exciton dissociation in degraded films became slower, so that after 1.6 ps, 0.2 a.u. and 0.1 a.u. of localised (S_a) and delocalised (S_o) singlets, respectively, persist. On the other hand, the total charge yield in the degraded films after several picoseconds (EADS2) is higher than that in pristine films, reaching 65%.

The dynamics of charge generation is in agreement with that in control samples, where the ultrafast charge yield decreased from 61% to 37% and the total charge yield improved from 67% to 72%. However, this increase of the total charge yield observed by TAS does not reflect the fate of generated polarons, since in a phase-segregated blend with many isolated domains of PCBM, generated polarons cannot be transported by hopping to the electrodes and do not contribute to the current. In conclusion, the underlying cross-linked PDMS-FUL 1 mg/ml layer does not induce any changes in the blend morphology stability.

4.6.3 PDMS-FUL 10 mg/ml

The EADS with respective fits, consisting of separate SADS, for the stack ITO/ZnO/XL PDMS-FUL (10 mg/ml)/PAL are shown in Figure 4.13. Corresponding concentrations of excited states for each EADS are illustrated in Figure 4.14.

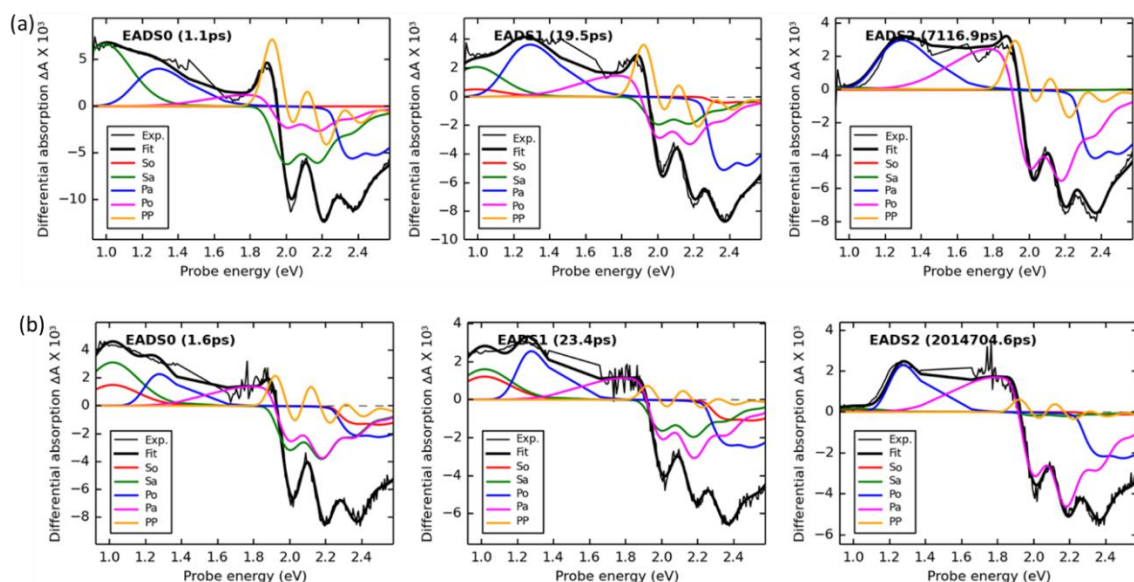


Figure 4.13. EADS of ITO/ZnO/XL PDMS 10 mg/ml/PAL stack, pristine (a) and degraded at 150 °C for 3 h (b), as obtained from the global analysis of experimental TA spectra using a 3 sequential steps model (thin solid curves, fitted lifetimes are given in the legends), spectral fits to the EADS (thick solid curves) and contributions to fits from polaron pair, localised and delocalised singlet exciton and polaron states with their respective bleach contributions (negative differential absorption).

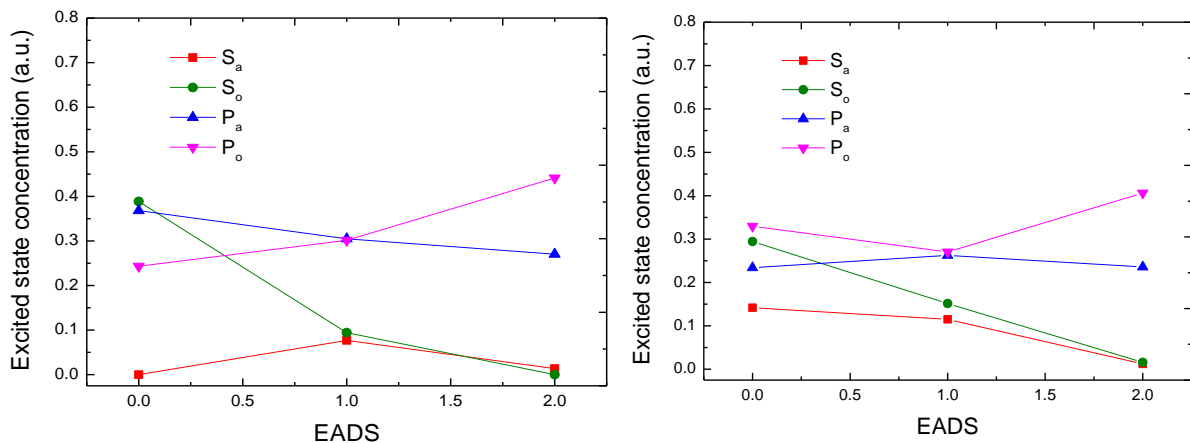


Figure 4.14. Evolution of excited states concentration according to their respective EADS in ITO/ZnO/PDMS 110 mg/ml/PAL film stack before (a) and after degradation (b): localised singlet excitons (S_a , red) and polarons (P_a , blue), delocalised singlet excitons (S_o , green) and polarons (P_o , magenta).

Interestingly, pristine films with PDMS-FUL 10 mg/ml show an absence of localised singlets (S_a) immediately after excitation, with their concentration slightly increasing over time. EADS0 shows a high population of localised polarons (P_a), 0.37 a.u., implying that the efficiency of exciton dissociation in the amorphous phase of P3HT is very high. Dissociation

of excitons in the ordered phase is less efficient, yielding only 0.22 a.u. of delocalised polarons, while 0.39 a.u. of delocalised excitons remain. Such distribution of excited states in the ordered phase of the donor indicates high crystallinity of P3HT in the blend. High levels of P3HT crystallinity are favourable for charge transport and are partially responsible for the current density of 9.48 mA/cm², which is higher than that in control samples (8.93 mA/cm²).

In general, the ultrafast charge yield in these stacks was 61% and the total charge yield rose to 71%, owing to the build-up of the delocalised polarons (P_o) in the last EADS. These values are in the typical range for P3HT:PCBM blends.

In degraded films (Figures 4.13b and 4.14b), there was a slight decrease in ultrafast localised polarons (P_a) to 0.22 a.u., in line with a rise in singlets in the amorphous phase, indicating the growth of amorphous P3HT domains. On the other hand, the singlets in the ordered phase dissociate more efficiently, giving rise to delocalised polarons (P_o) in EADS0 from 0.22 a.u. to 0.33 a.u. Thus, ultrafast charge yield in degraded blends is lower than that in pristine (56% and 61%, respectively). However, this difference is not sufficient to be attributed to drastic changes in the PAL morphology.

As reported previously, in typical P3HT:PCBM blends, the ultrafast charge yield decreases from 58% to 42% upon degradation.¹³ The nanomorphology of the blend in PDMS-FUL 10 mg/ml samples, which is indirectly observed through charge generation, did not show the same changes. Stabilisation of the nanomorphology is attributed to a presence of the compatibilising part of the PDMS-FUL layer, intermixed with the PAL molecules upon deposition.

The total charge yield in degraded PDMS-FUL 10 mg/ml samples decreased from 71% to 64%, also suggesting improved stability of the PAL morphology in comparison to a typical P3HT:PCBM blend (decrease of the extractable charge yield from 79% in pristine to 60% in degraded).¹³ Although the control sample of P3HT:PCBM blend in Section 4.5.1 showed an increase of extractable charge yield, these findings agrees with the observations of an inhomogeneous distribution of domains in degraded blends. If measured at different spots, the same degraded blend shows both increased and decreased charge generation, but in total the generated charges equally contribute to the extracted current, indicating that the polarons observed by TAS are not mobile. Therefore, it is difficult to directly correlate the total charge yield to the losses in current density. For that, transient photocurrent (TPC) measurements are needed, since they are capable of detecting only mobile charge carriers, *i.e.* not trapped within isolated domains of donor and acceptor. On the other hand, loss of ultrafast charge carriers is directly related to the morphology of the blend and therefore can be related to the changes in current density. The data concerning the charge yield and J_{SC} in pristine and degraded PDMS-FUL samples and control are presented in Table 4.4.

Table 4.4. Total charge yield and current density in pristine samples and losses of ultrafast charge yield and corresponding current density losses for the devices with cross-linked PDMS-FUL layers.

PDMS-FUL concentration	Total charge yield^a (%)	J_{sc}^b (mA/cm²)	Loss of ultrafast charge yield upon degradation^a (%)	Loss of J_{sc} upon degradation^b (%)
Control	67	8.93	47	35
1 mg/ml	61	8.71	37	47
10 mg/ml	71	9.48	8	22

(a) as obtained from TAS target analysis;

(b) as obtained from *J-V* curve measurements.

As seen from Table 4.4, higher total charge yield generally corresponds to higher values of the J_{sc} and in PDMS-FUL 10 mg/ml device is associated with the presence of compatibilising PDMS-FUL molecules that were not cross-linked.

With respect to degradation, the loss of ultrafast charge yield depends strongly on the presence of the intermixed PDMS-FUL molecules. Thus, the biggest changes in the ultrafast charge yield are observed in the control sample (47% loss) without any PDMS-FUL molecules and in PDMS-FUL 1 mg/ml (37%), where the extent of cross-linking is 100% and no PDMS-FUL molecules are intermixed with the PAL. Only 8% ultrafast charge yield loss in PDMS-FUL 10 mg/ml corresponds to the most stable current density, with only 22% J_{sc} loss. This agrees with the absorbance measurements, where 76% of the deposited film was not cross-linked, and therefore, would penetrate the PAL upon its subsequent deposition. Previous reports also demonstrated the advantages of the compatibilising layers for nanomorphology stabilisation, and current density stability, as a result.^{13–15}

On the other hand, the ultrafast charge loss in PDMS-FUL samples of all concentrations does not account for all of the current density degradation, implying that charge generation is not the only process that is affected by the thermal degradation. As demonstrated previously, the general loss of effective area, caused by partial delamination of photoactive layer from charge-collecting layers or migration of the blend components toward the wrong electrodes, is also responsible for the decrease in current density upon thermal degradation.¹³

4.7 Conclusions and suggestions for future work

Cross-linking properties of PDMS and PDMS-FUL polymers, whose synthesis and thermal behaviour were described in Sections 3.3 and 3.4, were successfully employed for engineering of ZnO/PAL interface. DSC thermograms (Section 3.4) of PDMS showed a broad exothermic peak at 110-140 °C that was attributed to the cross-linking within the bulk of the polymer. Cross-linking was confirmed by changes in the FTIR spectrum of PDMS upon heating, insolubility of the polymer in organic solvents and appearance of fluorescence under UV illumination.

Firstly, contact angle measurements showed that, when deposited onto ZnO, both PDMS and PDMS-FUL layers could be cross-linked, although the DSC thermogram of bulk PDMS-FUL did not show any exothermic peak that could be attributed to cross-linking, in contrast to the thermogram of PDMS. Upon cross-linking, the contact angle of the film did not change, indicating that the films were not cross-linked on the surface. However, after washing, the contact angles decreased slightly (from 85° to 70°) to account for chemical changes, occurring in the films.

Further measurements of absorbance showed that cross-linking in the layer depends on the film thickness. The films of PDMS and PDMS-FUL deposited from 1 mg/ml solution were the thinnest and, after washing, 100% of the layer absorbance was preserved, indicating 100% of the layer was cross-linked. Accordingly, with increase in solution concentration to 5 mg/ml, approximately 50% of the cross-linked film remained after washing. Of the films deposited from 10 mg/ml, approximately 20% remained after cross-linking and washing. Following simple calculations, in films deposited from 2-3 mg/ml solution cross-linking would be complete within the whole film. Also, it was suggested that in PDMS/PDMS-FUL 10 mg/ml and 5 mg/ml devices, the interfacial effect of the cross-linked layer could be combined with the compatibilising effect of the molecules intermixing with the PAL upon its subsequent deposition.

Indeed, device studies confirmed that interfacial layers had a beneficial effect on the initial performance of the cells, improving current density and fill factor, with the highest fill factor observed in the devices with the thickest (as observed from absorbance studies) cross-linked PDMS/PDMS-FUL layers.

However, the impact of PDMS and PDMS-FUL layers on the current density was different. In PDMS devices, the increase in amount of intermixed PDMS molecules led to the loss of current density, the lowest J_{sc} observed in PDMS 10 mg/ml samples. Nevertheless, the J_{sc} values of all PDMS samples were higher than those of control devices. This enhancement of J_{sc} was attributed to the improved contact between ZnO and photoactive layer and facilitated electron extraction through PDMS layer. On the other hand, in PDMS-FUL devices the

intermixed PDMS-FUL molecules had a beneficial effect on the current density, the highest value observed in PDMS-FUL 10 mg/ml devices with the highest amount of compatibilising molecules. These observations speak for the importance of the fullerene moiety for establishing of the compatibilising effect by PDMS-FUL polymers. TAS measurements confirmed that with an increase in the concentration of the compatibilising molecules, the total charge yield was improved, in agreement with improvement in J_{SC} .

Furthermore, PDMS and PDMS-FUL 10 mg/ml devices showed improved stability, in comparison to control devices, preserving 65% and 73% of its initial performance, respectively, against 58% in control samples. The improvement of device stability in PDMS/PDMS-FUL 10 mg/ml was attributed to the compatibilising effect of non-cross-linked PDMS and PDMS-FUL molecules in the blend. This was also indirectly observed from TAS measurements, where PDMS-FUL 10 mg/ml stacks showed more stable charge generation and only lost 8% of ultrafast charge yield *versus* 47% loss in control stack. Ultrafast charge yield in this case serves as an indirect measure of the blend morphology stability, and thus, indicates that compatibilising effect is at least partially responsible for stability improvement in PDMS-FUL 10 mg/ml sample. TAS measurements also confirmed that other processes, rather than charge generation, are responsible for the degradation of the devices.

All other devices, incorporating PDMS and PDMS-FUL 5 mg/ml and 1 mg/ml, showed degradation rates higher those in the control. The fastest degradation was observed in PDMS/PDMS-FUL 1 mg/ml devices. These devices contain only cross-linked layers and no intermixed molecules, therefore, enhanced degradation in these devices can only be explained by the presence of the interfacial layer. Simultaneous decrease of fill factor and current density suggests the loss of effective extraction area, due to delamination of the electron-transporting layer from the photoactive layer. The same effect is not so pronounced in PDMS and PDMS-FUL 10 mg/ml devices because the delamination losses are compensated by improvements in the bulk morphology.

A suggested explanation to enhanced delamination in PDMS/PDMS-FUL layer is the change in the mechanical properties of the cross-linked layer upon degradation, i.e. increase of polymer brittleness or nanohardness.^{16,17} Cross-linking was previously shown to affect both, with negative effects on the polymer stability.¹⁸ Furthermore, the delamination would be reflected in the change of extraction efficiency as measured by TPC in a complete device or other time-resolved measurements, sensitive only to mobile charge carriers, such as short circuit microsecond TAS. These studies will be subject of the future development work which will provide additional understanding for design of stable interface materials.

Furthermore, the fullerene attached to the PDMS chain was important for stabilisation of the devices. Thus, a major interest lies in modification of the PDMS chain with other pendent

molecules or even blocks, for example PDMS-P3HT block. Another interesting approach, involving cross-linkable PDMS, would be post-cross-linking layer modification, for example, by attachment of the fullerene molecules through thermal azide chemistry, which does not require solution reaction. These fullerene molecules, when covalently linked to the PDMS layer, would induce favourable vertical diffusion in the blend.

Since compatibilising properties of PDMS and PDMS-FUL have been demonstrated in this work, these polymers can be incorporated as ternary agents directly into the blend, as a stabilising additive. The stabilisation of the blend might be dependent on the molar mass of PDMS and the polymer:fullerene ratio in PDMS-FUL polymer, thus, different compatibiliser architectures should be studied. Also, the cross-linking of PDMS and PDMS-FUL with other molecules should be studied to understand in full how it behaves as a part of the blend.

Generally, cross-linked layers might be an interesting approach to interface engineering, which previously did not attract much attention due to a limited choice of the polymers that are capable of cross-linking and do not have insulating properties at the same time. Most of the reported layers comprise elaborate structures with attached cross-linking functionality.^{3,4,19} PDMS-FUL 10 mg/ml, on the other hand, is an example of simultaneous improvement of device efficiency and stability by addressing the blend nanomorphology and the electron-transporting interface with a simple cross-linkable material.

4.8 References

- (1) Liang, W.; Chang, C.; Lai, Y.; Cheng, S.; Chang, H.; Lai, Y.; Cheng, Y.; Wang, C.; Hsu, C. *Macromolecules* **2013**.
- (2) Veinot, J. G. C.; Marks, T. J. *Acc. Chem. Res.* **2005**, 38 (8), 632–643.
- (3) Cheng, Y.-J.; Hsieh, C.-H.; Li, P.-J.; Hsu, C.-S. *Adv. Funct. Mater.* **2011**, 21 (9), 1723–1732.
- (4) Cheng, Y.-J.; Hsieh, C.-H.; He, Y.; Hsu, C.-S.; Li, Y. *J. Am. Chem. Soc.* **2010**, 132 (49), 17381–17383.
- (5) Cheng, Y.-J.; Cao, F.-Y.; Lin, W.-C.; Chen, C.-H.; Hsieh, C.-H. *Chem. Mater.* **2011**, 23 (6), 1512–1518.
- (6) Sobhan, C. B.; Peterson, G. P. *Microscale and Nanoscale Heat Transfer: Fundamentals and Engineering Applications*; CRC Press, 2008.
- (7) Leo, A.; Hansch, C.; Elkins, D. *Chem. Rev.* **1971**, 71 (6), 525–616.

- (8) Rattanathamwat, N.; Wootthikanokkhan, J.; Nimitsiriwat, N.; Thanachayanont, C.; Asawapirom, U.; Keawprajak, A. *Int. J. Polym. Mater. Polym. Biomater.* **2014**.
- (9) Seeponkai, N.; Keaitsirisart, N.; Wootthikanokkhan, J.; Thanachayanont, C.; Chuangchote, S. *Int. J. Polym. Mater. Polym. Biomater.* **2013**, 63 (1), 33–40.
- (10) Richards, J. J.; Rice, A. H.; Nelson, R. D.; Kim, F. S.; Jenekhe, S. a.; Luscombe, C. K.; Pozzo, D. C. *Adv. Funct. Mater.* **2013**, 23 (4), 514–522.
- (11) Guo, J.; Ohkita, H.; Bente, H.; Ito, S. *J. Am. Chem. Soc.* **2009**, 131 (46), 16869–16880.
- (12) Guo, J.; Ohkita, H.; Bente, H.; Ito, S. *J. Am. Chem. Soc.* **2010**, No. 6, 6154–6164.
- (13) Isakova, A.; Dowland, S.; Karuthedath, S.; Distler, A.; Egelhaaf, H.-J.; Topham, P. D.; Lueer, L. *submitted* **2015**.
- (14) Sivula, K.; Ball, Z. T.; Watanabe, N.; Fréchet, J. M. J. *Adv. Mater.* **2006**, 18 (2), 206–210.
- (15) Gernigon, V.; Leveque, P.; Brochon, C.; Audinot, J.-N.; Leclerc, N.; Bechara, R.; Richard, F.; Heiser, T.; Hadziioannou, G. *Eur. Phys. Journal-Applied Phys.* **2011**, 56 (3), 34107.
- (16) Derue, L.; Dautel, O.; Tournebize, A.; Drees, M.; Pan, H.; Berthumeyrie, S.; Pavageau, B.; Cloutet, E.; Chambon, S.; Hirsch, L.; Rivaton, A.; Hudhomme, P.; Facchetti, A.; Wantz, G. *Adv. Mater.* **2014**, 5831–5838.
- (17) White, J. R. *Comptes Rendus Chim.* **2006**, 9 (11-12), 1396–1408.
- (18) Grossiord, N.; Kroon, J. M.; Andriessen, R.; Blom, P. W. M. *Org. Electron.* **2012**, 13 (3), 432–456.
- (19) Yan, H.; Scott, B. J.; Huang, Q.; Marks, T. J. *Adv. Mater.* **2004**, 16 (21), 1948–1953.

CHAPTER 5 8-HYDROXYQUINOLINE LIGAND

5.1 Introduction

As discussed in Sections 3.1 and 3.2, the general approach to interface stabilisation, chosen for this work, involved polymerising zinc-binding ligands and depositing resulting polymers so that they would form self-assembling monolayers (SAM) on the surface of zinc oxide (ZnO). These SAMs would lead to improved contact between ZnO and the photoactive layer (PAL) and reduce the recombination losses at the interface. In Section 3.2, modelling showed that quinoline had a great potential for zinc binding, thus, it was employed in further studies, discussed in this chapter.

5.2. Insight into 8-hydroxyquinoline binding

Although the choice of ligand has been backed up by modelling results in this project, literature reports also show that the 8-hydroxyquinoline moiety is highly suitable for binding zinc. Small molecule, 8-hydroxyquinolate-zinc (Znq_2) complexes have been extensively studied due to their pronounced luminescent properties. Znq_2 complexes have been reported both as light-emitters in OLED devices of green or yellow emission¹ or as electron-transporting layers in OLEDs.² Owing to their good processability, Znq_2 complexes have been extensively modified to yield a range of materials with various emitting properties.²⁻⁴ Alteration of substituents at positions 2 (R_3), 4 (R_2), and 5 (R_1) (Figure 5.1) allows fine tuning of the electronic properties of resulting complexes, including HOMO/LUMO levels, band gap and emission wavelength.⁴⁻⁷

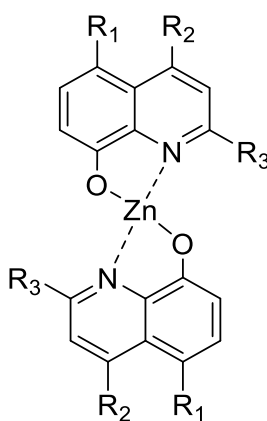


Figure 5.1. Generic structure of a Znq_2 complex.

Coordination polymers based on Znq_2 have also been widely reported in the literature since 1965, when Schiff-base coordination polymers were demonstrated by Horowitz *et al.*⁸ Later, Mei *et al.* reported polymerisable Znq_2 complexes.⁹ Furthermore, Wang *et al.*¹⁰ showed the controlled RAFT copolymerisation of 8-hydroxyquinoline-functionalised monomers with

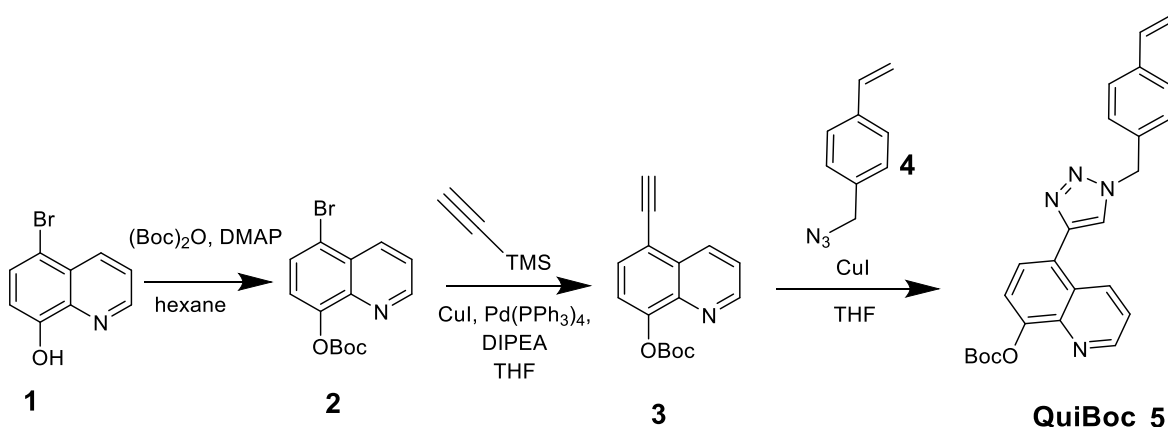
styrene co-monomers. In both examples, 8-hydroxyquinoline molecules were added to the polymers to avoid interchain cross-linked complexes. In the following sections, the synthesis and application of a novel 8-hydroxyquinoline-based polymer is discussed.

5.3. Synthesis and characterisation

This section reports synthesis of a polymer bearing pendent protected 8-hydroxyquinoline moieties. In the multi-step synthesis of the monomer, various previously reported reactions with high yields were adopted, and the polymerisation was carried out by reversible addition-fragmentation chain transfer polymerisation (RAFT).

5.3.1 Monomer synthesis

Synthesis of the monomer (QuiBoc) was achieved in several steps, each of them allowing high yields of the corresponding products (Scheme 5.1).

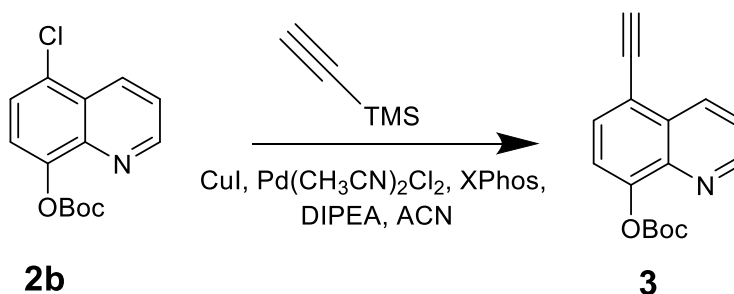


Scheme 5.1. Synthetic route toward the QuiBoc monomer.

The starting material, aryl bromide, was first protected with a *tert*-butoxycarbonyl (BOC) group. This group provides two major advantages: (i) it is stable in the mild basic conditions of Sonogashira coupling; (ii) it can be easily removed by chemical or thermal treatment.

Synthesis of 8-*tert*-butoxycarbonyloxy-5-ethynylquinoline (3) was carried out by Sonogashira coupling. This is an efficient way to form a C-C bond between the aryl bromide 2 (or a corresponding iodide) and trimethylsilylacetylene, whereas aryl chlorides are not converted under these conditions and normally require use of a Buchwald ligand and a copper salt.¹¹ In this work it was found that the coupling can be carried out using 2-dicyclohexylphosphino-2',4',6'-triisopropylbiphenyl (XPhos) ligand in combination with an acetonitrile palladium complex, both commercially available, without addition of copper salt (Scheme 5.2). Gelman

et al. have mentioned previously that copper salts tend to inhibit the reaction.¹² Furthermore, caesium carbonate, usually employed in aryl chloride cross-coupling as a base, cannot be used in this reaction as it would cause the protecting group to be removed. Thus, *N*-ethyldiisopropylamine (DIPEA) has been proved to be suitable here. Other ligands, such as (2-biphenyl)di-*tert*-butylphosphine (Johnphos) or 2-dicyclohexylphosphino-2',6'-diisopropoxybiphenyl (Ruphos), were not effective.



Scheme 5.2. Sonogashira coupling of the protected aryl chloride, using Buchwald ligand Xphos in acetonitrile (ACN).

4-vinylbenzyl azide, precursor **4**, was synthesised from commercially available 4-vinylbenzyl chloride. The most critical step of the overall synthesis was the coupling of 8-*tert*-butoxycarbonyloxy-5-ethynylquinoline **3** with 4-vinylbenzyl azide **4** which had to be carried out at room temperature to prevent any spontaneous polymerisation of **4** and other side reactions. It was observed that the reaction could proceed without a copper catalyst, but using a copper (I) salt increased the rate and conversion up to quantitative.

The efficiency of the reaction was confirmed by ¹H NMR spectroscopy where the signal corresponding to the terminal alkynyl proton at 3.5 ppm (labelled as H_a in Figure 5.2) of precursor **3** was significantly shifted to 7.73 ppm (Figure 5.2b) as the environment of this proton in the 1,2,3-triazole ring is more electronegative than that in the alkynyl C≡C bond (Figure 5.2a). Moreover, the splitting pattern of the quinoline protons has changed due to increase of the electronegativity in the triazole ring. Specifically, the splitting pattern of proton H_d has changed from a doublet of doublets in the spectrum of precursor **3** to a singlet in the spectrum of QuiBoc monomer **5**. This is associated with the changes of the chemical environment of the neighbouring protons, especially of the proton H_a, and the geometry of the triazole ring which would affect the spatial orientation of the proton and its chemical shift, as a result.

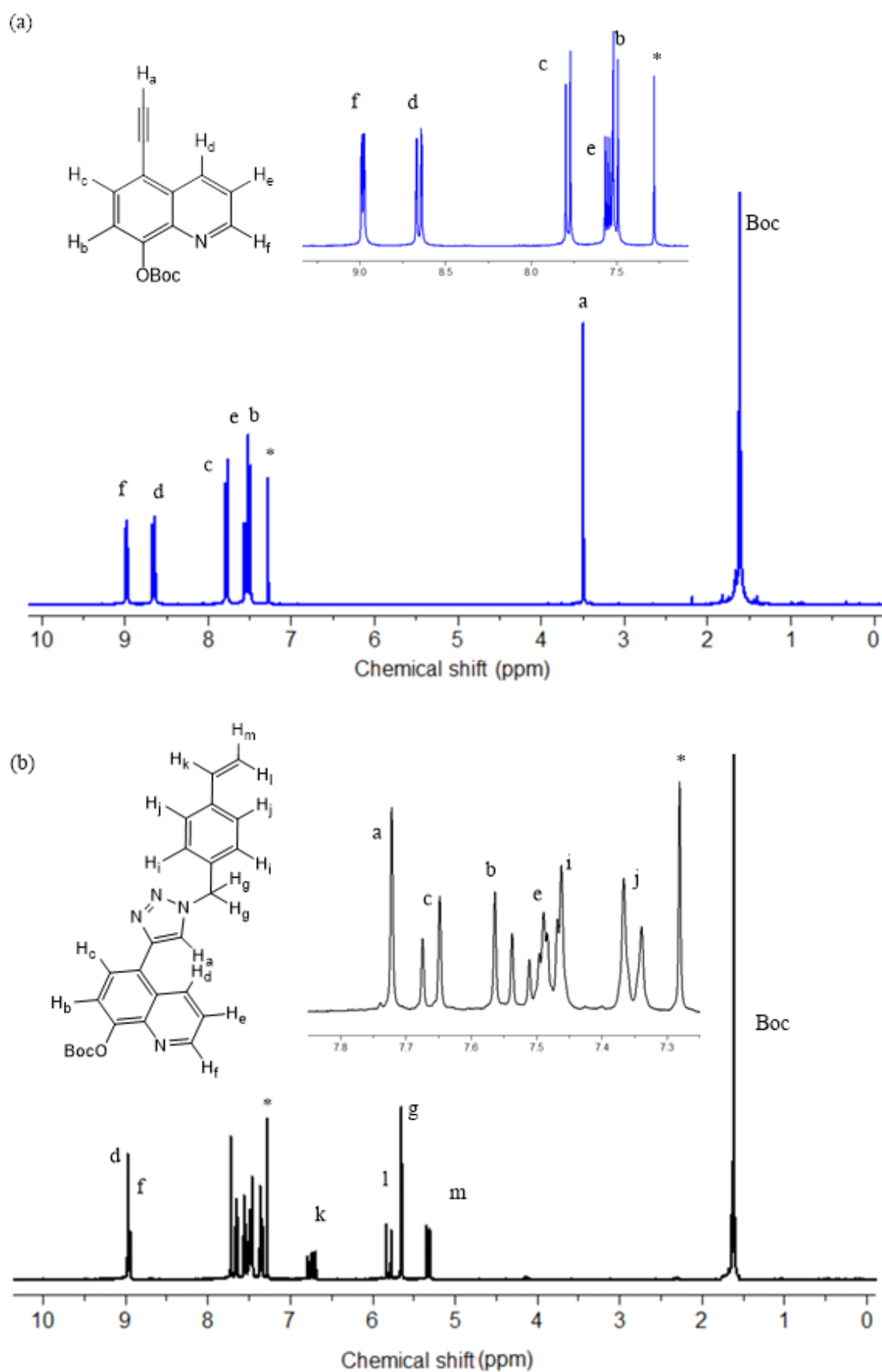


Figure 5.2. ^1H NMR spectra of precursor **3** (a) and QuiBoc monomer **5** (b).

In the FTIR spectrum of QuiBoc monomer (Figure 5.3), characteristic bands of precursor **3** are no longer observed: (i) stretch of the terminal alkyne at 3255 cm^{-1} ; (ii) bending of $-\text{C}\equiv\text{CH}$ presented by two bands at 635 cm^{-1} and 878 cm^{-1} ; (iii) weak stretch $-\text{C}\equiv\text{C}-$ at 2100 cm^{-1} and (iv) the C-H scissoring at 1472 cm^{-1} . Instead, the medium band at 1346 cm^{-1} indicated alkyl $-\text{CH}_2-$ deformation. The sharp band at 3112 cm^{-1} (stretching vibration) and 917 cm^{-1} (bending vibration) indicates the presence of alkenyl group. It is important that the protecting group is preserved throughout the synthetic route (band observed at 1750 cm^{-1}).

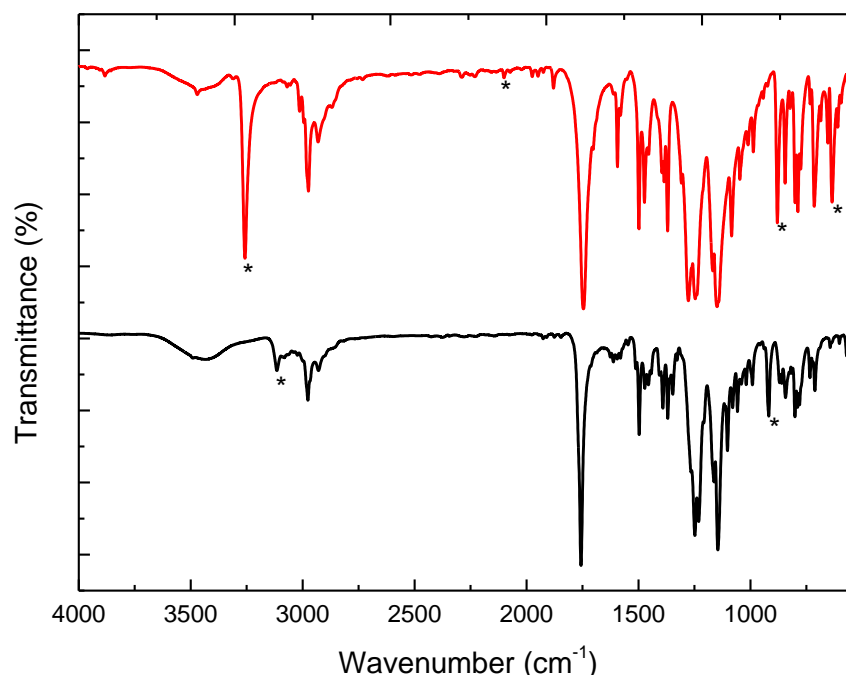
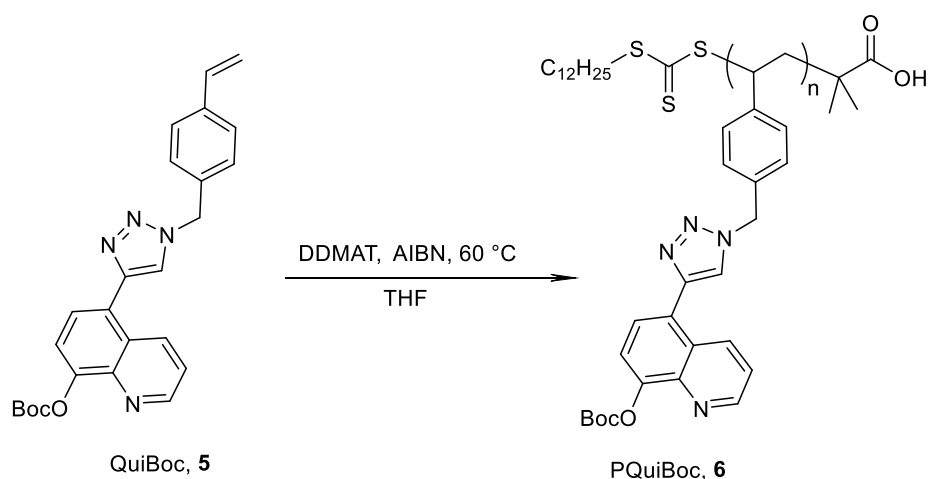


Figure 5.3. FTIR spectra of the monomer precursor **3** (top red) and monomer QuiBoc **5** (bottom black). Characteristic bands mentioned in the text are indicated with the asterisks*.

5.3.2. Polymerisation and deprotection

As has been discussed in Section 3.3.2, controlled RAFT polymerisation provides many advantages over conventional polymerisation. Here, RAFT was employed to produce well-defined polymers from 8-hydroxyquinoline bearing monomer QuiBoc **5** (Scheme 5.3).

As for PDMS/PDHS polymers reported in Chapter 3, 2-(dodecylthiocarbonothioylthio)-2-methylpropionic acid (DDMAT) was chosen as the CTA, owing to its efficiency in polymerisation of other styrene-based monomers. Based on the previous results, the initiator to CTA ratio was set to 1:1 ($[\text{AIBN}]_0/[\text{DDMAT}]_0 = 1.0$).



Scheme 5.3. RAFT polymerisation of QuiBoc monomer **5**.

The solvent, as well as the monomer concentration, was chosen based on solubility studies of the monomer in various organic solvents. QuiBoc monomer is only partially soluble in toluene, thus toluene cannot be used for the controlled polymerisation, whereas THF allowed a solvent to solids ratio of 10:1 (*i.e.* 10 ml of THF per 1 g of QuiBoc) to be attained. Polymerisations of QuiBoc with targeted D_p of 20, 40 and 100 were attempted; their results are summarised in Table 5.1.

Table 5.1. Summary of monomer conversion and molar mass data for the homopolymerisation of QuiBoc using AIBN and DDMAT in THF at 60 °C.

Target D_p	Time (h)	Conversion ^a (%)	$M_n^{\text{th b}}$ (kg/mol)	M_n^c (kg/mol)	D_p^a	M_w/M_n^c \mathcal{D}
20	36	91	8.9	6.2	14	1.29
40	42	84	17.5	12.4	28	1.24
100	-	-	43.3	-	-	-

(a) Calculated using ^1H NMR spectroscopy.

(b) Calculated based on the monomer conversion.

(c) Calculated by GPC against polystyrene standards in THF at 40 °C.

As can be observed from Table 5.1, polymerisation of QuiBoc with $D_p = 100$ was not successful. When all components of the system were charged into the flask and stirred during degassing, precipitation of the monomer from solution immediately took place. This could be attributed to the fact that small amount of DDMAT (the only component that was varied) did not prevent PQuiBoc complexation or crystallisation of the monomer and decreased its solubility in THF. Precipitation of the components from solution was observed if no DDMAT was added. Higher loads of DDMAT prevent the crystallisation of monomer out of solution.

The GPC traces of two final polymers, PQuiBoc₁₄ and PQuiBoc₂₈, are presented in Figure 5.4. It can be seen that the polymer peak for PQuiBoc₂₈ has a low molar mass shoulder, whereas the PQuiBoc₁₄ peak is unimodal. PQuiBoc was soluble in chlorinated organic solvents, such as chloroform, dichloromethane, and non-chlorinated polar aprotic solvents, such as acetone and tetrahydrofuran, partially soluble in diethyl ether at room temperature and completely insoluble in cold ether, hexane, toluene, alcohols and water.

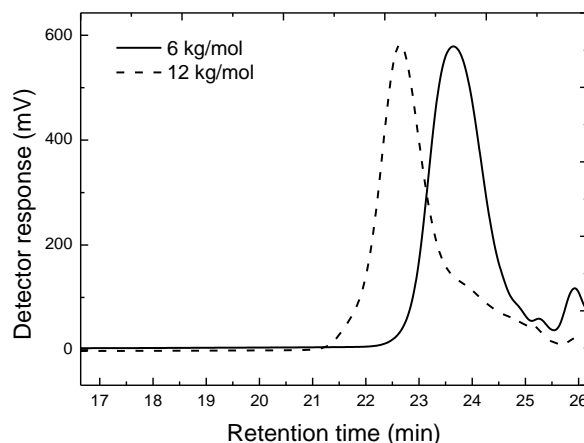
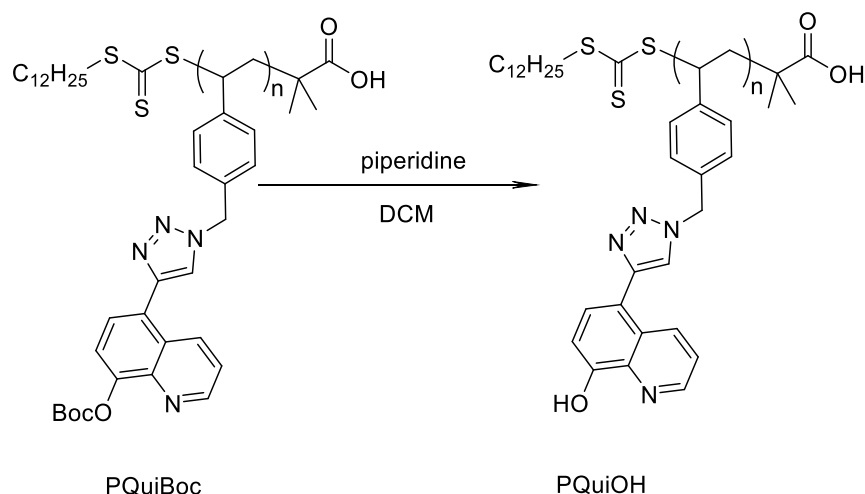


Figure 5.4. GPC traces of PQuiBoc₁₄ and PQuiBoc₂₈ produced by RAFT under following conditions: [AIBN]₀/[DDMAT]₀ = 1.0, QuiBoc:THF = 1:10 at 60 °C.

The removal of the BOC protecting group by both chemical and thermal treatment has been reported.^{13,14} Chemical treatment of the polymer with piperidine (basic deprotection) yielded a slightly yellow polymer, soluble in orthogonal (to its parental polymer) solvent, methanol (Scheme 5.4).



Scheme 5.4. Basic deprotection of PQuiBoc polymer with piperidine in solution.

The ¹H NMR spectra of PQuiBoc and resulting PQuiOH are presented in Figure 5.5. As can be seen from the spectra, the biggest changes are apparent in the aromatic region of the

spectra. Firstly, appearance of a new peak at 9.5 ppm can be observed, associated with cleavage of the BOC group to yield free aromatic hydroxyl group. Secondly, the broad peak at 1.5 ppm, corresponding to nine methyl protons of the BOC group, is not present in the spectrum of PQuiOH. Thirdly, the peak pattern in the aromatic region of PQuiOH is different from that of PQuiBoc, with some peaks becoming broader and some peaks shifting to the higher field regions, owing to the chemically different environment produced by the presence of the hydroxyl group on the aromatic ring.

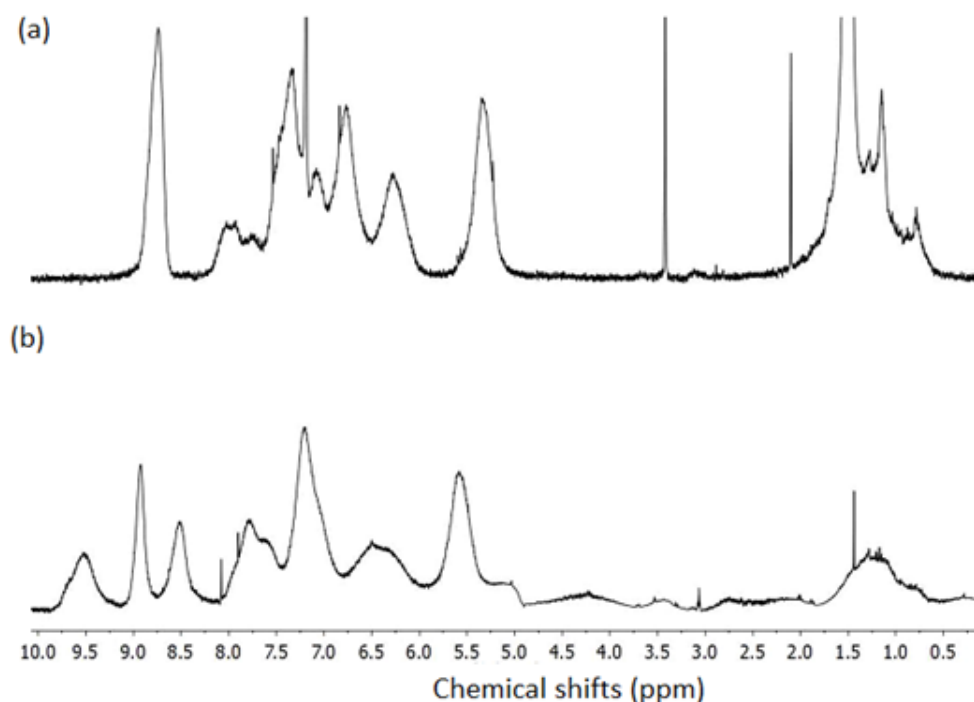


Figure 5.5. ^1H NMR spectra of PQuiBoc (a) and the corresponding deprotected PQuiOH (b).

To estimate the temperature of thermal removal of the BOC group, DSC measurements were performed (Figure 5.6). In agreement with previous literature reports, an endothermic peak with an onset at 160 °C and a midpoint at 175 °C is observed. This peak originates from cleavage of the BOC group and is no longer present in the second heating run. Furthermore, two other distinct thermal events can be seen. A broad peak at low temperatures is a measuring artefact, due to the presence of moisture in the sample during measuring. The glass transition temperature of PQuiBoc is clearly observed with an onset of 140 °C. Thus, BOC-group cleavage occurs in the bulk just above the glass transition of the polymer and is apparently accompanied by melting of the crystalline part of the polymer, resulting in a double peak at 160 °C. Interestingly, in the second heating run, the melting peak is no longer observed, but the T_g of the polymer after BOC group removal remains the same.

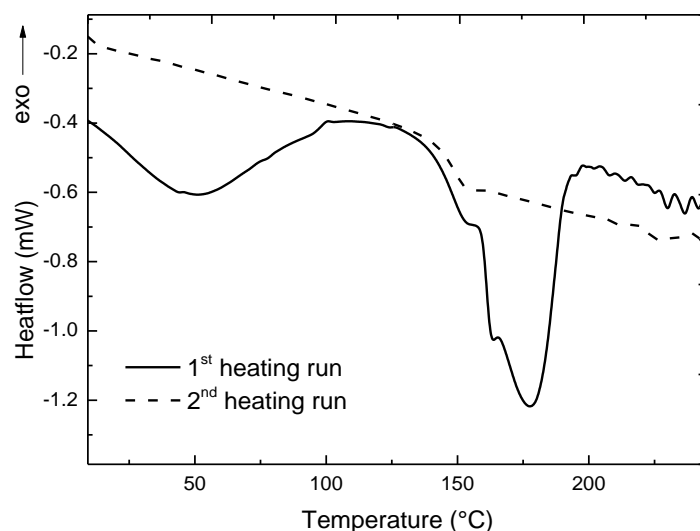


Figure 5.6. DSC thermograms of PQuiBoc₂₈ polymer.

For thermal deprotection, the films of PQuiBoc polymer were spin-coated onto glass substrates and heated in the air at 160 °C for 20 minutes. FTIR spectra of the pristine and heated films are shown in Figure 5.7. From the FTIR spectra it is clear that the aforementioned treatment is sufficient for complete removal of the BOC group. First of all, the carbonyl stretching band at 1760 cm⁻¹ is absent in the PQuiOH spectrum, and, secondly, a new band for O-H stretching is observed at 3370 cm⁻¹ which agrees with H-bonded hydroxyl groups (typical for thin film hydroxyl group arrangement).

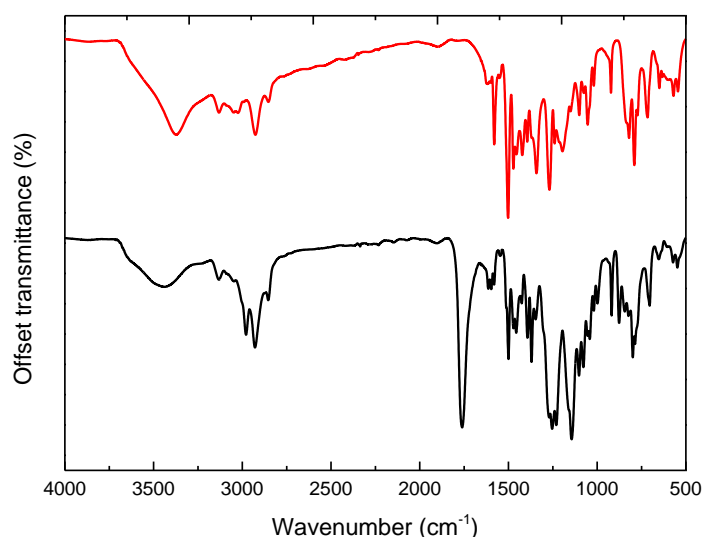


Figure 5.7. FTIR spectra of PQuiBoc₂₈ (black) and resulting PQuiOH₂₈ (red).

All further studies, including spectroscopic, electric studies and device fabrication, were performed using PQuiBoc₂₈ with molar mass approximately 12.4 kg/mol. For neatness, the degree of polymerisation is no longer denoted.

5.4 Optical and electronic properties

To understand the optical and electronic properties of PQuiBoc, UV-Vis spectroscopy and photoluminescence measurements were performed. As can be seen from the UV-Vis spectra (Figure 5.8), upon polymerisation the position of the main absorption maximum at ca. 310 nm is essentially unchanged. On the other hand, there is a significant decrease in absorption in the UV region at 262 nm (indicated with an arrow in Figure 5.8) upon polymerisation which can be explained by the loss of conjugation extension with the loss of the double bond electrons. Interestingly, when deposited as a thin film on quartz glass, PQuiBoc shows broad bathochromically shifted absorbance bands. The main aromatic absorbance at 310 nm is shifted to 325 nm and the deeper UV absorbance band is also shifted from 242 nm to 252 nm wavelength. This simultaneous small shift of all peaks suggests that this is not an electronic effect and it does not originate from the molecular stacking in the solid state, since it can actually be a solvent-dependent transition. Interestingly, significant broadening of the spectra in solid state is not typically observed and in this case is indicative of light scattering in the sample. Indeed, the films of PQuiBoc are not transparent due to aggregation of the polymer into micrometer scale structures as is discussed in the next sections.

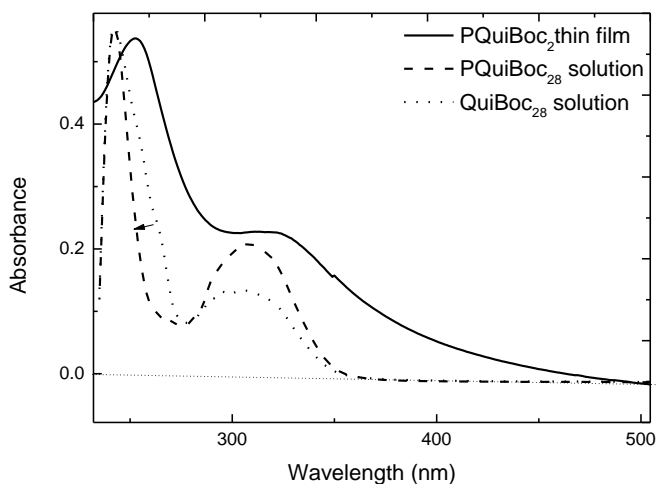


Figure 5.8. UV-Vis absorbance spectra of QuiBoc monomer in solution (dotted line), PQuiBoc polymer in solution (dashed line) and thin film (solid line). Quartz absorbance spectrum (dotted line) used to determine the baseline.

On the other hand, the photoluminescence spectra show that the emission of the monomer with a maximum at 400 nm evolves upon polymerisation into a very broad, bathochromically shifted band with a peak maximum at 450 nm (Figure 5.9). The bathochromic shift can have two explanations: (i) changes in the LUMO level of the polymer compared to monomer, or (ii) tight interactions that would lead to π - π stacking within the same molecule. A minor

hypsochromic shift is observed in the thin film spectrum, compared to that in solution, indicating the effect of solvent on the emission maximum.

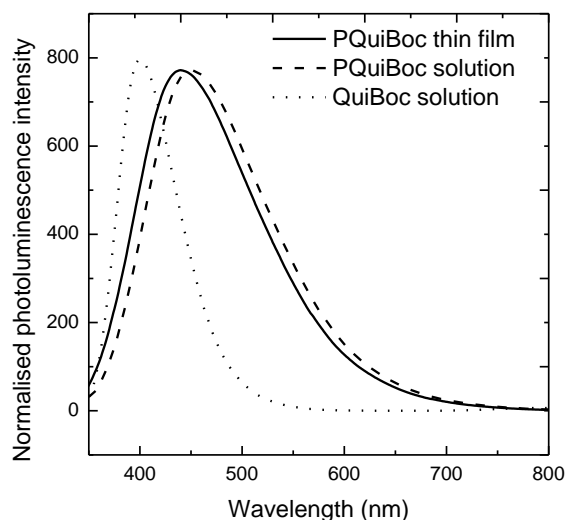


Figure 5.9. Normalised photoluminescence spectra of QuiBoc monomer in solution (dotted line) and PQuiBoc polymer in solution (dashed line) and in a thin film (solid line).

To obtain more insight into the spectral changes upon polymerisation, (time-dependent) density functional studies, (TD) DFT, were performed by Dr Johannes Gierschner at IMDEA Nanociencia (Madrid). First, the optimal geometry of the monomer was established to give an insight into possible intramolecular stacking axes (Figure 5.10).

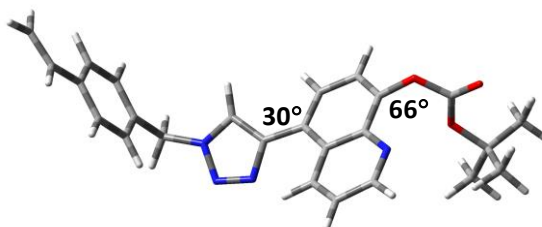


Figure 5.10. DFT calculated geometry of the QuiBoc monomer.

According to the TD DFT results (Table 5.2), the main absorption band of the monomer arises from the electronic transition to the first excited singlet state ($S_0 \rightarrow S_1$), calculated at 320 nm, close to the experimental value (310 nm). The excitation is ascribed to the HOMO \rightarrow LUMO transition, where the LUMO is localised in the quinoline unit (Figure 5.11) and the HOMO is delocalised over the quinoline and triazole units despite a significant twist of 30° (Figures 5.10 and 5.11). Since polymerisation does not affect the frontier molecular orbitals (MO), the main band of the polymer is identical to the monomer (Table 5.2 and Figure 5.11).

Table 5.2. Theoretical energies (E) of the electronic transition to the first excited singlet state (S_1) for the QuiBoc monomer and PQuiBoc, with oscillator strength (f) and configuration interaction (CI) description, as obtained from TD DFT modelling.

System	E eV (nm)	f	CI
Monomer QuiBoc	3.87 (320)	0.26	H→L (96%)
Polymer PQuiBoc	3.86 (320)	0.24	H→L (96%)

The deep UV absorption band of the monomer at 242 nm arises essentially from the styryl unit, which forms the HOMO-1 and LUMO+1 orbitals. Upon polymerisation, the C=C double bond is converted into a single bond, which causes a significant destabilisation of HOMO-1 and stabilisation of LUMO+1, resulting in a significant hypsochromic shift of the absorption band which is out of range of the spectra recorded.

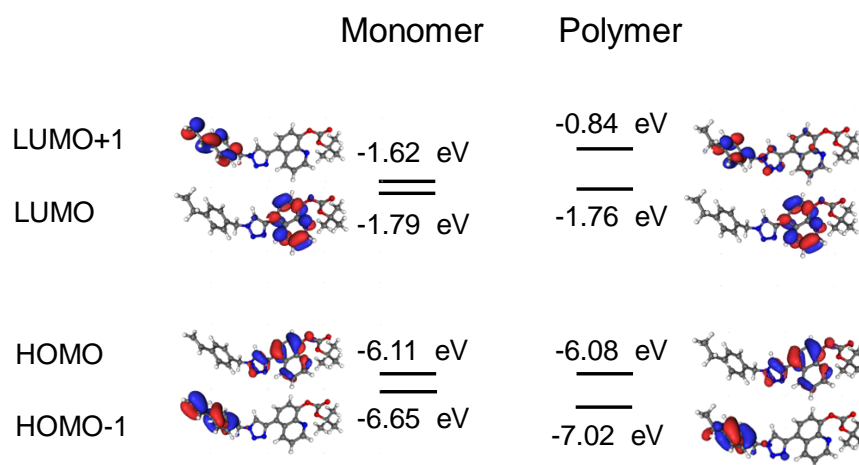


Figure 5.11. Frontier MOs of the monomer and polymer, calculated by TD DFT modelling.

Since according to Kasha's rule the emission originates from the lowest excited state (S_1), one might expect very similar fluorescence features for the monomer and polymer where the emission is of monomolecular origin.¹⁵ Thus, the strong bathochromic shift of the polymer emission (50 nm shift) is ascribed to the appearance of excimers, which are easily formed from the closely packed triazole-quinoline units. An excimer (or excited dimer) is a dimeric excited state formed by two or more stacked molecules or in some cases neighbouring repeat units of a polymer chain that share one bonded electronic surface only upon excitation.¹⁶ As a result, excimers normally have shorter lifetimes, but lower LUMO energies. In the case of PQuiBoc, the excimers are indicative of monomer stacking within one polymer chain which could be beneficial for facile charge transfer.¹⁷

To estimate the actual HOMO and LUMO levels of both monomer and polymer and how they correspond to the modelling results, cyclic voltammetry was employed. The measurements were made on thin films cast from a chloroform solution onto the platinum working electrode in order to best approximate the electronics of these materials in solid films in devices. The first reduction of PQuiBoc occurred with an onset of -1.3 V *versus* ferrocene (Fc). The LUMO position of this polymer is estimated at -3.7 eV (± 0.1) with reference to a 428 mV (5.1 eV) ferrocene halfwave potential. This LUMO position is well in line with that of 8-hydroxyquinoline (-1.8 eV *versus* Fc/Fc⁺), albeit lowered by 0.4 eV due to the electron-withdrawing triazole ring.¹⁸ Similar results were found for the monomer QuiBoc with LUMO values of -3.8 eV. In each case, the reduction cycles were irreversible.

The HOMO level of the polymer can be estimated from its optical bandgap using Equation 5.1 (Table 5.3):

$$\text{HOMO level energy,} \quad \text{HOMO} = \text{LUMO} - E_{g,\text{opt}} \text{ (eV)} \quad (\text{Equation 5.1})$$

It has to be noted that since the solid state UV-Vis spectrum is broadened due to very high level of light scattering in the film, it is not appropriate to estimate the optical band gap from solid state absorbance onset. Although the optical band gap estimated from the solution spectra is not precise, it gives an insight into the energy levels redistribution upon polymerisation.

Table 5.3. HOMO and LUMO levels of QuiBoc and PQuiBoc as estimated from cyclic voltammetry and UV-Vis absorption spectroscopy.

Compound	E _{red} (V) vs Fc/Fc ⁺	LUMO (eV)	E _{g,opt} (eV) ^a	HOMO ^b (eV)
QuiBoc monomer	-1.3	-3.8	3.4	-7.2
PQuiBoc polymer	-1.4	-3.7	3.4	-7.1

(a) Calculated from the UV-Vis absorption spectra in solution.

(b) Calculated according to Equation 5.1.

Obtained LUMO values for both monomer and polymer are very similar, in agreement with the modelling results, indicating that the bathochromic shift in the fluorescent spectrum is not associated with the difference in the first excited state (LUMO) energies, but with the self-organisation of the monomer units in the polymer.

Furthermore, the absorbance of PQuiBoc on ZnO and glass surfaces was studied at various annealing temperatures (Figure 5.12). PQuiBoc films were spin-coated onto the surface of ZnO and annealed for 20 min at T_g (140 °C) and T_{dep} (160 °C). In contrast to PQuiBoc deposited on glass, PQuiBoc on ZnO surface has more structured bands which are

hypsochromically shifted from 252 nm to 241 nm for the deep UV band and from 321 to 314 nm, for the main absorbance maximum. Thus, PQuiBoc deposited onto ZnO has similar absorbance to that of PQuiBoc in solution, suggesting the extent of the polymer aggregation to be different on ZnO surface.

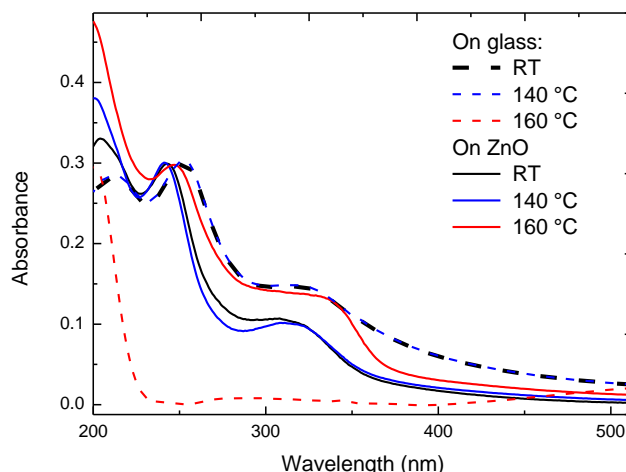


Figure 5.12. UV-Vis absorbance spectra of PQuiBoc polymer deposited onto glass (dashed lines) and ZnO surface (solid lines) and annealed at different temperatures.

PQuiBoc samples, as deposited and those annealed at 140 °C (T_g), have very similar absorbance spectra, indicating that there are no changes in electronic levels and therefore no electron transfer processes between ZnO and PQuiBoc layers. At this temperature, only chain rearrangement occurs in the polymer which does not lead to any change in electronic properties.

In contrast, upon deprotection of the polymer at 160 °C on glass, the main absorbance band disappears. This means that the transition to the first excited state in the polymer is complicated by the absence of the BOC protecting group, demonstrating its importance for stabilisation of the LUMO level. This statement is difficult to associate with the HOMO/LUMO distribution models (Figure 5.11) where the protecting group is barely responsible for the energy level redistribution.

On the other hand, when PQuiBoc is deposited and deprotected on ZnO, the main absorbance band bathochromically shifts from 321 nm to 337 nm. This agrees with an expected change of electronic levels of PQuiBoc upon deprotection and binding to ZnO as these processes occur concomitantly.

Further explanation of the binding process was obtained from the photoluminescence spectra (Figure 5.13). Clearly, upon deprotection and binding to zinc, the emission peak red shifts to 570 nm where the emission has yellow colour in agreement with emission colour of

the Znq_2 complexes reported by Hamada *et al.*¹ According to the observations from the absorbance spectra, deprotected PQuiOH has no excitation maximum at 330 nm and does not have any emission, indicating that BOC protecting group plays an important role in stabilisation of excited state of PQuiBoc.

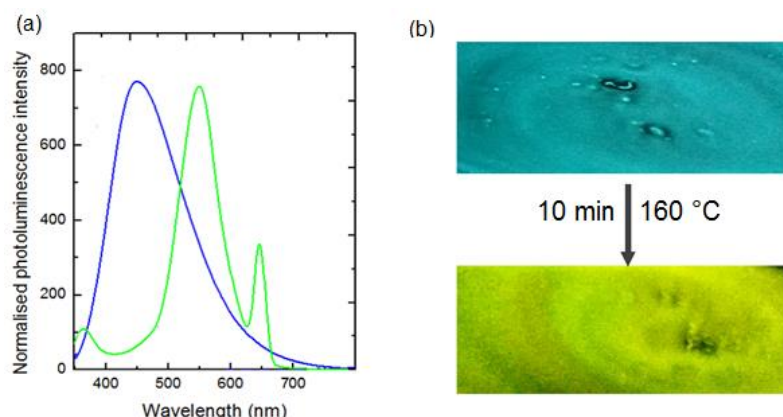


Figure 5.13. (a) Photoluminescence spectra of PQuiBoc film on ZnO before (blue line) and after deprotection (green) and (b) corresponding photographs of the films illuminated with a UV lamp at 330 nm.

5.5. Thin-film studies

5.5.1 SEM EDXA

A zinc binding experiment was performed as described in Section 3.5.1. The zinc binding capacity of the polymer was measured indirectly by assessing the zinc surface coverage using SEM/EDXA. As described in Section 3.5.1, this technique allows simultaneous observation of the surface features together with measuring the deposition of heavy metals (zinc) on the surface. This method is only semiquantitative, but it allows comparison of samples in terms of zinc binding capacity.

Here, zinc oxide (ZnO) nanoparticles were used to study zinc binding capacity to better correlate the results to binding of the polymer to the ZnO surface in a real device. They were deposited onto the polymer films from aqueous suspension, and, after annealing, the films were thoroughly washed to remove all non-bound ZnO from the surface. As shown for PDMS and PDHS (Section 3.5.1), the molar mass of the polymer had no effect on the zinc binding capacity of the polymer films, therefore for PQuiBoc only one molar mass was studied, 12.4 kg/mol (D_p of 28). In the case of PQuiBoc, the effect of the protecting group on zinc binding was important for its ZnO binding capacity. To study it, the polymer was annealed at 140 °C (T_g) and at 160 °C (T_{dep}).

When PQuiBoc was annealed at T_g (140 °C), ZnO surface coverage was shown to be 72% ($\pm 3.1\%$)¹, comparable to that resulting from the polymer annealed at its deprotection temperature (160 °C) for the same time (69%, $\pm 2.5\%$). These findings indicate that the protected PQuiBoc is also capable of forming bonds with ZnO, probably based on hydrogen bonds or van der Waals interactions. Indeed, BOC group has two oxygen centres to form hydrogen bonds with the surface hydroxyl groups, present in ZnO nanoparticles. Polystyrene, PS₂₄₀, used as a control showed negligible ZnO binding of 4.1% ($\pm 1.2\%$). Interestingly, this was different from previous measurements (for PDMS and PDHS, Section 3.5.1), where polystyrene had surface zinc coverage of 11%. This difference is attributed to the fact that in the previous measurements, zinc acetate was used for SEM/EDAX analysis. Zinc acetate and ZnO nanoparticles have different compositions and would establish a different binding pattern, thus, resulting in difference of surface coverage.

Furthermore, SEM images demonstrate, a change in quality of the formed films (Figure 5.14). PQuiBoc, annealed at 160 °C, resulted in visibly smoother films than if annealed at 140 °C. This smoothing is associated with the polymer deprotection and more extensive annealing and was further probed by means of atomic force microscopy (AFM). In terms of smoothing, it is difficult to decouple the effect of prolonged annealing from the deprotection.

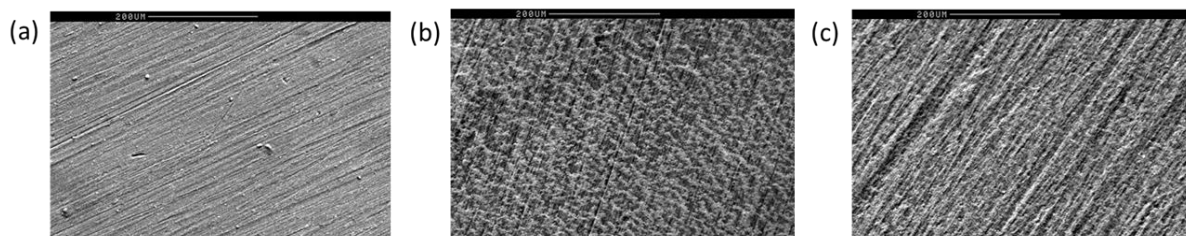


Figure 5.14. SEM images of the polymeric films with ZnO nanoparticles on the surface: (a) polystyrene, PS₂₄₀; (b) PQuiBoc annealed at 140 °C and (c) PQuiBoc annealed at deprotection temperature 160 °C.

5.5.2 Atomic Force Microscopy (AFM)

To study the surface topology of the films formed by PQuiBoc on the surface of zinc oxide (in contrast to SEM studies in Section 5.4.1, where ZnO was deposited onto the polymer surface), AFM measurements were performed in tapping mode. Topography images for PQuiBoc annealed at different temperatures are shown in Figure 5.15.



Figure 5.15. AFM topography images and corresponding 3D representations of PQuiBoc deposited on glass (a, e), deposited on ZnO (b, f) and annealed at 140 °C (c, g) or 160 °C (d, h).

It can be seen that the polymer has different affinities for different substrates. On glass, it forms cone-shaped structures that reach 1 μm in diameter and 140-180 nm in height, whereas the structures formed on a ZnO surface are more elliptical in base and have dimensions of 400-500 nm width, up to 1 μm length, and height of pillars varying from 80 to 130 nm. The difference in substrate affinities originates from possible bonds between the polymer and the substrate. As seen in Section 5.4.1, PQuiBoc polymer has a certain binding affinity for ZnO and thus, would rearrange into smaller features to allow better binding. On the other hand, this affinity of PQuiBoc for ZnO is far less pronounced than the dewetting of the film upon deposition.

Annealing of the polymer at 140 °C induces changes in the polymer topography so that the pillars smoothen and the roughness decreases (R_a 2x2 = 47 nm to R_a 2x2 = 39 nm). On the

other hand, the height of the pillars increases up to 160-180 nm. Deprotection of the polymer at 160 °C reduced the size of the pillars to 15-35 nm height and roughness to 11 nm due to rearrangement of the polymer chains for better binding to ZnO (better wettability).

Doctor blading of the P3HT:PCBM (1:0.8) active blend from 27 mg/ml xylene solution can yield films of 200-300 nm thickness, whereas spin-coating the same solution at 4,000 ppm can yield films even thinner (ca. 100-200 nm). Clearly, since the topographical features of PQuiBoc are so pronounced, the morphology of the PAL deposited onto PQuiBoc layer will be majorly affected by these features. Topography AFM images of the PAL deposited by spin-coating onto PQuiBoc are presented in Figure 5.16.



Figure 5.16. AFM topography images and corresponding 3D representations of P3HT:PCBM blend deposited by spin-coating from 27 mg/ml xylene solution at 4,000 rpm onto PQuiBoc non-annealed (a, e), annealed at 140 °C (b, f) and annealed at 160 °C (c, g) and also blend deposited directly onto ZnO (d, h). Schematic representation of each image shows blue pillars of PQuiBoc on ZnO and PAL (purple) deposited on the PQuiBoc surface.

Clearly, the pillars can be observed on the surface of the PAL deposited onto non-annealed PQuiBoc and annealed at 140 °C. The pillars on the surface of the PAL deposited onto non-annealed PQuiBoc are smaller than those of PQuiBoc only; they are maximum 10 nm high and 200 nm diameter (Figure 5.16, a and d) *versus* 0.5 μm diameter and 120 nm height pillars of PQuiBoc on ZnO.

Annealing of PQuiBoc at 140 °C on ZnO gave very big features of 160-180 nm height, but after deposition of the PAL, the features on the surface were 40-50 nm high and only 150-200 nm diameter (Figure 5.16, b and f). Assuming the thickness of the PAL [$d(PAL)$] to be similar in both samples, it can be approximately calculated from Equation 5.2:

$$\text{PAL thickness, } d(PAL) = h(PQuiBoc) - h(PQuiBoc+PAL), \quad (\text{Equation 5.2})$$

where $h(PQuiBoc)$ is the height of the pillars in PQuiBoc films and $h(PQuiBoc+PAL)$ is the height of the features on the surface of PAL deposited onto the PQuiBoc layer. Following these simple calculations, the thickness of the active layer deposited by spin-coating is 100-180 nm, which agrees with what was expected for the films of P3HT:PCBM, spin-coated from xylene solution of 27 mg/ml at the spin speed of 4,000 rpm.

Deprotection of PQuiBoc prior to deposition of PAL blend allowed an active layer with a smooth surface with an average roughness of $R_a \text{ } 2 \times 2 = 3.5 \text{ nm}$ to be fabricated. Moreover, fold-like features of 100-200 nm length and 4-6 nm height are observed on the topography images (Figure 5.16, c and g), whereas the surface of the PAL deposited directly onto ZnO is clearly featureless and smooth ($R_a \text{ } 2 \times 2 = 1.5 \text{ nm}$), with only measurement artefacts present.

It is difficult to estimate what implications this organisation of the PAL on the PQuiBoc surface has for the domain distribution within the photoactive blend or the device performance. These aspects are addressed in the further sections and correlated to the AFM topology of the films.

5.6. Quinoline polymer for electron transport

5.6.1 Device studies

Due to very deep HOMO levels, PQuiBoc has potential as a hole-blocking material. Even more so, the LUMO and HOMO levels of the polymer are very close to those of ZnO which is often used as a hole-blocking electron-transporting layer.¹⁹

PQuiBoc was incorporated into the cells as an electron-transporting layer to replace the ZnO layer in an inverted device. This followed two basic ideas: (a) to enhance electron transport through surface energy modification and (b) due to the fluorescence of the polymer upon UV excitation to increase the EQE through harvesting of the UV photons and converting them into usable visible photons (Figure 5.17).

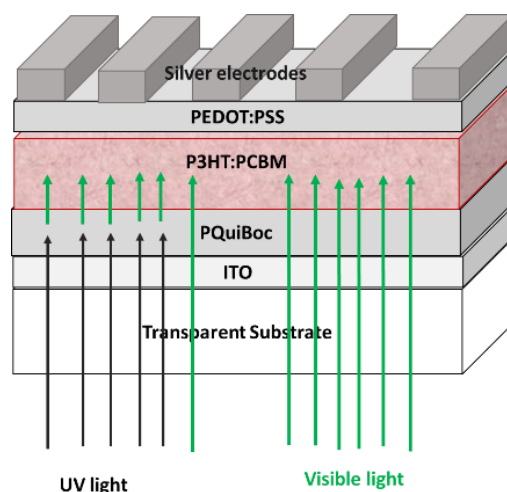


Figure 5.17. Schematic representation of the inverted architecture device stack with PQuiBoc as an electron-transporting layer.

In this study, PQuiBoc was deposited directly onto ITO from acetone at different concentrations to correlate the effect of layer thickness on the photovoltaic parameters of the devices (Figure 5.18). PQuiBoc was not annealed prior to PAL deposition, since deprotection, as seen in Section 5.3, would alter the electronic levels of the polymer and affect electron transport efficiency. After deposition of the electrode, the devices were annealed for 5 min at 140° C in vacuum to induce favourable nanomorphology of the blend. This is indicated, primarily, by the increase in the current density (J_{sc}) of conventional ZnO devices from 8.3 mA/cm² to 9.3 mA/cm². Other parameters, such as open circuit voltage and fill factor, did not change upon short annealing, indicating that this change is only due to improvements in nanomorphology.

As can be seen from Figure 5.18, the initial performance of the cells with quinoline polymer as an electron-transporting layer was much worse than that of the cells with conventionally used conducting ZnO, due to all performance parameters being lower. Lower fill factor and V_{oc} mainly indicate that the extraction in the sample with the new electron-transporting layer is not as efficient as in ZnO samples.²⁰ The possible reason is enhanced recombination at the PQuiBoc/PAL interface, mainly affecting fill factor and not the current density.

After 5 minutes of thermal treatment the cell parameters improved drastically, and the PCE of the PQuiBoc samples increased from 1.3-1.4% to 2-2.5%. Firstly, this improvement is associated with the increase in current density when the optimal morphology of P3HT:PCBM layer is established, in line with the improvements of ZnO devices. More importantly, increase in V_{oc} from ca. 0.4 V to 0.55 V and slight improvement in FF are observed. The enhancement of V_{oc} is difficult to attribute without further physical measurements, but it is likely to be associated with decrease of surface roughness upon annealing and improvement of ITO surface coverage by PQuiBoc, in line with the data from AFM measurements.

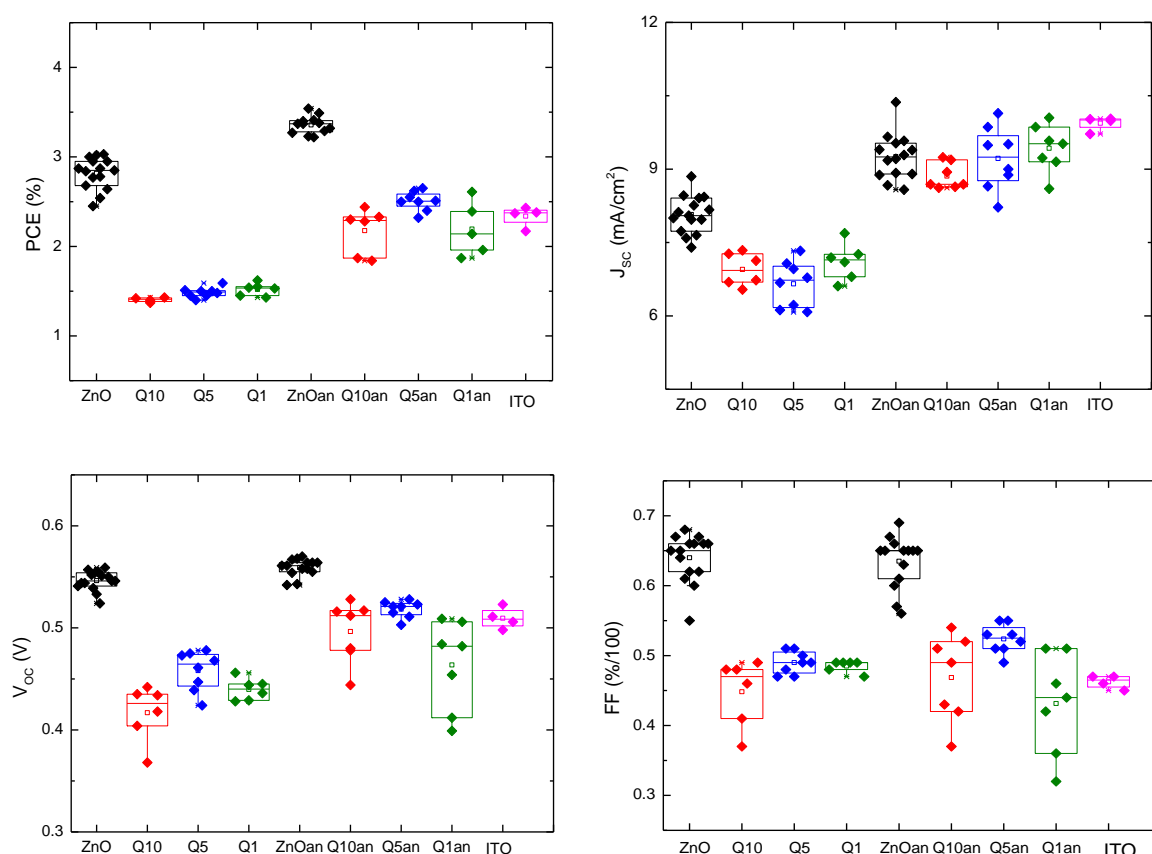


Figure 5.18. Distribution of key photovoltaic parameters of the cells incorporating ZnO and PQuiBoc as electron-transporting layers and bare ITO cells – before and after 5 min annealing at 140 °C (denoted as ‘an’), where QX indicates PQuiBoc layer deposited from X mg/ml acetone solution by doctor blading.

Performance of annealed samples was comparable to that of bare ITO samples, without any electron-transporting layer, although a PQuiBoc layer deposited from 5 mg/ml solution after 5 min of annealing showed superior fill factor (0.53 versus 0.46), indicating that this layer provides certain advantages for electron transport. On the other hand, incorporation of a PQuiBoc layer showed decreased J_{SC} values, which improved for the samples where PQuiBoc was deposited from 1 mg/ml concentration. Assuming the height of the pillars, observed in AFM, was solution concentration dependent, the main reason for the current density loss would be those pillars. As seen from AFM, the pillars would primarily affect the morphology of the blend. If this is the case, then the exciton dissociation and charge generation efficiency would be compromised, and as a result, J_{SC} is less than that in both ITO and ZnO cells even after annealing at 140 °C.

5.6.2. Transient absorption spectroscopy

To verify if the introduction of PQuiBoc pillars affects charge generation and if the change of the active morphology is the main reason for the current density loss, transient absorption spectroscopy studies were carried out on film stacks of ITO/PQuiBoc (10 mg/ml)/PAL, before and after short annealing (5 min at 140 °C). As discussed in Section 1.6, global fitting of the experimental TAS spectrum yields three evolution-associated differential spectra (EADS) with respective contribution of each excited state. These spectra are shown in Figure 5.19. It can be seen from the figure that immediately following excitation in the pristine stack, singlet contributions (both localised and delocalised, S_a and S_o) constitute almost entirely the whole spectrum (Figure 5.19a), whereas the polaron (P_a and P_o) absorption evolution can be observed only after 2 ps.

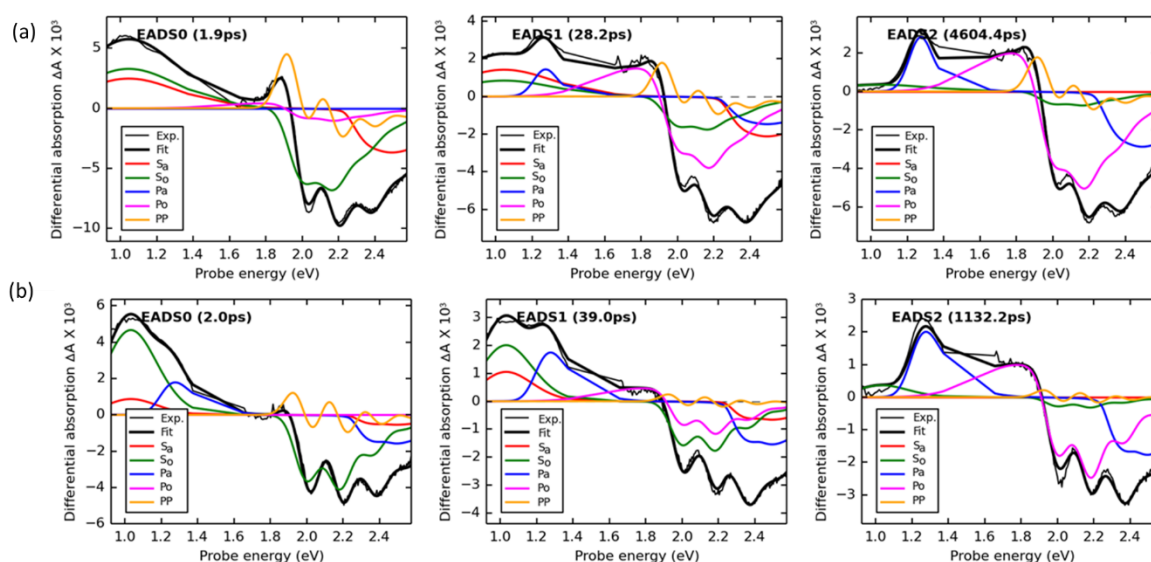


Figure 5.19. EADS of ITO/PQuiBoc (140 °C)/PAL stack before (a) and after 5 min annealing at 140 °C (b), as obtained from a global analysis of experimental TA spectra using a 3 sequential steps model (thin solid curves, fitted lifetimes are given in the legends), spectral fits to the EADS (thick solid curves) and contributions to fits from polaron pair, localised and delocalised singlet exciton and polaron states with their respective bleach contributions (negative differential absorption).

Indeed, calculations of the excited state concentrations showed that ultrafast charge generation in a pristine stack was compromised to the level where it reached only 9%, exclusively owing to delocalised polarons in the ordered phase (P_o), whereas the concentrations of localised (S_a) and delocalised (S_o) singlet excitons in EADS0 were 39% and 52% (Figure 5.20a). Over several hundred picoseconds, the build-up of generated charges was observed so that the total yield of charges available for extraction in EADS2 was 73%, similar to that typical for P3HT:PCBM cells. This means that the charge generation in the pristine PQuiBoc stack was diffusion-dependant, indicating that the size of P3HT

domains exceeds 4 nm, according to Guo *et al.*²¹ Moreover, ultrafast charge generation as low as 9% has never been reported for pristine P3HT:PCBM blends. In opposite, Howard *et al.* observed almost 100% ultrafast charge generation in regiorandom P3HT blends with a low morphological order.²² Thus, 9% ultrafast charge generation means that in pristine ITO/PQIBoc (140 °C)/PAL stack, there is a high extent of domain ordering. Obviously, the introduction of the PQIBoc layer has a detrimental effect on the ultrafast charge generation as it disrupts the donor/acceptor interfaces in the blend.

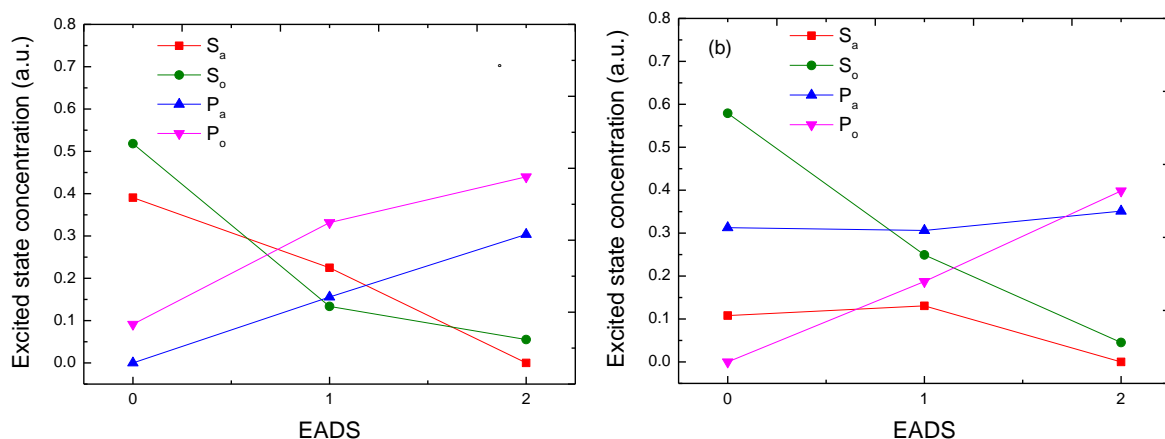


Figure 5.20. Evolution of excited state concentration according to their respective EADS for ITO/PQIBoc (140 °C)/PAL stack before (a) and after annealing (b) for 5 min at 140 °C: localised singlet excitons (S_a , red) and polarons (P_a , blue), delocalised singlet excitons (S_o , green) and polarons (P_o , magenta).

As seen in Figure 5.19b, after 5 min of thermal treatment, localised polaron (P_a) absorbance band appeared in EADS0, indicating improved ultrafast charge generation. On the other hand, the absorbance band of delocalised polarons (P_o) was absent. In total, owing to the localised polaron population, ultrafast charge generation improved to 31% (Figure 5.20b). Moreover, annealing drastically decreased the localised singlet population (S_a) at early times after excitation, allowing their ultrafast dissociation into polarons, but did not induce improvements in dissociation efficiency in crystalline regions of P3HT. In contrast, crystalline P3HT domains increased in size or number, due to the fact that the concentration of delocalised excitons (S_o) increased to 60% from 40%. Previously, annealing has been shown to induce crystallinity in P3HT, improving charge generation.²² From the TAS measurements it might be suggested that some border molecules from the amorphous regions of P3HT crystallised into domains, which consequently increased the available interface area for the excitons generated in the amorphous regions (Figure 5.21).

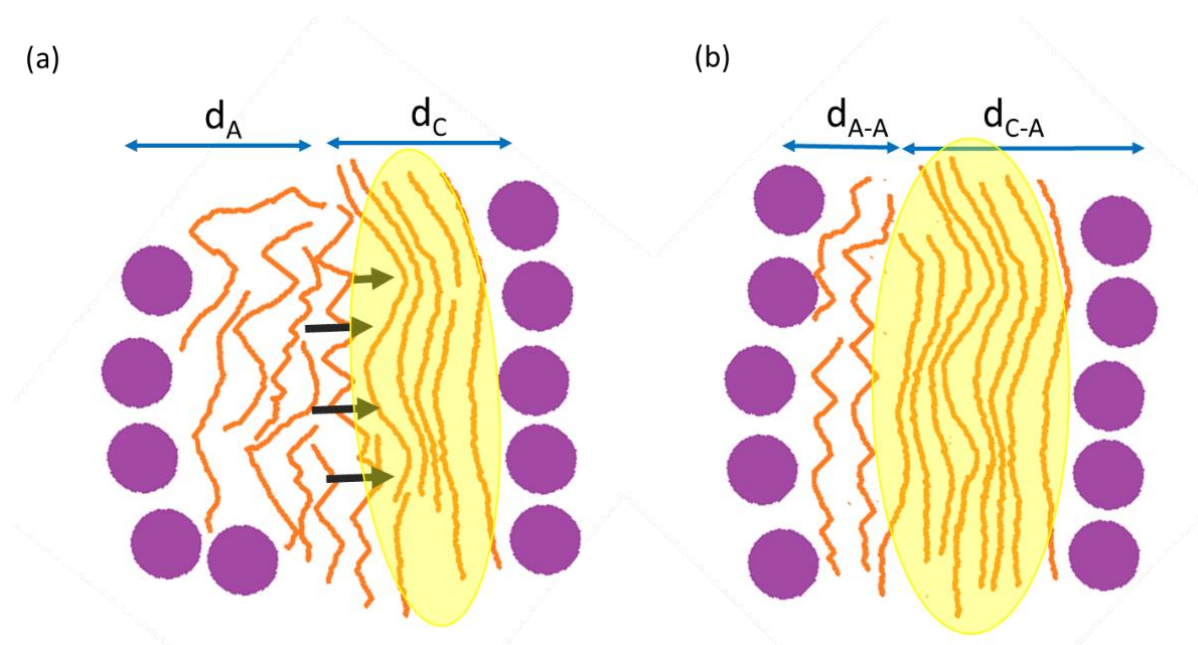


Figure 5.21. Simplified schematic representation of the nanomorphology organisation in P3HT:PCBM blend between two pillars of PQuiBoc (a) before and (b) after annealing at 140 °C for 5 min. Crystalline regions are highlighted with yellow. Migration of P3HT chains (orange) from amorphous region to crystalline region is indicated with black arrows. As a result of this migration, crystalline regions grow in size and the diffusion length for delocalised excitons (d_C) increases after annealing ($d_{C-A} > d_C$) whereas amorphous regions decrease in size and the diffusion length of the exciton in amorphous phase decreases ($d_{A-A} < d_A$).

On the other hand, the growth of crystalline domains only affects ultrafast charge generation. In the last EADS (Figures 5.19b and 5.20b), almost all of the delocalised excitons dissociated, thus increasing the extractable charge yield to 77%. This improvement is reflected by the increase in the current density after annealing from 7.1 to 8.9 mA/cm². In any case, total charge yield and current density in both pristine and annealed devices are typical for P3HT:PCBM cells.

5.6.3 Electron transport in PQuiBoc polymer

As observed from the photovoltaic studies of the devices and transient absorption spectroscopy of the film stacks, PQuiBoc is suitable as an electron-transporting layer, owing to its electronic levels being similar to those of ZnO. However, efficiency of PQuiBoc-incorporating devices is less than that of ZnO devices. Transient absorption spectroscopy measurements allow one to conclude that the blend nanomorphology is not the reason for low PCE, as the J_{SC} values are similar in PQuiBoc and ZnO devices. This is in line with the J -

V curves, where low fill factor and open circuit current are the main reason why PQuiBoc samples were not as efficient as the control samples. Since the fill factor is mostly determined by extraction and recombination at the interface, these are concluded to be less efficient in PQuiBoc than in ZnO devices. The fill factor does not change upon annealing, therefore it is not morphology dependent, and clearly suffers from incorporation of PQuiBoc layer. At the same time, V_{oc} slightly improves suggesting that V_{oc} is partially morphology-dependent and partially interface-dependent, as reported before.²³

Generally, although efficiency of the PQuiBoc devices is not comparable to that of ZnO devices, introduction of the PQuiBoc layer gives some improvement in contrast to bare ITO. Interestingly, the pillars of PQuiBoc formed on the surface disturb the nanomorphology of the layer so that ultrafast charge generation is decreased, but do not affect the total charge yield, and could possibly be used further to prevent phase segregation of the PAL components during thermal degradation, provided the problems of extraction and recombination efficiency at the interface could be solved. To understand what exactly causes enhanced recombination at the interface, further insight into the work function of ITO upon PQuiBoc deposition is needed.

5.7. Quinoline polymer as interfacial layer

5.7.1 Device studies

As initially intended, PQuiBoc in its deprotected form, PQuiOH, would be incorporated into the devices as an interfacial monolayer between the PAL and the electron-transporting ZnO. Upon deposition, however, PQuiBoc formed pillars of different size, dependent on the annealing temperature. Further device studies were carried out to estimate if PQuiBoc on ZnO could be beneficial for electron transport and what effect the reorganisation of the PAL around the pillars of PQuiBoc had on the performance of the cells.

Thus, PQuiBoc was incorporated into devices as an interfacial layer between ZnO and PAL (Figure 5.22), and prior to deposition of the PAL, PQuiBoc was annealed at different temperatures in line with the previous study (Section 5.4.2). The layer was treated in the air at 140 °C { T_g , [PQuiBoc (140)]} and at 160 °C { T_{dep} , [PQuiOH (160)]}. Also, devices without treatment were studied [PQuiBoc (RT)] against the control samples without the PQuiBoc layer. It should be noted that for this study the samples were deposited onto glass substrates, because the T_g of the PET is approximately 140 °C.

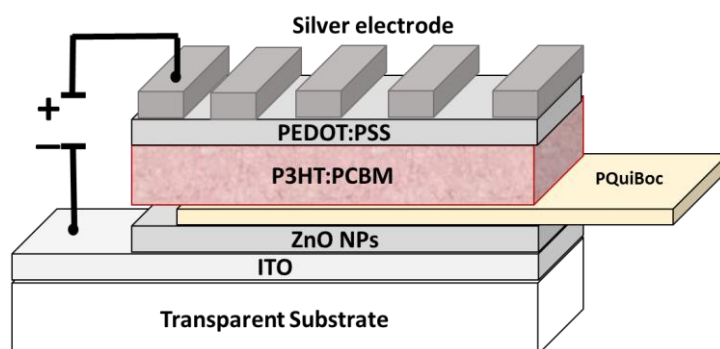


Figure 5.22. Schematic representation of the inverted architecture stack used to study the effect of PQuiBoc polymer as an interfacial layer on the stability of the cells.

Initial photovoltaic parameters for the devices with PQuiBoc annealed at different temperatures are presented in Table 5.4 and representative *J-V* curves in Figure 5.23. As can be seen from the table, the initial efficiency of the cells is compromised in PQuiBoc samples by reduction in fill factor and open circuit voltage, although the current density appears to increase with smoothing, caused by prolonged annealing, as seen previously from AFM.

Table 5.4. Initial average photovoltaic values obtained for solar cells incorporating PQuiBoc annealed at different temperatures, as an interfacial layer between ZnO and the PAL.

Sample	J_{sc} (mA/cm ²)	V_{oc} (mV)	FF	η , PCE, %
Control (no PQuiBoc)	10.13	569	0.62	3.59
no annealing, PQuiBoc (RT)	9.87	567	0.58	3.26
annealed at 140 °C, PQuiBoc (140)	10.22	563	0.51	2.95
annealed at 160 °C, PQuiOH (160)	10.53	555	0.47	2.71

The fill factor, as an indicator of the extraction and recombination processes at the interfaces, decreased with increasing annealing temperature. This is associated with the increase in PQuiBoc layer smoothness, as seen from AFM images (Section 5.4.2), and the ZnO coverage by PQuiBoc layer, as the pillars become smaller. It is difficult to decouple the smoothing effect at 160 °C from deprotection of PQuiBoc and corresponding changes in the electronic levels. In any case, the PQuiBoc layer is detrimental for the extraction, supposedly due to enhanced recombination at the PAL/PQuiBoc interface.

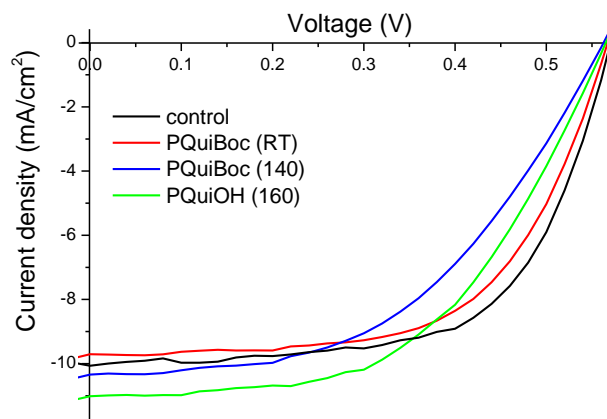


Figure 5.23. Representative *J-V* curves of the devices incorporating a PQuiBoc layer annealed at different temperatures prior to deposition of the PAL.

Furthermore, concomitant reduction of the open circuit voltage is also indicative of the interfacial problems. This could be explained by the charge extraction being hindered at the interface due to (i) increased work function of the ZnO or (ii) strong dipoles that are created upon deposition and then after the first irreversible reduction of the PQuiBoc layer.

On the other hand, the J_{SC} value is increasing with increase of annealing temperature, meaning that the morphology of the PAL benefits from the PQuiBoc layer. One of the reasons might be improved wetting of the PQuiBoc layer by the PAL blend. This arises from the changes in the surface energy; the contact angle for pristine PQuiBoc was 79° and upon annealing it increased to 86° , owing to reorganisation of the layer for better binding to ZnO. Typical water contact angle for ZnO is 30° , much lower than that of P3HT and PCBM (87° and 111° , respectively).^{24,25} Addition of PQuiBoc helps to increase compatibility between ZnO and the PAL. Surface energy modification has been previously shown to be beneficial for the morphology of the blend and leads to improvements in the current density.²⁶ The second possible explanation is that the pillars of PQuiBoc act as a support for the blend morphology. Further work should be carried out to distinguish the input of various factors, to mention transmission electron microscopy to estimate the blend organisation at the surface or ellipsometry to observe the vertical distribution of the blend components.

Further, the effect of the PQuiBoc layer on the stability of devices was studied. Devices with PQuiBoc deposited under different conditions were subjected to thermal stress at 140°C for 330 min in a vacuum, in the dark. Here, it is necessary to stress that post-deposition treatment of PQuiBoc was carried out in air, whereas thermal degradation of the complete cells was performed under inert conditions, to exclude completely any photooxidation or oxidation effects on device performance. Normalised average (for 4 devices) photovoltaic parameters are plotted against degradation time in Figure 5.24.

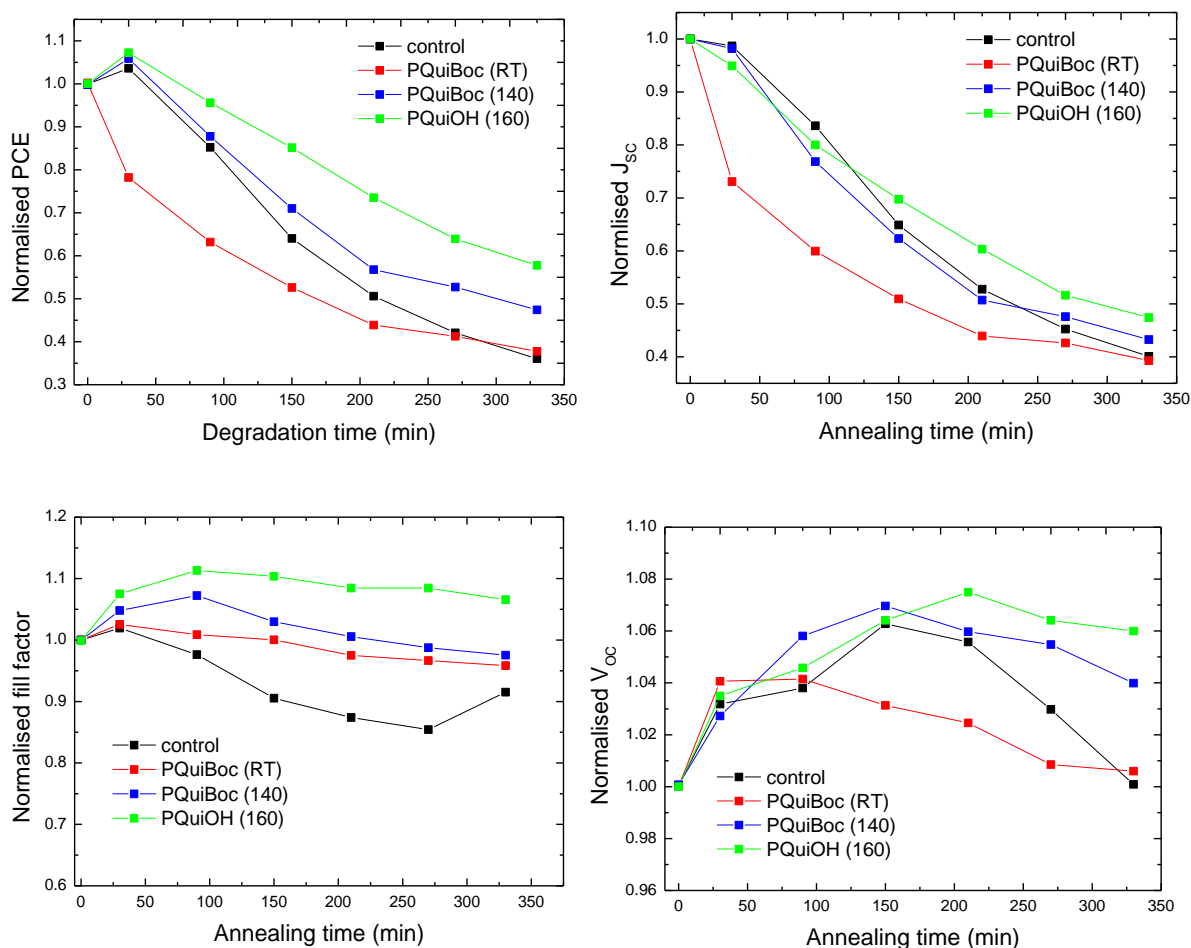


Figure 5.24. Normalised average photovoltaic parameters as a function of degradation time for devices incorporating PQuiBoc interfacial layer annealed at different temperatures post-deposition. Degradation was performed in the dark in vacuum for 330 min at 140 °C.

Figure 5.24 shows that introduction of the PQuiBoc interlayer has an effect on the stability of the devices. Interestingly, with increase of annealing temperature of the PQuiBoc layer, the stability improves. PQuiBoc (RT) shows the fastest loss of initial efficiency, although after 330 minutes the normalised efficiency is higher than that of the control sample, majorly due to a higher fill factor and open circuit voltage. PQuiBoc (140) and PQuiOH (160) enhance the stability of the cells, where all photovoltaic parameters are more stable to thermal treatment than those of the control. Interestingly, with PQuiOH (160), the fill factor experiences improvement over the first hour of annealing, increasing by 13% and then slowly decreasing by 4% in 4 h, whereas in the control, the fill factor quickly loses 15%. Gradual improvement of V_{oc} is also observed for PQuiBoc (140), PQuiOH (160) and the control. In sample PQuiBoc (140) and the control, V_{oc} reaches a maximum value after 120 min of annealing and for PQuiOH (160), after 200 minutes. After reaching the maximum value, V_{oc} remains rather constant with only a slight decrease of 3% in sample PQuiBoc (140), whereas the loss of V_{oc} in the control is approximately 7%, indicating that such long thermal treatment induced changes in the morphology of the sample in agreement with the loss of current density of

almost 60% in all samples. Unfortunately, the PQuiBoc layer did not show any pronounced effect on the current density.

Thus, the PQuiBoc layer annealed at 160 °C post-deposition might be of interest for further studies for the stability of the OPV devices. Obviously, only slight improvements in stability of the current density means that the morphology of the blend is not majorly affected by the PQuiBoc interlayer. In any case, introduction of the PQuiBoc layer was beneficial for the stability of the devices. In PQuiOH (160) the efficiency only dropped down to 58% of its initial value after 330 min of degradation, whereas in control it decreased to 36%. Thus, after degradation, the PCE of PQuiOH (160) was 1.5% ($\pm 0.06\%$) on average, and the PCE of the control was 1.2% ($\pm 0.3\%$). Further optimisation of PQuiBoc/Al interface could improve the initial efficiency and the stability of the device.

5.7.2 Transient absorption spectroscopy

To understand the reason for improvement of the current density in pristine PQuiOH (160) samples, transient absorption spectroscopy was employed to study the effect of the interlayer on the charge generation in the film stack ITO/ZnO/PQuiOH (160)/PAL as a pristine stack and after 3 hours of thermal stress at 150 °C. Global fitting of the experimental TA spectrum yielded three EADS with respective fits, consisting of separate SADS, representing the contribution of each excited state (Figure 5.25).

Evolution of excited states obtained from EADS fitting for P3HT:PCBM blends deposited onto ZnO/PQuiOH (160) and directly onto ZnO is shown in Figure 5.26. As can be seen from Figures 5.25 and 5.26, pristine stacks behave similarly to the typical P3HT:PCBM blends, where immediately following excitation, the main contributors to the absorption spectra are singlet excitons in the amorphous and ordered phases of P3HT (S_a and S_o , respectively) with a comparatively small input from localised polarons (P_a). Similarly to typical P3HT:PCBM blends (Figure 5.26, c and d), delocalised singlets (S_o) dissociated after 1.1 ps, whereas the localised singlets (S_a) persist over time in the big crystalline domains of P3HT, which they cannot escape immediately. Thus, the ultrafast charge yield in PQuiBoc sample was 50%, whereas that of control sample was 61%. The main reason is a lower concentration of delocalised excitons (S_o , 0.29 a.u. in PQuiBoc sample versus 0.18 a.u. in control sample) and higher concentration of localised polarons (P_a , 0.11 a.u. in PQuiBoc sample versus 0.25 a.u. in control sample). Furthermore, the total charge yield reaches 83% in the control sample and 70% in the PQuiBoc sample.

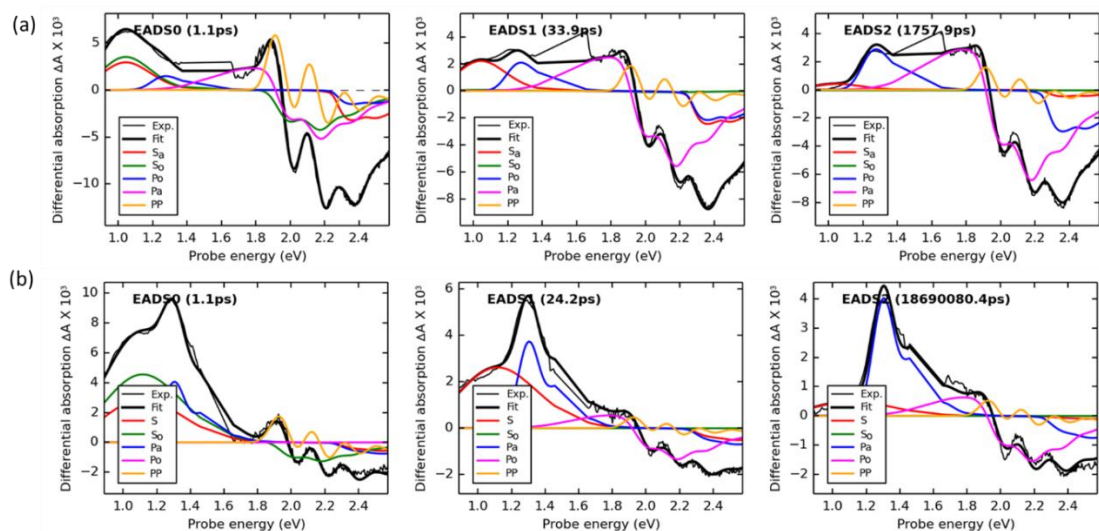


Figure 5.25. EADS of ITO/ZnO/PQOH(160)/PAL stack, pristine (a) and degraded at 140 °C for 5 h (b), as obtained from a global analysis of experimental TA spectra using a 3 sequential steps model (thin solid curves, fitted lifetimes are given in the legends), spectral fits to the EADS (thick solid curves) and contributions to fits from polaron pair, localised and delocalised singlet exciton and polaron states with their respective bleach contributions (negative differential absorption).

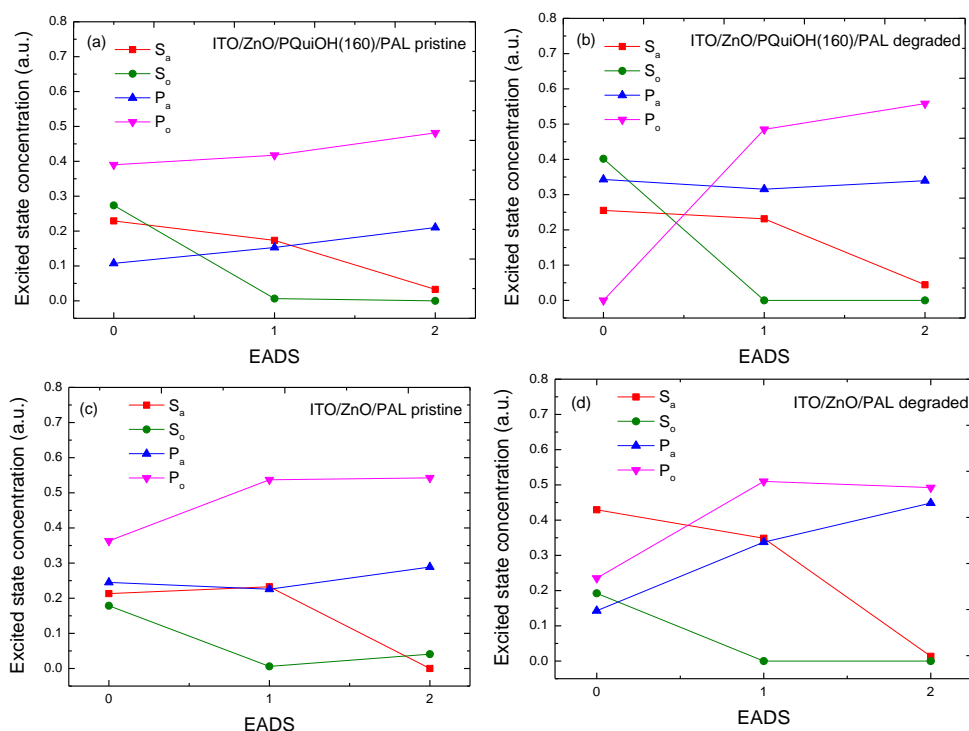


Figure 5.26. Evolution of excited states concentration according to their respective EADS in ITO/ZnO/PQOH(160)/PAL film stack before and after degradation (a and b, respectively) and ITO/ZnO/PAL stack (c and d, respectively): localised singlet excitons (S_a , red) and polarons (P_a , blue), delocalised singlet excitons (S_o , green) and polarons (P_o , magenta).

After degradation, an increased population of delocalised singlet excitons (S_o) is observed in the PQuiOH sample immediately following excitation, in contrast to the negligible population of delocalised polarons in the ordered phase (P_o). Ultrafast charge generation occurs only in the amorphous phase of P3HT, owing to localised polarons (P_a) of 0.34 a.u. concentration. Clearly, after degradation the ultrafast charge generation is lower than that in pristine cells (34% against that of 50% in pristine cells).

Within 1.1 ps following excitation, all delocalised excitons (S_o) reach the donor/acceptor interface and successfully dissociate to yield 0.55 a.u. delocalised polarons (P_o). As a result, the total charge yield in degraded PQuiBoc samples (90%) is much higher than that in pristine cells. This might be associated with the redistribution of PCBM in the polymer matrix, so that exciton dissociation happens at the single PCBM molecule/P3HT interface or at the small isolated islands. The polarons generated from such excitons are trapped within the islands and do not contribute to current density since they cannot be transported.

In the control sample, the same effect is also observed, but for localised singlets and polarons. Localised singlets (S_a) constitute the biggest contribution of the first EADS (0.43 a.u.) and gradually dissociate over the time of evolution into second and third EADS, meaning that the domain size increased above the exciton diffusion length. Thus, the ultrafast charge yield in the control sample is equal to 37% and the final charge yield reaches 94%. This increased charge yield might be associated with the molecules of PCBM diffused in the polymer matrix upon thermal treatment within the domains, improving the exciton dissociation.

Evidently, charge generation in PQuiBoc samples and the control sample are not very different, therefore, the explanation of the stabilising effect of PQuiBoc should be sought elsewhere. If the absorption, exciton dissociation and charge generation are very similar, the main difference should be in extraction and recombination processes. Indeed, from the photovoltaic parameters, it is clear that the effect of PQuiBoc on the stability of the blend morphology is negligible, whereas the stability of fill factor and open circuit voltage are much improved, although initial values are less than those in the control sample. It appears that extraction and recombination processes in the PQuiBoc devices have established an equilibrium that does not change with degradation. More detailed studies of recombination and extraction (at longer time scales) are necessary to distinguish their effects on the fill factor and open circuit voltage.

5.7.3 Interface stabilisation by a PQuiBoc layer

Photovoltaic studies of a PQuiBoc layer deposited onto a ZnO surface and annealed at different temperatures prior to deposition of the PAL blend showed that a PQuiBoc layer can induce improvements in the stability of the devices, although as a compromise of initial efficiency. Initially, PQuiBoc devices show improved current density values, increasing with the layer treatment temperature, and lower fill factor and open circuit voltage values. The performance of the cells can be correlated with AFM surface studies on PQuiBoc layers deposited onto ZnO. PQuiBoc has been seen to form micro-sized structures on the surface, whose size and height depended on the annealing temperature. Annealing the PQuiBoc layer at 140 °C produced large features on the surface of almost 200 nm height, whereas annealing at 160 °C (PQuiOH) induced surface smoothing so that the PAL deposited subsequently onto PQuiOH was also smooth and showed nanostructurisation. This nanostructurisation was likely to be the reason for a slight improvement of the current density in those samples. On the other hand, transient absorption spectroscopy studies proved that there was no significant difference in exciton dissociation and charge generation between the control and PQuiBoc samples. Therefore, the only factor that affected the performance of the PQuiBoc sample was the extraction-recombination equilibrium. From fill factor studies it was concluded that with the enhanced coverage of the ZnO surface by the PQuiBoc layer, upon post-deposition treatment, the recombination at the interface increased, leading to lower fill factors.

On the other hand, the fill factors seemed to improve in PQuiBoc samples when these were thermally degraded at 140 °C. The improvement was observed for the first 200 min of degradation, in line with increase of V_{OC} , so that after 150 min the efficiency of the control sample was similar to that of PQuiOH (160).

In summary, the final loss of efficiency in the control sample was almost 70%, whereas that in PQuiBoc sample, where the interfacial layer was annealed at 160 °C, was only 42%, demonstrating that an improvement in stability of the devices could be achieved with introduction of the interfacial PQuiBoc layers, although in this case as a trade-off between stability and efficiency. This result should be further used to guide the design of new materials for interface stabilisation.

5.8 Conclusions and suggestions for future work

New material was synthesised, based on the 8-hydroxyquinoline moiety that has been widely demonstrated to bind to zinc. Firstly, the QuiBoc monomer was synthesised from

commercially available reagents with relatively high yields, using Sonogashira cross-coupling and 'click' chemistry at different steps. Secondly, this monomer was polymerised by RAFT polymerisation (PQuiBoc) with high conversion and good control over molar mass with D_p of 20 (8.9 kg/mol) and 40 (17.5 kg/mol), although RAFT could not be employed for achievement of higher molar masses (D_p of 100) due to solubility issues. It was shown that PQuiBoc could be easily deprotected in solution by strong base piperidine or thermally (heating at 160 °C for 20 min) to give PQuiOH.

Electronic properties of PQuiBoc and QuiBoc were studied to estimate how polymerisation affected absorbance and emission. PQuiBoc polymer was shown to emit in the blue region of the visible spectrum with a maximum at 450 nm, which is bathochromically shifted as compared to the emission maximum of the monomer. Studies of the electronic levels by DFT showed that the emission difference originated, both in solution and solid state, from π - π stacking of the repeat units in the polymer chain. Moreover, electronic levels of PQuiBoc measured by cyclic voltammetry were similar to those of ZnO, normally used for electron transport in devices with inverted architecture. Substitution of ZnO by a polymeric material would give several advantages, the main of them being an elimination of the "S-shape" on the J - V curve, resulting from the intrinsic ZnO defects and accumulation of the trapped charges at the interface (as discussed in Section 1.4.4).²⁷⁻²⁹

In light of the above findings, PQuiBoc was first introduced as an electron-transporting layer, but was found to be less efficient than ZnO, majorly due to lower fill factor and open circuit voltage. Transient absorption spectroscopy measurements showed that the nanomorphology of the blend was not the reason, since the extractable charge yield was 73%, similar to that in typical P3HT:PCBM blends. The charge yield increased after 5 min of annealing at 140 °C in line with typically observed improvement of nanomorphology in the optimised blends. V_{oc} and FF also improve after annealing in the sample where PQuiBoc was deposited from 5 mg/ml solution. This improvement is associated with the decrease in roughness in annealed samples and increase in ITO surface coverage. As a result, upon short annealing, PQuiBoc 5 mg/ml samples showed performance superior to bare ITO samples, suggesting that PQuiBoc actually has a potential as electron-transporting layer if the wetting of ITO surface can be improved.

This can be achieved through various approaches. The first approach would be the incorporation of co-monomers increasing the affinity of PQuiBoc for ITO surface and wetting properties. The main difficulty here is that introduction of new moieties into the polymer will affect the electronic properties of PQuiBoc and result in different HOMO levels. Modelling of the co-monomer properties will be helpful for estimation of their suitability for application in electron-transporting polymer layer. The second approach would involve deposition of

PQuiBoc from a blend where one component would increase the wettability of ITO by this blend. The problem of affecting HOMO/LUMO levels by introducing the second component into the layer also exists for this approach, but can be used to tune the HOMO and LUMO levels for better electronic correlation between the PAL and the electron-transporting layer.

On the other hand, the extraction and recombination in PQuiBoc devices are still less efficient than those of ZnO-incorporating devices, indicating there is space for improvement of electronic coherence between the layers. Firstly, the effect of a PQuiBoc layer on the ITO work function should be studied. Secondly, as aforementioned, addition of co-monomers can be turned double advantageous if these co-monomers improve electronic levels and the work function of the ITO electrode.

Subsequently, PQuiBoc was deposited onto ZnO as an interfacial layer between the electron-transporting layer and P3HT:PCBM blend. The PQuiBoc layer was annealed at different temperatures to correlate the effect of deprotection with efficiency of the devices. It was shown that with the increase of post-deposition treatment temperature, the initial efficiency of the cells degraded, although current density increased from 10.13 mA/cm² (in samples without PQuiBoc) to 10.53 mA/cm² in samples with PQuiOH (160) layer. TAS showed that the charge generation in PQuiOH (160) devices was similar to that in control sample, therefore the improvement in the current density was attributed exclusively to better charge extraction. These findings were contradicted by lower FF and V_{OC} in pristine devices, especially pronounced in the cells where PQuiBoc was annealed at deprotection temperature. According to the AFM results, the coverage of ZnO by PQuiBoc increased with treatment temperature, therefore the PQuiBoc layer was suggested to increase surface recombination and, as a result, reduce the fill factor.

When the PQuiBoc devices were degraded, fill factor and open circuit voltage gradually reached their maximum values after several hours of heating and did not degrade significantly. Compared to the control sample, PQuiOH (160) devices lost only 42% of the initial PCE (versus 67% in control). This loss was attributed exclusively to charge generation reduction, originating from blend segregation. This charge generation reduction was reflected by the loss of current density, comparable to that in the control samples. PQuiBoc (140) devices also showed improved stability, having lost only 52% of their initial efficiency owing to stabilisation of the fill factor and open circuit voltage.

These findings indicate that a PQuiBoc interfacial layer deposited between ZnO and the PAL can potentially be used for stabilisation of the devices. Thermal annealing induces improvements in the interlayer charge transport process until extraction and recombination reach equilibrium. This equilibrium does not represent the best performance scenario, but is stable to thermally induced changes. Mobility studies in the PQuiBoc layer deposited at

different temperatures will shed light on the recombination-extraction equilibrium. Thus, dynamic processes occurring in newly-designed polymeric layers after deposition might be a key to establishing stable devices in the future and should be studied in detail to provide an insight into optimal materials design.

5.9 References

- (1) Hamada, Y.; Sano, T.; Fujita, M.; Fujii, T.; Nishio, Y.; Shibata, K. *Jpn. J. Appl. Phys.* **1993**, 32 (Part 2, No. 4A), L514–L515.
- (2) Donzé, N.; Péchy, P.; Grätzel, M.; Schaer, M.; Zuppiroli, L. *Chem. Phys. Lett.* **1999**, 315 (5-6), 405–410.
- (3) Du, N.; Mei, Q.; Lu, M. *Synth. Met.* **2005**, 149 (2-3), 193–197.
- (4) Fang, X.-M.; Huo, Y.-P.; Wei, Z.-G.; Yuan, G.-Z.; Huang, B.-H.; Zhu, S.-Z. *Tetrahedron* **2013**, 69 (47), 10052–10059.
- (5) Heiskanen, J. P.; Hormi, O. E. O. *Tetrahedron* **2009**, 65 (39), 8244–8249.
- (6) Montes, V. a; Pohl, R.; Shinar, J.; Anzenbacher, P. *Chemistry* **2006**, 12 (17), 4523–4535.
- (7) Omar, W. a. E.; Hormi, O. E. O. *Tetrahedron* **2009**, 65 (22), 4422–4428.
- (8) Horowitz, E.; Perros, T. P. Synthesis and thermal stability of bis(8-hydroxy-quinoline)-Schiff base coordination polymers <https://archive.org/details/jresv69An1p53> (accessed Jun 18, 2015).
- (9) Mei, Q.; Du, N.; Lu, M. *J. Appl. Polym. Sci.* **2006**, 99 (4), 1945–1952.
- (10) Wang, C.; Zhang, W.; Zhou, N.; Qiu, Y.; Cheng, Z.; Zhu, X. *Int. J. Polym. Sci.* **2010**, 2010, 1–7.
- (11) Gelman, D.; Buchwald, S. L. *Angew. Chemie-International Ed.* **2003**, 42 (48), 5993–5996.
- (12) Gelman, D.; Buchwald, S. L. *Angew. Chem. Int. Ed. Engl.* **2003**, 42 (48), 5993–5996.
- (13) Krakowiak, K. E.; Bradshaw, J. S. *Synth. Commun.* **1996**, 26 (21), 3999–4004.
- (14) Isidro-Llobet, A.; Alvarez, M.; Albericio, F. *Chem. Rev.* **2009**, 109 (6), 2455–2504.
- (15) Kasha, M. *Discuss. Faraday Soc.* **1950**, 9, 14.
- (16) Fox, R. B. *J. Chem. Phys.* **1972**, 57 (1), 534.
- (17) Birks, J. B. *Reports Prog. Phys.* **1975**, 38 (8), 903–974.
- (18) D'Souza, F.; Maligaspe, E.; Zandler, M. E.; Subbaiyan, N. K.; Ohkubo, K.; Fukuzumi, S. *J. Am. Chem. Soc.* **2008**, 130 (50), 16959–16967.
- (19) Chen, S.; Manders, J. R.; Tsang, S.-W.; So, F. *J. Mater. Chem.* **2012**, 22 (46), 24202.

- (20) Grossiord, N.; Kroon, J.; Andriessen, R.; Blom, P. *Org. Electron.* **2012**, *13* (3), 432–456.
- (21) Guo, J.; Ohkita, H.; Bente, H.; Ito, S. *J. Am. Chem. Soc.* **2009**, *131* (46), 16869–16880.
- (22) Howard, I.; Mauer, R.; Meister, M.; Laquai, F. *J. Am. Chem. Soc.* **2010**, *132* (42), 14866–14876.
- (23) Deibel, C.; Dyakonov, V. *Reports Prog. Phys.* **2010**, *73* (9), 96401.
- (24) Park, B.; Huh, Y. H.; Kim, M. *J. Mater. Chem.* **2010**, *20* (48), 10862.
- (25) Hau, S. K.; Cheng, Y.-J.; Yip, H.-L.; Zhang, Y.; Ma, H.; Jen, A. K.-Y. *ACS Appl. Mater. Interfaces* **2010**, *2* (7), 1892–1902.
- (26) Bulliard, X.; Ihn, S.-G.; Yun, S.; Kim, Y.; Choi, D.; Choi, J.-Y.; Kim, M.; Sim, M.; Park, J.-H.; Choi, W.; Cho, K. *Adv. Funct. Mater.* **2010**, *20* (24), 4381–4387.
- (27) Saive, R.; Mueller, C.; Schinke, J.; Lovrincic, R.; Kowalsky, W. *Appl. Phys. Lett.* **2013**, *103* (24), 243303.
- (28) Shao, S.; Zheng, K.; Zidek, K.; Chabera, P.; Pullerits, T.; Zhang, F. *Sol. Energy Mater. Sol. Cells* **2013**, *118* (118), 43–47.
- (29) Shao, S.; Zheng, K.; Pullerits, T.; Zhang, F. *ACS Appl. Mater. Interfaces* **2013**, *5* (2), 380–385.

CHAPTER 6 GENERAL CONCLUSIONS

6. General conclusions

Only recently the scientific community acknowledged the importance of interfaces in determining the thermal stability of organic solar cells. Various approaches to interface engineering were reported, as described in Section 1.7.3, most of them employing small molecules. In this work, the emphasis was made on design and application of polymers at zinc oxide/photoactive layer interface, in particular important for extraction of electrons. These polymeric layers are designed to improve contact between two layers, electronic coherence, wetting properties, stability to oxidation and delamination, decrease surface resistance and recombination, etc.

The main objectives of this research were:

- Synthesise new interfacial layers, based on the zinc-binding ligands, reported in literature;
- Study the effect of these interlayers on the efficiency of the pristine devices and stability of devices under accelerated thermal stress;
- Decouple interfacial degradation mechanism from the blend morphology changes in thermally degraded devices with the interfacial layers.

Two types of zinc-binding ligands have been chosen for this study, based on literature reports: 3,4-dihydroxybenzene and 8-hydroxyquinoline. The choice was supported by the computational modelling, performed by the project partner Hugo Santos Silva. Corresponding conclusions and suggestions for future work are presented in relevant sections, thus, in this chapter only the general conclusions are presented that were made throughout the synthesis, characterisation and modelling, performed in this work.

Initially, the main idea of this work was to study the effect of self-assembling polymeric monolayers on the device efficiency and stability. However, this approach has turned out to be arguable, since the polymeric layers do not form 'self-assembling monolayer's in the same form that the small molecules do. Thus, poly(3,4-dihydroxystyrene) (PDHS) when bound to zinc oxide and washed, formed a layer of 5-6 nm which was substantially thick and majorly affected the charge transport through this layer. When deposited onto ZnO, it increased its work function and therefore created an energy barrier for electron transport. This barrier was also observed for fullerene derivative, PDHS-FUL, in "S-shaped" *J-V* curves and by transient electric measurements, where recombination was as fast as several hundred nanoseconds, and the extraction was twice as slow (on a microsecond time scale). Because of their insulating properties, PDHS and PDHS-FUL were concluded to be unsuitable for application as interfacial layers.

On the other hand, parental polymer, poly(3,4-dimethoxystyrene) (PDMS), was successfully employed in its cross-linked form. Cross-linking of the interfacial layers provides several advantages, one of them being the subsequent deposition of the photoactive layer from the same solvent without the erosion of the underlying layers. Cross-linked PDMS and its fullerene derivative, PDMS-FUL, were beneficial for the initial efficiency of pristine devices, owing to their ability to improve electron extraction. In parallel, the stability of the devices was also improved, owing to the presence of non-cross-linked PDMS and PDMS-FUL molecules. These molecules intermixed with the photoactive blend and served as compatibilisers, preserving the blend morphology from phase segregation. This effect was also confirmed by transient absorption spectroscopy measurements, where ultrafast and total charge yields were observed through 'global' or 'targeted' analysis of the excited states of P3HT. This study points out the importance of comprehensive analysis of the processes, underlying the device efficiency, including those that do not seem to be obvious from the first sight.

The example of PDMS and PDMS-FUL cross-linked interfacial layers also demonstrates that straightforward approaches, involving facile syntheses, can be efficient in sophisticated systems, such as OPVs.

The second ligand, 8-hydroxyquinoline, was prompted by research in organic light-emitting diodes (OLEDs), where aluminium and zinc complexes of 8-hydroxyquinoline are used as light-emitting or electron-transporting materials. In a polymeric form (PQuiBoc), this ligand also demonstrated fluorescent properties, both in BOC-protected form and in deprotected Zn-bound form. The fluorescence was suggested as beneficial property, useful for converting the harmful UV-radiation into useful green (or blue) photons, especially in combination with deep HOMO levels of the polymer, suitable for electron transport. However, when used as electron-transporting layer instead of ZnO, devices with PQuiBoc were only slightly more efficient than those with bare ITO. More detailed analysis of the interface properties is needed, including measurements of the work function of ITO when PQuiBoc polymer is deposited onto it. The example of PDHS has already demonstrated that even the thinnest layers of polymer can negatively affect the work function of the electrode.

On the other hand, when deposited onto ZnO as an interfacial layer, PQuiBoc improved the device stability, although as a compromise of initial efficiency. AFM studies allowed to correlate the surface topography of the quinoline polymer layer to its effect on the stability of the devices. Smoother layer of deprotected PQuiOH affected extraction in pristine devices, resulting in lower fill factors, but upon thermal degradation, these fill factors did not experience such drastic loss as those in control devices without interfacial PQuiOH layer. Further analysis is needed to understand how the deprotection of the polymer influences charge transport through this layer. Upon deprotection, the BOC-group is cleaved and the 5-

hydroxyquinoline moiety binds to zinc oxide, changing the electronic levels of the layer (as observed from absorbance and fluorescent studies of PQuiBoc in Section 5.3). Only chains in contact with ZnO would be able to bind upon deprotection, whereas the rest of the chains would only lose the BOC group. Thus, deprotection yields two types of moieties in one layer with different electronic properties: PQuiOH-ZnO and PQuiOH. Understanding how this changes the HOMO and LUMO levels of the layer is the key to unravelling the mechanisms of stabilisation of devices by PQuiOH layer.

Generally, design of materials to be used at the ZnO/photoactive layer interface, unlike that of ternary agents in the bulk, requires more complex approach because it has to address several aspects:

1. Interfacial polymeric layer (IPL) should be compatible with the photoactive blend;
2. IPL should bind to ZnO, preferably by covalent interactions so that it would withstand washing by solvent;
3. IPL should be electronically coherent with the photoactive layer and ZnO to facilitate the electron transfer;
4. IPL should not have a detrimental effect on the work function of the ZnO layer;
5. IPL should be stable to thermal treatment, unless it induces uniform changes within the whole layer and is necessary for the IL performance (e.g., in case of cross-linking);
6. IPL should be synthesised in a facile and straightforward process.

Should these requirements be met, the polymeric layer can be used to stabilise the interface between ZnO and the photoactive layer without detrimental effect for the initial device efficiency. Although there are reports of interfacial polymeric layers of sophisticated structures that improve device efficiency and stability under illumination, the reports about stability under accelerated thermal stressed are very limited. Thus, research into IPL is strategically important for solving the problem of intrinsic instability of the devices at elevated temperatures under operational conditions to increase the lifetime of devices to the targeted 10 years.